School of Science
Department of Chemistry

Improving the efficiency of computation of free energy differences

Zoe Rebecca Taylor

This thesis is presented for the Degree of
Doctor of Philosophy
of
Curtin University

November 2011

Declaration

To the best of my knowledge and belief this thesis contains no material previously published by any other person except where due acknowledgment has been made.

This thesis contains no material which has been accepted for the award of any other degree or diploma in any university.

Signed: _____

Date: _____

Abstract

There has been a recent focus on investigating the properties of semi-conductors at the nanoscale as it is well known that the band-gap of semi-conducting materials is altered due to quantum confinement effects. The potential to fine-tune a material's properties based solely on particle size has raised significant interest both in experimental and computational studies. Zinc sulfide is one of the most studied metal sulfide semi-conductor minerals, due to its potential technological applications.

Computational studies of the structural and thermodynamic properties of zinc sulfide nanoparticles and bulk structures have been performed throughout this work. A variety of computational methods have been employed, including molecular dynamics, lattice dynamics, first principles calculations, and free energy techniques, such as metadynamics and free energy perturbation. The thermodynamic stability of zinc sulfide nanoparticles as a function of size and shape has been studied. Investigation of the phase space of these systems required the use of enhanced sampling methods. The metadynamics method was specifically utilised to explore as many structures as possible in combination with extensive simulations. The use of first principles methods for these exploratory simulations was found to be prohibitively expensive, and so force field methods were primarily utilised. Throughout this investigation several force fields were used to compare and contrast their accuracy, while first principles calculations were performed, where possible, to assist in the interpretation and validation of the results.

In the present study, two different collective variables, the trace of the inertia tensor and the Steinhardt bond order parameters, have been implemented and their performance in metadynamics compared. The trace of the inertia tensor was found to be useful for exploring clusters of small sizes, while the Q_4 Steinhardt parameter, which describes the crystalline order of a solid, is more applicable to larger clusters. Both of these metadynamics studies resulted in clusters displaying zeolite structural motifs, including the zeolite framework 'BCT'. This led us to investigate more thoroughly the stability of different zinc sulfide zeolite analogues, thereby highlighting the strengths and weaknesses of all the force fields employed. Many force fields are found to be unable to accurately represent the order of stability for bulk polymorphs. First principles calculations also highlighted that the BCT phase is less stable than either of the bulk polymorphs of zinc sulfide, in contrast

to the order of stability obtained by force fields lacking a torsional term, both from literature and the rigid ion model developed during the current study. The larger nanoparticles cleaved from wurtzite exhibited internal strain upon relaxation. A new hypothetical zeolite framework was constructed from the distorted core of these clusters, and was found to possess structural similarities with the 'APC' framework. The APC framework is composed of double crankshaft-chains with 'ABCABC...' stacking, while the hypothetical framework identified is formed by the same composite building unit with 'ABAB...' type stacking. For all the force fields used the new hypothetical framework was lower in energy than the APC framework, but higher in energy than sphalerite, wurtzite or the BCT phase.

Free energy differences between small ZnS clusters in vacuum were calculated using the path variable technique, and also using static methods within the quasi-harmonic approximation. Similar values were obtained using both of these methods, validating the path collective variables used with metadynamics as an effective means of obtaining free energy differences for clusters in vacuum.

In addition to clusters in vacuum, a number of studies of ZnS clusters in water were also performed. Both force field and first principles studies were employed to validate the ZnS-water interactions used for the binding energies of water to small clusters. As a further validation, the free energies of solvation of Zn^{2+} and S^{2-} in aqueous solution were calculated. The free energy of solvation for the sulfide anion was found to be close to the experimental value, while the parameters for Zn^{2+}-water were found to require substantial modification as the solvation free energy was in error by 500 kJ/mol. While newly derived ZnS-water parameters may prove to be superior for describing ZnS clusters in bulk water, a repetition of the binding energy calculations for individual water molecules bound to ZnS clusters gave energies 2-3 times greater than those obtained via first principles methods and using the five other force fields investigated. These results highlight the issues present when attempting to transfer a model fitted in a certain way to a different application. In particular, the many-body and polarisation effects present when modelling water need to be considered when parameterising ZnS-water interactions.

Acknowledgements

I would like to express my gratitude to my supervisors Prof. Julian Gale and Dr. Stefano Piana, whose support, guidance, incredible expertise and patience have made this thesis possible. I also need to thank them both for giving me the opportunity to travel to Italy and meet with experts in the field of free energy techniques. This was an invaluable experience that I will never forget.

To Prof. Kate Wright, I want you to know your unfailing optimism, advice and words of encouragement have always been greatly appreciated.

To the members of the coffee club and the terminal room (in all of their different iterations over the years) who have been a daily sounding board through all the good and the bad, I cannot thank you enough for your friendship. In particular I would like to thank Amy Bowater, Daniel Southam, Hanna Driessen, Nicole Becker, and Zak Hughes.

To my family and Paolo, thank you for putting up with the emotional roller-coaster throughout my PhD, your love and support has helped me in ways I cannot express, I only hope I can return the favour.

Finally, I acknowledge iVEC and the National Computational Infrastructure (NCI) for access to the computational resources which made this work possible, and the Australian government for provision of an APA scholarship.

Contents

List of Figures

List of Tables

Abbreviations

AMD	**A**cid **M**ine **D**rainage
BCT	**B**ody-**C**entred **T**etragonal
ccp	**c**ubic **c**lose **p**acking
CPMD	**C**ar-**P**arrinello **M**olecular **D**ynamics
CV	**C**ollective **V**ariable
DFT	**D**ensity **F**unctional **T**heory
fcc	**f**ace-**c**entred **c**ubic
FES	**F**ree **E**nergy **S**urface
GGA	**G**eneralised **G**radient **A**pproximation
HF	**H**artree-**F**ock
hcp	**h**exagonal **c**lose **p**acking
IZA	**I**nternational **Z**eolite **A**ssociation
IZA-SC	**I**nternational **Z**eolite **A**ssociation-**S**tructure Commission
KS	**K**ohn-**S**ham
LDA	**L**ocal **D**ensity **A**pproximation
MC	**M**onte **C**arlo
MEP	**M**inimum **E**nergy **P**ath
MetaD	**Metad**ynamics
MD	**M**olecular **D**ynamics
MEP	**M**inimum **E**nergy **P**ath
MM	**M**olecuar **M**odelling
PDF	**P**air **D**istribution **F**unction
PES	**P**otential **E**nergy **S**urface
PT	**P**arallel **T**empering

QM   **Q**uantum **M**echanics

SCF   **S**elf-**C**onsistent **F**ield

TST   **T**ransition **S**tate **T**heory

Chapter 1

Introduction

1.1 Nanoscience and Nanotechnology

Nanotechnology is an inter-disciplinary field encompassing physics, chemistry and engineering, and concerns the science and applications of systems which have at least one dimension measured in the range of 1-100 nm[1]. Materials with dimensions at the nano-scale have shown surprising characteristics, very different to those of bulk structures[2, 3]. Discoveries at this scale have led to the realisation that by understanding materials at the atomistic level, we may be able to tailor materials with specific physical properties[4].

There are have been a number of significant drivers for research in the field of nanotechnology. One of these is that the goal of device science is continued miniaturisation[5]. As there has been an increased demand for smaller, portable technologies, computational devices, such as microchips, have been engineered to be smaller and smaller. This trend was first described in 1965 by Moore [6], who observed that the number of transistors on silicon-based integrated circuits was doubling approximately every year. He later revised this in 1975[7] to doubling every two years, however it is now commonly quoted that the rate of increase doubles every 18 months. The microelectronics industry has managed to maintain this level of increased miniaturisation in devices, with the feature size of transisitors being driven from the micron scale down to approximately 30 nm[8]. However it faces major technical challenges if the feature sizes are to be miniaturised much further. As the dimensions of the semiconductor materials used in these devices gets down to the nanoscale the electronic and optical properties deviate from those

of the bulk material due to a phenomenon known as quantum confinement[9]. A thorough understanding of these size-dependent electronic properties in materials is necessary to continue to develop successful technological devices at a small scale.

Following on from this trend for miniaturisation and continued integration of nanomaterials into everyday technology, various discoveries of novel clusters at the nanoscale have been made in the past 50 years. As a result there has been growing concern of how engineered nanoparticles interact with our environment and ourselves[10]. If there is a significant difference in the behaviour of nanoparticles of a material in comparison to the bulk of the same material, then there is the question of how its behaviour in the environment has changed. The size range of nanoparticles is an additional cause of concern as they are at the same size range as many biomolecules and there is the possibility of absorption into biological systems[10]. There may be toxicological effects and other environmental hazards that need to be understood before a nano-scaled material can be considered safe to mass produce and use commercially[11]. Unfortunately, as nanoparticles of different materials will behave very differently to one another, it is almost impossible to provide a generalised summary of the hazards associated with all nanoparticles[12], and individual studies are necessary for different systems.

This introductory chapter will provide a broad overview of nanostructured materials, and nanoscale systems will be the focus of this thesis. However, before we can really compare and contrast the properties of nanoscale materials, it is necessary to first provide a brief introduction to the physics of the solid state in a context of bulk materials.

1.2   Electronic structure and band theory

In this section we will introduce the basics of electronic structure and band theory in bulk materials and summarise how these theories are significantly altered in the context of much smaller systems.

The electronic structure of a molecule can be represented as a linear combination of the atomic orbitals of its constituent atoms. In molecular orbital theory some of the electrons are "delocalised" and contribute to the intermolecular bonding where there are overlapping atomic orbitals [13]. In the extreme case, where we have an extended three-dimensional array of atoms in a solid, atomic orbitals throughout this array will take part in delocalised bonding throughout the solid. This is depicted in Figure 1.1, where we can consider the molecular orbitals in a system of increasing size. With only one atom, there is a given set of atomic orbitals of certain energies. Bringing a second atom into the picture will produce overlapping atomic orbitals, and so bonding and anti-bonding molecular orbitals will be formed. This will continue for all N atoms in a solid, until there will be N molecular orbitals contained with a band of finite width, bounded by the highest and lowest energy orbitals formed. For a system of very large N the high density of molecular orbitals separated by very small energy differences results in essentially a continuous energy "band". If there is a difference in the energy between the bonding and anti-bonding orbitals, and the two bands don't overlap, there exists what is known as a *band gap*.

The existence and size of the band gap will determine the electrical properties of the solid[15]. A schematic of the valence and conduction bands, and their electron
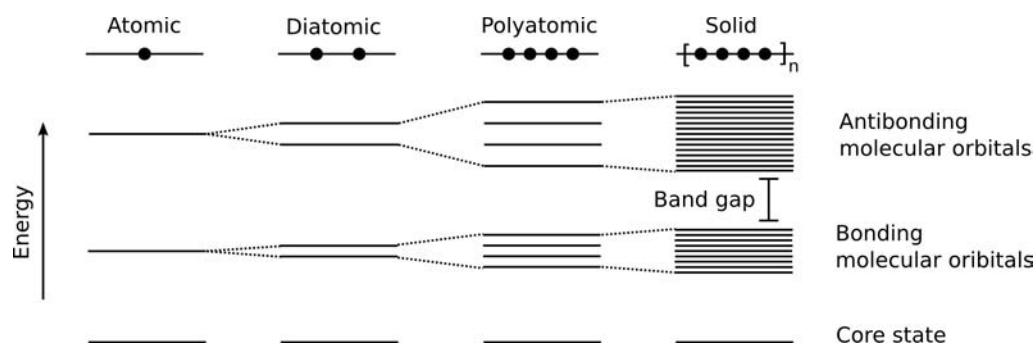
FIGURE 1.1:   Schematic showing the broadening of molecular orbitals into energy bands with an increasing linear chain of atoms. For a system of large N the high density of molecular orbitals results in essentially a continuous energy "band". Image adapted from Kelsall *et al.* [14].
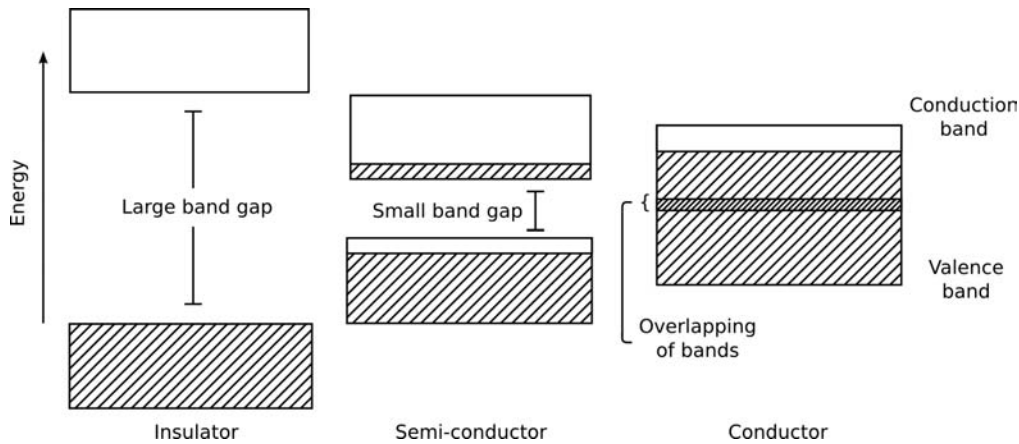
FIGURE 1.2: Schematic of the electron occupancy of allowed energy bands in insulators, semi-conductors and conductors. The degree of shading indicates the electron occupancy in each band. Image adapted from Poole Jr and Owens [3].

occupancy, for different types of materials is shown in Figure 1.2. Electrons can have energy values which exist within any of the bands, but cannot have energies corresponding to the values of the gaps between the bands[3]. The low energy bands, corresponding to the inner atomic levels are narrow and filled with electrons. The outer electrons are known as the *valence* electrons and are involved in bonding the crystal together; they occupy what is known as the *valence band*. When the valence band is full, and the band gap is on the order of $k_B T$, thermal energy will be enough to excite valence electrons and promote them across the band gap into the conduction band. The electrons will be mobile and the solid is able to conduct electricity. Materials such as this, with a small band gap that can be overcome by thermal energy, are known as *semiconductors*. In cases where the valence band is full, but the band gap is too large to allow electrons to be promoted from the valence to the conduction band, the material will not conduct electricity and is referred to as an *insulator*. If there is no band gap, and the valence and conduction bands overlap, the material is simply a *metal* (or *conductor*), as electrons are able to pass freely between the valence and conduction bands, and conduct electricity[15].

A semiconductor material can be 'doped' with small amounts of impurities which enhance the electrical conductance of the material[3]. The dopants can be acceptor atoms, which obtain electrons from the valence band, and leave behind positive charges called *holes* which also carry current. These types of semiconductors are known as *p*-type semiconductors, with positive-charge or "hole" conductivity.

Alternatively the dopants can be donor atoms, which give electrons to the conduction band, and these semiconductors are *n*-type semiconductors, with negative-charge or "electron" conductivity.

The combination of the excited electron and the hole it leaves behind in the valence band are known collectively as an *exciton*. There is a material-specific distance that exists between the excited electron and the hole in the valence band, and this is referred to as the *exciton Bohr radius*. In the context of bulk materials the exciton radius is very small in comparison to the dimensions of the bulk crystal, and for the most part the paths of excitons will be unimpeded by the size of the system.

The picture is very different when we consider a particle with dimensions at the same order of magnitude as the exciton radius. An exciton in a system at the nanoscale will not have the same freedom of movement as it had in the bulk - its movement will be restrained by the physical dimensions of the crystal. This phenomenon is known as *the quantum size effect*, or *quantum confinement*. In terms of the electronic structure, the almost continuous set of N energy levels in each band, for the bulk system of large N atoms, is replaced by far fewer discrete energy levels, and the energy difference between the two bands is increased[3, 16]. This electronic density of states falls somewhere between the atom and bulk. The significance of this change in band gap is depicted in Figure 1.3. In the case of a metal, the bulk material is clearly a conductor, but as the size of this system is reduced to small clusters of atoms, the energy range of the band widths decrease,
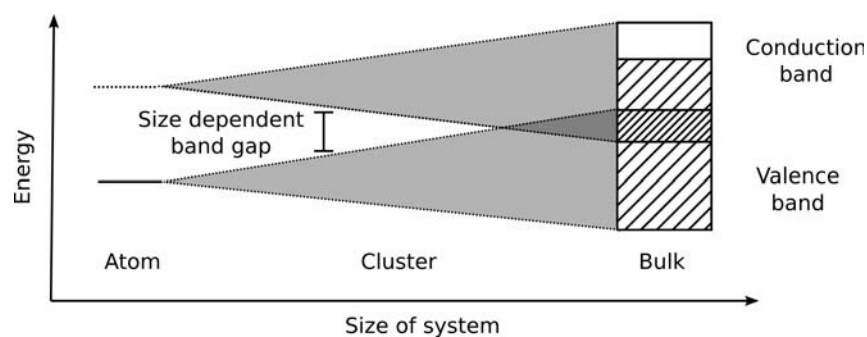
FIGURE 1.3: Schematic showing the size dependence of the band gap. Here a metallic material has been used as an example; in the bulk phase it is a conductor, but in smaller clusters of the material the energy bands will separate and a band gap will exist, making the clusters semi-conducting, and if the band gap is big enough - an insulating material. Image adapted from Ganteför [16].

and result in the formation of a band gap - significantly altering its electronic structure.

Specific studies where deviations from behaviour of "macrocrystals" have been observed in small scale systems will be discussed in later sections. First it is necessary to introduce another fundamental area of solid state physics which shows size-dependent behaviour, the theories of crystal structure, and geometry.

1.3   Crystal structure, polymorphism and geometry

The structure and morphology of a material can vary dramatically with a change in system size [17]. We will first introduce some of the fundamentals of the crystal structure and geometry found in bulk systems, before contrasting this with how these underlying theories are changed in the context of much smaller systems.

Bulk materials commonly exist as crystalline structures, with their atoms arranged in a regular manner[3]. Crystalline structures can be constructed by infinite repetition of identical structural units in space[15]. In simple crystalline solids the structural unit will be a single atom, such as in a solid metal like gold or silver. Other materials may have structural units of many atoms or molecules[15]. The structure of all crystals can be described in terms of a lattice, with structural units (an atom, or group of atoms) placed at the lattice points. The distinct lattice types for crystals are known as *Bravais lattices*. In two dimensions there are five distinct lattice types and these are shown in Figure 1.4, with their *unit cell* indicated. The unit cell is a set of points that can be replicated within the plane to generate the lattice. In the two dimensional Bravais lattices there are two
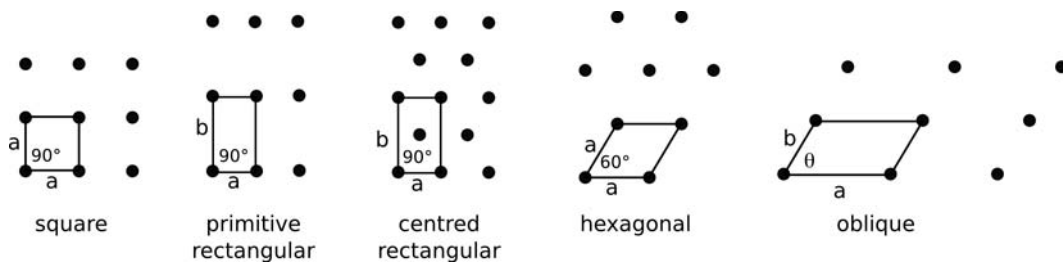
FIGURE 1.4: Illustration of the five Bravais lattices possible in two dimensions, the unit cells for each lattice are included in the diagram as lines.

lattice constants a and b for the modulus of the vectors, and θ, the angle between a and b.

In three dimensions there are six lattice constants, comprised of three side lengths a, b and c and three angles α (between b and c), β (between a and c) and γ (between a and b)[15]. In three dimensions there are 14 distinct lattice types; three exist with a cubic unit cell, and are shown in Figure 1.5.
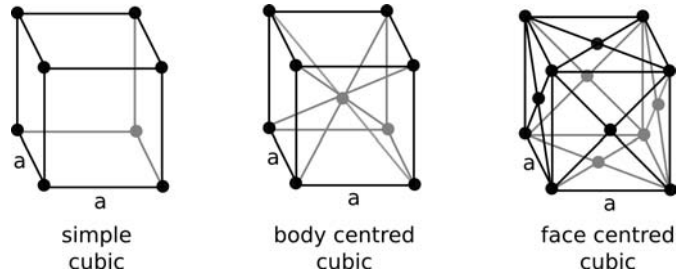
FIGURE 1.5: Illustration of the three cubic Bravais lattices possible in three dimensions.

In crystallography a notation known as Miller indices is used to define specific crystal planes. The Miller index of a plane is represented by three integers enclosed in parentheses, (hkl)[15]. The values of h, k and l are determined by finding the intercepts on the axes of the crystal cell (which can be either primitive or non-primitive) and taking the reciprocals of these. The values of the reciprocals are converted to integer values having the same ratio as the reciprocals. The Miller indices of common crystal planes of a cubic crystal are given in Figure 1.6.
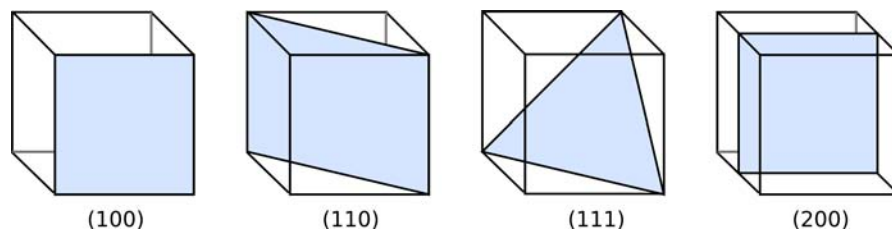
FIGURE 1.6: Illustration of the common cubic crystal planes and their Miller indices.

An important concept in solid state physics related to the Bravais lattices and Miller indices is the idea of reciprocal space, or k-space. For any three-dimensional lattice with primitive axis vectors $\mathbf{a}_1$, $\mathbf{a}_2$ and $\mathbf{a}_3$ the axis vectors $\mathbf{b}_1$, $\mathbf{b}_2$, $\mathbf{b}_3$ of *reciprocal space* can be constructed[15, 18]:

$$\mathbf{b}_1 = 2\pi \frac{\mathbf{a}_2 \times \mathbf{a}_3}{\mathbf{a}_1 \cdot \mathbf{a}_2 \times \mathbf{a}_3}; \quad \mathbf{b}_2 = 2\pi \frac{\mathbf{a}_3 \times \mathbf{a}_1}{\mathbf{a}_1 \cdot \mathbf{a}_2 \times \mathbf{a}_3}; \quad \mathbf{b}_3 = 2\pi \frac{\mathbf{a}_1 \times \mathbf{a}_2}{\mathbf{a}_1 \cdot \mathbf{a}_2 \times \mathbf{a}_3} \quad (1.1)$$

The Brillouin zone is a unique volume within reciprocal space[15]. The planes which define the boundaries of the Brillouin zone are perpendicular bisectors of the reciprocal lattice vectors drawn from the origin. The first Brillouin zone is the smallest volume that can be defined by these planes[15]. An example of a first Brillouin zone is given in Figure 1.7, where the first Brillouin zone for the face-centred cubic lattice is illustrated; the axes in this figure indicate the Brillouin zone is a volume in reciprocal space, or k-space, and points within reciprocal space are referred to as k-points. These zones are crucial to analysing and understanding the electronic energy-band structure of crystals. Later in this work we will consider some electronic structure calculations, and these require some understanding of the Brillouin zones and reciprocal space.
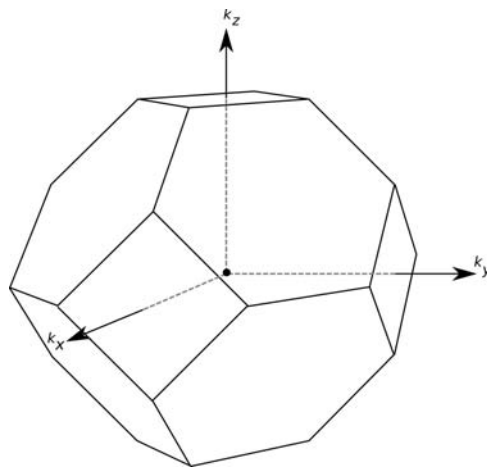
FIGURE 1.7: Illustration of the first Brillouin zone for an fcc lattice.

Crystal structures of many materials can be depicted in terms of close packing spheres, as illustrated in Figure 1.8. Close packing of equal-sized spheres in one plane produces a layer of spheres with hexagonal symmetry[19] (the first layer is indicated as layer A in Figure 1.8). A subsequent layer of spheres can be nested on top of the first layer; this layer becomes layer B. When adding a third layer of spheres to this sequence there is a choice to stack this layer directly over the atoms in the first layer, layer A, or to create a new layer C. The first option gives layers with a sequence of A-B-A-B..., and this form of packing is known as hexagonal close-packing (hcp). The second option has three distinct layers, and has a sequence of A-B-C-A-B-C..., and this packing is known as face centred cubic (fcc) or cubic close-packed (ccp).

Materials can usually exist in a number of structural forms, depending on the environmental conditions. When this is the case, the material exhibits what
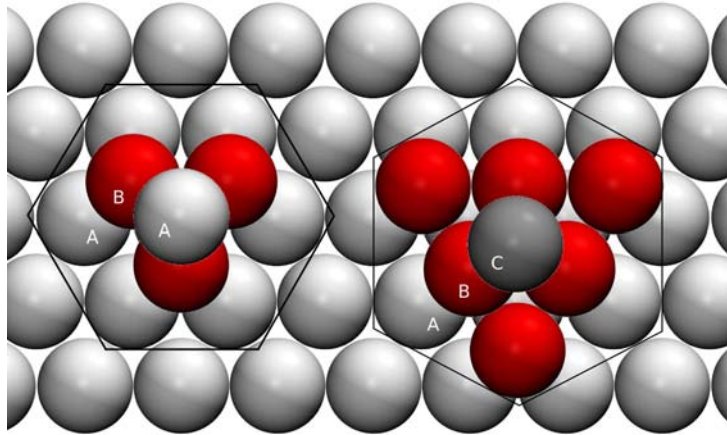
FIGURE 1.8: Illustration of close packing of spheres giving maximum density. Both structures are formed by alternate stacking of layers of spheres. On the left there is the hexagonal close-packed (hcp) structure, with alternating layers in the form (A-B-A-B...). Shown on the right is the face centred cubic (fcc) packing, where layers alternate in the sequence (A-B-C-A-B-C...).

is known as *polymorphism*, and each structural form is a *polymorph* of that material. Polymorphism can be exhibited in the simplest case for an element, and in this special case the terms allotropism and allotropes are often used. D.K. Chernov, a Russian scientist, was the first to document polymorphism in steel in 1868[20], and his work is an interesting example of early structural studies in bulk materials. Chernov was studying the heat treatment of steel, with the main goal of trying to discover why steel production could yield materials of very different quality - from extremely durable, to very defective, poor quality steel. Chernov methodically investigated the effects of the composition (primarily iron with small percentages of carbon), temperature and forging conditions on the structure and mechanical properties of steel. His investigation led him to discover critical points that correspond to the temperatures at which structural transformations occur in steel[20]. Ultimately Chernov was investigating polymorphism (or allotropism) of iron, which has been studied and confirmed in greater detail more recently[21–23]. Since his discoveries, he has been lauded as the "father of metallurgy", as his insights into how heat treatment influences the structure of the steel changed the fundamentals of metallurgy from a black-art to a science[24]. Iron has seven polymorphs, but the most commonly studied are austenite (γ-iron) and ferrite (α-iron). Chernov observed and documented transformations between these two polymorphs, with α-iron existing as a body centered cubic (bcc) crystal structure which transforms to the face centred cubic (fcc) structure of γ-iron when it is heated to 910°C.

Another example of a metal showing polymorphism in the context of close-packed structures is lead. In 1969 Takahashi *et al.* [25] showed that lead can transform from fcc packing to hcp packing under a pressure of 14 GPa. At pressures of about 100 GPa the hcp packed form of lead undergoes a transformation to body centred-cubic, bcc, which is no longer a close-packed structure[26]. These studies into the transformation to the bcc form were confirmed in the same year by Vanderborgh *et al.* [27]. More recently a pressure-temperature phase diagram of lead was produced by Kuznetsov *et al.* [28] to try to explore the fcc-hcp phase transition region in more detail.

If we take these examples of crystal structures for bulk materials and consider them in a context of finite nano-scale clusters, our observations will change. Clusters are finite objects, with a very high surface/volume ratio; this means they generally will have a large surface energy contribution, which will effect both the cluster properties and morphology[17]. Due to the large surface energy, many small clusters do not maintain the crystalline form found in their bulk counterparts. An example of this are metal clusters, such as gold or silver. Ordinarily, bulk gold takes on the close-packed face-centred cubic structure. Nanoclusters of gold instead have their atoms arranged in the densest way possible for these finite structures with large surface energy contributions. As a result, the lowest energy conformation for small cluster sizes gives an icosahedral morphology; an example of this crystal structure and packing is shown in Figure 1.9. This packing was first suggested in 1962 by Mackay[29] and has been repeatedly confirmed and investigated in experiments and simulations[30, 31].

Nanoparticles and some specific examples of materials, along with their size dependent properties, will be covered in following sections. First, we will look
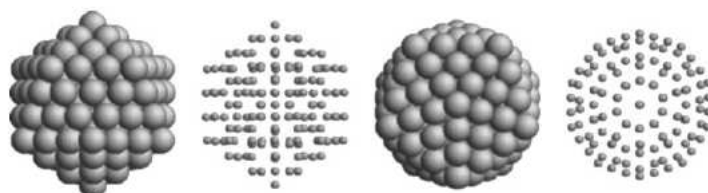
FIGURE 1.9: Example of icosahedral clusters commonly found in metal nanoclusters, for example gold and silver. Image reproduced from Baletto and Ferrando [17].

at a brief history of the discovery of carbon nanostructures, as it is an elegant example of a major, and fortuitous, discovery in nanoscience.

1.4   Carbon as an example of a nanomaterial

The discovery of carbon nanostructures initially drew the attention of the scientific community to nanoclusters, but the discoveries arrived via an indirect route. The interest in small particles of carbon originated from studies done throughout the 1970s into interstellar dust, the small particles of matter scattered between stars and galaxies[32]. As light passes through this interstellar dust it is absorbed or scattered by interstellar particles, reducing the light's intensity. Astrophysicists refer to this phenomenon as *optical extinction*, and it can be studied by measuring the intensity of light coming from stars[3]. Absorption spectra from stars are recorded in an attempt to understand the composition of interstellar dust. The ultraviolet portion of many of these extinction curves revealed a remarkable broad absorption hump around a wavelength of λ=220 nm[32]. This feature was considered remarkable as its position was almost constant in all ultraviolet spectra obtained[33–36], appearing to be a ubiquitous feature in interstellar dust. At the time of these observations the most accepted explanation for the hump at approximately 220 nm was particles of graphitic carbon. However, this theory was considered flawed by many, as the position and shape of the peaks in any extinction curve are usually very sensitive to the size and shapes of the particles producing them[37]. For the peak to remain almost unchanged from varied sources implied the dust grains managed to have nearly identical shape and size distributions, despite existing under very different conditions[37]. With such a conundrum, groups began to take an interest in proving this source of optical extinction.

Rohlfing *et al.* [38] were one of the first groups who tried to investigate carbon clusters of graphite dust in the laboratory to follow up these claims. They used laser vaporation of a graphite substrate with subsequent time-of-flight mass spectral analysis to try to observe the size distribution of graphite clusters. Their analysis showed distinct cluster size distributions, with both even and odd atom clusters of C_n appearing where $1 \leqslant n \leqslant 30$, but only even atom clusters of C_{2n} appeared for $20 \leqslant n \leqslant 90$. A time-of-flight mass spectrum of C_n for $1 \leqslant n \leqslant 100$ can be seen in Figure 1.10. They suggested that the reason for the preference for even numbered clusters was because they are comprised of carbyne $(-C \equiv C-)_n$.

They rejected other possibilities based on graphitic 6-membered rings, stating these clusters would have an equal preference for even or odd atom clusters.
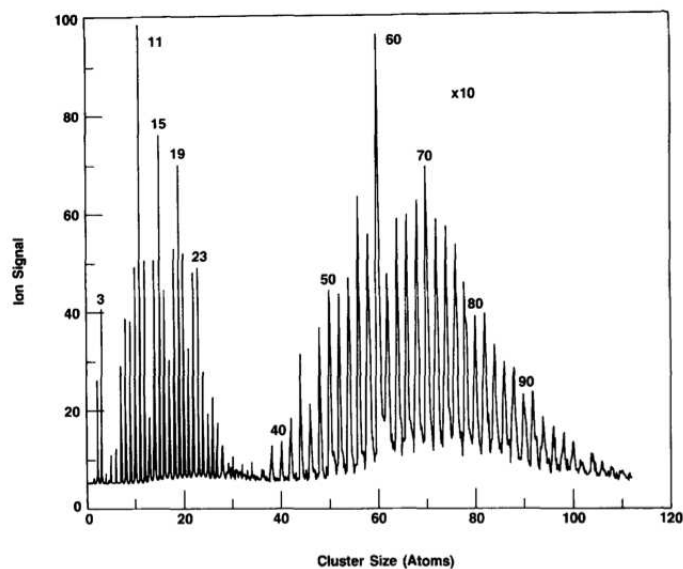
FIGURE 1.10: Time-of-flight mass spectrum taken from laser vaporisation of graphite substrate[38]. The spectrum is a combination of two spectra taken at differing voltages; the first optimised the detection of smaller clusters (C_n^+ where $1 \leq n \leq 30$), and the second optimised for detection of larger clusters (C_{2n}^+ where $20 \leq n \leq 50$). Image reproduced from Rohlfing *et al.* [38].

Kroto *et al.* [39] were particularly interested in the C_{60} peak in the time-of-flight mass spectrum obtained by Rohlfing *et al.* [38]. This spectrum is shown in Figure 1.10, where the C_{60} peak can be seen as the dominant peak for the larger clusters. Kroto *et al.* [39] managed to repeat these results, and found that by changing the experimental conditions they could increase the dominance of this peak, and managed to obtain a C_{60} peak which represented 50% of the total cluster abundance. Kroto's group speculated on what shape of molecule was giving this added stability and suggested a soccer-ball shaped molecule consisting of hexagons and pentagons, they also suggested that this could be a widely found isomer considering its high stability in harsh conditions. Their proposed structure is depicted in Figure 1.11.

Haddon *et al.* [40] performed some theoretical investigations into the electronic structure and bonding in the proposed structure of C_{60}. They found that all the σ bonds in the proposed molecule are fully satisfied by neighbouring atoms, and with very little strain on the bond angles. In comparison, a graphite particle of the same scale would have a significant number of unsatisfied valences, making it an unlikely alternative[40]. They also speculated that the high symmetry of C_{60}
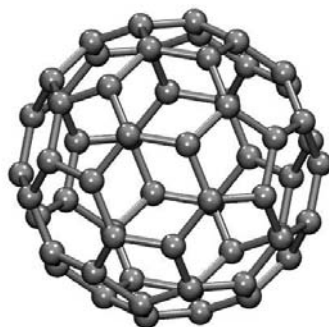
FIGURE 1.11: Structure of buckminsterfullerene, C_{60}. This geodesic dome structure of C_{60} was proposed by Kroto *et al.* [39] in 1985. Three members of the group, H.W. Kroto, R.E. Smalley and R.F. Curl Jr., were awarded a Nobel Prize in Chemistry in 1996 for their discovery.

would result in very simple Raman and IR spectra, with only four fundamental modes for the IR spectrum. Krätschmer *et al.* [41] produced carbon dust via vaporisation of graphite at high pressures to do their own studies on the structure of C_{60}. They performed ultraviolet and infrared absorption spectrometry on their carbon dust sample to see if they could reproduce the absorption peak at λ=220 nm found in the absorption spectra of interstellar dust. They not only managed to reproduce the expected UV absorption band at λ=220 nm, but also the four infrared vibrational modes that were previously suggested by Haddon *et al.* [40]. Krätschmer *et al.* [42] continued this work in the same year, and managed to refine their methods of producing C_{60} molecules, so that they could be concentrated into a solid form, enabling them to perform X-ray diffraction studies. Their X-ray diffraction data combined with IR spectral data confirmed the C_{60} molecules have the spherical structure proposed by Kroto *et al.* [39].

The original hypothesis of Kroto *et al.* [39] eventually led to the award of a Nobel Prize in Chemistry in 1996. A new field of carbon chemistry was opened up by their discovery, and "fullerenes" have become accepted as the third allotrope of carbon, next to the allotropes graphite and diamond.

Interestingly, Osawa [43] had proposed the football shaped structure in 1970, more than a decade earlier, in a chemistry journal in Japan. He was involved with studies on "superaromatic" structures such as corranulene - which he noted forms one portion of the 'football' structure of C_{60} which he also hypothesised. Published only in Japanese, and with little follow-up interest at the time, this work went essentially unnoticed. A retrospective of his work was published more recently[44].

The second lauded discovery in carbon nanostructures was that of carbon nanotubes. Synthesis of carbon nanotubes occurred a few years after the reporting of buckminsterfullerene and other closed-cage fullerenes, being first synthesised and reported in 1991[45]. Carbon nanotubes are composed of sheets of graphite 'rolled up' into a cylinder as shown in Figure 1.12. They can occur as either single-walled nanotubes or multi-walled nanotubes - where the multi-walled nanotubes are composed of concentric single-walled carbon nanotubes[46]. The properties of individual nanotubes depend on their dimensions (diameter and length) and also in which direction along the graphite sheet the tubes are rolled. The structure of nanotubes can be described in terms of the chirality or helicity of the graphene tube, illustrated in Figure 1.13. The electronic properties of carbon nanotubes are significantly altered by this helicity.

The chirality of the carbon nanotube has a significant effect on the material properties. In particular, tube chirality is known to have a strong impact on the electronic properties of carbon nanotubes. Metallic and semiconducting behaviours have been observed in carbon nanotubes, depending on the chirality[46, 47].

The properties of carbon nanotubes have caused a lot of interest in the materials sector - due to an elastic modulus almost equal to that of diamond, and strengths 10-100 times greater than that of steel along the axis of the tube, while being a much lighter material[46]. Iijima *et al.* [49] studied the flexibility of carbon nanotubes using high resolution electron microscopy and molecular dynamics simulations. They found the nanotubes, while strong along the axis of the tube,
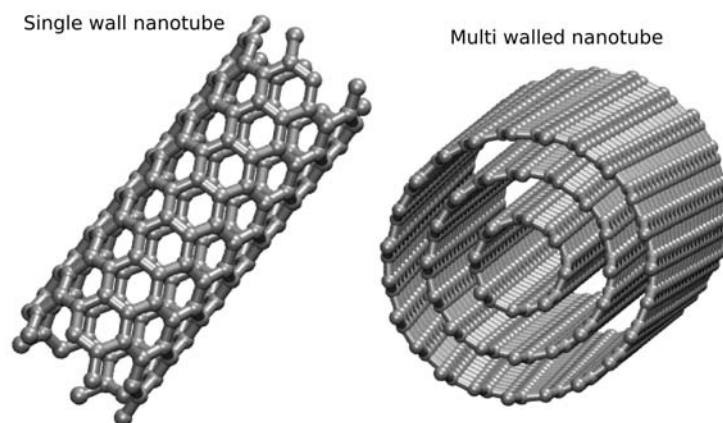
FIGURE 1.12: Schematic showing how a sheet (or sheets) of graphene can form single and multi-walled carbon nanotubes.
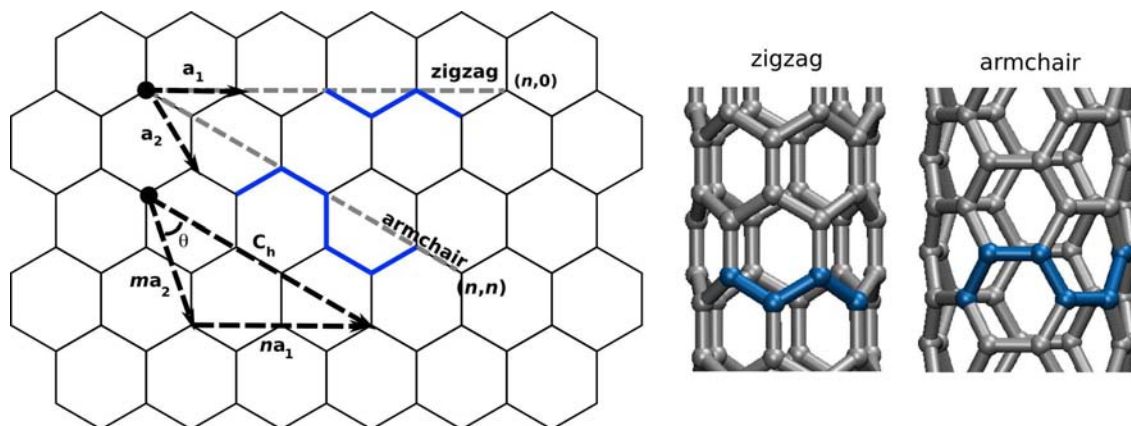
FIGURE 1.13: Schematic of a 2D graphene sheet with lattice vectors $\mathbf{a_1}$ and $\mathbf{a_2}$, and the chiral ("wrapping") vector $\mathbf{C_h}$, where $\mathbf{C_h} = n\mathbf{a_1} + m\mathbf{a_2}$. The extreme cases are indicated in grey, where $(n, 0)$ gives a zig-zag arrangement, and (n, n) gives the armchair arrangement. Images adapted from Odom *et al.* [48] and Thostenson *et al.* [46].

are easily deformed. Their studies did show a surprising amount of structural flexibility though, with the nanotubes able to reversibly recover from bends of up to $110°$.

The discovery of carbon nanostructures had a significant impact on the scientific world. The idea that nanoscience could be our means of making novel materials through rational design was not fully embraced until building blocks, such as carbon nanostructures, became widely available to a range of scientific disciplines[4]. For this reason it is relevant to discuss the history of the discovery of carbon nanostructures, before we introduce other examples of studies into nanoparticles in the following section.

1.5 Nanoparticles

Nanoparticles are often defined as a collection of atoms or molecules, with at least one dimension in the size range of 1-100 nm[3]. However, a general definition based purely on size doesn't distinguish between large molecules, such as biomolecules that can exist at nanoscale dimensions, and nanoparticles. Additionally, the size range of what can be considered a nanoparticle will vary for different compounds. This was exemplified in Section 1.2, where we introduced that the electronic properties of nanoparticles are distinct from the bulk when the dimensions of the nanoparticle are on the order of the exciton radius. Since this radius will vary

depending on the material we cannot give an absolute definition of a "nanoparticle" based on a strict size range, as it won't necessarily include all materials. It is more accurate to define the size range of nanoparticles for a given material as any size below which any of its properties deviate significantly from that of the bulk material[11].

As the size of the system is significantly reduced from a bulk "macrocrystal" the electronic structure appears more like that found in discrete molecules than in an infinite solid[1, 50, 51]

In the mid-1980's Brus [50, 52] studied the electronic properties of small clusters of semiconducting materials at Bell Laboratories. Using cadmium sulfide (CdS) as an example, in which the $1s$ exciton has a radius of approximately 60 Å, Brus [50] suggested that if crystallites were reaching this size limit, the exciton interactions with the surface would dominate its dynamics. In this case he calculated that size effects would produce a very different energy scheme in comparison to a much larger (bulk-like) crystal. Brus [51, 53] continued these studies in the following years. As experimental techniques developed in the 1980's that enabled size-controlled production of colloidal particles of 15-50 Å, these theoretical calculations could be confirmed. Later studies into nanocrystals of CdS have shown the band gap can be tuned between 2.5 and 4 eV depending on the size of the particles[2, 54].

One visible result of this size dependent band gap is that the colour of the material can change with the size of the particle, as illustrated in Figure 1.14. The colour of a material is determined by the absorption of light at specific wavelengths. Absorption occurs when photons from incident light induce electrons to make transitions between low energy occupied levels to higher energy unoccupied levels[3]. Murray *et al.* [55] synthesised CdSe nanoparticles of various sizes, ranging between 12 to 115 Å. They showed the effects of quantum confinement, with the particles of different sizes clearly absorbing different wavelengths of light.

As well as changes in properties such as band gap, the phase stability of a solid can vary widely depending on the size of the particle. This has been observed in many materials including zirconium dioxide[56–58], titanium dioxide[59, 60], alumina[61] and carbon[62]. Titanium dioxide for example, exhibits size-dependent phase transitions between three different polymorphs, anatase, brookite and rutile[63]. At the macroscopic scale, rutile is more stable than anatase or brookite, while at

the nanoscale anatase is the more stable polymorph. Previous studies performed by Zhang and Banfield [60] have shown that at particle diameters less than 14 nm anatase is the preferred polymorph, not rutile[60]. The role of the brookite polymorph was not clearly understood; *i.e.* whether anatase converted to brookite or vice versa. Calorimetric data for the transformation enthalpies of these three phases suggested that the order of stability was rutile > brookite > anatase, while other groups found brookite to be more stable[64, 65]. Zhang and Banfield [63] later examined the impact of size on the phase stability and transformation via X-ray diffraction analysis of titania samples consisting of nanocrystalline anatase and brookite. They found brookite to be stable at the nanoscale, but as an intermediate phase between anatase and rutile. Titanium dioxide phase transitions at the nanoscale have proven to be an interesting example in the literature. Individual groups were each studying different sizes of TiO_2 nanoparticles and apparently contradictory results were obtained. In reality it was the size-dependent nature of the problem providing the discrepancies.

Size-dependent phase transitions have been studied in detail also for CdSe semiconductor nanocrystals. Nanoparticles of CdSe with a radius between 10 Å and 30 Å are particularly interesting as they are almost perfectly crystalline, maintaining the wurtzite structure of the bulk. Tolbert and Alivisatos [66] have looked at pressure induced phase transformations from wurtzite to rock-salt packing in nanocrystals of CdSe and compared these results to those for the bulk structure. They found the thermodynamics and kinetics of these transitions were vastly altered within the finite systems relative to the bulk. In the bulk, a phase transition can be induced at approximately 3 GPa. However, for the
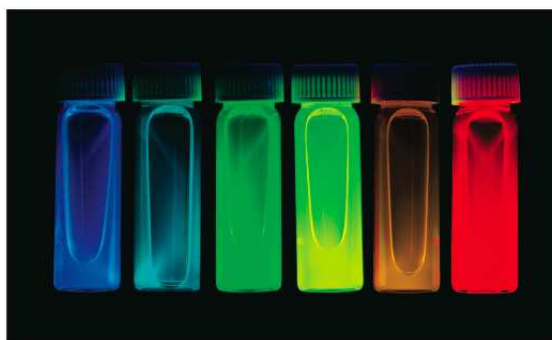
FIGURE 1.14: The emission wavelength of CdSe quantum dots can be tuned on the basis of particle size as shown in this image. Vials of different sizes of CdSe quantum dots under UV light show emission of different wavelengths of light. Image reproduced from Alivisatos [4].

nanocrystals the structure was much more stable and 9 GPa was required to induce the same phase transition from wurtzite to rock-salt. At an even smaller size scale, CdSe has also been shown to have very stable nanoparticles at sizes $(CdSe)_{33}$ and $(CdSe)_{34}$ [67]. Using time-of-flight mass spectrometry, Kasuya *et al.* [67] discovered highly stable particles for n=13, 33 and 34, for not only $(CdSe)_n$ but also $(CdS)_n$, $(ZnSe)_n$ and $(ZnS)_n$. At this size range the surface energy is so large that the nanoparticles are predicted to not have a wurtzite or rock-salt structure, but structures composed of 4- and 6- member rings. Kasuya *et al.* [67] performed some simulations in order to determine the lowest energy configuration for the most stable CdSe clusters they found from the mass spectra; examples of the resulting structures are shown below in Figure 1.15. The structures are significantly different to the bulk structure one would expect for CdSe.
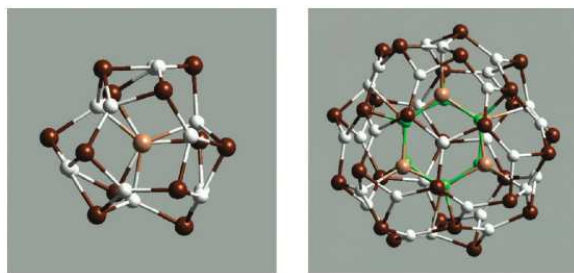
FIGURE 1.15: The most stable $(CdSe)_{13}$ and $(CdSe)_{34}$ clusters as calculated by Kasuya *et al.* [67] using first principles calculations. Images reproduced from Kasuya *et al.* [67].

Zaziski *et al.* [68] continued the studies of Tolbert and Alivisatos [66] on phase changes in CdSe. They investigated the possibility of reversible phase transformation in nanorods. Zaziski *et al.* [68] thought this would be an interesting study, as nanoparticles less than 5 nm in diameter undergo reversible phase transformations, but extended solids form distinct domains of different phases. They hoped that nanorods may show some attributes of both of these transformations, with an aspect ratio of 1:10. They found that the volume change that occurs when a phase transition is imposed caused the nanorods to fracture into subdomains small enough to undergo the phase change without further cracking[68].

The fact that these similar structures and properties are exhibited by a variety of materials is no surprise. The materials studied by Tolbert and Alivisatos [66], Zaziski *et al.* [68] and Kasuya *et al.* [67] are all grouped into a category

of compounds known as the chalcogenides, and will be discussed in more detail in the next section before focusing on one member of this family, namely zinc sulfide.

1.6 Chalcogenides

Chalcogens are the chemical elements in group 16 of the periodic table. The lightest element in the chalcogen family is oxygen (O), with the following elements being sulfur (S), selenium (Se), tellurium (Te), polonium (Po) and the synthetic element ununhexium (Uuh). Compounds comprised of heavier chalcogens are grouped together and referred to as chalcogenides, which usually refers to the more commonly found compounds - sulfides, selenides or tellenides. The reason for this collective grouping away from oxides is that chalcogens have moderate electronegativity in comparison to oxygen. The Pauling electronegativity of oxygen is 3.44 while S is 2.58, Se 2.55 and Te 2.1[69]. This difference in electronegativity results in chalcogenides having very different crystal structures to oxides, and led to them being grouped separately based on their structural differences.

Many chalcogenides have close-packed anions. This arrangement gives the largest distance between anion pairs, but the densest packing of atoms, like those seen in metals. Cubic close packing (ccp), hexagonal close packing (hcp) and body centred close packing are often seen.

In our studies we will be focusing on zinc sulfide in particular. Before introducing the structure, properties and previous studies of zinc sulfide, some background on sulfide minerals will be given.

1.6.1 Sulfides

Many sulfide minerals have been the focus of scientific investigation for two major reasons, the first being that ores containing these minerals are often the source of valuable metals, and the second being that many sulfide minerals have properties that make them useful for potential applications in the electronics industry[70]. We will now look at these two applications of sulfide minerals in more detail.

Metal sulfides are one of the most important groups of ore minerals as supply of most of the worlds non-ferrous metals comes from these ores. Interest in sulfide chemistry originally arose from the need to separate valuable metals from raw sulfide ores[71]. The industrial processing of sulfides requires the removal of a large amount of unwanted ore material to obtain concentrated valuable metals. Because of this the specific surface chemistry and reactivity of sulfide ores became a focus for research projects in this field. Sulfide surfaces have also been implicated as catalysts for reactions to assemble the first complex molecules required for life to exist on our planet[72]. Active hydrothermal systems were found in deep oceans, which initially encouraged these ideas and research into the interactions between microbes and sulfide minerals[73]. Environmental concerns arise from the mining of sulfide ores, where the waste products have the potential to damage or destroy surrounding habitats[71, 74]. Sulfides can react with natural water sources, acidifying them and possibly dissolving ores which contain toxic elements[74]. Synthesised analogs of sulfide minerals are also of interest to the materials industry because of their electrical, magnetic and optical properties. Particular interest has grown in sulfide nanoparticles as the size-tunable properties for these semiconductor systems may offer opportunities to develop new technologies[75].

Metal sulfide minerals occur as crystalline structures with a tetrahedral or octahedral coordination of the cation, depending on the metal in the mineral[19]. In some cases the crystalline structure may be slightly distorted from the regular tetrahedral and octahedral coordination. Sulfide structures are often described in terms of the close packed structures introduced in Section 1.3, where the sulfide anions take on one of the close-packed structures, and the metal ions are located at some or all of the octahedral or tetrahedral interstitial points between the anions[19]. Sulfide ions prefer asymmetric surroundings and are highly polarisable, giving sulfide minerals very different structures to other minerals, such as metal oxides, where the oxide ion is less polarisable[19]. Some of the more commonly found metal sulfides exhibit *polymorphism*. For example, FeS_2 occurs as both pyrite and marcasite, and ZnS occurs as sphalerite and wurtzite[19]. Polymorphs can differ drastically, where the nearest-neighbour coordinations will be different between the two structures, or subtly, where the difference occurs at distant neighbouring ions.

All sulfide minerals of the non-transition elements are diamagnetic insulators

or semiconductors[76]. Sulfides of the transition metals have more complicated electronic structures due to the presence of d-orbital electrons. In these minerals there may be overlap between the bands, or none at all, offering many more possibilities for these materials. They could be p- or n-type semiconductors, diamagnetic or even exhibit temperature-dependent paramagnetism[76]. This vast range of possiblities means the electrical and magnetic properties of sulfide minerals cannot be generalised and need to be studied individually. One generalisation that can be made is that the sulfides, with the wide range of possible electronic and magnetic properties, have great promise for use in technological applications. This technological value of sulfide minerals becomes even more apparent when we consider the previous discussions, that nanoparticles have properties that are strongly dependent on the composition, size and shape of the particle.

1.7   Zinc sulfide

The material focused on throughout this thesis is zinc sulfide. The following section will provide the background regarding some of the previous studies of zinc sulfide. The properties of bulk zinc sulfide will be introduced first, followed by summaries of more recent studies into the structure and properties of nanoparticles of zinc sulfide.

1.7.1   Structure and polymorphism

Zinc sulfide occurs as two main polymorphs, sphalerite, also known as zinc blende, (β-ZnS) and wurtzite (α-ZnS), shown in Figure 1.16. These two forms are actually *polytypes*, which is a form of polymorphism where the structure forms in layers that can have different stacking sequences[19]. Both of these polytypes of ZnS are comprised of close-packed layers of corner-sharing ZnS_4 tetrahedra, but as implied by the term polytype, they differ in the stacking of the layers. Sphalerite takes the cubic close-packed form, with layers alternating in an (A-B-C-A-B-C...) sequence, and wurtzite is a hexagonal close-packed structure where the layers alternate in an (A-B-A-B...) sequence[69], as already illustrated in Figure 1.8 in Section 1.3. Zinc sulfide does occur as many more polytypes than these strictly defined wurtzite and sphalerite layering sequences[77]. These layers can actually
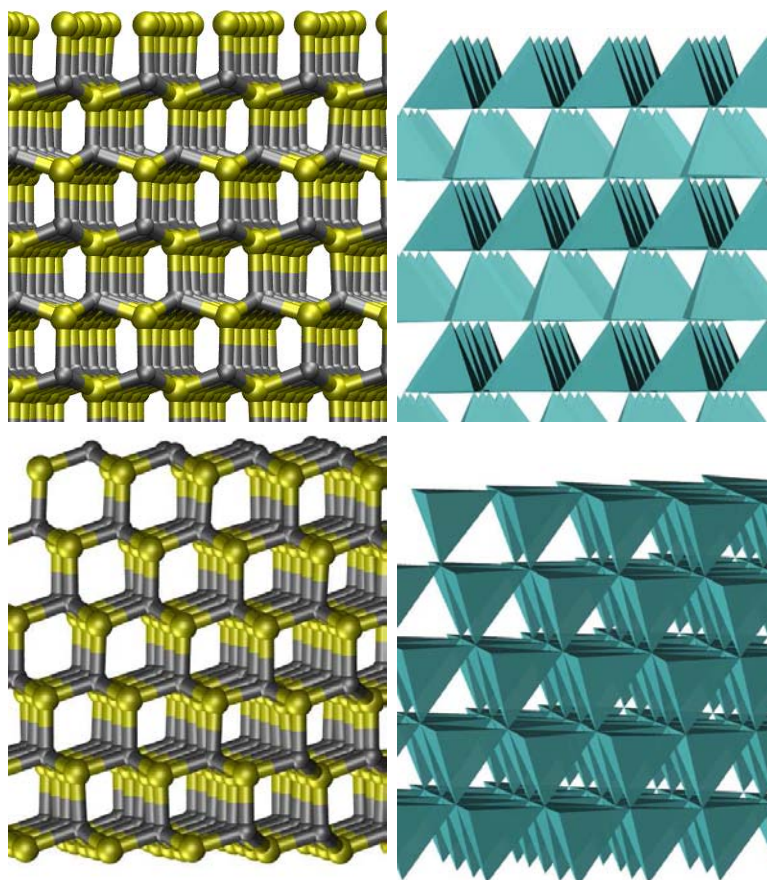
FIGURE 1.16: Wurtzite (top images) and sphalerite (bottom images) crystal structures. The ball and stick models show sulfur atoms as yellow and zinc atoms as grey. Polyhedral representation is shown for sulfur atoms only, the A-B-A-B and A-B-C stacking patterns can be seen.

form in any combination of stacking along the c-direction of a hexagonal unit cell. Structures with periodicities on the order of hundreds of Angstroms have been reported[77, 78]. At atmospheric pressure and room temperature the bulk sphalerite phase is slightly more stable than the wurtzite phase, with a free energy difference quoted in thermodynamic tables as $\sim$10 kJ mol^{-1}[79], while more recent studies estimate a difference of 2 kJ mol^{-1}[80]. Wurtzite is generally accepted as the stable form at high temperatures[81], though both wurtzite and sphalerite can be found to coexist in naturally occurring mineral ores[19].

Scott and Barnes [82] were interested in studying how these supposed polymorphs could coexist under the same environmental conditions, when the purported temperature for wurtzite to be stable was 1020 °C[81] and discrepencies in reported phase-transtion temperatures were present in the literature. They investigated what effect the stoichiometry of ZnS had on the phase equilibria by generating

single crystals of sphalerite and wurtzite at various pH levels and temperatures. They found that the discrepancies in the literature were not anomalies, but indicated the phase changes were highly dependent on the kinetics of the reaction, which were not explicitly considered in previous literature reports. Their studies into the kinetics of the phase transitions explain how wurtzite can also be found as a stable, naturally occurring mineral when it is traditionally considered the "high-temperature" phase. The kinetic dependancies they found showed there is an equilibria between wurtzite and sphalerite, where wurtzite is intrinsically sulfur-deficient relative to sphalerite at a given temperature[82]:

$$
\overset{\textit{wurtzite}}{\text{ZnS}_{1-x}} + \frac{1}{2}\left(x - 1 + \frac{1}{1-y}\right)\text{S}_2 \leftrightarrows \overset{\textit{sphalerite}}{\left(\frac{1}{1-y}\right)\text{Zn}_{1-y}\text{S}} \tag{1.2}
$$
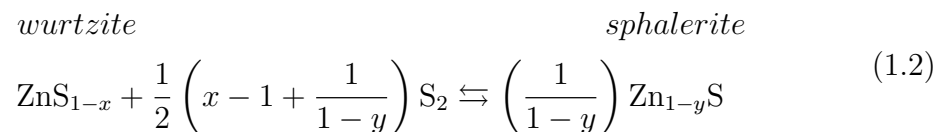
Strict polymorphs have the same stoichiometry. However, sphalerite and wurtzite have slight differences in their zinc/sulfur ratios, with sphalerite having a slightly higher S:Zn ratio than wurtzite. These stoichiometric variations, and deviation from strict polymorphism means that the two polytypes sphalerite and wurtzite can coexist stably over a range of temperatures and pressures[19]. The work done by Scott and Barnes [82] notes that the stoichiometry of ZnS may vary over a range of 0.9% sulfur; a value that seems small but is vital to the stability of the zinc sulfide phases.

1.7.2 Previous studies of bulk zinc sulfide

There have been many previous studies performed into the bulk and surface properties of ZnS. Here we present some of these, with an emphasis on those using theoretical methods as these will be the most relevant to our own studies.

As discussed in the previous section, the number of polytypes of ZnS is almost limitless as layers of ZnS can stack in different formations, yielding not only the A-B-A-B and A-B-C-A-B-C stacked hexagonal and cubic polytypes, but any mixed combination of these. Engel and Needs [77] performed first principles calculations on polytypes of bulk ZnS, with an interest in determining if there were any common structural features between the lowest energy polytypes of ZnS. Similar studies

had been performed for SiC, which exhibits polymorphism in the same fashion as
ZnS, which led them to try to apply these same techniques to zinc sulfide. They
examined five different polytypes, two of which were sphalerite and wurtzite, and
the remaining three were polytypes with mixed sphalerite and wurtzite layers.
The significant finding from these energy calculations is that the energy differences
between these polytypes were very small in comparison to the spread of energies
of polytypes in other materials, as shown in Figure 1.17.
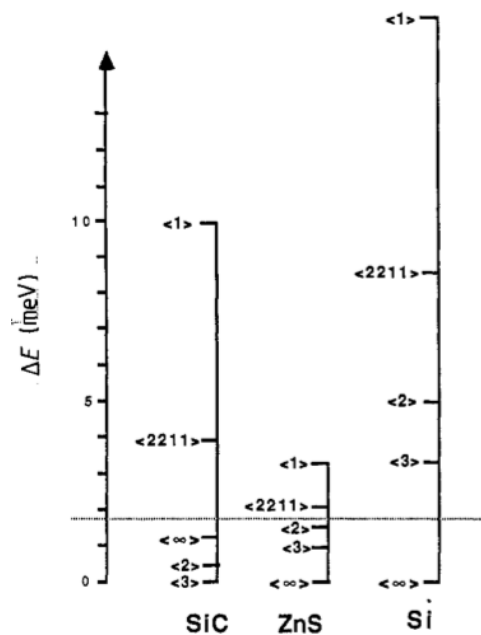
FIGURE 1.17: Energy differences per unit of ZnS, Si or SiC of different polytypes
optimised using first principles calculations. The spread of the energy differences
between polytypes of ZnS is much lower than that for SiC, a material which
exhibits polytypism in a similar fashion to ZnS. $\langle \infty \rangle$ is sphalerite, and $\langle 1 \rangle$
wurtzite. Image reproduced from Engel and Needs [77].

Engel and Needs [83] performed further studies on ZnS, with the aim to improve
the calculated properties of cubic zinc sulfide using first principles methods. They
found that if the Zn $3d$ electrons are included the pseudopotential (*i.e.* they are
considered core electrons) the nonlinear core exchange-correlation correction of
Louie *et al.* [84] needs to be applied to obtain reasonable results. A number of
other groups have also successfully used first principles and *ab initio* methods to
accurately predict the structural and elastic properties of ZnS[85–87].

Classical methods have also been used to model bulk zinc sulfide. Wright and
Jackson [88] developed a set of interatomic potentials for modelling ZnS. Their
potentials accurately predicted the physical properties of sphalerite and wurtzite,

and they used these to simulate defects. These potentials were later used again
by Wright *et al.* [89] to investigate the surface energies and stabilities of ZnS
sphalerite. Their studies showed that the {110} surface was the most stable.
However, a higher ratio of S (implying Zn vacancies) resulted in the {111} surface
being favoured. Benkabou *et al.* [90] also developed a forcefield for simulating
the II-VI semiconductor compounds CdS, CdSe, ZnS and ZnSe. Their potential
parameters were fitted on experimental data and their calculations were successful
in accurately modelling the experimental values known for lattice constants, bulk
moduli and cohesive energy.

Wang and Duke [91] developed tight-binding models to calculate atomic and
electronic structure of ZnS cleavage surfaces. Their calculations showed similar
reconstructions for all three three cleavage surfaces investigated - the (110)
surface of sphalerite and the (10$\bar{1}$0) and (11$\bar{2}$0) surface of wurtzite. For each
of these surfaces they found the sulfur atoms relaxed outwards, as illustrated
in Figure 1.18. Continuing on from these studies, Duke and Wang [92]
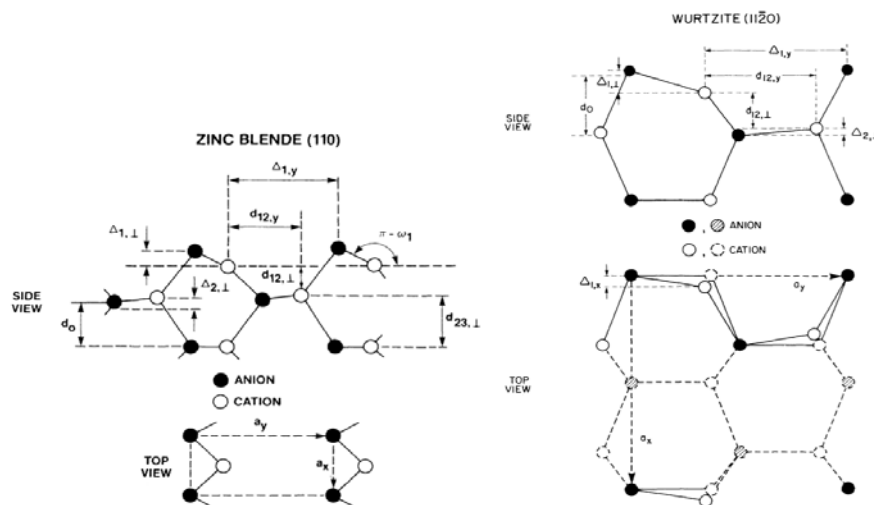
FIGURE 1.18: Relaxed surfaces for zinc-blende (110) (left) and wurtzite
(11$\bar{2}$0)(right). Image reproduced from Wang and Duke [91].

investigated the mechanism of surface reconstruction on the cleavage faces of other
wurtzite-structure materials. Their studies used tight-binding models to calculate
the energies and energy minimisation techniques to optimise the structures of
cleavage surfaces (10$\bar{1}$0) and (11$\bar{2}$0). They studied not only ZnS but also ZnSe,
ZnO, CdS and CdSe. They found that each surface relaxed in a way analogous
to sphalerite (zinc-blende) (110) surface, where surface layer anions relax outward
(from the surface) and cations relax inward. These studies were complemented by

a review of atomic and electronic structure of tetrahedrally coordinated compound semiconductor interfaces, published in the same year by Duke [93].

Hamad *et al.* [94] investigated the crystal structure and morphology of ZnS using a forcefield they developed. Their study includes not only the non-polar surfaces studied by Engel and Needs [77] but also the polar surfaces, enabling the crystal morphology to be predicted. The crystal morphologies for sphalerite and wurtzite are shown in Figure 1.19.
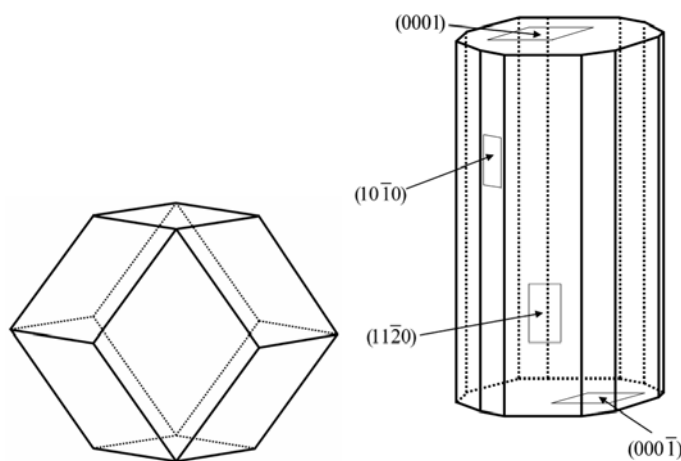
FIGURE 1.19: Calculated crystal morphology of sphalerite (left) where only the [110] surface is found, and wurzite (right) forming a hexagonal rod morphology. Image reproduced from Hamad *et al.* [94].

More recently Wright and Gale [95] developed a set of interatomic potentials for zinc sulfide and cadmium sulfide. The reason they looked at both of these materials is that they both have two stable polymorphs, wurtzite and sphalerite, and they are both materials with semiconducting properties. However, the sphalerite form is the more stable polymorph of zinc sulfide, and the less stable polymorph of cadmium sulfide. At the time their paper was published there had been a number of classical atomistic studies done on the zinc sulfide system, however none had managed to accurately describe the preference for sphalerite over wurtzite. The focus of their study was not only to develop a forcefield which accurately describes the interactions between zinc and sulfur, but that is able to model the slight energy difference between the two stable polymorphs sphalerite and wurtzite.

1.7.3 Previous studies at the nanoscale

The kinetics of the formation of zinc sulfide nanoparticles have been studied experimentally[96]. Zhang *et al.* [96] focussed on investigating how the experimental conditions of synthesising ZnS nanoparticles would affect the size and phase constitution of the nanoparticles. They successfully synthesised nanoparticles of ZnS with mixed stacking sequences - both cubic and hexagonal stacking. They found the stacking in nanoparticulate zinc sulfide to be primarily controlled by the kinetics of precipitation[96]. The mixed stacking in their nanoparticles implied that the probabilities of forming wurtzite layers and sphalerite layers under their experimental conditions were approximately the same. They also found if the conditions were set for a rapid precipitation that sphalerite was the favoured structure. The mixed-phase nanoparticles they developed had different optical properties to single phase sphalerite or wurtzite nanoparticles, suggesting that control of defects in nanoparticles could lead to new technological applications.

More recently the same group conducted similar studies, looking at the effect of NaOH concentration on the morphology of zinc sulfide nanoparticles[97]. Some of their results are shown in Figure 1.20. The studies showed marked differences in morphology depending on the concentration of NaOH, with structures varying from microspheres, flower-like structures and nanosheets[97].
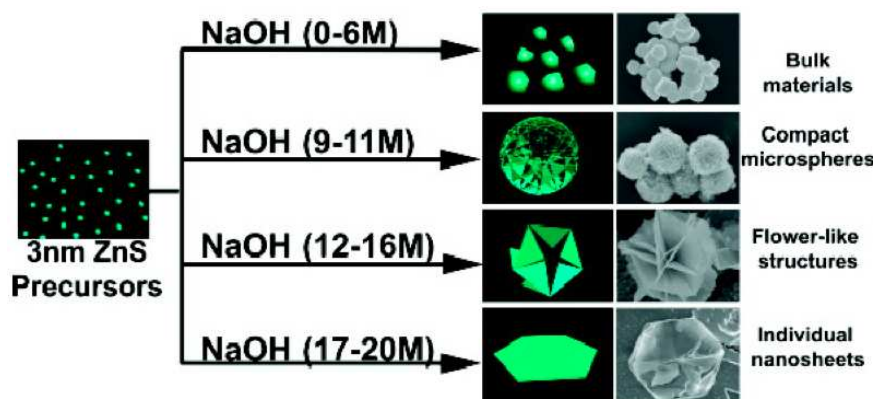
FIGURE 1.20: The dependence of the morphology of ZnS on concentration of NaOH was observed by Ren *et al.* [97]. Image reproduced from Ren *et al.* [97].

Comprehensive studies of ZnS nanoparticles involving thermodynamic analysis, molecular dynamics and experiment found that smaller wurtzite nanoparticles are more thermodynamically stable than sphalerite[98]; a reversal in the trend

observed for the bulk. Zhang *et al.* [98] were interested in doing a thorough study of the phase stability of zinc sulfide nanoparticles primarily due to inconsistent reports in the literature. A number of studies[99, 100] in the past had predicted the surface energy of wurtzite was higher than that for sphalerite, while more recently, with the increased interest in nanoparticles, groups have found conflicting results where nanoparticles of ZnS preferred the wurtzite form over sphalerite[101, 102]. Molecular dynamics simulations of zinc sulfide surfaces in vacuum performed by Zhang *et al.* [98] predicted that the average surface energies for sphalerite and wurtzite are 0.86 and 0.57 Jm^{-2}, respectively. This implies that sphalerite nanoparticles are less stable due to a higher surface energy, supporting the experimental evidence that wurtzite is the preferred phase at this scale. Gilbert *et al.* [103] performed extended X-ray absorption work which showed that nanoparticles could not be considered as small pieces of bulk material. They found considerable internal strain in the nanoparticles due to the competing relaxations from the irregular surfaces of the particles.

Compressibility and bulk moduli of materials are also size-dependent[104]. Gilbert *et al.* [104] studied the compressibility of a range of sizes of nanoparticles and found that nanoparticles smaller than 6 nm in diameter showed up to a 40% reduction in bulk modulus.

Qadri *et al.* [102, 105] have performed studies on pressure and temperature-induced phase transitions in zinc sulfide. Their first study[105] looked at the size dependence of temperature-induced phase transitions. In the bulk, sphalerite undergoes a phase transition to wurtzite at 1020 °C. Qadri *et al.* [105] observed zinc sulfide nanoparticles transform to wurtzite at temperatures as low as 400 °C. They concluded that the equilibrium transition temperature for the sphalerite-to-wurtzite transition in ZnS nanoparticles was vastly reduced from the value for bulk ZnS. Studies on the influence of particle size on pressure-induced phase transformation were also interesting. As pressure was applied to ZnS nanoparticles of approximately 25 nm size they transformed very quickly to the sphalerite phase, and finally onto a rock salt structure[102]. As the pressure was reduced the particles did not return to the original wurtzite phase, but back to the intermediate sphalerite phase.

More recently Zhang *et al.* [98] have done further studies into the thermodynamic stabilities of zinc sulfide nanoparticles in vacuum and in water. They found an even greater difference in the temperature required to induce a phase transition

(in comparison to bulk studies), with 7 nm nanoparticles of zinc sulfide in the sphalerite phase requiring only 25 °C to induce a phase change. Simulations were also performed on even smaller nanoparticles of 3 nm and the activation energy required to go from sphalerite to wurtzite structures was approximately 5 kJmol^{-1}, which they took to imply a different mechanism of phase change when zinc sulfide particles are at the nano-scale. These studies showed that at the nanoscale the wurtzite structure is more thermodynamically stable than sphalerite. The group did some experimental studies on phase transitions in zinc sulfide nanoparticles where they heated 3 nm ZnS nanoparticles in vacuum over the range 350-750 °C and successfully induced a phase change from sphalerite to wurtzite. However, the same experiment performed in moist air gave no clear conversion from sphalerite to wurtzite - showing that chemisorbed water may play a role in stabilising nanocrystalline sphalerite[98].

Zhang *et al.* [106] also performed further studies on the effect of water absorption on the phase of zinc sulfide nanoparticles. Their group did experimental studies and simulations on different sized nanoparticles, from 2-5 nm and with different initial structures (either wurtzite or sphalerite). Nanoparticles were shown to be stabilised by adsorbed water molecules, with increased order throughout the particle up to the surface. Reversible structural transformations were observed when the particles had adsorbed methanol on the surface, and when this methanol was evaporated off. The particle size and the nature of the surrounding environment of nanoparticles can clearly have a marked effect on what structure and reactivity nanoparticles will have[106]. This highlights the importance of studying the stability of nanoparticles in 'natural' environments if nanoparticles are to become more commonplace in future technologies and devices.

Continuing studies performed by Zhang *et al.* [107] investigated the differences in binding energy between water molecules and varying sizes of ZnS particles - from nanoscale, to aggregated nanoparticles, to the bulk. They used temperature programmed desorption (TPD) and also MD studies. They found that the binding energy is higher on nanoparticles than on bulk crystals. This was explained in relation to the curvature of the nanoparticles surface, where the water molecules will not be arranged as close together as they would be on the bulk surface, resulting in an increased binding energy between the water molecules and the nanoparticle. Additionally, more water molecules can be absorbed on highly curved surfaces of smaller nanoparticles than on nanoparticle aggregates or bulk
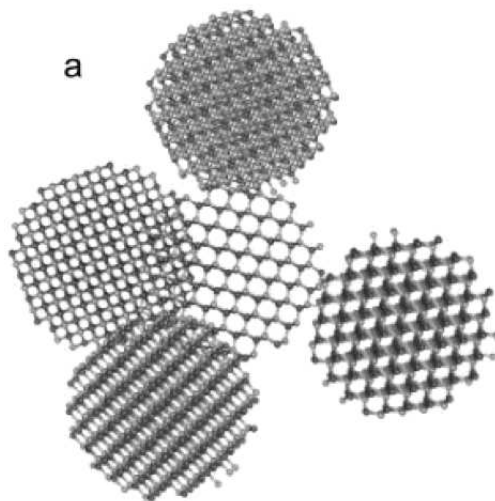
FIGURE 1.21: Aggregation of 3 nm zinc sulfide nanoparticles obtained from MD studies of Zhang and Banfield [108]. Image reproduced from Zhang and Banfield [108].

crystals, as the surface area is much greater in the isolated nanoparticle systems. The group concluded that these two factors could prove to be important when assessing the impact of nanoparticles in the environment.

After completing their studies into the phase stability of nanoparticles in vacuum and in water, Zhang and Banfield [108] began studying the effect of aggregation of zinc sulfide nanoparticles on the phase transformation. Reversible aggregation-disaggregation had previously been studied in 3 nm ZnS nanoparticles[109]. The study showed that the transformation from sphalerite to wurtzite as the nanoparticles aggregated occurred by surface nucleation. The group's previous studies[98] on 3 nm ZnS sphalerite nanoparticles in vacuum suggested the same surface nucleation mechanism for transforming into wurtzite.

Due to the growing concerns about the use of nanoparticles in industry and products, many groups are focussing their studies on the interaction of nanoparticles with solvents, particularly water - to try to get an indication of how the nanoparticles may transform if they are released into the environment[12].

Additionally, the presence of zinc and sulfur in biological systems and their mineral forms in geological systems had led to the study of nucleation of these structures in water being of interest. Hamad *et al.* [110] used forcefield methods to perform simulations of zinc sulfide nucleation in solution. Multiple simulations were performed with different concentrations of Zn^{2+} and S^{2-} species in water, to

simulate and investigate nucleation processes of zinc sulfide. Zinc sulfide clusters of varied stoichiometry were found to form, but always in two or three coordinated states, with the smaller clusters being square or hexagonal planar structures. Larger three dimensional clusters were eventually formed in the high concentration simulations, and these clusters also maintained the three-coordinated clusters, formed by hexagons and squares. Hamad *et al.* [94] have performed studies looking at surface structures and the overall morphology of ZnS using both first principles techniques and forcefield methods. In this study they derived forcefield parameters for simulating zinc sulfide, which they used in later studies of small nanoparticles of ZnS in vacuum to investigate cluster formation[111–113]. Clusters of the form $(ZnS)_n$ were investigated, where $n = 10 - 47, 50, 60, 70, 80$; some of these are depicted in Figure 1.22. These studies showed that at these very small cluster sizes the tetrahedral formation of ZnS was no longer observed - neither wurtzite or sphalerite appeared as a dominant motif. Instead three-coordinated ZnS was found, with clusters forming open 'bubble' clusters.

One of the more exploratory methods for finding new phases of nanoparticles was used by Roberts and Johnston [114], where they used a genetic algorithm to evolve structures and determine a global minimum structure for $(MgO)_n$ clusters for n=10-35. This technique was used by Burnin and BelBruno [115], Burnin *et al.* [116] to similarly find the global minimum structure for $(ZnS)_n$ clusters for n=1-16.
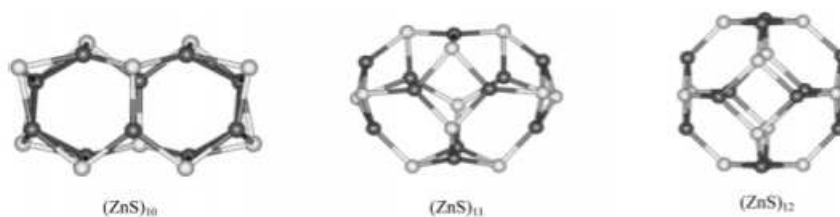
FIGURE 1.22: Examples of the bubble-like formations zinc sulfide can possess at the lower limits of the nanoscale. Image reproduced from Spanó *et al.* [111].

Our studies will focus on methods which have an investigative nature similar to that of the genetic algorithm methods, where there does not exist an *a priori* bias to any particular structure. These will be discussed in later chapters, but first some background information on general theoretical and computational chemistry will be given.

Chapter 2

Computational Methods

2.1   Introduction

Theoretical chemistry is a field of chemistry that uses mathematical methods and the fundamental laws of physics to study physical and chemical processes[117]. Prior to the invention of computers, the size and complexity of the systems that could be studied in a theoretical manner were very limited due to the overwhelming quantity of mathematical operations required. With the introduction of computers many theoretical chemistry problems could be solved or investigated within a reasonable time-span and with increasing accuracy. Continuing technological advances in computational performance has led to the birth of computational chemistry, a field which encompasses many computational methods for simulating and analysing the behaviour of molecular systems[118]. One of the difficult starting points in computational chemistry is deciding which methods and level of theory are appropriate for a given problem[117].

This chapter will first introduce two distinctly different theoretical approaches to obtain the energy of a system - electronic structure and force field methods.

2.2   Electronic structure methods

The theoretical basis for electronic structure methods is the branch of science known as quantum mechanics. Due to the fact that electrons possess properties

of particles and waves they cannot be described by classical physics, so alternate theories are required[117]. Quantum mechanics explicitly represents the electrons in a calculation, enabling the derivation of properties that rely on the electronic distribution and also to investigate chemical reactions[118]. These methods are primarily concerned with the solution of the Schrödinger equation[118–120]. The time-independent form is described by:

$$\mathscr{H}\Psi(\vec{x}_1, \vec{x}_2, \ldots, \vec{x}_N, \vec{R}_1, \vec{R}_2, \ldots, \vec{R}_M) = E\Psi(\vec{x}_1, \vec{x}_2, \ldots, \vec{x}_N, \vec{R}_1, \vec{R}_2, \ldots, \vec{R}_M) \quad (2.1)$$

Here $\mathscr{H}$ is the Hamiltonian operator for a molecular system of M nuclei and N electrons. $\mathscr{H}$ is a differential operator which represents the total energy of the system[119], and using the system of atomic units is defined by;

$$\mathscr{H} = -\frac{1}{2}\sum_{i=1}^{N}\nabla_i^2 - \frac{1}{2}\sum_{A=1}^{M}\frac{1}{M_A}\nabla_A^2 - \sum_{i=1}^{N}\sum_{A=1}^{M}\frac{Z_A}{r_{iA}} + \sum_{i=1}^{N}\sum_{j>i}^{N}\frac{1}{r_{ij}} + \sum_{A=1}^{M}\sum_{B>A}^{M}\frac{Z_A Z_B}{R_{AB}} \quad (2.2)$$

where A and B run over the M nuclei and i and j refer to the N electrons in the system, M_A is the mass of nucleus A, Z_A and Z_B are the nuclear charges of nuclei A and B respectively, r_{ij} is the distance between electrons i and j, R_{AB} is the distance between nuclei A and B and, finally, r_{iA} is the distance between electron i and nuclei A. The first two terms represent the kinetic energy of the electrons and the nuclei, respectively. ∇_q^2 is the Laplacian operator, which can be defined as a sum of differential operators in Cartesian coordinates;

$$\nabla_q^2 = \frac{\partial^2}{\partial x^2} + \frac{\partial^2}{\partial y^2} + \frac{\partial^2}{\partial z^2} \quad (2.3)$$

The remaining three terms of the Hamiltonian are potential energy terms, representing the attractive interactions between nuclei and electrons, and repulsive potentials resulting from electron-electron and nucleus-nucleus interactions.

$\Psi(\vec{x}_1, \vec{x}_2, \ldots, \vec{x}_N, \vec{R}_1, \vec{R}_2, \ldots, \vec{R}_M)$ in (2.1) is the wave function of the system, which depends on the spatial and spin coordinates of the electrons, collectively represented by $\vec{x}_i$, and the spatial coordinates of the nuclei, $\vec{R}_i$. Finally, E is the energy of the system described by the wavefunction Ψ.

The Schrödinger equation can only be solved exactly for a few problems. No exact solution can be found for systems that involve three or more interacting particles. Instead, to successfully use quantum mechanics to investigate larger problems,

we seek approximations to the true solutions of the Schrödinger equation[118]. Methods that generate solutions without reference to experimental data are known as *ab initio* methods, from the latin "from the beginning".

2.2.1 The Born-Oppenheimer approximation

The Born-Oppenheimer approximation[121] enables the electronic and nuclear motions to be separated[118, 119]. The mass of a nucleus is much greater than the mass of an electron in a system, and as a result the nuclei have much smaller velocities than the electrons. When considering electronic structure methods we assume that within the timescale it takes for electrons to relax to the ground state, the slower nuclei will not have changed position, and can be considered stationary[118, 119]. This assumption also implicitly applies to force-field methods, which do not explicitly represent electrons within a system. With this assumption the kinetic energy of the nuclei in Equation (2.1) can be treated classically[120], leaving us with the electronic Hamiltonion:

$$\mathscr{H}_{elec} = -\frac{1}{2}\sum_{i=1}^{N}\nabla_i^2 - \sum_{i=1}^{N}\sum_{A=1}^{M}\frac{Z_A}{r_{iA}} + \sum_{i=1}^{N}\sum_{j>i}^{N}\frac{1}{r_{ij}} \tag{2.4}$$

Mathematically, the Born-Oppenheimer approximation is the assumption that the nuclear and electronic wave functions are separable;

$$\Psi_{total} = \Psi_{electrons}\Psi_{nuclei} \tag{2.5}$$

therefore;

$$\mathscr{H}_{elec}\Psi_{total} = E_{elec}\Psi_{total} \tag{2.6}$$

and;

$$E_{total} = E_{elec} + E_{nuc} \tag{2.7}$$

With this assumption, we can fix the nuclei at a set of positions, $\mathbf{R}$, and solve for the electronic wavefunction. If this is done over a range of $\mathbf{R}$ values a potential energy surface with respect to the movement of the nuclei can be obtained.

Throughout this section on electronic structure methods we will refer to $\mathscr{H}_{elec}$ as $\mathscr{H}$ for simplicity.

2.2.2 Antisymmetry Requirement

Electrons are fermions, and as such they must obey Pauli's exclusion principle, whereby two electrons of the same spin may not occupy the same state. In the context of electronic wave functions, mathematically this means that Ψ must be antisymmetric when two electrons are interchanged[120], a requirement described by Equation (2.8):

$$\Psi(\vec{x}_1, \vec{x}_2, \ldots, \vec{x}_i, \vec{x}_j, \ldots, \vec{x}_N) = -\Psi(\vec{x}_1, \vec{x}_2, \ldots, \vec{x}_j, \vec{x}_i, \ldots, \vec{x}_N) \qquad (2.8)$$

2.2.3 Variational Principle

As mentioned in the first section of this chapter, the Schrödinger equation cannot be solved analytically for more than three interacting particles. It is, however, possible to systematically refine an approximate solution to the wave function, leading us closer to the ground state energy of the system, E_0. This is as a result of the variational principle, which states that the energy of an approximate wave function is always greater than, or equal to, the true ground state energy[119];

$$\langle \Psi_{trial} | \mathscr{H} | \Psi_{trial} \rangle = E_{trial} \geq E_0 = \langle \Psi_0 | \mathscr{H} | \Psi_0 \rangle \qquad (2.9)$$

where the *equality* holds only if Ψ_{trial} is identical to Ψ_0. This gives us a measure of the quality of a wave function[120] - the lower the energy obtained, the closer our approximate wave function is to the exact wave function, Ψ_0.

This can be expressed as:

$$E_0 = \min_{\Psi \to N} E[\Psi] = \min_{\Psi \to N} \langle \Psi | \mathscr{H}_{elec} | \Psi \rangle \qquad (2.10)$$

Where $\Psi \to N$ represents that Ψ is an allowed N-electron wave function. Performing this search across all possible functions is too cumbersome for most systems, so a subset of eligible functions is usually chosen to perform the minimisation described in Equation (2.10)[119]. The resulting energy from this minimisation will be the best approximation from the chosen subset. This principle is the basis for the quantum mechanical methods we will discuss in the following sections.

2.2.4   The Hartree-Fock Approximation

The Hartree-Fock (HF) method approximates the N-electron wave function as a determinant of N one-electron wave functions $\chi_i(\vec{x}_i)$, known as a Slater determinant[122], Φ_{SD}:

$$\Psi_0 \approx \Phi_{SD} = \frac{1}{\sqrt{N!}} \begin{vmatrix} \chi_1(\vec{x}_1) & \chi_2(\vec{x}_1) & \dots & \chi_N(\vec{x}_1) \\ \chi_1(\vec{x}_2) & \chi_2(\vec{x}_2) & \dots & \chi_N(\vec{x}_2) \\ \vdots & \vdots & & \vdots \\ \chi_1(\vec{x}_N) & \chi_2(\vec{x}_N) & \dots & \chi_N(\vec{x}_N) \end{vmatrix} \qquad (2.11)$$

The Slater determinant is often written in short-hand, showing only the diagonal elements:

$$\Phi_{SD} = \frac{1}{\sqrt{N!}} \det \left\{ \chi_1(\vec{x}_1), \chi_2(\vec{x}_2), \dots, \chi_N(\vec{x}_N) \right\} \qquad (2.12)$$

The Slater determinant satisfies the antisymmetry requirement introduced in Section 2.2.2, as the determinant will change sign when an exchange of two rows or two columns is made. The one-electron functions $\chi_i(\vec{x}_i)$ are known as spin orbitals. They are written as a product of a spatial orbital $\psi_i(\vec{r})$ and one of two spin functions, $\alpha(s)$ or $\beta(s)$, which correspond to spin up and spin down, respectively:

$$\chi(\vec{x}) = \psi(\vec{r})\sigma(s); \quad \sigma = \alpha, \beta \qquad (2.13)$$

The only flexibility in the Slater determinant is the choice of spin orbitals. As a result of this, E_0 can be minimised with respect to the choice of spin orbital, giving us the Hartree-Fock equations:

$$\hat{f}\chi_i = \epsilon_i \chi_i; \quad i = 1, 2, \dots, N \qquad (2.14)$$

These N equations are eigenvalue equations, where ϵ_i are Lagrange multipliers, and are the eigenvalues of operator $\hat{f}$. The Fock operator $\hat{f}$ is a one electron operator defined by[119]:

$$\hat{f} = -\frac{1}{2}\nabla_i^2 - \sum_A^M \frac{Z_A}{r_{iA}} + V_{HF}(i) \qquad (2.15)$$

The first two terms are the kinetic energy and the potential energy resulting from electron-nucleus attraction. $V_{HF}(i)$ is the Hartree-Fock potential which attempts

to describe the average electron-electron repulsion felt by the ith electron due to the remaining N-1 electrons.

The Fock operators depend on the spin orbitals, as these are required to describe the Hartree-Fock potential $V_{HF}(i)$. This means the solution to the eigenvalue depends on itself and as a result an iterative process is required to minimise E_{HF}. This iterative technique is known as the *self-consistent field* (SCF) procedure[119]. Generally, an initial 'guess' of the starting orbitals is used to start the iterative procedure, and the HF equations are solved. The new set of orbitals obtained are used in the following iteration and so on until the output orbitals from sequential solutions are within a predefined threshold.

The Hartree-Fock approximation will always over-estimate the energy with respect to the exact ground state energy E_0. The difference between these two values is known as the correlation energy:

$$E_C = E_0 - E_{HF} \tag{2.16}$$

E_C is always negative, and is a measure of the error introduced by the Hartree-Fock approximation. The over-estimation in energy calculated by the Hartree-Fock method is caused by the electrostatic repulsions being calculated in an average manner. This generally allows electrons to move too close to each other and causes the electron-electron repulsion term to be too large. As the energy is always over-estimated, the HF approximation clearly obeys the variational principle we introduced in the previous section.

As the electron-electron interactions are only treated in an average way, a single Slater determinant is not an exact wavefunction of N interacting electrons. The Slater determinant is an eigenfunction of a Hamiltonian operator, which is itself a sum of Fock operators given in Equation (2.15):

$$\mathscr{H}_{HF}\Phi_{SD} = E_{HF}^0 \Phi_{SD} = \sum_i^N \hat{f}_i \Phi_{SD} \tag{2.17}$$

An important property of the system described by Equation (2.17) is that it describes a system of N electrons which do not explicitly interact with each other but experience an average potential V_{HF} - making the Slater determinant an exact

wave function of N *non-interacting* particles[119]. This feature which will be discussed again in the next section regarding Density Functional Theory.

2.2.5 Density Functional Theory

Hohenberg and Kohn [123] provided the first theories upon which density functional theory (DFT) was developed. Their work showed that the N-electron wave functions can be replaced by a simpler quantity - the electron density. The electron density is explicitly defined later in this chapter as the function $\rho(\vec{r})$ in Equation (2.22), however it is worth mentioning here that it is a measure of the probability of an electron occupying a small region of space around point $\vec{r}$. Throughout this chapter we will often omit the $\vec{r}$ for simplicity and generally refer to the electron density as ρ or the ground state electron density as ρ_0.

As a result of the work of Hohenberg and Kohn [123], it is possible to represent the ground state energy as a functional of the ground state electron density[119]:

$$E_0[\rho_0] = T[\rho_0] + E_{ee}[\rho_0] + E_{Ne}[\rho_0] \tag{2.18}$$

A functional is a "function of a function", in this case ρ_0 (the ground state electron density) is the function of the functional E_0. The final term of Equation (2.18), the potential energy attributed to the nuclei-electron attraction can be considered 'system dependent', while in theory the first two terms are universal. The system independent parts can be grouped into a new quantity known as the Hohenberg-Kohn functional $F_{HK}[\rho]$;

$$F_{HK}[\rho] = T[\rho] + E_{ee}[\rho] \tag{2.19}$$

where $T[\rho]$ is the kinetic energy, and $E_{ee}[\rho]$ the electron-electron interactions. $E_{ee}[\rho]$ is given by Equation (2.20);

$$E_{ee}[\rho] = \frac{1}{2} \int \int \frac{\rho(\vec{r}_1)\rho(\vec{r}_2)}{r_{12}} d\vec{r}_1 d\vec{r}_2 + E_{ncl}[\rho] = J[\rho] + E_{ncl}[\rho] \tag{2.20}$$

where $J[\rho]$ represents the well-known classical Coulomb part, and $E_{ncl}[\rho]$ groups together a variety of non-classical contributions to the electron-electron interactions, including self-interaction, exchange and correlation. The result is that

for F_{HK} there are two major unknowns - $T[\rho]$ and $E_{ncl}[\rho]$, and density functional theory methods are devoted to calculating estimates of these components.

The variational principle also applies to the ground state energy functional - the $F_{HK}[\rho]$ which delivers the ground state of the system will give the lowest energy only if the input density is the true ground state density ρ_0:

$$E_0 \leq E[\tilde{\rho}] = T[\tilde{\rho}] + E_{Ne}[\tilde{\rho}] + E_{ee}[\tilde{\rho}] \qquad (2.21)$$

Thus any trial density $\tilde{\rho}(\vec{r})$ given to Equation (2.21) will provide an E value which is an upper bound of the true ground state energy E_0. There is an important condition which must be met for this statement to hold true; that the given density must be related to a valid antisymmetric wave function. Densities which satisfy this condition are known as *N-representable*[119].

In reality, many N-electron wave functions can yield the same density, however the correct ground state wave function will be the one which gives the lowest energy[119]. In the context of HK the wave function Ψ associated with a given density is not accessible. In addition to the fact that many wave functions could yield the same density, there is the additional problem of sign. The density is related to the square of a real wave function Ψ[119];

$$\rho(\vec{r}) = N \int \ldots \int |\Psi(\vec{x}_1, \vec{x}_2, \ldots, \vec{x}_N)|^2 dx_1 d\vec{x}_2 \ldots d\vec{x}_N \qquad (2.22)$$

so there are always at least two possible wave functions that could correspond to a given density; $+\Psi$ or $-\Psi$, and there is no way to know which is the true wave function for a given ρ.

The theories devised by Hohenberg and Kohn [123] laid the foundation for DFT. However, it did not provide a practical means for constructing the functional that will yield the ground state energy, or an estimate to this energy. Their theorems provide a proof that a direct relationship exists between the ground state density $\rho_0(\vec{r})$ and the ground state energy E_0. Kohn and Sham [124] continued to build on this foundation and suggested a means for estimating F_{HK} - the 'universal' portion of the ground state energy.

Kohn and Sham [124] used aspects of the Hartree-Fock scheme discussed in the previous section. We showed the Slater determinant can be considered an exact wave function of a system of N non-interacting electrons moving in the potential

V_{HF}[119]. The kinetic energy for such a system is given by[119]:

$$T_{HF} = -\frac{1}{2} \sum_i^N \langle \chi_i | \nabla^2 | \chi_i \rangle \tag{2.23}$$

The spin orbitals χ_i in Equation (2.23) are chosen such that the resulting E_{HF} is at a minimum achievable value:

$$E_{HF} = \min_{\Phi_{SD} \to N} \langle \Phi_{SD} | \hat{T} + \hat{V}_{Ne} + \hat{V}_{ee} | \Phi_{SD} \rangle \tag{2.24}$$

The methods introduced by Kohn and Sham [124] aim to exploit these equations derived from the Hartree-Fock approximation, which relate to a non-interacting system of fermions, in order to calculate the major part of the kinetic energy for an interacting system of fermions.

It is possible to construct a non-interacting reference system with a Hamiltonian given by:

$$\hat{H}_S = -\frac{1}{2} \sum_i^N \nabla_i^2 + \sum_i^N V_S(\vec{r}_i) \tag{2.25}$$

This equation does not include any electron-electron interactions - so it describes a non-interacting system of electrons. The ground state wave function in Kohn-Sham theory is again represented by a Slater determinant, Θ_S, comprised of N one-electron Kohn-Sham wave functions, φ_N, similarly defined as Equation (2.11). Additionally the spin orbitals, φ_i, are determined in a way analogous to Equation (2.14):

$$\hat{f}_{KS} \varphi_i = \epsilon_i \varphi_i \tag{2.26}$$

where the one-electron Kohn-Sham operator is defined by:

$$\hat{f}_{KS} = -\frac{1}{2} \nabla^2 + V_s(\vec{r}) \tag{2.27}$$

The connection between the non-interacting system defined by these Kohn-Sham operators is to choose an effective potential, V_s, in such a way that the resulting density equals the ground state density of the target system of interacting electrons:

$$\rho_s(\vec{r}) = \sum_i^N \sum_s |\varphi_i(\vec{r}, s)|^2 = \rho_0(\vec{r}) \tag{2.28}$$

The method of Kohn and Sham [124] aims to compute exactly as much of the kinetic energy as is possible, and approximate the remainder. They used the equation below to determine the exact kinetic energy of the non-interacting reference system; with the requirement that the density of this non-interacting system is the same as our real interacting system of fermions:

$$T_s = -\frac{1}{2}\sum_i^N \langle \varphi_i | \nabla^2 | \varphi \rangle \tag{2.29}$$

However, the kinetic energy of the non-interacting system is not equal to that of the interacting system, (*i.e.* $T_S \neq T$)[119]. Kohn and Sham [124] accounted for this difference by introducing a new term, E_{XC}, to the functional $F[\rho]$;

$$F[\rho(\vec{r})] = T_S[\rho(\vec{r})] + J[\rho(\vec{r})] + E_{XC}[\rho(\vec{r})] \tag{2.30}$$

where E_{XC}, the exchange-correlation energy, is defined by:

$$E_{XC}[\rho] = (T[\rho] - T_S[\rho]) + (E_{ee} - J[\rho]) = T_C[\rho] + E_{ncl}[\rho] \tag{2.31}$$

The exchange-correlation functional groups together all of the unknown quantities. It contains the correction for non-classical effects of self interaction, exchange and correlation, and also the remaining portion of the kinetic energy. The energy expression for our real interacting system of electrons is given by:

$$E[\rho(\vec{r})] = T_S[\rho] + J[\rho] + E_{XC}[\rho] + E_{Ne}[\rho] \tag{2.32}$$

The term for which the form is unknown is the exchange-correlation energy.

If we apply the variational principle we will find that the orbitals need to fulfil the following equation:

$$\left(-\frac{1}{2}\nabla^2 + V_{eff}(\vec{r})\right)\varphi_i = \epsilon_i \varphi_i \tag{2.33}$$

Comparing this to Equations (2.26) and (2.27), which apply to a non-interacting reference system it is clear that $V_{eff} = V_S$:

$$V_S(\vec{r}) \equiv V_{eff}(\vec{r}) = \int \frac{\rho(\vec{r}_2)}{r_{12}} d\vec{r}_2 + V_{XC}(\vec{r}_1) - \sum_A^M \frac{Z_A}{r_{1A}} \tag{2.34}$$

The Kohn-Sham one-electron equations need to be solved iteratively via the same

self-consistent field method introduced for the Hartree-Fock approximation in the previous section. Here the process begins by determining the potential V_S approximately, which is used to determine the one-electron Kohn-Sham operators $\hat{f}^{KS}$. The one-electron operators allow us to determine the spin orbitals φ_i and we can use these to calculate the electron density $\rho_s(\vec{r})$, and finally the energy from Equation (2.32). As V_S depends on the density, the process can be repeated iteratively until convergence of the energy is achieved.

Other than two fundamental approximations, that of Born-Oppenheimer and the assumption we are dealing with time-independent wave functions, the only approximation in the Kohn-Sham formalism we have described is due to the fact that the form of V_{XC} and E_{XC} are unknown. As a consequence of this, the quality of any density functional calculation depends strongly on the chosen form of the exchange-correlation functional.

2.2.5.1 Exchange Correlation Functionals

The starting point for many exchange-correlation functionals is the model system known as a uniform electron gas[119]. The reason for this is that a uniform electron gas is one of the few systems for which the exchange and correlation energy functionals are known to a very high accuracy. Though this model system is a relatively poor representation of the density in most atomic or molecular systems, it is a convenient place to at least begin approximating an exchange-correlation functional. A form of exchange-correlation functional based on the density of a uniform electron gas is known as the local density approximation (LDA), which is written as;

$$E_{XC}^{LDA}[\rho] = \int \rho(\vec{r})\varepsilon_{XC}(\rho(\vec{r}))d\vec{r} \qquad (2.35)$$

where $\varepsilon_{XC}(\rho(\vec{r}))$ is the exchange-correlation energy per particle of a uniform electron gas of density $\rho(\vec{r})$, and is weighted with the probability $\rho(\vec{r})$ that there is an electron at this position in space[119]. ε_{XC} can be broken down into its constituent parts:

$$\varepsilon_{XC}(\rho(\vec{r})) = \varepsilon_X(\rho(\vec{r})) + \varepsilon_C(\rho(\vec{r})) \qquad (2.36)$$

The exchange part, ε_X, was derived in the 1920's by Bloch and Dirac[119]:

$$\varepsilon_X(\rho(\vec{r})) = -\frac{3}{4}\sqrt[3]{\frac{3\rho(\vec{r})}{\pi}} \qquad (2.37)$$

However, an explicit form for ε_C, the correlation part of ε_{XC} is not known. Quantum Monte Carlo simulations have been performed by Ceperley and Alder [125], which have led to highly accurate estimations of this value for a uniform electron gas. Most of the popular functionals that have been implemented for ε_C interpolate the results of the Monte Carlo simulations of Ceperley and Alder [125]. Two of the most widely used of these are produced by Vosko *et al.* [126] and Perdew and Wang [127], commonly abbreviated as VWN and PW92, respectively. One disadvantage to the LDA exchange-correlation functional is that while it is generally quite accurate for solid-state calculations of structure, it significantly overestimates binding energies, making it inapplicable to many problems in chemistry[119].

Another set of exchange-correlation functionals was defined in the early eighties which attempted to overcome the inaccuracies of LDA; these are known as generalized gradient approximations (GGA). These functionals are based around the idea of using not only the density $\rho(\vec{r})$, but to supplement the density with information concerning the gradient of the charge density, $\nabla\rho(\vec{r})$. This in effect takes into account the inhomogeneous nature of most atomic and molecular systems, something which is neglected by using the uniform electron gas model. The GGA functionals are of the general form:

$$E_{XC}^{GGA}[\rho_\alpha, \rho_\beta, \nabla\rho_\alpha, \nabla\rho_\beta] = \int f(\rho_\alpha, \rho_\beta, \nabla\rho_\alpha, \nabla\rho_\beta) d\vec{r} \qquad (2.38)$$

E_{XC}^{GGA} can be split into its exchange and correlation portions:

$$E_{XC}^{GGA} = E_X^{GGA} + E_C^{GGA} \qquad (2.39)$$

Generally approximations are determined for each of the separate terms, and the exchange portion for GGA is given by the following equation:

$$E_X^{GGA} = E_X^{LDA} - \sum_\sigma \int F(s_\sigma)\rho_\sigma^{4/3}(\vec{r}) d\vec{r} \qquad (2.40)$$

The argument s_ρ is known as a reduced density gradient for a given spin σ:

$$s_\sigma(\vec{r}) = \frac{|\nabla\rho_\sigma(\vec{r})|}{\rho_\sigma^{4/3}(\vec{r})} \qquad (2.41)$$

s_ρ is a 'local inhomogeneity' parameter. The functional F in Equation (2.40) can take many forms, and there have been a number suggested in the literature to date, for example a functional known simply as B or B88 by Becke [128] and another version developed later known as B96[129]. Many other GGA functionals exist, either as correlation functionals, E_C^{GGA}, such as LYP by Lee *et al.* [130], and functionals which include both exchange and correlation, such as the PBE functional of Perdew *et al.* [131].

Hybrid functionals also exist, where the exchange-correlation functional is defined as a combination of 'exact' exchange and density functional exchange-correlation functionals. The method was initially introduced by Becke [132], and in the same year he introduced a functional known as B3[133]. Stephens *et al.* [134] performed some modifications to the original B3 functional and the resulting B3LYP functional is one of the most popular hybrid functionals currently in use.

2.2.6 Basis Sets

One final and significant aspect of the implementation of DFT or HF is the choice of basis set. A basis set is a set of functions which, in their simplest form, represent atomic orbitals. These functions can be combined together to create molecular orbitals - a method known as the linear combination of atomic orbitals (LCAO)[119]. When the LCAO method was first developed the set of basis functions $\{\eta_\mu\}$ resembled the known atomic orbitals of the hydrogen atom. However, the basis functions in use today do not necessarily resemble atomic functions anymore. A purely numerical approach to solving the KS equations is possible for simple cases, but is too demanding for most applications. For DFT to become a routine technique a simplified approach for expanding the KS molecular orbitals was required. Roothaan [135] developed a LCAO approach for achieving the expansion of molecular orbitals, a method we will describe here as it is the scheme most commonly applied in DFT programs.

In the LCAO approach of Roothaan [135] a set of L basis functions $\{\eta_\mu\}$ are used to linearly expand the orbitals:

$$\varphi_i = \sum_{\mu=1}^{L} c_{\mu i} \eta_\mu \qquad (2.42)$$

For a complete set of basis functions every spin orbital φ_i would be exactly expressed by Equation (2.42). In reality the implementation of the basis functions must be finite and therefore incomplete, so it is important to choose the set of basis functions such that the linear combination given by (2.42) provides a satisfactory approximation to the Kohn-Sham orbitals.

Substituting this definition of φ into the Kohn-Sham Equation (2.26) we obtain:

$$\hat{f}^{KS} \sum_{\mu=1}^{L} c_{vi} \eta_v(\vec{r_i}) = \varphi_i \sum_{\mu=1}^{L} c_{\mu i} \eta_\mu \qquad (2.43)$$

Multiplying the equation on the left with a basis function η_μ we get L equations;

$$\sum_{v=1}^{L} c_{vi} \int \eta_\mu(\vec{r_1}) \hat{f}^{KS}(\vec{r_1}) \eta_v(\vec{r_1}) d\vec{r_1} = \varepsilon_i \sum_{v=1}^{L} c_{vi} \int \eta_\mu(\vec{r_1}) \eta_v(\vec{r_1}) d\vec{r_1} \qquad (2.44)$$

where $1 \leq i \leq L$. The integrals on each side of Equation (2.44) ultimately define two matrices. The integrals on the left hand side define the elements of the Kohn-Sham matrix, $\mathbf{F}^{KS}$, while the integrals on the right define the elements of the overlap matrix, $\mathbf{S}$. Both of these matrices are symmetric and LxL dimensional. The remaining terms from Equation (2.44) can also be described as matrices, where the expansion vectors are given by:

$$\mathbf{C} = \begin{pmatrix} c_{11} & c_{12} & \dots & c_{1L} \\ c_{21} & c_{22} & \dots & c_{2L} \\ \vdots & \vdots & & \vdots \\ c_{L1} & c_{L2} & \dots & c_{LL} \end{pmatrix} \qquad (2.45)$$

and ε is a diagonal matrix of the orbital energies:

$$\boldsymbol{\varepsilon} = \begin{pmatrix} \varepsilon_1 & 0 & \dots & 0 \\ 0 & \varepsilon_2 & \dots & 0 \\ \vdots & \vdots & & \vdots \\ 0 & 0 & \dots & \varepsilon_L \end{pmatrix} \qquad (2.46)$$

Finally we have an equation for the LCAO expansion that can be defined solely by these matrices:

$$\mathbf{F}^{KS}\mathbf{C} = \mathbf{S}\mathbf{C}\boldsymbol{\varepsilon} \qquad (2.47)$$

This compact equation derived by Roothaan [135] significantly reduced the complexity of LCAO expansion in the context of HF theory. A non-linear optimisation problem comprised of integro-differential equations has been reduced to an optimisation problem based on standard linear algebra - a solution easy to implement in a computational sense.

In wave function based methods, such as Hartree-Fock, the basis set $\{\eta_\mu\}$ is often comprised of Gaussian-orbitals (GTOs) of the form:

$$\eta^{Gaussian} = N x^l y^m z^n \exp(-\alpha r^2) \tag{2.48}$$

where N is a normalisation factor, α determines how compact (large values of α) or diffuse (small values of α) the resulting function is. The values l, m and n are used to classify the orbital as s-, $p-$, $d-$ (or higher) functions, where $L = l + m + n$ and for s-functions $L = 0$, p-functions $L = 1$ and so on. x, y and z are cartesian coordinates and r^2 is defined as $x^2 + y^2 + z^2$.

GTO basis functions are quite popular as efficient algorithms exist for analytically calculating the associated integrals. Slater-type orbitals (STO) are a more intuitive choice for basis functions, as they mimic the exact eigenfunctions, or atomic oribtals, of the hydrogen atom:

$$\eta^{Slater} = N r^{n-1} \exp(-\zeta r) Y_{lm}(\Theta, \phi) \tag{2.49}$$

Generally, at least three times as many GTO functions are required as STO functions to achieve the same level of accuracy[119]. However, no analytical technique currently exists for evaluating all the multi-centre integrals when using STO functions. As a result, the GTO method is often much more computationally efficient, even when many more GTO functions are required than if STO functions were used.

Often GTO basis sets are used in a form known as contracted GTO basis sets where several GTO Gaussian functions are combined in a fixed linear combination to obtain a contracted Gaussian function (CGF):

$$\eta_\pi^{CGF} = \sum_a^A d_{a\tau} \eta_a^{Gaussian} \tag{2.50}$$

The contraction coefficient, $d_{a\tau}$, can be chosen in such a way that the CGF closely resembles a single STO function, while still taking advantage of the quick computation of the GTOs. The simplest expansion of molecular orbitals uses only one basis function for each atomic orbital and is known as a minimal basis set. An example of this is known as the STO-3G basis set, where three Gaussian functions are combined into one CGF. Results from basis sets such as this are not often used now that larger basis sets can be computationally afforded[119]. An extra level of sophistication was achieved when "double-zeta" basis sets were introduced. The name double-zeta comes from the use of the greek letter "zeta" (ζ) in the exponent of the STO, and the use of two zeta functions for each orbital - hence double-zeta. Analogously, minimal basis sets can be called single-zeta, and basis sets with three or four zeta functions for each orbital are known as triple- or quadruple-zeta, respectively. Commonly only the valence shell electrons are treated with double (or more) functions, and the inner core electrons remain modelled with single functions (minimal sets). When this scheme is implemented it is known as a "split-valence" basis set. Examples of these include 3-21G, 6-31G and 6-311G developed by John Pople and coworkers[136, 137].

In many applications polarisation functions are applied, adding yet another level of sophistication to the technique. A basis set augmented by polarisation functions includes functions of higher angular momentum than the highest occupied orbital in a given system - for example having p-functions for modelling hydrogen. Incorporating these functions allows orbitals to distort from their original atomic symmetry, and adapt to their surrounding environment. Polarised double-zeta, triple-zeta or split-valence basis sets are commonly employed in DFT, as they offer an acceptable balance between accuracy and computational efficiency.

2.2.7   SIESTA methodology

The SIESTA methodology[138] is one approach to DFT which aims to achieve computational linear scaling with respect to the size of the system being modelled, making it feasible to perform DFT calculations on larger systems. The SIESTA methodology attempts this through 'locality', whereby the orbitals are defined to tend to zero at a defined radius. With this implementation many of the interactions between atoms are naturally 'cut-off' at a defined distance. In this way, the number

of interactions per atom is constant even if the size of the system is increased; as a result the cost of the calculations performed in this way will scale $O(N)$.

SIESTA makes use of pseudopotentials to model the core electrons of the system. In theory, all electrons should be included in a calculation, however the core electrons of an atom can be considered relatively unperturbed regardless of the chemical changes and bonding that occurs between atoms. A pseudopotential can be used to model the effective potential due to the nucleus and core electrons up to a given radius of an atom, such that only the valence electrons are explicitly included in the calculation. Within the core radius a smoothed potential is used with the constraint that it must match the true potential at the boundary. Pseudopotentials are often used as an easy way to reduce the computational expense of a DFT calculation with a limited impact on the accuracy of the calculation. A separate program is combined with the SIESTA package known as 'atom' which can generate desired pseudopotentials according to a number of schemes, with the Troullier-Martins[139] scheme being one of the most popular.

Basis sets within SIESTA are 'physically motivated', in that they take a form similar to the traditional atomic orbitals. The default basis set is comprised of Pseudo Atomic Orbitals (PAO), where atomic basis orbitals are calculated as a product of a numerical radial function and a spherical harmonic. For computational convenience the numerical radial function is tabulated on a logarithmic radial grid, rather than using an approximate analytical form. The implementation of PAOs in SIESTA supports multiple-zeta basis sets, with a double-zeta polarised (DZP) recommended as the minimum level of sophistication. An additional approximation is introduced in the implementation of PAOs in SIESTA, where the tails of the PAOs are modified to go smoothly to zero at a given radius. This is known as radial confinement, and the choice of radius allows the user to opt for higher precision, when using large radii, or greater computational efficiency, when using smaller radii.

The electron density is also represented on a uniform Cartesian grid. This improves computational efficiency, but it does introduce some numerical errors when calculations are performed using the electron density. While the numerical integration performed at the grid points is correct, errors arise because integration performed between adjacent grid points is only an estimate, and the precision of these calculations will thus depend on the fineness of the grid used; this value is

defined with a mesh cut-off, typically of magnitude 80 to 400 Ry depending on the basis set in use[140].

The SIESTA methodology uses some additional techniques for improving the efficiency of calculations performed on periodic systems. A method devised by Monkhorst and Pack [141] is used in SIESTA for selecting a uniform grid of K-points to be used for integration across the Brillouin zone. The user is able to define a K-grid cut-off, a distance value which in essence allows similar systems to achieve comparable convergence due to the formalism of Moreno and Soler [142].

2.2.8   Periodicity

For any simulation of periodic (bulk) systems it is necessary to employ periodic boundary conditions (PBC). The simulation cell, often a form with right-angles (cubic, orthorhombic or tetragonal), is replicated in all directions to form an infinite lattice.
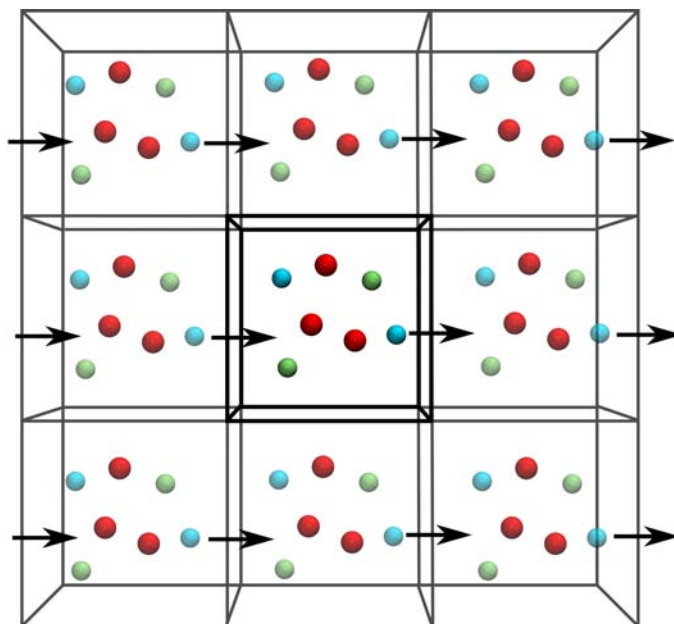
FIGURE 2.1: Illustration of periodic boundary conditions. The movement of a particle is shown, moving to and from the simulation cell (shown in black) and the surrounding replica images.

If a molecule leaves the cell during the simulation, it is replaced by an image particle that enters from the opposite side of the box[143]. An example of periodic boundary conditions applied to a simple system is shown in Figure 2.1. The motion

of a particle is shown moving from one edge of the simulation cell, shown in black, through the other side of the box. This process is implemented to minimise surface effects, which would otherwise occur at the boundaries of the cell. Any 'box' or cell shape can be used as long as it can be translated in all three dimensions forming a continuous supercell.

Generally, PBC can be used in two or three dimensions depending on the system being studied (*i.e.* a surface vs. an infinite crystal lattice). However, in the context of SIESTA, all systems are required to have three-dimensional PBC, even if the system is finite in one or more dimensions, such as for a molecule or a surface[140]. This is a consequence of the use of Fast Fourier Transform libraries in the implementation of SIESTA. In cases where there is no real need for periodicity, such as molecules, the simulation cell size needs to be chosen such that there is no overlap between the basis functions of images, otherwise the molecule will be interacting with its neighbouring images.

Now that we have briefly covered the background of first principles calculations, we will introduce force field methods that will be extensively used throughout this work.

2.3 Molecular Mechanics

Many problems that we would like to consider in computational chemistry are just too large to be considered routinely using quantum mechanics. Force field methods (also known as molecular mechanics, or abbreviated to MM) do not consider the movements of electrons. Instead the energy of a system is calculated as a function of the nuclear positions[118], as explained earlier with respect to the Born-Oppenheimer approximation in Equation (2.2.1). In force field methods the molecules are modelled in a simplified way, using a "ball and spring" representation of atoms and bonds. The bond, or spring, which connects two atoms, can stretch or compress depending on the inter- or intra-molecular forces acting on those atoms. Each atom is represented as a single particle, and can be considered simply as a 'ball'.

The different interactions, or potentials, used to model a system are collectively referred to as a force field. Each component describes the potential energy of a
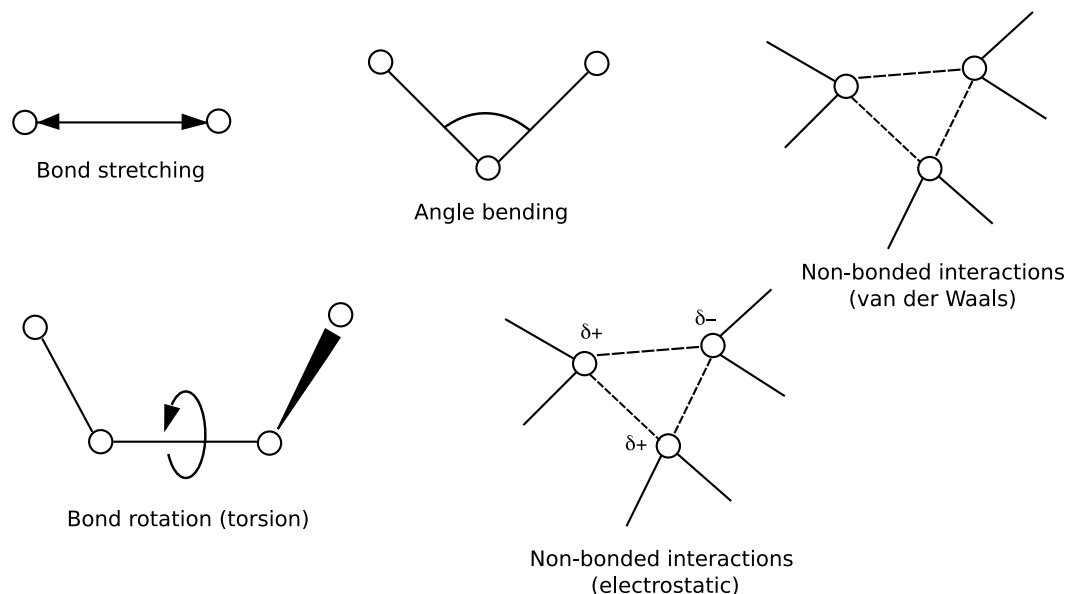
FIGURE 2.2:   Representation of the non-bonded and bonded interactions
contributing to a molecular mechanics force field. Image adapted from Leach
[118].
.

specific interaction, and summed together the total force field potential energy can
be obtained;

$$U_{FF} = U_{str} + U_{bend} + U_{torsional} + U_{vdw} + U_{electrostatic} + U_{oop} + U_{cross} \qquad (2.51)$$

where U_{str} represents the energy required for stretching the bond between two
atoms, U_{bend} represents the energy required for bending between three atoms, U_{tors}
the energy required for rotation about the middle bond in a 4-atom sequence, and
U_{oop} the energy required to distort the geometry of a central atom out-of-plane from
its neighbours. U_{vdw} represents the interactions between non-bonded atoms, while
$U_{electrostatic}$ represents the electrostatic interactions and U_{cross} represents coupling
between the first three bonded terms[117].

Generally, *ab initio* quantum mechanical information or experimental observations
are used to parameterise the behaviour of atoms and bonds in a given force
field[144]. Each of the terms in the potential force-field are discussed in more
detail in the following sections on intra- and intermolecular interactions.

2.3.1 Intramolecular interactions (Short-range interactions)

2.3.1.1 Bond stretching

Bond stretching can be described in different ways: here we will discuss two commonly used potentials, the harmonic form and the Morse potential, both illustrated in Figure 2.3.
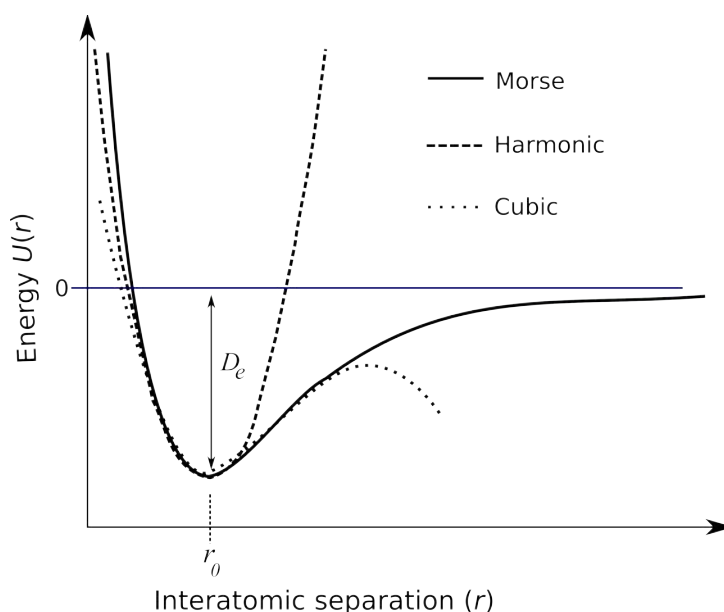
FIGURE 2.3: Three commonly used forms for the potential energy $U(r)$ with respect to the interatomic distance r; the harmonic form (dashed line), Morse potential (bold line) and cubic form (dotted line).

The simplest bond stretching potential is modelled using the harmonic form, which was used in some of the first formulations of molecular mechanics[145, 146]. The harmonic form is also known as Hooke's law, which effectively models the bond between two atoms as a "spring". The energy varies with the square of the displacement from a reference bond length, r_0:

$$U(r) = \frac{k}{2}(r - r_0)^2 \tag{2.52}$$

The variable k is a force constant, or spring constant, which denotes how stiff the "spring" is that connects atoms i and j. The reference bond length r_0 is the bond length adopted when all the other terms in the force field are zero.

Another functional form is the Morse potential[147], given in equation (2.53);

$$U(r) = D_e \left[(1 - e^{-a(r-r_0)})^2 - 1 \right] \tag{2.53}$$

where r is the distance between atoms i and j, r_0 is the equilibrium bond distance, D_e is the depth of the well and a specifies the curvature about the minimum of the potential form. The Morse potential is not very efficient to compute due to the presence of an exponential term. Since bonds in a MM calculation will not usually deviate very far from equilibrium values, a simpler potential form, such as Hooke's law, can often be used. Hooke's law gives a good approximation to the shape of the potential energy curve at the bottom of the well, but is less accurate away from equilibrium. Higher terms can be included to get a model which behaves similarly to the Morse potential for small displacements, for example:

$$U(r) = \frac{k}{2}(r - r_0)^2 [1 + k'(r - r_0) + k''(r - r_0)^2 + k'''(r - r_0)^3 ...] \tag{2.54}$$

Problems are also evident with the cubic form given in Equation (2.54). When the bond length is very far from equilibrium the potential energy will pass through a maximum before dropping away, as illustrated in Figure 2.3. Due to this, a cubic form can only be used when the structure is inside the potential well and close to equilibrium geometry.

2.3.1.2   Angle bending

Angle bends are also commonly described using Hooke's law (*i.e.* a harmonic potential), to model how flexible an angle is between three atoms i, j and k:

$$U(\theta_{jik}) = \frac{k_B}{2}(\theta_{jik} - \theta_0)^2 \tag{2.55}$$

Similar to the definition for bond stretching, this form is a measure of the deviation of the angle θ_{jik} from a reference angle θ_0, where k_B is a force constant which indicates how stiff the spring is across the angle between three atoms.

2.3.1.3 Torsional terms

The torsional energy of a system is much softer than the angle-bending and bond-stretching terms, which in contrast require a large amount of energy to significantly deform the system. Torsional potentials are used to emulate the preference for certain conformational isomers, where rotation about the torsional bond results in distinct minima and maxima, usually at staggered and eclipsed conformations. A simple example of this is butane ($CH_3CH_2CH_2CH_3$), where rotation about the central carbon-carbon bond results in four distinct stationary points and two conformational isomers lying at energy minima, as illustrated in Figure 2.4. The 'staggered' conformations are those for which the torsional angle is 60° or 180°. The substituents at either end group are at a maximum distance from each other and as a result these conformations are usually energy minima. There are two staggered conformations for butane, the "gauche" and "anti" form, with the "anti" being the lowest energy minima at 180°. The 'eclipsed' conformations have a torsional angle of 0°, resulting in the substituents of the end groups essentially overlapping each other. This state is highly unfavoured due to steric hinderance, so these eclipsed conformations are usually energy maxima[148].

The torsional energy must also be periodic in the angle ω; it will at least be periodic about 360° and depending on the system the periodicity may be more frequent. The periodicity is typically represented by a cosine series expansion;

$$U(\omega) = \sum_{n=0}^{N} \frac{V_n}{2}[1 + \cos{(n\omega - \gamma)}] \tag{2.56}$$

where V_n indicates the height of the barrier of rotation about the *j-k* bond, n is the periodicity and γ is the phase angle.

2.3.2 Intermolecular interactions (Long-range interactions)

Long-range interactions play an important role in crystalline structures. Non-bonded terms in MM force fields are usually broken down into two groups - electrostatic interactions and van der Waals terms. Electrostatic interactions
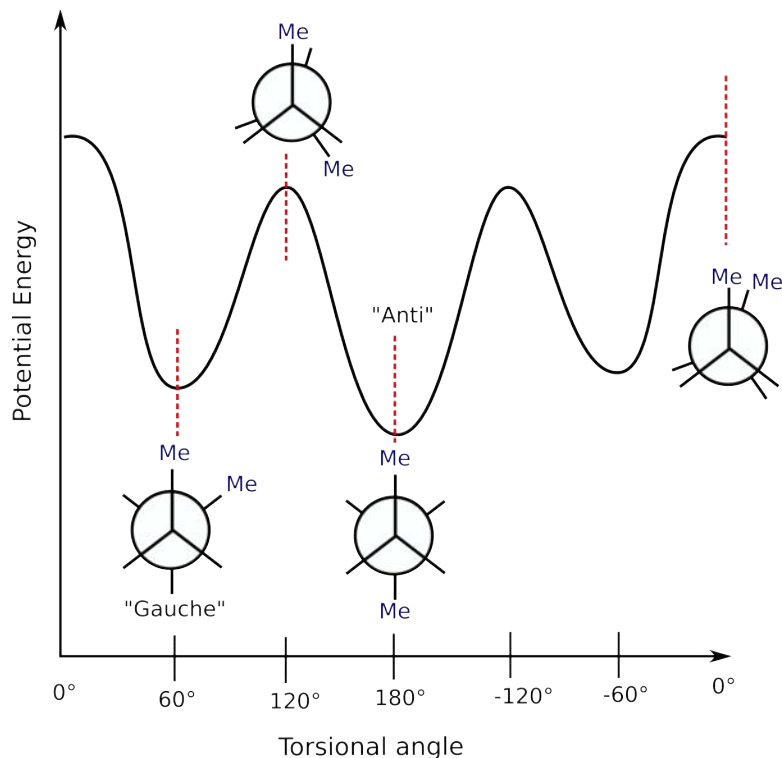
FIGURE 2.4: The potential energy surface of butane, plotted with respect to the torsional angle. Newman projections of four conformational isomers are shown, where "Me" represents a methyl group, and hydrogens are not shown for simplicity. Image adapted from Morrison and Boyd [148]

can be computed using a variety of different methods, described in the following section.

2.3.2.1 Direct summation

The charge distribution throughout a molecule can be represented as an arrangement of fractional point charges designed to reproduce the molecule's electrostatic properties. The electrostatic interaction between two molecules (or different parts of the same molecule) can be calculated via Coulomb's law, given in equation (2.57);

$$U(r) = \sum_{i=1}^{N_A} \sum_{j=1}^{N_B} \frac{q_i q_j}{4\pi\epsilon_0 r} \tag{2.57}$$

where N_A and N_B represent the number of point charges in the two molecules A and B, q_i and q_j are the magnitudes of point charges i and j, r is the distance between point charges of atoms i and j, and ϵ_0 is a physical constant known as the permittivity of free space.

One of the major problems with actually trying to implement long-range interactions such as these is the extent of their range. This Coulombic charge-charge interaction is particularly problematic because of its slow decay, proportional to r^{-1}. Various methods have been developed to provide an adequate treatment of long-range forces, some of which will be introduced here, with the Ewald summation for periodic systems being covered in the next section.

The simplest means of eliminating the long-distance problem of the Coulombic sum is to implement a cut-off radius, r_{cut}:

$$U(r_{ij}) = \frac{q_i q_j}{4\pi\epsilon_0} \left\{ \frac{1}{r_{ij}} - \frac{1}{r_{cut}} \right\} \tag{2.58}$$

One of the major problems with this method is that it is *conditionally convergent*, and if the charge of the sphere bounded by r_{cut} has a net charge the Coulomb energy calculated will be incorrect.

The cell multipole method was devised by Ding *et al.* [149] in an attempt to calculate the Coulombic forces without the same problems of convergence. The simulation cell is broken into smaller regions, and a multipole is calculated for each region. Wolf *et al.* [150] also introduced a method for efficiently summing the Coulombic interactions in periodic systems in real space by imposing charge neutrality in the cut-off sphere. However, we will focus on the most widely employed method, known as the Ewald summation.

2.3.2.2 Ewald summation

The Ewald sum[143, 151] is a method devised to efficiently sum the interaction between all ions and their periodic images[118, 143]. A particle interacts with all other particles in the simulation box, and with all of their images in an infinite array of periodic cells. The charge-charge contribution to the potential energy from all pairs of charges in the simulation box can be written according to Coulomb's law;

$$U = \frac{1}{2} \sideset{}{'}\sum_{|\mathbf{n}|=0} \sum_{i=1}^{N} \sum_{j=1}^{N} \frac{q_i q_j}{4\pi\epsilon_0 |\mathbf{r}_{ij} + \mathbf{n}|} \tag{2.59}$$

where $\mathbf{n}$ is the set of lattice points. The prime ($'$) on the first summation indicates that if $i=j$ and $|\mathbf{n}|=0$ the term is not included in the summation - which ultimately means that the particle is interacting with other ions and its periodic images, but

not itself. The main problem with this summation, as mentioned previously, is that it converges very slowly, if at all. The Ewald sum attempts to convert this summation into two quickly converging series. The first trick with the Ewald summation is to place a Gaussian charge distribution of opposite sign at the position of each of the fractional charges, effectively neutralising the charge[118]:

$$\rho_i(\mathbf{r}) = \frac{q_i \alpha^3}{\pi^{3/2}} \exp(-\alpha^2 r^2) \tag{2.60}$$

The real space sum becomes a sum of the interactions between the charges plus the neutralising distributions. This dual summation is given by;

$$U_{\text{real}} = \frac{1}{2} \sum_{i=1}^{N} \sum_{j=1}^{N} \sum_{|\mathbf{n}|=0}' \frac{q_i q_j}{4\pi\epsilon_0} \frac{\text{erfc}(\alpha|\mathbf{r}_{ij} + \mathbf{n}|)}{|\mathbf{r}_{ij} + \mathbf{n}|} \tag{2.61}$$

where erfc is the complementary error function, which is given by[118]:

$$\text{erfc}(x) = \frac{2}{\sqrt{\pi}} \int_x^\infty e^{-t^2} dt \tag{2.62}$$

The crux of this summation is that it converges very rapidly, and beyond a finite cut-off distance its contribution can be considered negligible. A second contribution must be computed to subtract the first neutralising distribution, and is given by equation (2.63):

$$U_{\text{recip}} = \frac{1}{2} \sum_{k \neq 0}^{N} \sum_{i=1}^{N} \sum_{j=1}^{N} \frac{1}{V} \frac{q_1 q_j}{4\pi\epsilon_0} \frac{4\pi}{k^2} \exp\left(-\frac{k^2}{4\alpha^2}\right) \exp(i\mathbf{k} \cdot \mathbf{r}) \tag{2.63}$$

This summation is done in *reciprocal space*, with $\mathbf{k}$ being a reciprocal vector $\mathbf{k} = 2\pi\mathbf{n}/L^2$ and is rapidly convergent as it involves smooth Gaussian functions only[118]. The number of terms included increases with the width of the Gaussians given in Equation (2.60). A balance needs to be found between the real- and reciprocal-space summations, as the real-space summations converge rapidly for large values of α and the reciprocal-space summations at small values of α. The choice of α can therefore significantly alter the speed of convergence of the Ewald summation.

2.3.2.3 Polarisability

For ionic materials the polarisability of ions is not represented by fixed partial charges. One of the simplest methods for modelling the polarisability of atoms is to use point ion dipole polarisability, an idea first introduced by Silberstein [152, 153, 154]. Applequist *et al.* [155] used point ion dipole polarisability to determine atom polarisation in polyatomic molecules. This was initially formulated as a 'monopole-dipole' interaction. However, Applequist [156] expanded on the original formulation to include contributions due to multipoles of any order, such as quadrupoles. In this method the induced dipole moment of an atom is defined by;

$$\mu = \alpha E_f \tag{2.64}$$

where α is the 'polarisability tensor' of a given atom, and E_f the electric field acting on that atom. The energy of this polarisation interaction is given by:

$$U_{polarisation} = -\frac{1}{2}\alpha E_f^2 \tag{2.65}$$

This method has been used in the past for treatment of polarisability of π-bonded molecules[157], and for ionic crystals[158].

An alternative method of representing polarisability was developed by Dick and Overhauser [159]. They devised what is known as the shell model to try to mimic the effects of ion polarisation. In this model the ion is represented by a core linked to a massless shell by a harmonic spring, as depicted in Figure 2.5.
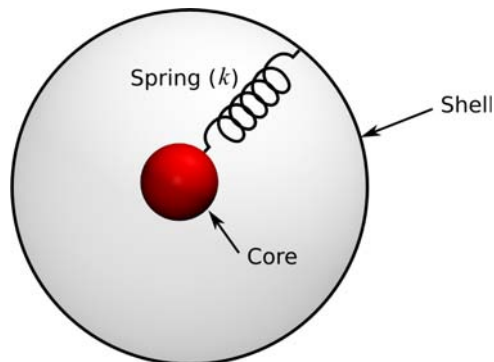
FIGURE 2.5: Schematic of the core-shell concept used to model the polarisability of an atom. The massless (or almost massless, in the case of the adiabatic model) shell is anchored to the core via a harmonic spring, possessing the spring constant k.

Both the core and the shell have a charge associated with them. When an electric field is applied to the molecule, each shell maintains its charge but moves with respect to its associated core[118]. The isolated ion polarisability of each species is given by;

$$\frac{Y^2}{k} \tag{2.66}$$

where k is the spring constant of the harmonic spring and Y is the charge on the shell. This model is often referred to as the static shell model, or relaxed shell model. Conventionally the short-range forces act on the shell and the Coulombic potential is applied to both the shell and the core[160, 161]. The short-range forces effectively 'damp' the polarisability, making it environment-dependent and offering a more realistic representation of polarisability. In dense ionic crystal lattices the polarisability of the ion will be quite low, represented by a stiff spring constant, while in finite systems the environment will have less of a 'damping' effect and the polarisability of the ions will increase.

Mitchell and Fincham [162] developed a modified version of the shell model known as the dynamic shell method, or finite mass shell method, in which both the shell and the core have a mass. The method is implemented such that a small fraction of the mass of the core is attributed to the shell, and the vibrations of the spring connecting the core and the shell are defined by;

$$v = \frac{1}{2\pi} \left[\frac{k}{x(1-x)m} \right]^{1/2} \tag{2.67}$$

where M is the mass of the ion, k the spring constant, and x is a variable which enables the user to tune the vibrational frequency.

Representing the polarisability of an atom using the shell model does have additional computational costs. In the case of the static shell model, where the shells are massless, the shells must be relaxed at each time step to allow them to 'follow' the core. In the case of the finite mass shell method the shells are not relaxed at each step, instead they are a dynamic 'particle' in their own right. This method has the additional cost of calculating the movement of the shells, which unfortunately demands a much smaller time step due to the smaller mass of the shells (and the resulting increased vibrational frequency).

2.3.2.4 van der Waals forces

Electrostatic interactions are not the only long-range (non-bonded) interactions in a system, as there are also van der Waals interactions. At intermediate distances there is a slight interaction between electron clouds due to spontaneous coupled dipoles, and these interactions provide some attractive force between relatively distant molecules or parts of molecules; these interactions are known as van der Waals forces. A popular potential form that is used to model the van der Waals forces between two atoms is the Lennard-Jones (LJ) potential[163, 164], given by Equation (2.68).

$$U_{LJ}(r) = 4\epsilon \left[\left(\frac{\sigma}{r} \right)^{12} - \left(\frac{\sigma}{r} \right)^{6} \right] \tag{2.68}$$

The LJ potential has two parameters, σ for the collision diameter and ϵ for the well depth, as indicated in Figure 2.6. Short-range interactions are included in the LJ potential as a repulsive contribution, which are due to the Pauli exclusion principle rather than van der Waals forces. This repulsive contribution is due to the twelfth power term, while the attractive component is given by the sixth power term. The repulsive part is rapidly calculated as it's the square of the sixth power term, but this is generally too steep for systems other than rare gases[118]. The LJ potential given in Equation (2.68) is also referred to as a 12-6 LJ potential due to the values of the exponents. However, other values can be used depending on the system being modelled. The LJ potential is also commonly described by another equivalent form:

$$U_{LJ}(r) = \frac{A}{r^{12}} - \frac{B}{r^{6}} \tag{2.69}$$

Alternative potentials like the Buckingham potential[165] can be used, which try to give a more realistic interaction:

$$U(r) = \epsilon \left[\frac{6}{\alpha - 6} \exp \left[-\alpha \left(\frac{r}{r_m} - 1 \right) \right] - \frac{\alpha}{\alpha - 6} \left(\frac{r_m}{r} \right)^{6} \right] \tag{2.70}$$

or more commonly described by the equivalent expression:

$$U(r) = A \exp \left[-\frac{r}{\rho} \right] - \frac{C}{r^{6}} \tag{2.71}$$

One possible disadvantage to the Buckingham potential is that it can give artificially strong attraction at very close distances if the variable C is non-zero, as shown in Figure 2.6. Care has to be taken with the atom positions when using
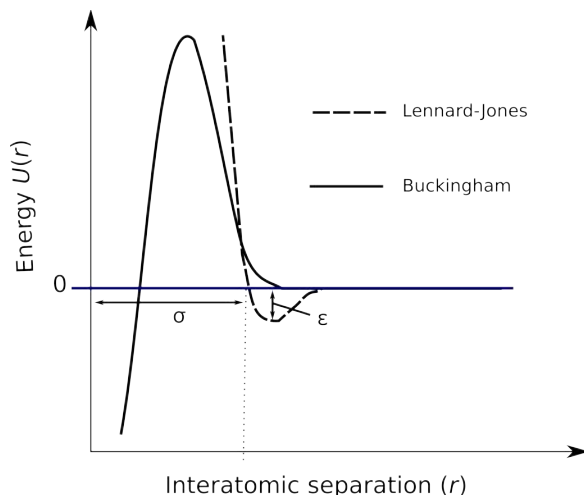
FIGURE 2.6: Illustration of the functional forms of Lennard-Jones (dashed
line) and Buckingham (solid line) potentials. The energy for the Buckingham
potential tends to $-\infty$ when the interatomic distance goes to zero.

the Buckingham potential, if atoms become too close they will 'fuse together' and
the energy will tend to $-\infty$.

2.3.3   Cut-off radii

The non-bonded interactions theoretically should be calculated between every
atom pair in the system. However, this problem leads to a cost that scales
as $O(N^2)$. Additionally, non-bonded interactions, such as the van der Waals
forces, decay rapidly with distance due to the r^{-6} term; and there is little value
in calculating the interactions beyond this region of decay[118]. This means a
cut-off radius can be implemented, giving a distance at which the long range
interactions should be truncated and reducing the computational complexity of
these calculations.

In practice, the computational advantage of a cut-off distance is enhanced by
introducing a neighbour list. A neighbour list contains a separate record for
each atom, and each record shows which atoms are within the defined cut-off
radius of that atom (*i.e.* its neighbours)[166]. This list is updated at regular
intervals throughout the simulation, but is overall more computationally efficient
than computing the distances between atoms at each step to determine which
atoms should be included in the calculation of a non-bonded contribution.

2.3.4 Periodic boundary conditions

We have already introduced periodic boundary conditions (PBC) in Section 2.2.8 in our discussion of electronic structure methods. The same principles of PBC apply to force field methods.

Having introduced the foundations to computational chemistry, we will explore methods for exploration of potential and free energy surfaces in the next chapter.

Chapter 3

Exploring energy landscapes

3.1 Introduction

In the previous chapter we introduced two methods for determining the energy of a given system, namely using quantum or molecular mechanics. Now we will consider methods which allow us to explore the energy surface of a system, beginning with so-called static methods. Many of the static methods we will cover are often referred to as optimisation algorithms, as they can be implemented solely to drive the system down to a local minimum. We will also introduce some basic classical statistical mechanics, which gives the grounding for molecular dynamics, and this will form the second half of the chapter - 'dynamic' methods for exploring the potential energy surface, and methods for calculating free energy differences between two states.

3.2 Static methods

As some or all of the nuclei move the energy of the system will change[118]. We gave a simple example of this in Section 2.3.1.3, where we described how rotation around the torsional angle in butane resulted in four stationary points on the energy surface, and two conformational isomers lying at energy minima. This is an example where the energy is considered to be a function of a single coordinate, the torsional angle, and a 2-dimensional plot of energy vs. torsional angle can be drawn, as we showed in Figure 2.4. As more coordinates are involved, this graph

would become a complicated multi-dimensional surface rather than 2-dimensional. Movement to different areas on this multi-dimensional surface results in changes in the system energy; this surface is generally known as the "potential energy surface"[118]. Even for small systems the potential energy surface is a complicated, multi-dimensional function of the coordinates.

Stationary points are regions on the energy surface where the first derivative of the energy with respect to the coordinates is zero. These points are of particular interest as these indicate either stable structures, where the stationary point is a *minimum*, or transition states, where the stationary point is a *saddle point* between two valleys[118].

There will generally be many minima on the energy surface, but the one with the lowest energy is known as the global energy minimum[118]. Minimisation methods often use derivatives from a certain point on the surface to determine where to move in the next step. The direction of the first derivative (the gradient) of the energy shows in which general direction the minimum lies, and the magnitude of the gradient gives the steepness of the local slope[118]. The system can be moved to a lower energy configuration by moving each atom in response to the force acting on it, which will be the negative of the gradient.

Other static methods aim to calculate the minimum energy path (MEP) between reactants and products moving on the potential energy surface, *i.e.*, at 0 Kelvin. These methods can be considered static methods, as the algorithms used to explore the energy surface do not require the evolution of the system with molecular dynamics. One of the challenges of these methods is to find a saddle-point on a multidimensional surface[167]. However, once it has been located the information on the curvature of the surface around the saddle point and in the minima can be utilised with Transition State Theory methods [168, 169] which will then give access to the rate constants. The MEP can then also be used to define the "reaction coordinate", some one dimensional coordinate that describes the progression of the reaction[170].

For a complete overview of the techniques developed to accurately locate saddle points we refer the reader to the review paper by Olsen *et al.* [171] and a chapter by Henkelman *et al.* [167]. Here we briefly describe some of the most commonly used approaches.

3.2.1   The Taylor series

Let us begin our discussion of optimisation with a Taylor series expansion of the PES, as the majority of optimisation algorithms are based on varied levels of truncation of the Taylor series. Any smooth and continuous function can be represented by a Taylor series, an infinite sum of terms determined from the derivatives at a single point, x[118, 172]:

$$f(x + \delta x) \approx f(x) + \frac{\delta x}{1!} f'(x) + \frac{\delta x^2}{2!} f''(x) + \cdots + \frac{\delta x^n}{n!} f^{(n)}(x) \qquad (3.1)$$

This can also be represented succinctly using Sigma notation:

$$\sum_{n=0}^{\infty} \frac{\delta x^n}{n!} f^{(n)}(x) \qquad (3.2)$$

Truncating the Taylor series gives approximations to the function $f(x + \delta x)$, and increasing the number of terms in the Taylor series increases the accuracy of this approximation. Additionally, the approximation is valid as δx tends towards zero.

3.2.2   Local Optimisation

3.2.2.1   Steepest Descents

The steepest descent method[173, 174] is one of the simplest optimisation methods available. The method can be considered to use a first order truncation of the Taylor series - as only the first derivatives are used. The system moves in steps which are proportional to the negative of the gradient, $-\mathbf{g}_k$. This can be compared to walking straight downhill with varied step sizes. The direction can be represented by a $3N$-dimensional unit vector, $\mathbf{s}_k$[118, 172]:

$$\mathbf{s}_k = -\mathbf{g}_k / |\mathbf{g}_k| \qquad (3.3)$$

This gives the direction in which the system should move, then the magnitude of the step size can be determined using a line-search method or arbitrary step sizes. The line search is an iterative procedure which finds three points along a line such that the middle point is of lower energy than the outer points. The algorithm continues in this way, reducing the distance between the three points until the

minimum is found along the given vector. An alternative method is the arbitrary step size, such that;

$$\mathbf{x}_{k+1} = \mathbf{x}_k + \lambda_k \mathbf{s}_k \tag{3.4}$$

where λ_k is the step size, and $\mathbf{x}$ are the coordinates of the system. If the first iteration leads to a decrease in energy, the step size is increased. This repeats until there is an increase in energy and the step size is reduced and increased in this way until a minimum energy value is found within a specified threshold. One disadvantage of the steepest descent method is that if the energy well is very steep, many small steps will be performed to try to find the minimum. Additionally, as the method approaches the minimum the step size may decrease and the search will slow down[118].

3.2.2.2 Conjugate Gradient Methods

The conjugate gradient (CG) method[175] makes some improvements to the steepest descent method by considering the history of the gradients previously visited to move more efficiently towards the minimum. As with the steepest descent method, only the first order derivatives are considered. The CG method steps in the direction $\mathbf{v}_k$ from a point $\mathbf{x}_k$. $\mathbf{v}_k$ is calculated from the gradient at the point, $\mathbf{g}_k$, and the previous direction vector, $\mathbf{v}_{k-1}$, via Equation (3.5)[172];

$$\mathbf{v}_k = -\mathbf{g}_k + \gamma_k \mathbf{v}_{k-1} \tag{3.5}$$

where γ_k is a scalar constant:

$$\gamma_k = \frac{\mathbf{g}_k \cdot \mathbf{g}_k}{\mathbf{g}_{k-1} \cdot \mathbf{g}_{k-1}} \tag{3.6}$$

The first step of the CG method is a steepest descent-like move, using only the gradient at the current point to determine in which direction to step. This is necessary as Equation (3.5) requires the direction from the previous step, $\mathbf{v}_{k-1}$, to perform the next iteration, and clearly there is no previous step information available when the method is first initiated.

Both the line search and arbitrary step methods can be used in CG. One advantage to the CG method is that it does not give the same oscillatory behaviour in narrow valleys as the steepest descents method[118].

3.2.2.3   Newton-Raphson based methods

The Newton-Raphson method is a second-derivative method for optimisation[117, 176, 177]. A quadratic approximation to the Taylor expansion around a point x is made:

$$f(x + \delta x) \approx f(x) + f'(x)\delta x + \frac{1}{2}f''(x)\delta x^2 \qquad (3.7)$$

A requirement is imposed such that the gradient of this equation is required to be a stationary point, $\partial f(x + \delta x)/\partial x = 0$, yielding:

$$f'(x + \delta x) \approx f'(x) + f''(x)\delta x \qquad (3.8)$$

$$\approx 0 \quad \text{if at a stationary point} \qquad (3.9)$$

Equation (3.9) can be rearranged to estimate the next step, δx, to move closer to the minimum:

$$\delta x = -\frac{f'(x)}{f''(x)} \qquad (3.10)$$

If the PES is perfectly quadratic then the Newton-Raphson method will step directly into the minimum in one step. Generally this is not the case, so the Newton-Raphson formula is used iteratively to step across the potential energy surface towards stationary points.

One disadvantage of this method is the requirement to calculate the inverse of the Hessian matrix ($f''(x)^{-1}$, or $\mathbf{H}^{-1}$) at each step, making the process ideal for small systems of approximately a few hundred atoms or less[118].

3.2.2.4   Quasi-Newtonian methods

A number of optimisation methods exist which are based on variants of the Newton-Raphson method and will be discussed in the following sections. However, we would like to note that there is another subset of methods known as quasi-Newtonian methods which attempt to avoid the drawback of calculating the inverse Hessian matrix, $\mathbf{H}^{-1}$. This is achieved by starting with an approximation to the inverse Hessian matrix and gradually updating this approximation based only on first derivative information, the gradient vectors[172]. In this way an estimation of $\mathbf{H}^{-1}$ can be iteratively constructed.

At each iteration new positions $\mathbf{x}_{k+1}$ are obtained according to[118];

$$\mathbf{x}_{k+1} = \mathbf{x}_k - \mathbf{B}_k\mathbf{g}_k \qquad (3.11)$$

where $\mathbf{x}_k$ are the current coordinates and $\mathbf{B}_k$ is the current approximation to the inverse Hessian matrix; again $\mathbf{g}_k$ is the gradient at the current point. Once the new position is obtained, the approximate Hessian can be updated. The formulae used to update the Hessian matrix, to $\mathbf{B}_{k+1}$, is the key difference between distinct quasi-Newtonian methods. However, they all generally use only the current and previous coordinates and gradients. Two well-known quasi-Newton methods are the Davidon-Fletcher-Powell (DFP)[178–181] and Broyden-Fletcher-Goldfarb-Shanno (BFGS)[182–186] methods. We direct the reader to Press *et al.* [176] for a detailed description of their implementation.

3.2.3   Transition state location

3.2.3.1   Synchronous transit

The synchronous-transit method was introduced by Halgren and Lipscomb [187] in 1977 and involves the interpolation of coordinates between a starting (reactant) and finishing (product) state. The maximum point along this interpolated line is determined, and this essentially comprises the linear synchronous transit (LST) portion of the method proposed by Halgren and Lipscomb [187]. Once this point is determined a quadratic synchronous transit (QST) pathway is defined, whereby a maximum is determined by moving laterally up the valley from this point to find the 'true' ridge maximum or transition state.

3.2.3.2   Dewar, Healy and Stewart

Dewar *et al.* [188] also introduced a method of finding transition states which involves two images of the system. Again the end points, reactants and products, are connected by a reaction coordinate. Each state is iteratively moved towards each other until they are within a predetermined distance, and can be considered on the saddle point between the original states[188]. This is achieved by first calculating the energy of the two states[167]. The state with the lowest energy is displaced slightly towards the other state, generally 5% of the way as suggested in

the original paper[188]. Once this displacement is made, the structure is allowed to relax, but the new distance between the two states is constrained to remain the same. This repeats, with the distance between the two states decreasing and the lower energy state being displaced and then relaxed, until the two states have walked close enough to each other to be within some threshold value and can be considered to be at the saddle point. A method similar to this is known as the ridge method and was introduced later by Ionova and Carter [189]. Again, two states are allowed to step towards each other in an attempt to locate the saddle point.

3.2.3.3 Rational Functional Optimisation (RFO)

Banerjee *et al.* [190] introduced an algorithm in 1985 that systematically locates stationary points, starting from an arbitrary point on the potential energy surface. As with the Newton-Raphson technique, this method uses the second derivatives to determine information about the curvature of the nearby surface[190]. However in RFO the Hessian matrix is diagonalised, and the character of the resulting Hessian eigenvalues is used to determine where the system lies - a maximum, minimum or saddle point. This allows the system to optimise to any general stationary point of specified order by following any given mode of the Hessian[190].

The RFO method is quite a powerful tool for exploring an energy surface. However, in our work we only use the RFO technique as an optimisation method. For optimisation, RFO is most effective relatively close to the minimum, and for this reason it is generally used after CG or SD has been used to get to the approximate region.

3.2.3.4 Nudged elastic band

The nudged elastic band (NEB) method was introduced by Jónsson *et al.* [191] as a method for determining the lowest energy path between two stable configurations. In the nudged elastic band (NEB) method a string of replicas of the system is created. Each replica 'image' is generally initially constructed from a direct linear interpolation between the reactant and product configurations. The string of all of the images is represented by $[\mathbf{R}_0, \mathbf{R}_1, \mathbf{R}_2, \ldots, \mathbf{R}_N]$, the end points are fixed and assumed to be the initial and final states, $\mathbf{R}_0 = \mathbf{R}$ and $\mathbf{R}_N = \mathbf{P}$, while the other

images are allowed to move on the energy surface. This construction imitates an elastic band comprised of $N-1$ beads and N springs with spring constant k:

$$S(\mathbf{R}_1, \ldots, \mathbf{R}_N) = \sum_{i=1}^{N-1} E(\mathbf{R}_i) + \sum_{i=1}^{N} \frac{k}{2}(\mathbf{R}_i - \mathbf{R}_{i-1})^2 \qquad (3.12)$$

Each replica is then optimised, relaxing each image towards the minimum energy path (MEP)[191]. The method implemented by the original authors uses a velocity Verlet type algorithm, where the velocities and coordinates of the atoms in each image are updated based on the force evaluated at the current coordinates. If the velocities are brought to zero at each step the overall result is a steepest descent minimisation. In this way, the chain of configurations which initially lay in a linear fashion between the reactants and products is able to relax across the potential energy surface into the minimum energy path, with the only constraint being that the initial and final states are fixed points.

There are a few problems with the above method; first the images tend to slide down towards the end points, leaving the saddle point region (the region of interest) poorly explored, particularly if the spring constant, k, is too small (*i.e.*, the springs are too soft). The method can also tend to 'cut corners', as the replicas are pulled off the MEP by spring forces in regions where the MEP is curved. This is likely to occur if k is too large (*i.e.*, the springs are too rigid). Both of these problems can be resolved with an additional force projection, known as 'nudging', and this is where the method gains its name[167]. The nudging is achieved by applying the parallel component of the spring forces and the perpendicular component of the true forces at each image. Refinements to the original NEB method have been developed, in particular the climbing image NEB[192], and improvements in the calculation of the tangent for applying the spring forces to each image[193].

The static methods discussed in this section, and other methods outside the scope of this work, are often collectively referred to as *lattice dynamics*. We refer the reader to other references such as Gale [194] and Parker *et al.* [195] for a more detailed summary of these methods. This concludes our discussion of static methods available for exploring energy surfaces. What follows in the next section is a brief background to classical statistical mechanics, which leads us into molecular dynamics simulations and dynamic methods for exploring potential energy surfaces.

3.3   Classical Statistical Mechanics

Statistical mechanics forms the foundation for the computational methods that will be used throughout this thesis. In this section we will cover some basic statistical mechanics theory which will provide the background to the free energy methods that will be covered in more detail in the remainder of this chapter. Statistical mechanics is a field which encompasses probability theories that can be applied to large systems of moving particles. This approach enables macroscopic or bulk properties to be explained from microscopic behaviour.

When talking about a classical system this usually refers to a system having a large number of molecules, N, and occupying a large volume, V. The system is regarded as isolated, such that the energy is a constant of the motion[196]. This system can be uniquely defined by $3N$ canonical coordinates, $\mathbf{q}_1, ..., \mathbf{q}_N$ and $3N$ canonical momenta $\mathbf{p}_1, ..., \mathbf{p}_N$.

The $6N$-dimensional space $\{\mathbf{q}_1, ..., \mathbf{q}_N; \mathbf{p}_1, ..., \mathbf{p}_N\}$ spanned by the position and momenta is usually referred to as the phase space of the system[196]. The collection of points in the phase space that satisfy the macroscopic constraints (eg. the system volume) form what is known as the *ensemble*[197]. Statistical mechanics provides the tools to connect every thermodynamic observable to the ensemble average of a suitable microscopic quantity. The simplest ensemble is that of a system in isolation, where no energy is transferred to and from the surroundings. This ensemble is called the *microcanonical ensemble* or NVE, where every accessible point of the the phase space must fulfil the constraint that the number of particles, N, volume, V, and energy E remain constant.

The above is formally different from what can be obtained from a MD simulation, which corresponds to a time average of the microscopic quantities. However, a theoretical justification for considering the two approaches equivalent is given by the *ergodicity principle*[197]. If we consider a system in isolation, the ergodicity principle can be stated in the following way: *an infinitely long trajectory will visit every point of the phase space with equal probability.* This can be expressed mathematically as follows;

$$< C > = \ \frac{\int \mathrm{d}^N \mathbf{p} \ \mathrm{d}^N \mathbf{q} \ C \ \delta(E(\mathbf{p}, \mathbf{q}) - E_0)}{\int \mathrm{d}^N \mathbf{p} \ \mathrm{d}^N \mathbf{q} \ \delta(E(\mathbf{p}, \mathbf{q}) - E_0)} \ = \ \lim_{t \to \infty} \frac{1}{t} \int_0^t \ \mathrm{d}\tau \ C(\tau) \qquad (3.13)$$

where C is any thermodynamic macroscopic observable and the δ function in the statistical mechanics definition ensures that only iso-energetic states are visited. The denominator is the normalisation constant which corresponds to the total number of accessible states[197]. Obviously it not feasible to generate an infinitely long trajectory and, apart from the force field accuracy, the length of the simulations is therefore the main source of inaccuracy. Additionally, if the potential energy surface has large energy barriers (*i.e.*, not an NVE ensemble), the ergodicity principle is unlikely to hold as there will be regions of phase space inaccessible on a reasonable timeframe.

Although the microcanonical ensemble is mathematically the easiest to treat, the constant energy constraint means it is irrelevant to compare NVE simulations to experiments. Other ensembles need to be considered, like the canonical (NVT) or isothermal-isobaric (NPT) ensembles. Changing the ensemble has no consequences on the way we calculate the thermodynamic quantities as averages on the generated trajectories, provided that we integrate the equations of motion with an algorithm suitable to correctly enforce the macroscopic constraints. For example, in the canonical ensemble states with different energies are now accessible and the probability that every state is visited depends on its energy and is proportional to the Boltzmann factor, $\exp(-\beta E)$, where β is $\frac{1}{k_B T}$. Hence, the statistical mechanics definition of a macroscopic observable becomes;

$$< C > \ = \ \frac{\int \mathrm{d}^N \mathbf{p} \ \mathrm{d}^N \mathbf{q} \ C \ \exp(-\beta E(\mathbf{p}, \mathbf{q}))}{\int \mathrm{d}^N \mathbf{p} \ \mathrm{d}^N \mathbf{q} \ \exp(-\beta E(\mathbf{p}, \mathbf{q}))} \tag{3.14}$$

where the normalisation constant is now the $6N$ dimensional integral of the Boltzmann factor. This is an extremely important quantity and is usually referred to as the *partition* function[197];

$$Q(N, V, T) \ = \ \int \mathrm{d}^N \mathbf{p} \ \mathrm{d}^N \mathbf{q} \ \exp(-\beta E(\mathbf{p}, \mathbf{q})). \tag{3.15}$$

The importance of the partition function lies in the fact that if we were able to compute the partition function analytically we would have knowledge of all the possible states of our system. The partition function could then be used to compute usually inaccessible properties. In particular, the partition function would allow us to calculate the free energy of the system;

$$A \ = \ -k_B T \ln Q(N, V, T) \tag{3.16}$$

where A is the Helmholtz free energy. Analogously the Gibbs free energy, G, can be obtained as the logarithm of the NPT partition function:

$$G = -k_B T \ln Q(N, P, T) \tag{3.17}$$

Since this is an almost impossible task for any system of real interest, different techniques have been developed over the last few decades to enhance the sampling of the phase space and calculate free energy differences;

$$\Delta A = A_b - A_a = -k_B T \ln \frac{Q_b(N, V, T)}{Q_a(N, V, T)}, \tag{3.18}$$

which are more easily accessible than absolute free energies. Later in this chapter we will give an overview of these advanced techniques, focussing on those which we used in the present work. First, we'll introduce two conventional methods for exploring phase space, and obtaining averages relevant to statistical mechanics.

3.4   Monte Carlo Simulations

The Monte Carlo method provides one of the simplest approaches to statistical mechanics. Although this method is not used in the present work, it is worth mentioning its existence and its differences to molecular dynamics (the method we predominantly use in our work). The partition function given in Equation (3.15), and the observable in Equation (3.14), both require the total energy of the system as a parameter. This total energy is a function of coordinates, $\mathbf{q}$, and momenta, $\mathbf{p}$ and can also be represented as a Hamiltonian comprised of two components, the kinetic and potential energies[118, 197]:

$$\mathscr{H}(\mathbf{p}^N, \mathbf{q}^N) = \sum_{i=1}^{N} \frac{|\mathbf{p}_i|^2}{2m} + \mathscr{V}(\mathbf{q}^N) \tag{3.19}$$

The potential energy portion of the Hamiltonian must be calculated numerically[198]. There are two drawbacks to using conventional numerical methods, such as Simpson's rule, to evaluate this integral. The first drawback is that the number of evaluations required for a $3N$-dimensional integral is astronomically large. The second drawback is that for most systems - assuming we could perform all of the evaluations - the majority of configurations generated

would have a Boltzmann factor that is incredibly small (*i.e.*, the configuration is highly unfavourable)[198]. The conclusion that can be drawn is that better techniques are necessary for calculating thermal averages, and Monte Carlo is one of these.

One potential technique for solving the numerical integration problem and calculating thermodynamic averages could be to explore the phase space in a random fashion[118]. The simplest example of this is an estimation of π by generating a set of random points across a square region. If a circle is drawn bounded by the square, as shown in Figure 3.1, the ratio of the random points within the circle over the points in the square will be an estimate of $\frac{\pi r^2}{4r^2}$, ultimately yielding an estimate of $\pi/4$.
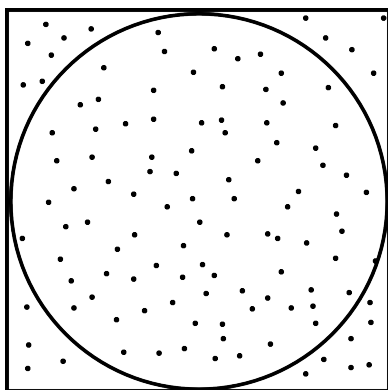
FIGURE 3.1: Points randomly sampled over a square region can be used to offer an estimate of π by taking the ratio of points from the area of the circle within the square over the total points. Image adapted from Leach [118].

Unfortunately, attempting to use this same logic to estimate the partition function is much less effective. Again, this is primarily due to the fact that a large number of configurations will have very small Boltzmann factors.

A method was devised by Metropolis *et al.* [199] to avoid this situation, whereby the simulation favours the generation of configurations with large contributions to the Boltzmann factor. This method is known as *importance sampling*, or the Metropolis approach to Monte Carlo. The method involves first generating a random configuration at each iteration. This is achieved by making a random change to the current configuration. Usually only the coordinates of one of the particles in the system is changed up to a maximum displacement value, δr_{max}. If this new configuration is lower in energy than the previous one, the new configuration becomes the starting point for the next iteration. If the new

configuration is higher in energy than the old one, its probability of acceptance is given according to the following criterion[118, 198];

$$\text{rand}(0, 1) \leq \exp(-\Delta \mathscr{V}(\mathbf{r}^N)/k_B T) \qquad (3.20)$$

where rand(0,1) is a random number generated between 0 and 1, and $\Delta \mathscr{V}$ is the energy increase for the step. Following this scheme, states that are lower in energy will always be accepted, and according to the Metropolis criterion of Equation (3.20), the higher energy states will occasionally be accepted and become the new starting configuration for the next iteration. In this way the accepted configurations are biased towards those which have a significant contribution to the integral of the partition function[118]. The magnitude of δr_{max} used to generate each random configuration will directly affect the percentage of accepted trial moves. Generally this is chosen so that about 50% of the iterations are accepted. If this value is too small then moves will be accepted at a high rate but the phase space will not be efficiently explored. Alternatively if the value is too large then a lot of time will be wasted generating trial moves which are almost always rejected as they are more likely to be unfavourable configurations.

The Monte Carlo method is a time independent method, and in some cases this may not be the desired approach for investigating a system. For example, if we are interested in the transport or diffusion properties of a system, these are time-dependent properties and the chosen method of simulation needs to explore the system in a time dependent way. For these problems there are time-dependent methods, such as molecular dynamics. This is the method we predominantly use in our studies and will be discussed in the next section.

3.5 Molecular Dynamics

In molecular dynamics (MD) methods, configurations are generated sequentially by calculating the movement of each atom using classical mechanics. Each successive frame is obtained by solving the differential equations of Newton's second law, $F = ma$:

$$\frac{d^2 x_i}{dt^2} = \frac{F_{x_i}}{m_i} \qquad (3.21)$$

Equation (3.21) describes the motion of a particle of mass m_i along one coordinate (x_i) with F_{x_i} representing the force acting on the particle[118].

One of the main justifications for the MD method is that the statistical ensemble averages we have discussed in Section 3.3 are the equivalent of time averages obtained from a trajectory of a system (*i.e.*, the ergodic hypothesis holds).

Early molecular dynamics simulations performed by Alder and Wainwright [200] used hard-sphere potentials to describe the interactions between particles where the atoms would move at constant velocities in straight lines between perfectly elastic collisions. Since these early developments, the intermolecular interactions have evolved to become more realistic atomic models. The forces felt by each particle are not due to simple elastic collisions, instead there is a more complex relationship between the forces felt by each particle and the surrounding particles with which they interact. This is due to the use of continuous potentials, where the movement of all the particles are coupled together, creating a many-body problem[118, 143, 198]. This problem cannot be solved analytically and requires the use of finite difference methods to integrate the equations of motion.

3.5.1   Integration of the equations of motion

In finite difference techniques the integration is broken down into small steps, each separated by a fixed time, δt. The forces on each particle at time t are calculated as a sum of the interactions with the rest of the particles in the system. The forces enable us to calculate the acceleration of the particles. Using this information we can then find the positions and velocities at time $t + \delta t$. Once the particles are in their new positions the process is repeated to determine the positions and velocities at the next time step[118, 143, 198].

There are many ways to integrate the equations of motion using finite difference methods. All of these assume that the positions, velocities and accelerations can

be approximated as Taylor series expansions at time t;

$$\mathbf{r}(t+\delta t) = \mathbf{r}(t) + \mathbf{v}(t)\delta t + \frac{1}{2}\mathbf{a}(t)\delta t^2 + \frac{1}{6}\mathbf{b}(t)\delta t^3 + \frac{1}{24}\mathbf{c}(t)\delta t^4 + \dots \quad (3.22)$$

$$\mathbf{v}(t+\delta t) = \mathbf{v}(t) + \mathbf{a}(t)\delta t + \frac{1}{2}\mathbf{b}(t)\delta t^2 + \frac{1}{6}\mathbf{c}(t)\delta t^3 + \dots \quad (3.23)$$

$$\mathbf{a}(t+\delta t) = \mathbf{a}(t) + \mathbf{b}(t)\delta t + \frac{1}{2}\mathbf{c}(t)\delta t^2 + \dots \quad (3.24)$$

$$\mathbf{b}(t+\delta t) = \mathbf{b}(t) + \mathbf{c}(t)\delta t + \dots \quad (3.25)$$

where $\mathbf{r}$ is the position, $\mathbf{v}$ is the velocities (the first derivative of the position with respect to time), $\mathbf{a}$ is the acceleration (the second derivative of the position with respect to time), and $\mathbf{b}$ and $\mathbf{c}$ are the third and fourth derivatives respectively. The Verlet algorithm[201] is one of the most commonly used integration methods in MD simulations. The Verlet algorithm calculates the positions at time $t + \delta t$ by using the positions, $\mathbf{r}$, and accelerations, $\mathbf{a}$, at time t, and the positions from the previous step, $t - \delta t$[118]:

$$\mathbf{r}(t+\delta t) = \mathbf{r}(t) + \mathbf{v}(t)\delta t + \frac{1}{2}\mathbf{a}(t)\delta t^2 + \dots \quad (3.26)$$

$$\mathbf{r}(t-\delta t) = \mathbf{r}(t) - \mathbf{v}(t)\delta t + \frac{1}{2}\mathbf{a}(t)\delta t^2 - \dots \quad (3.27)$$

Adding the two equations (3.26) and (3.27) gives:

$$\mathbf{r}(t+\delta t) = 2\mathbf{r}(t) - \mathbf{r}(t-\delta t) + \delta t^2 \mathbf{a}(t) + \vartheta(\delta t^4) \quad (3.28)$$

The velocities are not explicitly represented in the Verlet algorithm but they can be calculated knowing the positions at consecutive time steps and δt:

$$\mathbf{v}(t) = \frac{\mathbf{r}(t+\delta t) - \mathbf{r}(t-\delta t)}{2\delta t} + \vartheta(\delta t^2) \quad (3.29)$$

One disadvantage of this method is that the velocities are not available until the next step has been computed. Another disadvantage of the Verlet method is that, as seen in equation (3.28), there is an error given by $\vartheta(\delta t^4)$, while equation (3.29) has an error proportional to $\vartheta(\delta t^2)$. As these will be computed at a finite timestep, truncation errors may occur resulting in a loss of precision in the overall propogation[118].

The *velocity* Verlet method[202] manages to give positions, velocities and accelerations at the same time t. The velocity Verlet method is implemented

as a three-stage procedure given by equations (3.30)-(3.32)

$$\mathbf{v}(t + \frac{1}{2}\delta t) = \mathbf{v}(t) + \frac{1}{2}\mathbf{a}(t)\delta t \tag{3.30}$$

$$\mathbf{r}(t + \delta t) = \mathbf{r}(t) + \mathbf{v}(t)\delta t + \frac{1}{2}\mathbf{a}(t)\delta t^2 = \mathbf{r}(t) + \mathbf{v}(t + \frac{1}{2}\delta t)\delta t \tag{3.31}$$

$$\mathbf{v}(t + \delta t) = \mathbf{v}(t) + \frac{1}{2}\delta t[\mathbf{a}(t) + \mathbf{a}(t + \delta t)] \tag{3.32}$$

Another variation of the Verlet method is known as the *leap-frog* algorithm[203] which follows:

$$\mathbf{r}(t + \delta t) = \mathbf{r}(t) + \delta t\mathbf{v}(t + \frac{1}{2}\delta t) \tag{3.33}$$

$$\mathbf{v}(t + \frac{1}{2}\delta t) = \mathbf{v}(t - \frac{1}{2}\delta t) + \delta t\mathbf{a}(t) \tag{3.34}$$

The leap-frog algorithm first calculates the velocities at time $t + \delta t$ using the velocities at the previous 'half time step', $t - \frac{1}{2}\delta t$, and the accelerations at time t. The positions at $t + \delta t$ can be calculated from the current positions and the velocity calculated for time $t + \frac{1}{2}\delta t$. The velocities at time t can then be calculated using:

$$\mathbf{v}(t) = \frac{1}{2}[\mathbf{v}(t + \frac{1}{2}\delta t) + \mathbf{v}(t - \frac{1}{2}\delta t)] \tag{3.35}$$

In this way, the velocities and positions 'leap-frog' over each other. One advantage to this method over the original Verlet method is that the velocities are explicitly known; however the fact that the positions and velocities are not synchronised due to the 'leap-frogging' means that the kinetic energy contribution to the total energy will never be determined for the same frame for which the positions are known[118].

Another subset of integration algorithms exist known as predictor-corrector integration methods[204]. In these methods there is a prediction step, whereby the positions, velocities and accelerations of the particles at the next time step, $t + \delta t$, are predicted using the Taylor series expansions introduced in Equations (3.22)-(3.25). The forces at the new positions are evaluated to give the accelerations, $\mathbf{a}(t + \delta t)$. A comparison of these accelerations and those predicted from the Taylor series expansion, $\mathbf{a}^p(t + \delta t)$, is made, giving $\Delta\mathbf{a}(t + \delta t)$:

$$\Delta\mathbf{a}(t + \delta t) = \mathbf{a}^p(t + \delta t) - \mathbf{a}(t + \delta t) \tag{3.36}$$

This difference is used in the correction step of the algorithm, where the predicted values are corrected according to;

$$\mathbf{r}^c(t + \delta t) = \mathbf{r}^p(t + \delta t) + c_0 \Delta \mathbf{a}(t + \delta t) \tag{3.37}$$

$$\mathbf{v}^c(t + \delta t) = \mathbf{v}^p(t + \delta t) + c_1 \Delta \mathbf{a}(t + \delta t) \tag{3.38}$$

$$\mathbf{a}^c(t + \delta t)/2 = \mathbf{a}^p(t + \delta t)/2 + c_2 \Delta \mathbf{a}(t + \delta t) \tag{3.39}$$

$$\mathbf{b}^c(t + \delta t)/6 = \mathbf{b}^p(t + \delta t)/6 + c_3 \Delta \mathbf{a}(t + \delta t) \tag{3.40}$$

where the superscripts c and p indicate 'corrected' and 'predicted' respectively. The coefficients are chosen depending upon the order of the Taylor series expansion[204]. The Gear algorithm allows the user to use as many terms in the Taylor series expansion as desired, so the integration calculations have the potential to be more accurate than in the algorithms already introduced. One obvious disadvantage to this method is that each time step requires two costly force evaluations, and for this reason the more efficient algorithms such as velocity Verlet are more commonly utilised[118].

3.5.2 Conserved quantity

The choice of the size of the time step is not a trivial one. If the time step is too small the trajectory will only cover a fraction of phase space. If the time step is too large instabilities could appear in the trajectory, for example where a collision should have occurred perhaps atoms are left overlapping one another in the calculation of the next frame, or the particles may have passed each other entirely. The time step needs to be smaller than the fastest vibration desired to be modelled in the simulation so that these unwanted side effects are unlikely to occur, and therefore is related to the mass of the lightest particle in the system.

3.6 Constant temperature MD

The molecular dynamics equations described in Section 3.5 provide averages that correspond very closely to the microcanonical ensemble, NVE, where the number of molecules (N), volume (V) and energy (E) remain constant. Since experiments are usually performed at a constant temperature or constant pressure, it is generally

more useful to implement molecular dynamics in a non-microcanonical ensemble, such as NVT or NPT. To do this in molecular dynamics we need to adapt the equations we use so that they have a thermostat or barostat applied.

The temperature of the system is a time average of the kinetic energy:

$$\langle \mathscr{K} \rangle_{NVT} = \frac{3}{2} N k_B T \tag{3.41}$$

The simplest implementation of a thermostat is to scale the velocities at each time-step to the desired temperature, as introduced by Woodcock [205]. If the temperature at time t is $T(t)$ and the velocities are scaled by a factor λ the temperature change is given by:

$$\Delta T = \frac{1}{2} \sum_{i=1}^{N} \frac{2}{3} \frac{m_i (\lambda v_i)^2}{N k_B} - \frac{1}{2} \sum_{i=1}^{N} \frac{2}{3} \frac{m_i v_i^2}{N k_B} = (\lambda^2 - 1) T(t) \tag{3.42}$$

$$\lambda = \sqrt{T_{new}/T(t)} \tag{3.43}$$

The temperature in the simulation is maintained by scaling the velocities by λ at each time-step. A simple velocity-scaling algorithm such as this aims to maintain the kinetic energy, $\sum p^2/2m$, constant throughout the simulation. However, this does not reproduce a canonical phase-space distribution of states. Other more complicated algorithms strive to produce canonical ensembles so that the temperature fluctuates with a distribution proportional to $\exp(-\sum p^2/2mk_B T)$[143].

3.6.1 Berendsen thermostat

Another velocity-scaling thermostat was developed by Berendsen[206] in which the temperature is maintained at a given value by coupling the system to an external heat bath that is fixed at the desired temperature. The bath is a source of thermal energy which supplies or removes heat from the system as needed. Velocites are scaled at each step such that the rate of change of temperature is given by equation (3.44).

$$\frac{dT(t)}{dt} = \frac{1}{\tau}(T_{bath} - T(t)) \tag{3.44}$$

τ is the coupling parameter which determines how tightly the heat bath and the system are coupled together. A large value of τ gives weak coupling, and small values of τ provides strong coupling with the heat bath. The scaling factor for the velocities is given by equation (3.45)

$$\lambda = \left[1 + \frac{\delta t}{\tau} \left(\frac{T_{bath}}{T(t)} \right) \right]^{1/2} \qquad (3.45)$$

This type of velocity scaling method can artificially prolong the temperature differences between different components of the system, such as the solute and solvent. Due to this, rigorous canonical averages are not obtained from these simulations either[143]. Other methods, like stochastic collision or extended system methods, are able to provide rigorous canonical ensembles if implemented properly[143].

3.6.2 Andersen thermostat

The Andersen thermostat[207] is a *stochastic collision* method of maintaining the temperature of a system. Particles are randomly chosen at intervals and velocites reassigned by random selection from the Maxwell-Boltzmann distribution[198]. This is equivalent to the system being coupled with a heat bath that randomly emits 'thermal particles' which collide with the atoms in the system[198]. The strength of the coupling to the heat bath is given by v, which represents the frequency of stochastic collisions. If successive collisions are uncorrelated the distribution of time intervals between successive stochastic collisions is a Poisson distribution given by equation (3.46);

$$P(t) = v \cdot e^{-vt} \qquad (3.46)$$

where $P(t)\Delta t$ is the probability that an interval between collisions is between time t and $t + \Delta t$.

3.6.3 Nosé-Hoover thermostat

In *extended system* methods, the heat bath is considered an integral part of the system[198]. The heat bath is represented by an additional degree of freedom [208]

included by using an extended-Lagrangian method. The heat bath is an additional coordinate, s, in a Lagrangian N-body system:

$$\mathscr{L}_{Nose} = \sum_{i=1}^{N} \frac{m_i}{2} s^2 \dot{\mathbf{r}}_i^2 - U(\mathbf{r}^N) + \frac{Q}{2}\dot{\mathbf{s}}^2 - \frac{L}{\beta}\ln s \qquad (3.47)$$

The variable Q is an effective mass associated with the additional coordinate s. The momenta obtained from the variables $\mathbf{r}_i$ and s can be obtained from the Lagrangian, where:

$$\mathbf{p}_i = \frac{\partial \mathscr{L}}{\partial \dot{\mathbf{r}}_i} = m_i s^2 \dot{\mathbf{r}}_i \qquad (3.48)$$

$$p_s = \frac{\partial \mathscr{L}}{\partial \dot{s}} = Q\dot{s} \qquad (3.49)$$

$$\mathscr{H}_{Nose} = \sum_{i=1}^{N} \frac{\mathbf{p}_i^2}{2m_i s^2} + U(\mathbf{r}^N) + \frac{p_s^2}{2Q} + L\frac{\ln s}{\beta} \qquad (3.50)$$

The equations of motion for the virtual variables, $\mathbf{p}$, $\mathbf{r}$ and t can be derived from the Nosé Hamiltonian given in equation (3.50):

$$\frac{d\mathbf{r}_i}{dt} = \frac{\partial \mathscr{H}_{Nose}}{\partial \mathbf{p}_i} = \mathbf{p}_i/(m_i s^2) \qquad (3.51)$$

$$\frac{d\mathbf{p}_i}{dt} = -\frac{\partial \mathscr{H}_{Nose}}{\partial \mathbf{r}_i} = \frac{\partial U(\mathbf{r}^N)}{\partial \mathbf{r}_i} \qquad (3.52)$$

$$\frac{ds}{dt} = \frac{\partial \mathscr{H}_{Nose}}{\partial p_s} = p_s/Q \qquad (3.53)$$

$$\frac{dp_s}{dt} = -\frac{\partial \mathscr{H}_{Nose}}{\partial s} = \left(\sum_i p_i^2/(m_i s^2) - \frac{L}{\beta}\right)/s \qquad (3.54)$$

Hoover simplified Nosé's equations further by introducing a thermodynamic friction coefficient $\xi = s'p'_s/Q$, giving the equations of motion:

$$\dot{\mathbf{r}}_i = \mathbf{p}_i/m_i \tag{3.55}$$

$$\dot{\mathbf{p}}_i = -\frac{\partial U(\mathbf{r}^N)}{\partial \mathbf{r}_i} - \xi \mathbf{p}_i \tag{3.56}$$

$$\dot{\xi} = \left(\sum_i p_i^2/m_i - \frac{L}{\beta} \right) /Q \tag{3.57}$$

$$\dot{s}/s = \frac{d \ln s}{dt} = \xi \tag{3.58}$$

$$\mathscr{H}_{Nose} = \sum_{i=1}^{N} \frac{\mathbf{p}_i^2}{2m_i} + U(\mathbf{r}^N) + \frac{\xi^2 Q}{2} + L\frac{\ln s}{\beta} \tag{3.59}$$

3.7 Barostats for constant presssure (NPT)

In addition to wanting to specify the temperature of a MD simulation, it may also be desired to specify a constant pressure for the system. A macroscopic system achieves constant pressure by altering its volume. Thus for isobaric simulations, the volume of the simulation cell is allowed to adjust to maintain the pressure at a constant value (or to fluctuate around a desired value). The amount of volume fluctuation is related to the isothermal compressibility κ given in equation (3.60):

$$\kappa = -\frac{1}{V} \left(\frac{\partial V}{\partial P} \right)_T \tag{3.60}$$

Many of the methods for maintaining the pressure in a simulation are equivalent to those used for temperature control. As in the previous section, the simplest barostat is to scale the volume, but again this does not provide us with rigorous ensemble averages[118, 143].

3.7.1 Berendsen barostat

Instead the system can be coupled to a "pressure bath", having parallels to the thermostats which use a "heat bath". In these methods the rate of change of

pressure is given by[143];

$$\frac{dP(t)}{dt} = \frac{1}{\tau_p}(P_{bath} - P(t)) \tag{3.61}$$

where τ_p is the coupling constant, P_{bath} is the pressure of the "bath", and $P(t)$ is the pressure at time t. The volume of the simulation box is scaled by a factor λ, given by equation (3.62).

$$\lambda = 1 - \kappa\frac{\delta t}{\tau_p}(P - P_{bath}) \tag{3.62}$$

This scaling is equivalent to scaling the coordinates by a factor of $\lambda^{1/3}$, so the new positions are given by equation (3.63):

$$\mathbf{r}_i^{'} = \lambda^{1/3}\mathbf{r}_i \tag{3.63}$$

3.7.2   Andersen barostat

The Andersen barostat is an extended system method of pressure-coupling. As with the extended system thermostat, an extra degree of freedom is added to the Hamiltonian[118, 143]. The kinetic energy related to the extra degree of freedom is given by $\frac{1}{2}Q(dV/dt)^2$, with Q being the 'mass' of this pressure variable[118].

3.8   Rare events

Rare events are infrequent processes that occur due to spontaneous fluctuations in a system[209]. The processes themselves usually proceed very quickly, on timescales that are orders of magnitudes smaller than the time between each event occurring. For example, the timescale between nucleation events will be much greater than the time of the nucleation itself[210].

Classical computational methods, such as molecular dynamics, can be used to explore the phase space of a system, helping us to understand the properties of materials. However, a typical molecular dynamics simulation usually explores only a limited region of phase space, due to the large time required for the system to overcome high energy barriers that separate different configurations.

MD simulations usually require a timestep of the order of femtoseconds and can generally only be feasibly performed for a simulation time of the order of hundreds of nanoseconds. With the relatively short simulation time accessible to classical MD, these simulations are unlikely to 'uncover' rare events that would spontaneously occur within much longer timeframes. An illustration of this concept is shown in Figure 3.2. In this system, the energy barriers between minima are significantly greater than $k_B T$, and the probability of the system crossing the saddle point is very small compared to that of being in the deep minimum. If we wish the system to explore a rare event we need to 'help' the simulation to find these inaccessible regions of the free energy surface using specialised techniques[198, 209].
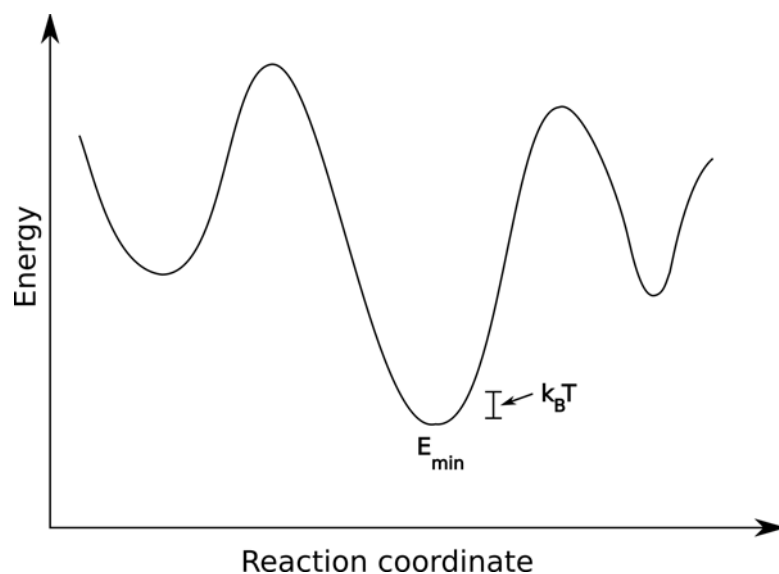
FIGURE 3.2: Example potential energy surface. If the system starts in the local minima E_{min}, an unbiased MD simulation is unlikely to explore configurations outside of this energy well, as the thermal energy will not be sufficient to get into the surrounding local minima.

Among the many techniques that have been developed to enhance the exploration of the phase space and to calculate reactions rates and/or extract free energy profiles we provide a brief overview of Umbrella Sampling[211, 212], Parallel Tempering[213], Steered MD[214], Blue Moon Ensemble[215], Transition Path Sampling[216] and the Forward Flux method[217], which should give the reader a taste of the variety of ways similar problems can be tackled. In the following chapter we will spend more time going into the details of another method, metadynamics[218] (MetaD), which we believe combines the advantages of some of these techniques and alleviates some of their limitations. Metadynamics has

been successfully applied to a wide variety of problems, ranging from protein folding to crystal structure prediction through basic chemical reactions and geochemistry[219–225] and is the major tool used in our studies.

3.9   Free Energy methods

One of the limitations of the previously described static methods in Section 3.2 is that they are designed to work at 0 K, where entropic effects are negligible. This may be a reasonable approximation for many systems, like crystals, but is inappropriate for biological systems, or when a liquid phase is involved. Therefore a whole new category of methods has been developed to deal with entropy and sampling issues. In general, free energy techniques do not calculate absolute free energies but only differences in free energy. Classical statistical mechanics equations were briefly introduced in Section 3.3, and we covered the idea that entropic properties cannot be directly determined from standard methods alone. We will consider looking at the equations and definitions of free energy within the same context, and computational methods available to calculate differences in free energy.

In the previous chapter we introduced the fundamental formula for the Helmholtz free energy, A, for the canonical ensemble in terms of the Hamiltonian, $\mathcal{H}(\mathbf{p}, \mathbf{q})$ [118, 226], where we found A is given by;

$$
\begin{aligned}
A(N, V, T) &= -k_B T \ln Q \\
&= k_B T \ln \left(\iint d\mathbf{p}^N d\mathbf{q}^N \exp\left(-\frac{\mathcal{H}(\mathbf{p}^N, \mathbf{q}^N)}{k_B T} \right) \rho(\mathbf{p}^N, \mathbf{q}^N) \right)
\end{aligned}
\tag{3.64}
$$

where V is the volume of the system, T the absolute temperature and k_B Boltzmann's constant. The definition of a system's absolute free energy is riddled with computational difficulties; for example, the value of the free energy is dependent on a $6N$-dimensional integral carried out over phase space. This is compounded by the fact that the logarithm is a monotonically increasing function, and the integrand is always positive. As a result, as more regions of phase space are included in the integration, the free energy will become progressively lower. In practice, the absolute free energy can only be calculated for a small number of model systems - for which the total accessible phase space can be calculated[226].

Instead free energy differences between closely related states can be calculated using a variety of methods which can be grouped into three categories:

- Methods calculating free energy difference between two thermodynamic conditions, *e.g.*, different pressures

- Methods calculating free energy difference between systems described by different Hamiltonians, *e.g.*, solvation free energy of an ion

- Methods calculating free energy difference between two separate regions of the phase space, *e.g.*, umbrella sampling

First, we will briefly touch on Free Energy Perturbation, a method which fits in the second category; we will then dedicate the rest of the chapter to describing free energy methods from the final category, as they are the most relevant to this work.

3.9.1 Free Energy Perturbation

Zwanzig [227] introduced a means of calculating the free energy difference between two systems described by two different Hamiltonians, $\mathscr{H}_a(\mathbf{p}^N, \mathbf{q}^N)$ and $\mathscr{H}_b(\mathbf{p}^N, \mathbf{q}^N)$ with a protocol called free energy perturbation (FEP). This technique is commonly used to perform "alchemical" transformations, where one species is transformed into another and the free energy difference associated with the transformation is calculated. Solvation free energies of ions or molecules can be calculated using FEP.

The method is based on the well known statistical mechanics relation:

$$\Delta A_{a \to b} = -k_B T \ln \frac{Q_b}{Q_a}. \tag{3.65}$$

First of all we can simplify this equation by noting that the kinetic term of the partition function is constant in the two Hamiltonians and it cancels out:

$$\Delta A_{a \to b} = -k_B T \ln \frac{\int \mathrm{d}^N \mathbf{q} \ \exp(-\beta U_b(\mathbf{q}))}{\int \mathrm{d}^N \mathbf{q} \ \exp(-\beta U_a(\mathbf{q}))} \ = \ -k_B T \ln \frac{Z_b}{Z_a}. \tag{3.66}$$

This leaves us with the ratio of the configurational partition functions, Z_a and Z_b. This expression can be manipulated by multiplying the numerator by the

expression $\exp(\beta U_a(\mathbf{q})) \exp(-\beta U_a(\mathbf{q}))$[228]:

$$\Delta A_{a \to b} = -k_B T \ln \frac{\int d^N \mathbf{q} \ \exp(-\beta U_b(\mathbf{q})) \exp(\beta U_a(\mathbf{q})) \exp(-\beta U_a(\mathbf{q}))}{\int d^N \mathbf{q} \ \exp(-\beta U_a(\mathbf{q}))} \quad (3.67)$$

$$= -k_B T \ln \frac{\int d^N \mathbf{q} \ \exp(-\beta \Delta U(\mathbf{q})) \exp(-\beta U_a(\mathbf{q}))}{\int d^N \mathbf{q} \ \exp(-\beta U_a(\mathbf{q}))} \quad (3.68)$$

$$(3.69)$$

This effectively multiplies the numerator by 1 while enabling the variable $\Delta U(\mathbf{q})$ to to be 'introduced' into the equation. Remembering Equation 3.14, the above rearrangement corresponds to the thermodynamic average of $\exp(-\beta \Delta U)$ calculated along a MD trajectory generated by the Hamiltonian $\mathscr{H}_a$:

$$\Delta A_{a \to b} = -k_B T \ln \langle e^{-\beta \Delta U} \rangle_a \quad (3.70)$$

or analogously:

$$\Delta A_{b \to a} = -k_B T \ln \langle e^{\beta \Delta U} \rangle_b \quad (3.71)$$

where $\Delta U = U_b - U_a$. Although the derivation is quite straightforward and does not include any approximations, it is of limited practical use in the case when large perturbations are applied because of the poor sampling of phase space. To alleviate this problem a procedure called staging is used. In this procedure a number of intermediate states are introduced between the two states of interest and the system is progressively perturbed from one to the next, until the final state is reached[228]. This procedure ensures that every perturbation is small and therefore that the sampling will be accurate and the overall free energy difference can be obtained as the sum of all the intermediate contributions. Without losing generality we can write the potential energy as a linear combination of U_a and U_b:

$$U_{\lambda_i} = \lambda_i U_b + (1 - \lambda_i) U_a \quad (3.72)$$

where λ_i is called the perturbation parameter and $\lambda_i = 0$ corresponds to state a and $\lambda_i = 1$ to state b. The FEP equation can then be rewritten as:

$$\Delta A_{a \to b} = \sum_{i=0}^{N-1} \Delta A_{\lambda_i \to \lambda_{i+1}} = \sum_{i=0}^{N-1} -k_B T \ln \langle e^{-\beta \Delta U_{\lambda_i, \lambda_{i+1}}} \rangle_{\lambda_i}. \quad (3.73)$$

where λ_i identifies the intermediate stages of the perturbation. The optimal number of intermediate states depends on the problem; generally the greater the difference between the starting and final state the more intermediate states are necessary[228]. λ_i can be seen as a perturbation parameter which allows for going from state a to state b. For example, when determining the solvation free energy of an ion, λ can simply be a scaling factor that perturbs to zero the interactions between the ion and the solvent.

As a final remark, this technique is quite similar to the thermodynamic integration method, although some fundamental differences appear in the formalism. In particular, in thermodynamic integration the derivative of the Hamiltonian with respect to the perturbation parameter has to be calculated and then integrated along the whole path[197]:

$$\Delta A = \int_a^b d\lambda \left\langle \frac{\partial \mathscr{H}}{\partial \lambda} \right\rangle_\lambda \qquad (3.74)$$

3.9.2 Reaction coordinates and collective variables

The free energy is a complicated function of $6N$ vectorial variables. Fortunately, most of the time we are only interested in calculating the free energy *difference* between two regions of phase space. Examples of this are the free energy difference between two conformations of a protein or the free energy profile of a chemical reaction. To achieve this goal it is useful to define a collective variable (CV) onto which we want to project the free energy hyper-surface. This CV is usually user-defined and in principle it can be any function of the $3N$ atomic coordinates. It is important to note here that the user-defined CV is formally different from the true reaction coordinate, which corresponds to the minimum free energy path (MFP) and is usually unknown. In some simple cases the CV can be chosen very intuitively and can provide a good approximation to the true reaction coordinate. In general this is not possible, and a combination of several CVs will be necessary to describe the system of interest.

In this context, the free energy projected on a given reaction coordinate is usually referred to as the potential of mean force (PMF) and mathematically can be expressed as[229, 230];

$$A(\xi) = \int d^N\mathbf{p} \, d^N\mathbf{q} \, \delta(\xi' - \xi) \exp(-\beta\mathscr{H}) = -k_B T \ln P(\xi) \qquad (3.75)$$

where $P(\xi)$ is the probability distribution along the reaction coordinate, ξ. In principle, $P(\xi)$ can be calculated directly in a long MD run, provided the system will explore every relevant portion of the phase space for long enough to obtain a converged distribution. However, as we have already discussed, this is often not possible and several techniques have been developed to enhance the sampling and calculate directly $P(\xi)$ or $A(\xi)$. A brief overview of few of these techniques is given below.

3.9.3   Parallel tempering

One of the easiest ways to escape from deep local minima and to boost the exploration of the free energy landscape is to increase the temperature in the simulation. Although this is a pretty simple workaround, it has the obvious drawback that the free energy landscape at higher temperatures may be significantly different from the one we are interested in. In order to alleviate this problem, Hansmann [213] suggested a method called *parallel tempering* which consists of simultaneously running a number of simulations and periodically swapping the configurations between them. Each of these simulations is usually called a *replica* and is run at a different temperature. In this technique, the higher temperature replicas have a better chance to explore a wider portion of the phase space and the swapping procedure, performed using the Metropolis criterion [199], ensures that each low energy configuration found by the high temperature replicas "travels" down to a low temperature replica. The end result is that the sampling capabilities of the low temperature replica have been enhanced. It has been demonstrated that the sampling of the phase space in the low temperature replica is consistent with the canonical ensemble, hence no artefacts are introduced by swapping the configurations. Therefore, the replica at the lowest temperature during the "short" time achievable in a MD simulation has performed a better and more homogeneous exploration of the phase space and the PMF along any CV of interest can be obtained from the direct calculation of the probability distribution. However, a disadvantage of this method is that the configuration swaps break the trajectory into short fragments and therefore any information on the dynamics of the system is lost.

The method can be applied both to MC or MD methods, and can also be combined with other enhanced sampling methods on top of these, as will be evident in the following chapter.

3.9.4 Hyperdynamics

Another possible way to enhance the sampling of the phase space is to disfavour the low energy configurations. This can be done by increasing their energy, which has the net effect of reducing the barriers between minima, and therefore helps avoid scenarios where the system remains trapped in local minima. This idea was exploited by Voter [231] who developed a method for accelerating infrequent events in MD simulations known as *hyperdynamics.*

A positive biasing potential is applied to the system only in the region surrounding the energy minima leaving the transition states untouched. This is achieved by calculating the Hessian matrix and constructing a function of its eigenvalues and eigenvectors. This function is such that it is zero if one of the eigenvalues is negative and its largest value at the minimum. This is illustrated in Figure 3.3 where the solid line indicates the potential of the system, and the dashed line the potential when corrected by the bias. The calculation of the bias, ΔV_b, requires
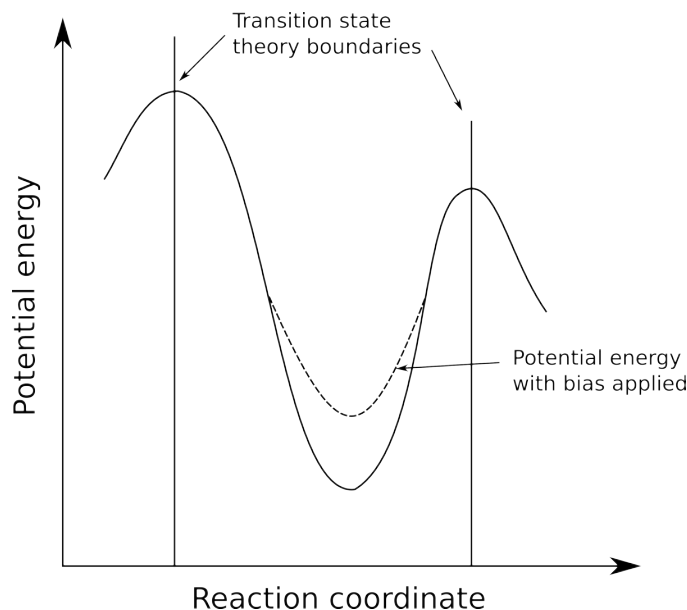

FIGURE 3.3: Example of a potential energy surface, V (solid line) and the same potential surface with a bias applied, $V + \Delta V_b$ (dashed line). The saddle points of the energy well are unaffected by the bias ΔV_b. Image adapted from Voter [231].

the expensive calculation of the second derivatives of the potential to construct the Hessian matrix. Although this is feasible for small systems it becomes prohibitive if the system has more than few thousand atoms. Voter later expanded this method [232], by suggesting that the bias potential can be approximated from the fluctuations of the system in the space of a suitable reaction coordinate, making it a less computationally expensive technique to use. A complete review of this and other related techniques can be found in Voter *et al.* [233].

3.9.5   Steered MD

If we are interested in calculating the free energy profile along a given single CV which displays a high energy barrier, a possible approach involves mechanically steering the system along the CV by applying a restraint force. The system can be dragged from the initial state, a, to the final state, b, and work done in this process can be calculated[197]. There exists in thermodynamics an inequality known as the work-free-energy inequality which states that the work done to induce a transformation is always greater or equal to the free energy difference between the two states;

$$\langle W_{a\to b}\rangle \geq \Delta A \tag{3.76}$$

where $\langle W_{a\to b}\rangle$ is the average over an ensemble of measurements of the work along the same path. In Equation 3.76 the equality holds when the work is done reversibly. Therefore, this inequality allows us to set an upper bound to the free energy of the transformation but not to get its precise value. A major step forward was done by Jarzynski [214] who proved that;

$$\langle e^{-\beta W_{a\to b}}\rangle = e^{-\beta A_{a\to b}}. \tag{3.77}$$

which takes the name of the Jarzynski equality. Its demonstration is not trivial and out of the scope of this overview so we limit ourselves to comment on its importance. Equation 3.77 implies that the calculated free energy difference is independent of the path between A and B, and the rate at which the dragging along this path is done. Ultimately this enables equilibrium information to be obtained from an ensemble of non-equilibrium simulations. However, despite its importance, the Jarzynski equality is of limited use because it requires the knowledge of the initial and final states, and also a reasonable guess at the reaction coordinate to be

used in the steering process. In particular, if the reaction coordinate is not known the use of more than one CV to describe the process of interest is impractical.

3.9.6 Umbrella sampling

The Umbrella Sampling (US) method was introduced by Torrie and Valleau [211, 212] and it is based on a general statistical mechanics concept called *re-weighting* which allows for extracting the thermodynamic average of a quantity in a system described by a given Hamiltonian, even if we perform a simulation with a different Hamiltonian. To demonstrate this concept we follow a procedure similar to the one used for the FEP technique. Let's assume that the system we are interested in is described by the Hamiltonian, $\mathscr{H}_0$, but we need to run a simulation using a different Hamiltonian, $\mathscr{H}_1$, to solve the equations of motion which is related to $\mathscr{H}_0$ by the following relation;

$$\mathscr{H}_1 = \mathscr{H}_0 + w \tag{3.78}$$

where w is a positive function of the atomic coordinates that is usually called a bias potential. As described previously in Equation (3.14), the thermodynamic value of a given quantity C in the ensemble described by $\mathscr{H}_0$ is:

$$
\begin{aligned}
\langle C \rangle_0 &= \frac{\int \mathrm{d}x \ C \exp(-\beta \mathscr{H}_0)}{\int \mathrm{d}x \ \exp(-\beta \mathscr{H}_0)} \\
&= \frac{\int \mathrm{d}x \ C \exp(-\beta \mathscr{H}_0) \exp(+\beta \mathscr{H}_1) \exp(-\beta \mathscr{H}_1)}{\int \mathrm{d}x \ \exp(-\beta \mathscr{H}_0) \exp(+\beta \mathscr{H}_1) \exp(-\beta \mathscr{H}_1)}
\end{aligned}
\tag{3.79}
$$

Substituting $\mathscr{H}_0 + w$ for $\mathscr{H}_1$, as described in Equation (3.78), our equation reduces to;

$$= \frac{\int \mathrm{d}x \ C \exp(+\beta w) \exp(-\beta \mathscr{H}_1)}{\int \mathrm{d}x \ \exp(+\beta w) \exp(-\beta \mathscr{H}_1)} \tag{3.80}$$

which can be rearranged to give:

$$= \frac{\int \mathrm{d}x \ C \exp(-\beta \mathscr{H}_1) \exp(+\beta w)}{\int \mathrm{d}x \ \exp(-\beta \mathscr{H}_1) \exp(+\beta w)} \tag{3.81}$$

Referring to Equation (3.14), we find this finally simplifies to:

$$\langle C \rangle_0 = \frac{\langle C \exp(+\beta w)\rangle_1}{\langle \exp(+\beta w)\rangle_1} \tag{3.82}$$

Throughout all these manipulations in Equations (3.79)-(3.82) the 0 or 1 indicate which Hamiltonian is used to perform the calculation. Torrie and Valleau [211, 212] extended this concept to the case where the bias potential is applied to constrain a system on a given reaction coordinate, ξ, and the quantity of interest is the probability distribution projected on the reaction coordinate $P(\xi)$. In this case it is easy to prove that;

$$P_0(\xi) \;=\; e^{[+\beta w(\xi)+\eta]} P_1(\xi) \tag{3.83}$$

where η is an arbitrary constant. Hence, once we know the un-biased probability distribution we can extract the PMF by using Equation 3.75:

$$\phi(\xi) = -k_B T \ln P_1 - w(\xi) - \eta \tag{3.84}$$

The potential of this method becomes immediately evident if we think of performing a series of biased simulations with the constraint potential in different positions, so that the whole portion of interest of ξ_i is accurately explored. One problem that remains is that of the alignment of the separate portions of PMFs that are calculated in this fashion. One possible approach is to tune the η_i values in such a way that the sequence of $\phi_i(\xi)$ for a smooth continuous function or alternatively a self consistent algorithm can be used to automatise this process. This is known as the weighted histogram analysis method (WHAM)[234] and has several advantages, including the possibility to accurately estimate the error.

The US technique is useful and powerful when we have only one reaction coordinate but it becomes extremely expensive when 2 CVs are used and impractical for 3 or more CVs. The method also requires the definition of a suitable CV and of the initial and destination points (from a to b along a reaction coordinate), while it has limited use for a "blind" exploration of the free energy landscape.

3.9.7   Blue moon ensemble

A method known as the *blue moon ensemble* method was introduced in 1989 by Carter *et al.* [215] and improved and re-introduced in 1998 by Sprik and Ciccotti

[235]. This method aims to calculate the PMF along a selected CV and it is based on the Thermodynamic Integration scheme[235] that we briefly introduced in Equation (3.74), where the perturbation parameter is substituted with a point on a selected CV, ξ.

$$A(\xi) = \int_{\xi_1}^{\xi_2} d\xi' \left\langle \frac{\partial \mathscr{H}}{\partial \xi'} \right\rangle_{\xi'} \tag{3.85}$$

Here the thermodynamic average is calculated at fixed ξ. This is achieved by performing constrained MD simulations at different values of ξ and averaging the *constraint force*, $\partial \mathscr{H}/\partial \xi'$, which is necessary to apply to keep ξ constant[197].

A detailed description of the algorithms required for the implementation of this method have been outlined by Komeiji [236] and here we limit ourselves to give a general overview on its advantages and disadvantages. Like the US method, an advantage of the blue-moon ensemble method is that higher levels of accuracy can easily be achieved by increasing the sampling at each location of ξ. This is particularly important in the high energy regions that would be very rarely visited[229]. However, the method does have some disadvantages. A problem inherent to its constrained dynamics is that there may exist several pathways between states a and b, or the choice of the CV is not appropriate. As a result, the calculated PMF may be extremely accurate on the chosen path, but not representative of the true reaction mechanism[229]. Another limitation to the use of this method is the complexity of the machinery that has to be implemented to constrain the system to a given value of ξ, which is usually done with an iterative procedure that may become too computationally expensive for a complex CV.

3.9.8 Transition path sampling

Transition path sampling (TPS) is a method introduced by Dellago *et al.* [237, 238, 239]. Unlike the previous methods, TPS gives direct access to the transition rates while the free energy can be obtained by a non-trivial procedure in combination with the Umbrella Sampling technique.

TPS is based on a generalisation of the standard Monte Carlo simulation method[216]. The standard form of Monte Carlo is based on the importance sampling of the configuration space whilst the TPS aims to perform an importance sampling of the space of the reactive trajectories of a specified time length[197]. Dellago *et al.* [237, 238, 239] generalised the standard statistical mechanics

equations and applied them to calculate the probability distribution of the reactive paths and their properties. The starting point of this method is a reactive trajectory, generated by any means, and then further trajectories are generated by the "shooting" algorithm which ensures that the reactive trajectory space is properly sampled. In simple terms, the shooting algorithm consists of changing the momentum of one atom in a random position of the old trajectory and then evolving the atom's coordinates backward and forward in time for the predefined length and then accept or reject the trajectory according to whether it is reactive or not. These algorithms provide an efficient means of 'harvesting' trajectories with the correct probability distribution $P(\xi)$ in what is usually referred to as the *transition path ensemble*.

The transition path sampling method is useful when the user knows the start and end states, and is curious to find what the intermediate transition states may be. However the transition path ensemble constrains the distributions to include only pathways that start at state a and end with state b within a given time length. This means the distribution of configurations along the pathways deviates from the equilibrium distributions, and the probability distribution $P(\xi)$ cannot be calculated from the trajectories of a transition path simulation. As a result, free energy profiles cannot be obtained directly but a further Umbrella Sampling calculation in the transition path space has to be performed, which makes this technique less useful for calculating the free energy.

3.9.9 Forward flux

Another technique that is predominantly used for the calculation of transition rates, while the free energy profile can be obtained as a "byproduct" of the simulation, is the forward flux (FF) method which was introduced by Allen *et al.* [217]. This technique requires the definition of the initial and final states and of a number of non-intersecting interfaces between them. This can be effectively done by the use of one (or more) CVs, although if the simulation is carried out correctly the final result does not depend on the specific CV(s) used. In simple terms, this technique consists of starting a large number of simulations from an ensemble of points at each interface (the first one being the product state) and stopping them either when the successive interface is reached or when the product state is reached.

The rate constant for the whole process can then be expressed as the products of the transition probabilities from one interface to the successive one:

$$k_{a \to b} \; = \; CP(\lambda_N, \lambda_0) = C \prod_{i=0}^{N-1} P(\lambda_{i+1}, \lambda_i) \qquad (3.86)$$

where $P(\lambda_i + 1, \lambda_i)$ is the probability the the interface λ_{i+1} is reached from the interface λ_i and it can be readily calculated as the ratio between the number of simulations that reach the interface λ_{i+1} over the total number of those initiated at the interface λ_i. In Equation 3.86 the normalisation constant C is the ratio between the flux of trajectories that cross the first interface and the fraction of reactive trajectories generated.

There are several important technical aspects for the correct implementation of this method, but a detailed treatment of them is beyond the scope of this review since the forward flux method is not used in our work.

3.10 Conclusion

Here we have introduced a wide range of free energy methods for exploring energy surfaces. However, many of these methods require the knowledge of the end state of the system in advance. In our studies we wish to investigate the possible structures of nanoparticles of zinc sulfide, and the free energy differences between these structures, without an *a priori* bias. In other words, we don't know in advance which structures we would like to locate so we need a method which has the capability to explore possible configurations without being directed towards any one configuration. The method most suited for our problem is *metadynamics*, which will be covered in detail in the following chapter.

Chapter 4

Metadynamics

4.1 Introduction

In the previous chapter we discussed a variety of methods available for enhancing the exploration of potential energy surfaces, and for calculating the free energy differences between different states of a system. In this chapter we will continue this discussion, but provide the background of one particular method known as metadynamics (MetaD)[218], which we will use in this study.

The metadynamics method involves the evolution of a collective coordinate, generally some system descriptor, and a continual biasing of the forces with a history-dependent Gaussian term. The history-dependent Gaussian terms accumulate as the simulation progresses and discourage the system from revisiting the same region on the free energy surface (FES)[218]. Metadynamics is a particularly useful method for exploring the FES of a system without an *a priori* bias, that is, the end-state isn't already known, and neither is the path to travel to the new states.

Laio and Parrinello [218] combined ideas of dimensional reduction[240] of the FES with concepts from adaptive bias potential methods such as the local-elevation method of Huber *et al.* [241]. The method Laio and Parrinello [218] devised allows the system to explore and escape wells on the free energy surface, and also allows determination of the FES, and free energy differences between areas on the FES.

The basis of the metadynamics method is the identification of a collective variable (CV), s, and the addition of a time dependent bias potential, acting on s, to the

Hamiltonian. The time dependent potential takes the form of a sum of Gaussians added to $\mathscr{H}^0$, such that the new Hamiltonian of the system is expressed by Equation (4.1);

$$\mathscr{H}'(\mathbf{p},\mathbf{q},t) = \mathscr{H}^0(\mathbf{p},\mathbf{q}) + \sum_{t'\leq t} W e^{-\frac{|s-s^{t'}|^2}{2\delta\sigma^2}} \tag{4.1}$$

where W is the height of the Gaussians and $\delta\sigma$ the width. This equation applies when only one reaction coordinate is used, but the metadynamics method can be applied to any number of CVs and when this is the case multi-dimensional Gaussians are required. Examples of appropriate collective variables will be given in the following sections. The usefulness of the method is derived from how the history dependent Gaussian terms accumulate, and encourage the system to explore different regions of phase space[218]. As the simulation progresses, Gaussian terms accumulate and 'fill' the current well in the free energy surface, eventually pushing the system into other wells. Ultimately this method allows the system to explore other regions of phase space that may ordinarily be inaccessible with an unbiased MD simulation due to the timescale problem.
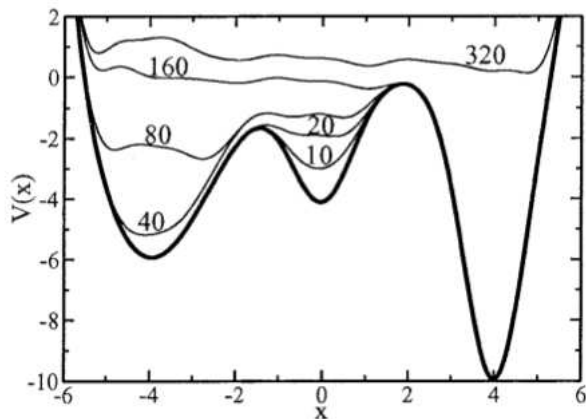

FIGURE 4.1: Example of evolution of a system through phase space using metadynamics. Successive iterations are indicated by thin lines across the energy surface, labelled by the iteration number. Image reproduced from Laio and Parrinello [218].

This whole process is succinctly illustrated by Figure 4.1. In this image the system starts in the middle minimum; the evolution of the system (and filling of the energy wells) is indicated by the thin lines on the graph, labelled with the number of added Gaussians. After 20 Gaussians have been added the system is still in the middle

minimum, but it is essentially filled, while successive iterations push the system into the left hand minimum. The process continues to fill the left region of the surface until 160 Gaussians have been added and eventually pushes the system to the right hand minimum.

When metadynamics is performed for sufficiently large amounts of time $(t \to \infty)$, the negative of the sum of Gaussian terms provides an estimation of the free energy surface of the system:

$$\lim_{t \to \infty} \quad -\sum_{t' \leq t} W e^{-\frac{|s - s^{t'}|^2}{2\delta\sigma^2}} \to A(s) \tag{4.2}$$

A study of how accurately the sum of the Gaussians reproduces the free energy surface has been performed by Laio *et al.* [242]. They found the error at time t of a MetaD simulation is given by;

$$\bar{\epsilon} = C(d)\sqrt{\frac{S\delta\sigma}{D\tau_G}\frac{W}{\beta}} \tag{4.3}$$

where $C(d)$ is an empirical constant that depends on the number of CVs (d), S is the size of the explored free energy basin, D is the diffusion coefficient, τ_G is the time interval between adding Gaussians, and finally W and $\delta\sigma$ are the height and width of the Gaussian terms. The simulations are particularly influenced by the Gaussian parameters W and $\delta\sigma$. If the Gaussian bias is quite large, the system will rapidly find new regions of the potential energy surface, but the 'resolution' of the free energy surface will be low. Alternatively, small Gaussian parameters can be used. In this instance the system may take a long time to fill one well on the FES and travel to the next well, but the accumulated Gaussians will be a more accurate representation of the true FES.

4.2 Enhanced metadynamics methods

Since the introduction of the metadynamics method a variety of modifications have been proposed that attempt to improve on different drawbacks of the original method. We will briefly introduce some of these additions before providing an overview of some of the problems MetaD has been applied to.

4.2.1   Well-tempered metadynamics

One of the potential problems of the metadynamics method is that it is difficult to
know when a metadynamics run can be terminated[243]. Generally the calculated
free energy difference between two states does not converge to a stationary value,
but fluctuates around the real value as we continue to add Gaussians into the
bias potential. A possible workaround is to perform a series of MetaD runs
with decreasing Gaussian heights. One obvious disadvantage to this is that the
user must decide when to stop a simulation and restart with smaller Gaussians.
Barducci *et al.* [243] introduced an extension to the metadynamics method known
as 'well-tempered metadynamics', which alleviates the problem of convergence by
introducing Gaussians with a variable height. In this method, the heights of the
Gaussians change throughout the simulation, according to;

$$W = \omega e^{[V(s,t)/\Delta T]} \tau_G \tag{4.4}$$

where ΔT is an adjustable parameter and ω is the initial rate of depositing
Gaussians. In this way the height of the Gaussians, W, are determined by the
bias that has already accumulated throughout the simulation. In areas that have
already been well-traversed the Gaussian height will be smaller, and conversely,
areas which have not been explored will initially have large Gaussian terms. One
difference between the well-tempered MetaD scheme and the original method is
that the FES is not directly mapped out by the inverse sum of the added bias,
instead it is defined by:

$$\lim_{t\to\infty} \quad V(s,t) \to -\frac{\Delta T}{\Delta T + T} \quad A(s) \tag{4.5}$$

Eventually as more regions of the potential energy surface have been traversed the
Gaussian height decreases towards zero[244].

4.2.2   Replica exchange metadynamics

Another development of MetaD was devised by Bussi *et al.* [221] who combined
the replica exchange method of parallel tempering[213], introduced in the previous
chapter, and the metadynamics method. The method, known as replica exchange
MetaD, involves multiple metadynamics simulations, or 'replicas', to be run in

parallel at different temperatures. Each replica uses the same set of collective variables, however a separate bias potential is accrued for each of them. An attempt to swap the coordinates from adjacent temperatures is performed at a predetermined frequency and accepted according to the Metropolis criterion of the Monte Carlo method, where the energy terms include the MetaD bias. If the move is accepted the coordinates, q, are swapped and the momenta, p, are scaled to accommodate the temperature of the replica. They found that this combination of methods resulted in a more efficient exploration of phase space in comparison to either method used alone.

4.2.3 Bias-exchange MetaD

Piana and Laio [245] investigated the use of the replica exchange metadynamics method of Bussi *et al.* [221] with a slight modification. They used the same idea of combining replica exchange and metadynamics, however instead of the replicas being run at different temperatures, the time dependent potentials in each replica are acting on different collective variables[245]. As with replica exchange MetaD, Monte Carlo swaps are attempted according to the Metropolis criterion. If the move is accepted the bias potential is exchanged. Each replica has a small number of CVs, often only one, and consequently each replica has only a limited portion of phase space to explore. The main advantage of using the bias-exchange MetaD method is that it enables the exploration of a complicated multi-dimensional FES by performing a set of low-dimensional MetaD runs.

Unfortunately a multi-dimensional FES cannot be directly reconstructed from the separate bias generated by each replica. Instead, a 'neutral' replica, which has no bias applied, needs to be included. The neutral replica run will sample approximately the canonical ensemble and the FES can be calculated directly from the partition function, as described in the previous chapter.

4.2.4 Reconnaissance metadynamics

A new algorithm has been recently developed by Tribello *et al.* [246] known as Reconnaissance Metadynamics. The authors of this method realised that the lack of knowledge of a 'good' collective variable for use in a MetaD simulation is a significant limitation in setting up meaningful calculations. While using

multiple collective variables in an attempt to model the true reaction coordinate is feasible with MetaD, the cost of the simulation increases exponentially with the dimensionality[246]. The reconnaissance metadynamics method attempts to overcome this by allowing the bias to 'learn' as the simulation progresses, significantly enhancing the exploration of phase space.

The method uses a clustering algorithm combined with principal component analysis to efficiently explore phase space. The cluster analysis algorithms[247, 248] are used at regular intervals to analyse the trajectory and obtain statistics related to the basins explored on the free energy surface. The statistics are used to determine the ideal shape a Gaussian should have to exactly fill the basin near the minimum. The advantage of this is to avoid the situation where a large ill-fitting Gaussian may be placed in the middle of a basin, creating 'spurious low energy features' - basically creating two 'new' minima on either side of the Gaussian which again need to be filled. The Gaussians which are placed are multi-dimensional, as the method has been developed for use with many CVs. A further speed-up is obtained by placing multi-dimensional Gaussians with increasing size, rather than placing a large quantity of small Gaussians.

In contrast to the normal metadynamics method the bias potential generated during a reconnaissance MetaD run does not reproduce the free energy profile, so other methods, such as umbrella sampling, need to be implemented if the FES is required. The greatest advantage of reconnaissance MetaD is its ability to use a theoretically unlimited number of CVs without the same increase in computational cost found in the normal MetaD method. In the authors words, the method "gives one a feel for the lie of the land", allowing the separate basins on the free energy surface to be quickly located.

4.3   Previous studies using MetaD

To study rare events with MD, the reaction coordinates of a given process need to be described by one or more collective variables. The collective variables are some quantifiable property of the system or its components, such as the average coordination number, or the distance between two atoms. In this section we will attempt to summarise some of the work that has been done using the

metadynamics method. We have attempted to categorise the previous studies into different groups based on the application:

- Predicting crystal structures

- Investigating reaction mechanisms

- Biological molecules

These studies all require specific collective variables to bias the metadynamics simulations in order to explore the regions of phase space relevant to the process being investigated. The choice of collective variable isn't a trivial one, and if a poor choice is made, or the problem is a multi-dimensional one, the simulations may result in a poorly converged free energy surface or even a completely wrong profile[221].

4.3.1 Predicting crystal structures

Crystal structure prediction is an ongoing challenge[249], and metadynamics is one of the many methods that has been applied to try to tackle this problem. In particular, there is a method based on the concepts of the Parrinello-Rahman method[250], in which the volume and the shape of the MD cell are variable over time. If the pressure of a system is increased under this regime it is possible to force a crystal structure to undergo phase transitions, and the Parrinello-Rahman method allows the cell parameters to transform and accommodate new crystal structures. One drawback to this method is that there is often a significant energy barrier to be overcome to transform from one crystal structure to another, even with a dynamic cell. This is a fundamental limitation of MD, and to achieve the desired phase transition using the Parrinello-Rahman method over-pressurisation of the system is usually required. Unfortunately under these conditions it is likely intermediate phases of interest may be missed[225]. Martoňák *et al.* [225] thought to try to enhance the exploration of solid phases using the cell variables as the collective variables in metadynamics. They used the simulation cell vector matrix, $\mathbf{h}$, a matrix comprised of the MD supercell edges, $(\vec{a}, \vec{b}, \vec{c})$, as the collective variables.
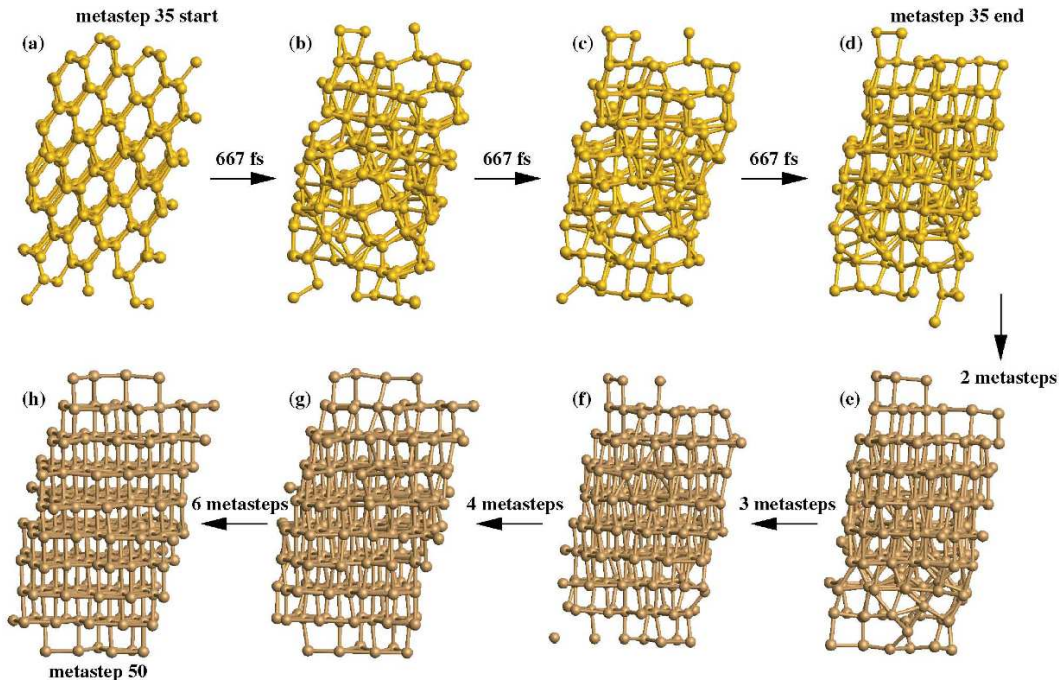
FIGURE 4.2:   Phase transitions seen for silicon during a metadynamics simulation[225], transforming from diamond structure at **(a)**, to a new crystal structure at **(d)**, and finally to the formation of simple hexagonal (SH) at **(h)**. Image reproduced from Martoňák *et al.* [225].

At ambient pressure the stable form of Si is the diamond structure while at higher pressures it may be found in the metastable β-tin form or a stable simple hexagonal (SH) phase. Figure 4.2 shows frames taken along the MetaD trajectory which shows the transition from diamond to SH.

An estimation of the transition pressure for the diamond to SH transformation with the common tangent procedure for the model potential used gives a value of 15.5 GPa. However, attempts to simulate this transformation by pressurising the system using the Parrinello-Rahman method results in the transition occurring at 44 GPa. This over-estimation of the transition pressure is related to the high free energy barrier that has to be overcome during the short time accessible by MD (eg. in the order of ns). Martoňák *et al.* [225] showed that MetaD was able to reproduce the transition at 16 GPa. Although in principle the metadynamics technique is able to push the system out of the free energy cell of the diamond structure to find any other allowed polymorphs, the authors chose to perform their simulations just above the estimated transition pressure so that the driving force was towards the desired polymorph, ie. SH. Examples where exploration of polymorphs were performed without considering pressure effects can be found in Raiteri *et al.* [251] and Zykova-Timan *et al.* [252].

Martonák *et al.* [253] later used the same method in 2006 to perform phase transitions on silica, SiO_2. In this study they were particularly interested in understanding the step-wise pressure-induced transformation from fourfold-coordinated Si in α-quartz into sixfold-coordinated stishovite at high pressure. Varying the starting super-cell parameters and the metadynamics parameters their simulations explored a number of different phases. The phase transitions explored included α-quartz to quartz II, followed by a transition to stishovite. They also reported an anatase structure, which had previously not been reported for silica. The potential they were using to model the silicate was known as the BKS[254] potential, and has been extensively used in the literature to study silicate structures. Two years prior to the study done by Martonák *et al.* [253] the BKS potential had been used to produce a phase diagram for known silica structures[255], proposing the BKS potential as the most accurate potential to use when modelling silica. The phase diagram did not include anatase, and in fact the study done by Martonák *et al.* [253] indicates the BKS potential has some artefacts, such as yielding anatase as the most stable phase under certain conditions. Metadynamics proved itself to be not only useful for exploring previously undetected phases for a system, but also for testing the potential model being used. Martoňák *et al.* [256] continued these studies and reported a more detailed discussion of their results a year later. In this study they simulated the transition from 4- to 6- coordinated silica in an effort to understand the transformation pathways used to form high-pressure silicates.
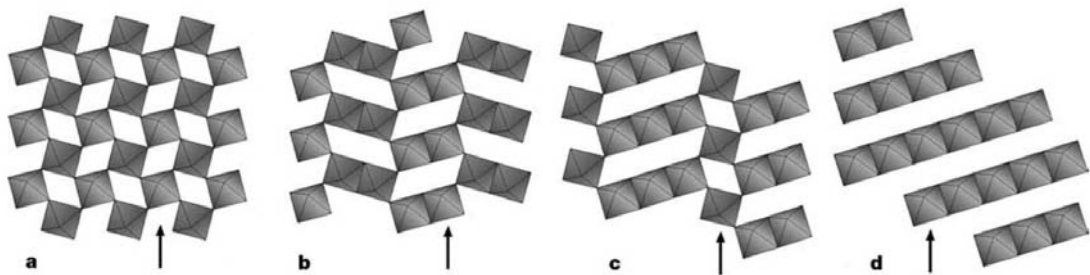

FIGURE 4.3: Schematic showing the intermediate polytypes found in the transformation of $(Mg,Fe)SiO_3$ from perovskite to post-perovskite. The most likely slip planes to achieve the next polytype are indicated with an arrow. Image reproduced from Oganov *et al.* [257]

Oganov *et al.* [257] investigated phase transitions in $(Mg,Fe)SiO_3$, believed to be the main mineral phase of the Earth's lower mantle. They were interested in how $(Mg,Fe)SiO_3$ transformed from perovskite to post-perovskite at the lower mantle pressure. Using the collective variables introduced by Martoňák *et al.* [225] they

used metadynamics to observe phase transitions in this material. They found a number of intermediate polytypes, where planes of atoms in the perovskite phase were sliding and forming stacking faults, before arriving at the post-perovskite phase. A schematic of this transformation is shown in Figure 4.3.

Their simulations suggested that the easiest plastic deformation of the material occurred in the [110] slip plane instead of the expected [010] plane. With this study the authors could provide an explanation of the anisotropy in the propagation velocity of the seismic waves through the lower mantle.

One problem that is inherent to this method is that the phases being explored must have commensurate unit cells. The smaller the supercell is, the greater this constraint will be on the phases being explored.

4.3.2 Investigating reaction mechanisms

Stirling *et al.* [220] used metadynamics combined with the Car-Parrinello MD (CPMD) method[258] to investigate the transformation between azulene and napthalene, as depicted in Figure 4.4. The Car-Parrinello MD method enables first principles MD to be performed, which means chemical reactions involving bonds breaking and forming can be simulated. The transformation of azulene to napthalene is of particular interest as it involves the rearrangement of a non-benzenoid aromatic structure to a benzenoid aromatic structure. In this particular study Stirling *et al.* [220] used coordination numbers as collective variables for C-C and C-H bonds to investigate the transformation between the two molecules.
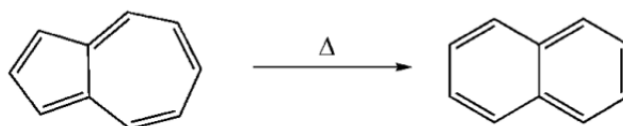

FIGURE 4.4: Transformation of azulene to napthalene. Image reproduced from
Stirling *et al.* [220]

There are two known mechanisms for the transition from azulene to napthlene, and the path explored by the MetaD simulations could be restrained by specifying a maximum distance allowed between certain atoms, which forces the system to explore the transition states expected. Once the system attained the transition
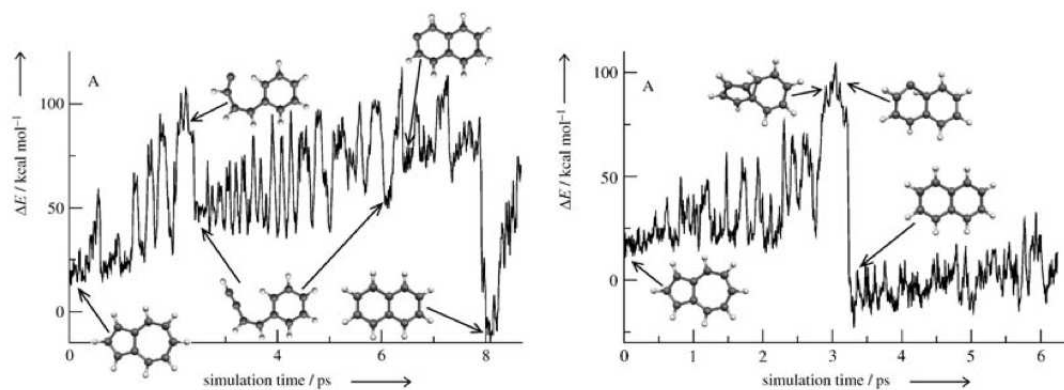
FIGURE 4.5: Two different reaction mechanisms Stirling *et al.* [220] investigated in their study of the azulene-to-napthalene transformation. Image reproduced from Stirling *et al.* [220]

state for a certain pathway the restraints were released and the system allowed to continue exploring other structures - at which point the system moves to the desired product, napthalene.

Given the short time-scale currently achievable by first principles MD an accurate free energy profile is not attainable; this study was primarily a proof of concept that MetaD can be successfully coupled to first principles simulations.

Metadynamics was also used by Blumberger *et al.* [224] for the investigation of the hydrolysis of formamide in alkaline aqueous solutions. The nucleophilic attack of an amide bond by hydroxide is barrierless and highly exothermic in the gas phase, while in alkaline aqueous solution the formation of the tetrahedral intermediate is the rate-determining step and results in a free energy of activation of about 21 kJ mol^{-1}[224]. This barrier for the reaction has been referred to as "solvent induced", and assumed to be due to the large free energy of solvation of the hydroxide ion, which needs to be partly overcome for the transition-state to form. The reaction they investigated is depicted in Figure 4.6, where it is not yet fully understood what mechanism is undergone for the hydroxide ion to form a tetrahedral intermediate with the carbonyl bond of formamide. As with the reaction studied by Stirling *et al.* [220], this reaction has two proposed mechanisms that are able to fulfil the experimental observations. Both mechanisms are shown in Figure 4.7. The reaction labelled A) shows the direct nucleophilic attack of the OH$^-$ onto the carbonyl bond. The reaction mechanism labelled B) is the alternative mechanism, where the nucleophile is a water molecule coordinated
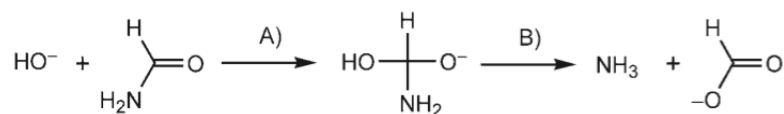
FIGURE 4.6: Hydrolysis of formamide in alkaline aqueous solution. The first reaction is the formation of the tetrahedral intermediate, and is the rate-limiting step, while the second reaction is the dissociation of the tetrahedral intermediate into the products. Image reproduced from Blumberger *et al.* [224].
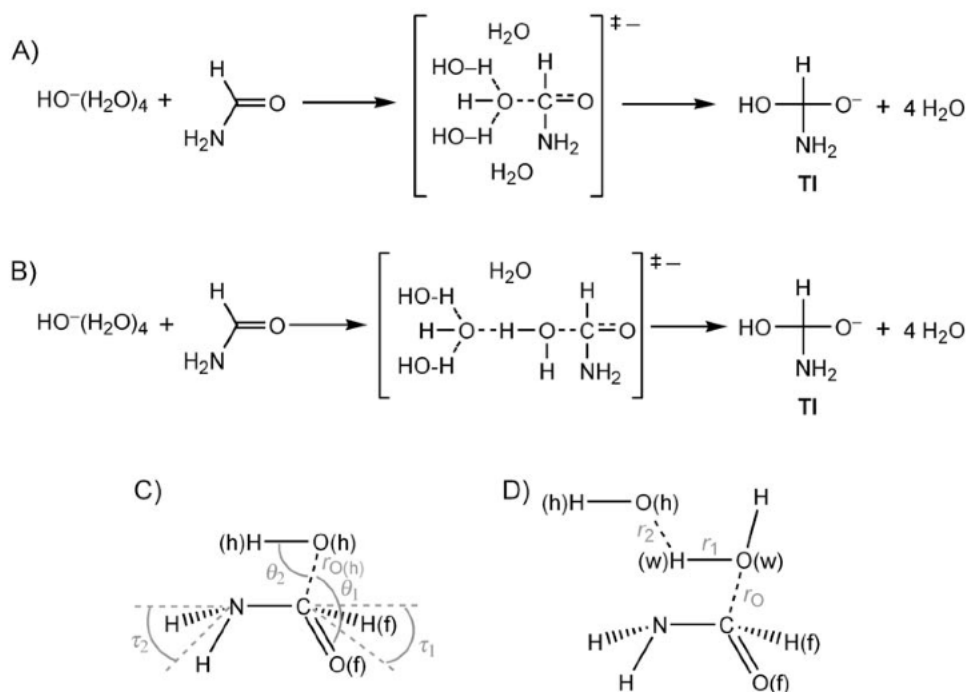

FIGURE 4.7: Two mechanisms for the hydrolysis of formamide in alkaline aqueous solution. Reaction A) shows direct nucleophilic attack and Reaction B) shows the general-base mechanism. C) and D) show the labelling of atoms and bonds for umbrella sampling and metadynamics respectively. Image reproduced from Blumberger *et al.* [224].

to hydroxide. The oxygen atom of water attacks the carbonyl bond while simultaneously donating a proton to hydroxide, which is acting as a general-base. CPMD was used combined with metadynamics to investigate the general-base mechanism. They used the distance, r_o, between the carbon atom of formamide and the oxygen atom of the water molecule, O(w), that separates hydroxide and formamide as their first CV. The second CV is the distance between the hydrogen atom of the water, H(w), and the hydroxide $r_H = r_2 - r_1$- a value which indicates the progress of hydrogen transfer. Blumberger *et al.* [224] also studied the direct nucleophilic reaction mechanism using Umbrella Sampling (US) of the C-O(h) distance, $r_{O_{(h)}}$. Both their simulations predicted a transition state at $r_{O_{(h)}}$=1.9 Å

between the starting states and final tetrahedral intermediate, however they found that the hydrogen transfer from a water molecule to hydroxide, shown in the mechanism Reaction B, is completed well before the observed intermediate is formed. This suggests that the electrophilic character of the formamide is too weak to react with a water molecule coordinated to sodium hydroxide, and instead direct nucleophilic attack by the oxygen in sodium hydroxide is the more likely pathway[224].

Again, the use of a first-principles MD method meant that an accurate estimation of the free energy barriers was not achievable within the short simulation time.

In the next section we will introduce the most recent application where metadynamics has been used, namely the exploration of the complex potential surfaces of biological molecules.

4.3.3 Biological molecules

One of the other interesting problems that metadynamics has been applied to is that of conformational search in biological molecules. The problem of protein folding is a challenge that remains unsolved for the field of molecular biology[221]. The long time-scale it takes for a protein to achieve its folded state in solution, of the order of milliseconds or more, is one of the reasons it has been difficult, if not impossible, to study these systems without using enhanced sampling methods[259]. There are examples where the folding and unfolding of parts of proteins, or small fast-folding proteins have been explored using only MD. One example of this is the work done by Duan and Kollman [259] where they explored the folding pathway of the villin headpiece subdomain, in explicit water. Another study by Pande and Rokhsar [260] investigated the folding and unfolding pathways of a β-hairpin fragment of a protein. Both of these studies provide some insight into the folding (and unfolding) pathway, but they are high-temperature simulations (to start the system in an unfolded state). The authors of these papers admit it is possible a low-temperature folding pathway may be entirely unexplored by their simulations, and it is one severe limitation on their technique. Enhanced sampling methods enable the complex potential energy surface of a biological molecule to be explored in a shorter simulation time, and without the limitation of performing simulations at high temperature.
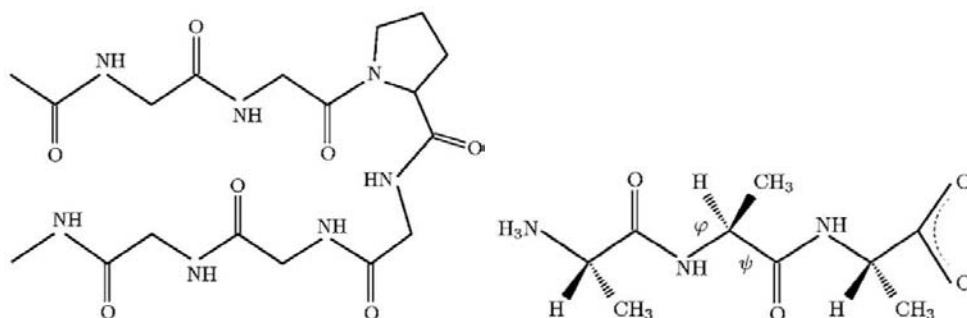
FIGURE 4.8: The two peptides explored in the metadynamics study by Babin *et al.* [223]. Ace-(Gly)$_2$-Pro-(Gly)$_3$-Nme shown in the β-hairpin formation (left) and trialanine (right).

Babin *et al.* [223] used both metadynamics and umbrella sampling to explore the free energy surface of two small peptides. The first of these was Ace-(Gly)$_2$-Pro-(Gly)$_3$-Nme, which folds into a β-hairpin configuration, and the second small peptide was trialanine; both are shown in Figure 4.8. Their first study for Ace-(Gly)$_2$-Pro-(Gly)$_3$-Nme used the radius of gyration of the heavy atoms as the collective variable;

$$R_{gyr} = \sqrt{\sum_i \left(\mathbf{r}_i - \frac{1}{N_b} \sum_j \mathbf{r}_j \right)^2} \tag{4.6}$$

where the summations run over the N_b heavy atoms of the backbone. For the investigation of trialanine they did two studies, one in explicit solvent and the other in implicit solvent. The collective variables they used for this study were the pair of dihedral angles (ϕ, ψ), also indicated in Figure 4.8. Their studies showed metadynamics was a useful tool for exploring the free energy landscapes of both the peptides investigated with the collective variables they chose. The authors were particularly concerned with the free energy error in the metadynamics method, and they showed that umbrella sampling could be successfully used to correct the results obtained from their metadynamics simulations. They compared their corrected free energy surfaces with those obtained from replica-exchange metadynamics and showed there was a very good agreement between the two[223].

Bussi *et al.* [221] used a combination of parallel tempering[213] and metadynamics to calculate the free-energy landscape of the folding β-hairpin in explicit water. They used two collective variables to explore the folded and unfolded states of their protein. The first CV they used was the radius of gyration for the heavy atoms of the backbone, as already given for the study of Babin *et al.* [223] in Equation

(4.6). The second CV they used was the number of hydrogen bonds along the backbone, which could help distinguish between a molten globule 'structure' and the folded structure as this information is related to the secondary structure of the protein. This number is evaluated by[221]:

$$N_\mathrm{H} = \sum_{i\in\mathrm{O}} \sum_{j\in\mathrm{H}} \frac{1 - \left(\dfrac{(\mathbf{r}_i - \mathbf{r}_j)}{d_0}\right)^6}{1 - \left(\dfrac{(\mathbf{r}_i - \mathbf{r}_j)}{d_0}\right)^{12}} \tag{4.7}$$

Equation (4.7) corresponds to the coordination number of the oxygens to the hydrogens. The coordination number is represented by a continuous function, as illustrated in Figure 4.9. It should be noted that using a coordination number to assess whether a hydrogen bond exists is a simplification. Generally there would also be the angle (O-H-O) used in conjunction with the distance to assess whether a hydrogen bond is present[118]. The value d_0 defines the 'cut-off' region of the function, where hydrogen bonds are either included or excluded. The only discontinuity is when $\mathbf{r}_i - \mathbf{r}_j = d_0$, which is an easily accounted for singularity.
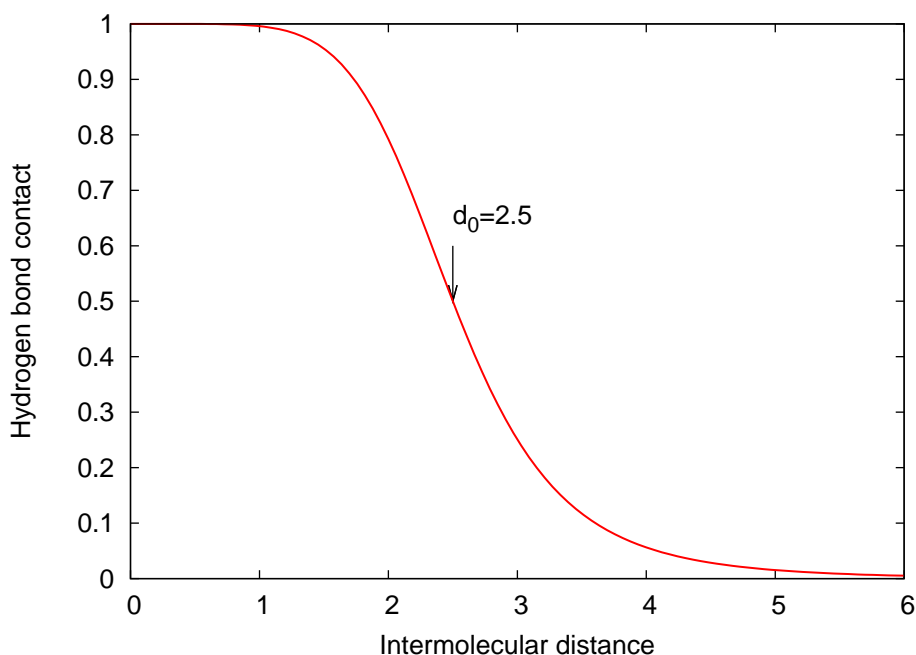

FIGURE 4.9: Example of the tapering function used for the calculation of hydrogen bonds. For the study done by Bussi *et al.* [221], they used a value of d_0=2.5 Å for the cut-off radius for a hydrogen-bond. Using Equation (4.7), the value d_0 should be at the midpoint of the tapered region, as shown on this plot.

The exponent values of 6 and 12 in Equation (4.7) define how steep the tapering region will be around d_0.

Bussi *et al.* [221] showed that combining parallel tempering with metadynamics was effective in further enhancing the exploration of phase space, as shown in Figure 4.10. The system jumps to the second energy basin much quicker than with the simulation performed with only metadynamics. The simulations performed by Bussi *et al.* [221] show that combining the two methods can enhance the exploration of phase space for biological molecules.
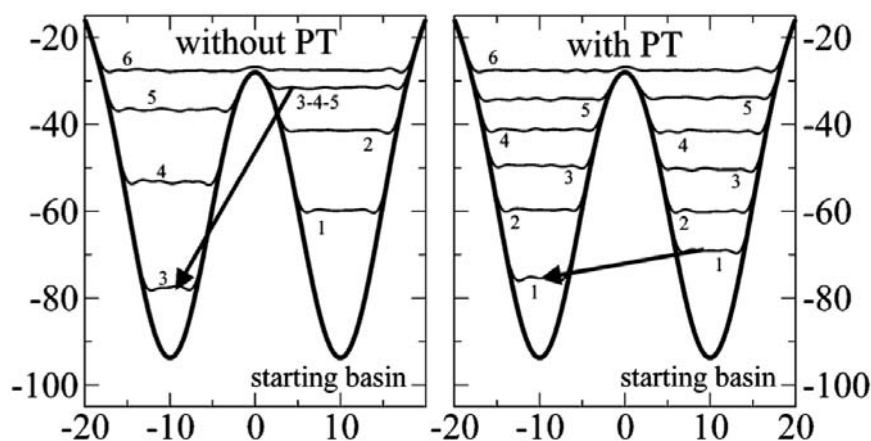
FIGURE 4.10: Comparison of the exploration of a two-basin energy profile using metadynamics (left) and using metadynamics combined with parallel tempering (right). The thin lines show subsequent images of the metadynamics filling. Image reproduced from Bussi *et al.* [221].

A study done by Piana and Laio [245] followed on from this work of Bussi *et al.* [221]. We have already introduced their method, bias-exchange metadynamics, where exchanges are allowed to occur between replica simulations where each replica evolves at the same temperature but along different CVs. The simulations they performed to test the efficacy of bias exchange MetaD were atomistic simulations in explicit solvent of the folding of a tryptophan cage 'miniprotein'[245]. Five CVs were used for this study, the number of Cγ contacts, number of Cα contacts, number of backbone H-bonds, α dihedral fraction, Φ_α, and the dihedral correlation, Φ_{corr}. In general the carbon atom attached to the carboxyl group of an amino acid is known as the alpha carbon, denoted Cα, the next carbon in the chain the beta carbon or Cβ and the third carbon in the chain the gamma carbon or Cγ and so on.

The number of contacts are calculated using a continuous tapering function of the same form used by Bussi *et al.* [221]:

$$N = \sum_{i=0}^{N-1} \sum_{j=i+1}^{N} \frac{1 - \left(\frac{(\mathbf{r}_i - \mathbf{r}_j)}{d_0}\right)^8}{1 - \left(\frac{(\mathbf{r}_i - \mathbf{r}_j)}{d_0}\right)^{10}} \tag{4.8}$$

where $\mathbf{r}_i$ and $\mathbf{r}_j$ are the coordinates for atoms i and j being considered in the calculation, and the values of d_0 were different depending on the CV being considered. The number of contacts refers to the number of a specified atom considered to be 'in contact', or within a specified cut-off distance from each other. In this case the specified cut-offs were $d_0 = 5.0, 6.5$ and 2.0 Å for Cγ contacts, Cα contacts and hydrogen bonds respectively.

The helicity of the backbone, Φ_α is given by;

$$\Phi_\alpha = \sum_{i=1}^{N} \frac{1}{2}[1 + cos(\varphi_i - \varphi_0)] \tag{4.9}$$

where φ_i is the backbone dihedral angle of residue i, and $\varphi_0 = -45°$.

The dihedral correlation is given by;

$$\Phi_{corr} = \sum_{i=2}^{N} \sqrt{[1 + cos^2(\varphi_i - \varphi_{i-1})]} \tag{4.10}$$

The variables chosen for the folding of the protein were based on whether they would describe a possible free energy barrier. For example, the number of hydrogen bonds CV describes the free energy barriers associated with the formation or disruption of hydrogen bonds. Similarly, the helicity and dihedral correlation variables, Φ_α and Φ_{corr}, describe the free energy barriers associated with conformational changes in the backbone of the structure. The number of Cγ contacts CV describes barriers associated with the formation or disruption of hydrophobic clusters, and the number of Cα contacts CV describes barriers associated with the transition between compact and extended structures. Piana and Laio [245] showed their method to be very effective in folding the protein within a few nanoseconds of simulation, and also exploring the free energy surface within a few tens of nanoseconds.

After the success of the bias exchange MetaD method, Piana [261] used the same method to study structural transitions in DNA. The process of interest was 'DNA melting', or helix-coil transitions, where the DNA double helix dissociates to form two single strands of DNA. They used the CVs introduced in their previous study with the Trp-cage folding to investigate these structural changes in three short sequences of DNA.

4.4   Collective variables for finite systems

Aspects of all of the above works have links to our own studies performed using metadynamics. The focus of the present work has been application of different collective variables in systems where they haven't been used before, predominantly focusing on the phase transitions seen in nanoscale materials. In these finite systems there are no periodic boundary conditions providing a continuous repeated cell throughout space. For this reason, the Parrinello-Rahman-like method of Martoňák *et al.* [225] mentioned in Section 4.3.1 isn't applicable as there are no cell parameters.

Here we will introduce two of the collective variables we have focused on. First we have the *inertia tensor*, and secondly a set of values known as *the Steinhardt parameters*.

4.4.1   Inertia tensor

In this study the first objective is to explore the use of the inertia tensor of a system as the collective variable for metadynamics to drive the system to new structures. This collective variable will yield trajectories in which the shape of the system (a nanoparticle) changes as the moment of inertia tensor of the system evolves. Before we discuss the results of these studies, we need to introduce what the inertia tensor is, and how this value is derived for a given system.

In the context of classical mechanics of rigid bodies, there is a physical property known as *inertia*. The inertia is a measure of a systems resistance to change in motion and is directly related to the mass of the object[262]. This property applies for linear motion, but if a body is free to rotate about any axes it also possesses

a resistance to rotational motion. This rotational resistance is described by the *moment of inertia*, and it is related not just to the mass, but how the mass of the system is distributed with respect to a given axis. The scalar moment of inertia for a point with mass m is given by;

$$I = mr^2 \qquad (4.11)$$

where r is the distance from the axis of rotation. The moment of inertia is an additive quantity, so if a system is comprised of N points of masses m_i and distances r_i to the rotation axis, the total moment of inertia is given by the sum of the moments of inertia for each point:

$$I = \sum_{i=1}^{N} m_i r_i^2 \qquad (4.12)$$

For an object, different axes of rotation will have different moments of inertia about those axes. Only if the system is symmetrical will different axes of rotation have the same moments of inertia. For this reason it is convenient to summarise all of the moments of inertia along each axis by a quantity known as the moment of inertia tensor[263], defined as;

$$\mathbf{I} = \begin{bmatrix} I_{11} & I_{12} & I_{13} \\ I_{21} & I_{22} & I_{23} \\ I_{31} & I_{32} & I_{33} \end{bmatrix} \qquad (4.13)$$

where each component of the moment of inertia tensor is given by;

$$I_{11} = I_{xx} = \sum_{i=1}^{N} m_i(y_i^2 + z_i^2) \tag{4.14}$$

$$I_{22} = I_{yy} = \sum_{i=1}^{N} m_i(x_i^2 + z_i^2) \tag{4.15}$$

$$I_{33} = I_{zz} = \sum_{i=1}^{N} m_i(x_i^2 + y_i^2) \tag{4.16}$$

$$I_{12} = I_{xy} = -\sum_{i=1}^{N} m_i x_i y_i \tag{4.17}$$

$$I_{13} = I_{xz} = -\sum_{i=1}^{N} m_i x_i z_i \tag{4.18}$$

$$I_{23} = I_{yz} = -\sum_{i=1}^{N} m_i y_i z_i \tag{4.19}$$

and $I_{12} = I_{21}$, $I_{13} = I_{31}$ and $I_{23} = I_{32}$, as $\mathbf{I}$ is a symmetric tensor. The distance of each particle i from the centre of mass of the system is given by r_i, with components x_i, y_i and z_i. In this study we have used the trace of the inertia tensor, which is given by the sum of the diagonal matrix elements of the moment of inertia tensor, $\mathbf{I}$:

$$Tr(\mathbf{I}) = I_{11} + I_{22} + I_{33} \tag{4.20}$$

The trace of inertia tensor is rotationally invariant. This means if the system is rotated, the value for that state will not change. This is an important property for any CV when studying an aperiodic system; it should give a unique value for a system state, regardless of its orientation. In this case, the trace of inertia tensor has a small value when particles are arranged in a compact, spherical distribution and its value increases as the system becomes elongated. When the system is comprised of particles all with the same mass the trace of the inertia tensor is related to the gyration radius, as defined in Equation (4.21):

$$R_g = \sqrt{\frac{1}{2} \cdot \frac{Tr(\mathbf{I})}{\sum_i^N m_i}} = \sqrt{\frac{\sum_i^N m_i \cdot |r_i - r_{CoM}|^2}{\sum_i^N m_i}} \tag{4.21}$$

where r_i is the position of particle i and r_{CoM} is the position of the centre of mass of the system. The centre of mass of the system, r_{CoM}, is an average of the

positions of the particles in system, r_i, weighted by the masses of the particles, m:

$$r_{CoM} = \frac{\sum\limits_{i=1}^{N} m_i r_i}{\sum\limits_{i=1}^{N} m_i} \tag{4.22}$$

The gyration radius has been used with other CVs for investigating protein conformations[221, 261]. However, the masses of the atoms are not included in the calculation of the gyration radius. Additionally, a CV like the gyration radius has not been used for studying phases of ionic systems as is done in this study.

Using the diagonal components of the inertia tensor explicitly, we find we can represent the trace of inertia in a simplified form, given by Equation (4.25):

$$Tr(\mathbf{I}) = I_{11} + I_{22} + I_{33} \tag{4.23}$$

$$= \sum_{i=1}^{N} m_i \cdot (y_i^2 + z_i^2) + \sum_{i=1}^{N} m \cdot (x_i^2 + z_i^2) + \sum_{i=1}^{N} m \cdot (x_i^2 + y_i^2) \tag{4.24}$$

$$= 2 \cdot \sum_i m_i \cdot |r_i - r_{CoM}|^2 \tag{4.25}$$

The derivative for this CV, s, that we will need for the implementation of this CV in MetaD is given by:

$$\frac{\partial s}{\partial r_i} = 2 \cdot \sum_i 2 \cdot m_i \cdot |r_i - r_{CoM}| \tag{4.26}$$

4.4.2 Steinhardt parameters

The second collective variable used in the present study is a parameter which estimates the level of crystallinity or orientational order in a system. This parameter was introduced in 1981 by Steinhardt *et al.* [264, 265]. The development of a measurement for local and extended bond orientational order was inspired by studies done decades earlier into the dense packing of hard-sphere systems[266]. The packing of identical spheres has been a problem for centuries. Johannes Kepler first proposed a solution to the problem in 1611; he speculated the most efficient packing of identical spheres would be to arrange the spheres in layers, with each sphere nesting in the hollow of three spheres beneath it[267, 268]. This problem
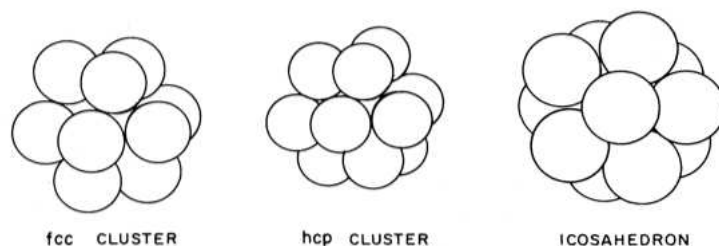
FIGURE 4.11: A depiction of different types of packing possible with a 13-atom particle cluster. The fcc and hcp clusters can be repeated in all three directions, while the icosahedron has 5-fold symmetry which makes repetition in this way impossible. Image reproduced from Steinhardt *et al.* [265].

has been named the *Kepler Conjecture*. Spheres which are packed in this way - close-packed - have an average density given by:

$$\frac{\pi}{3\sqrt{2}} \simeq 0.74048 \qquad (4.27)$$

In the context of close packed spheres the density is the proportion of the volume of the container (in the case of a crystal, this will be the unit cell) that is taken up by the spheres. Kepler's conjecture states that the density given by Equation (4.27) is the highest possible density for a crystalline lattice of identical spheres. This conjecture has remained unproven until recently. In 1992 Hales [269] outlined a solution to the Kepler conjecture, and recently attempted to solve this using a method of proof by exhaustion[268], where all possible individual solutions to the problem are solved. The results of Hales' proof by exhaustion have been accepted as "99% certain", and he is currently continuing these studies using computational methods to formalise his proof[270].

When we consider the packing density of hard spheres in a small cluster, there are "non-crystalline" ways in which we can pack the spheres. Three ways of packing a small system of 13 hard-spheres are shown in Figure 4.11. There are two "crystallographic" clusters which represent nuclei of fcc and hcp crystals, and a third structure which is an icosahedral structure with 5-fold symmetry which is not a crystallographic arrangement. The fcc and hcp structures have already been introduced in Chapter 1. The packing of clusters in this way was discussed decades ago by Frank [266] and Mackay [29]. In 1952 Frank [266] observed that an icosahedral arrangement of Lennard-Jones particles was lower in energy than fcc or hcp crystallographic clusters. He suggested that the supercooling of simple liquid

metals was made possible by the existence of these icosahedral clusters. Mackay [29] looked at non-crystallographic icosahedral structures, such as the 13-atom particle cluster, but also looked at larger clusters obeying the same rules. In these studies, Mackay [29] was particularly interested in the density of the icosahedral structure, as a comparison with crystallographic close-packed structures. He found that the highest density icosahedral structure was the smallest, with 13 atoms, with a density of approximately 0.726. Mackay [29] suggested that the trend of decreasing density with the increased number of atoms would lead the icosahedral structures to be unfavourable for larger clusters. An example of a larger icosahedral cluster of 147 particles is given in Figure 4.12.
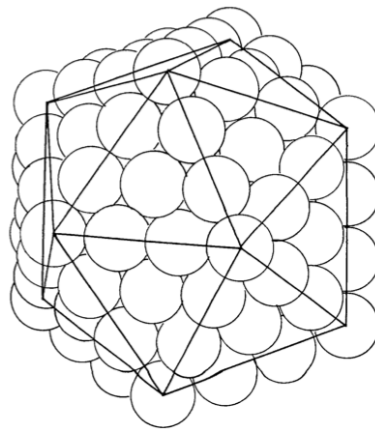
FIGURE 4.12: Example 'Mackay cluster' of 147 hard spheres with icosahedral packing. Image reproduced from Mackay [29].

Inspired by these studies, Steinhardt *et al.* [265] aimed to develop a set of parameters that could be used to measure the local and extended orientational symmetry of computer-generated models of liquids and gases. The idea of using spherical harmonics to determine bond-order orientations for cubic symmetry was introduced around the same time by Nelson and Toner [271], and Steinhardt *et al.* [264] continued this idea, using it first for the investigation of icosahedral order in a liquid.

Analysis using a Steinhardt parameter[264, 265], Q_l, begins by first defining which atoms are the neighbours of a particle. Each vector, $\mathbf{r}_{ij}$, that joins a particle, i, to its neighbour, j, is called a bond, and a set of numbers, $Y_l^m(\theta(\mathbf{r}_{ij}), \phi(\mathbf{r}_{ij}))$ are associated to each bond as depicted in Figure 4.13.

Here $Y_l^m(\theta(\mathbf{r}_{ij}), \phi(\mathbf{r}_{ij}))$ are spherical harmonics, while $\theta(\mathbf{r}_{ij})$ and $\phi(\mathbf{r}_{ij})$ are the polar and azimuthal angles of vector $\mathbf{r}_{ij}$ with respect to an arbitrary reference
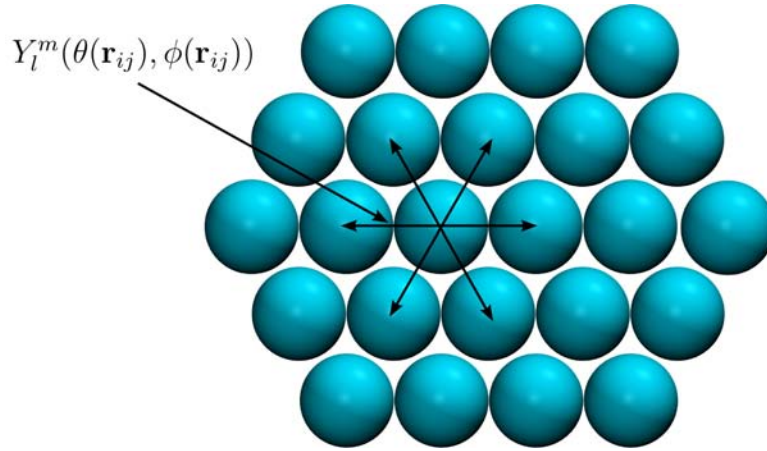
FIGURE 4.13: Spherical harmonics Y_l^m are calculated for each vector $\mathbf{r}_{ij}$, connecting atom i to its neighbouring atoms j to determine the orientational order around atom i.

frame. The average of these values gives an idea of the *local order* around a particle, given by Equation 4.28:

$$q_{lm}(i) = \frac{1}{N_b(i)} \sum_{j=1}^{N_b(i)} Y_l^m(\theta(\mathbf{r}_{ij}), \phi(\mathbf{r}_{ij})) \tag{4.28}$$

A rotationally invariant form of the local order parameter, q_l, is defined by Equation 4.29:

$$q_l(i) = \left(\frac{4\pi}{2l+1} \sum_{m=-l}^{l} |q_{lm}|^2 \right)^{1/2} \tag{4.29}$$

Averaging $q_{lm}(i)$ over all the N atoms in the system a *global* rotationally invariant order parameter, Q_l, can be obtained:

$$Q_l = \left(\frac{4\pi}{2l+1} \sum_{m=-l}^{l} |\bar{Q}_{lm}|^2 \right)^{1/2} \tag{4.30}$$

where:

$$\bar{Q}_{lm} = \frac{\sum\limits_{i=1}^{N} N_b(i) \, q_{lm}(i)}{\sum\limits_{i=1}^{N} N_b(i)} \tag{4.31}$$

The global order parameter is the Steinhardt parameter we have chosen to focus on, as it is a rotationally invariant quantity that indicates the overall crystalline order of the system. The Q_l quantity adopts unique values for a given crystal

structure. Non-zero averages occur for $l = 4, 6, 8$ in samples of cubic symmetry and $l = 6, 8$ for icosahedral systems. For this reason global Q_4 and Q_6 values are more commonly utilised for analysis; some of the Q_4 and Q_6 values for simple cluster geometries are summarised in Table 4.1. Due to the geometry of the Steinhardt parameters, they are a very effective tool for analysing the crystallinity of a system.

TABLE 4.1: Steinhardt parameters for some simple crystal structures[272].

Steinhardt parameters		
Geometry	Q_4	Q_6
Icosahedral	0	0.66332
fcc	0.19094	0.57452
hcp	0.09722	0.48476
bcc	0.03637	0.51069
sc	0.76376	0.35355
liquid	0	0

To implement the Steinhardt parameter, Q_l, as a collective variable in metadynamics we need to be able to compute the derivatives, to calculate the forces applied to the atoms in the system due to the CV The overall derivatives we require are given by Equation 4.32:

$$\frac{\partial Q_l}{\partial x_i} = \frac{1}{2}\left(\frac{4\pi}{2l+1}\sum_{m=-l}^{l}|\bar{Q}_{lm}|^2\right)^{-\frac{1}{2}} \cdot \left(\frac{\partial \sum_{m=-l}^{l}|\bar{Q}_{lm}|^2}{\partial x_i}\right) \tag{4.32}$$

Expanding the final term in the derivative down into its constituents we have:

$$\left(\frac{\partial \sum_{m=-l}^{l}|\bar{Q}_{lm}|^2}{\partial x_i}\right) = \sum_{m=-l}^{l}\frac{\partial|\bar{Q}_{lm}|^2}{\partial x_i} = \sum_{m=-l}^{l}\frac{\partial|\frac{1}{N_b}\sum Q_{lm}(\mathbf{r}_{ij})|^2}{\partial x_i} \tag{4.33}$$

Before we give a literature review of previous studies that have used Steinhardt parameters, we will cover some more of the mathematics behind this method.

4.4.2.1   Spherical Harmonics

In order to implement the Steinhardt parameters as CVs for metadynamics, we need to be able to first calculate the spherical harmonics and their derivatives. A spherical harmonic, $Y_l^m(\theta, \phi)$, is a complex function with two real arguments θ and ϕ[273]. The values of θ and ϕ run in the ranges: $0 \leq \theta \leq \pi$ and $0 \leq \phi \leq 2\pi$ and the two parameters l and m take values $l = 0, 1, 2, \ldots$ and $m = l, l - 1, l - 2, \ldots, -l + 2, -l$. As a result, any given l value has $(2l + 1)$ functions associated with it, corresponding to the possible m values.

Listed in this section are the derivatives of the $P_l^m(\cos \theta)$ function, which form part of the calculations we need for metadynamics. Note that where $\sin \theta$ is present in the spherical harmonics it has been substituted with the equivalent $(1 - \cos^2 \theta)^{\frac{1}{2}}$ for the ease of differentiating $P_l^m(\cos \theta)$ with respect to $\cos \theta$. First of all, the spherical harmonics are defined as:

$$Y_l^m(\theta, \phi) = \sqrt{\frac{(2l + 1)(l - m)!}{4\pi(l + m)!}} \cdot P_l^m(\cos \theta) \cdot e^{im\phi} \qquad (4.34)$$

There are three identities required for calculation of the associated Legendre polynomials[274] $P_l^m(x)$, where in the case of spherical harmonics $x = cos\theta$.

$$P_l^{-m}(x) = (-1)^m \frac{(l - m)!}{(l + m)!} P_l^m \qquad (4.35)$$

and

$$P_l^m(x) = (-1)^m (1 - x^2)^{m/2} \frac{d^m}{dx^m}(P_l(x)) \qquad (4.36)$$

and finally:

$$P_l(x) = \frac{1}{2^l l!} \frac{d^l}{dx^l}([x^2 - 1]^l) \qquad (4.37)$$

The real portion of the spherical harmonics can be visualised, and we have provided images of these for $l=4$ in Figure 4.14. What can quickly be ascertained from these images is the *orientational* nature of these mathematical forms. It is this quality that provides the Steinhardt parameters a means of indicating the orientational order around a given point.
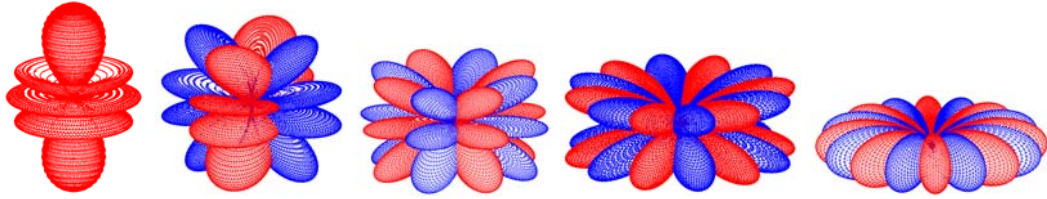
FIGURE 4.14: Visualisation of the real component of the spherical harmonics with $l=4$. From left to right we have $m=0$, ± 1, ± 2, ± 3, ± 4. The positive spherical harmonics are shown in red, and the negative in blue.

The spherical harmonics satisfy identity (4.38) which enables us to calculate the spherical harmonics with negative m values from the positive m values. For this reason, only the equations for $m = 0... + l$ are given.

$$Y_l^{-m}(\theta, \phi) = (-1)^{-m} \cdot Y_l^m(\theta, \phi) \tag{4.38}$$

4.4.2.2 Equations for calculating Q_6

The spherical harmonics for $l = 6$ are given by the following equations:

$$Y_6^0(\theta, \phi) = \frac{1}{32}\sqrt{\frac{13}{\pi}} \cdot (231\cos^6\theta - 315\cos^4\theta + 105\cos^2\theta - 5) \tag{4.39}$$

$$Y_6^1(\theta, \phi) = -\frac{1}{16}\sqrt{\frac{273}{2\pi}} \cdot e^{i\phi} \cdot \sin\theta \cdot (33\cos^5\theta - 30\cos^3\theta + 5\cos\theta) \tag{4.40}$$

$$Y_6^2(\theta, \phi) = \frac{1}{64}\sqrt{\frac{1365}{\pi}} \cdot e^{2i\phi} \cdot \sin^2\theta \cdot (33\cos^4\theta - 18\cos^2\theta + 1) \tag{4.41}$$

$$Y_6^3(\theta, \phi) = -\frac{1}{32}\sqrt{\frac{1365}{\pi}} \cdot e^{3i\phi} \cdot \sin^3\theta \cdot (11\cos^3\theta - 3\cos\theta) \tag{4.42}$$

$$Y_6^4(\theta, \phi) = \frac{3}{32}\sqrt{\frac{91}{2\pi}} \cdot e^{4i\phi} \cdot \sin^4\theta \cdot (11\cos^2\theta - 1) \tag{4.43}$$

$$Y_6^5(\theta, \phi) = -\frac{3}{32}\sqrt{\frac{1001}{\pi}} \cdot e^{5i\phi} \cdot \sin^5\theta \cos\theta \tag{4.44}$$

$$Y_6^6(\theta, \phi) = \frac{1}{64}\sqrt{\frac{3003}{\pi}} \cdot e^{6i\phi} \cdot \sin^6\theta \tag{4.45}$$

From these equations of the spherical harmonics for $l = 6$ we have $P_6^m(\cos\theta)$, from which we can calculate $\dfrac{dP_6^m(\cos\theta)}{d\cos\theta}$:

$$P_6^0(\cos\theta) = (231\cos^6\theta - 315\cos^4\theta + 105\cos^2\theta - 5) \tag{4.46}$$

$$\frac{dP_6^0(\cos\theta)}{d\cos\theta} = 1386\cos^5\theta - 1260\cos^3\theta + 210\cos\theta \tag{4.47}$$

$$P_6^1(\cos\theta) = (1 - \cos^2\theta)^{\frac{1}{2}} \cdot (33\cos^5\theta - 30\cos^3\theta + 5\cos\theta) \tag{4.48}$$

$$\frac{dP_6^1(\cos\theta)}{d\cos\theta} = -(1 - \cos^2\theta)^{-\frac{1}{2}} \cdot (33\cos^6\theta - 30\cos^4\theta + 5\cos^2\theta)$$
$$+ (1 - \cos^2\theta)^{\frac{1}{2}} \cdot (165\cos^4\theta - 90\cos^2\theta + 5) \tag{4.49}$$

$$P_6^2(\cos\theta) = (1 - \cos^2\theta) \cdot (33cos^4\theta - 18\cos^2\theta + 1) \tag{4.50}$$

$$\frac{dP_6^2(\cos\theta)}{d\cos\theta} = -198 \cdot \cos^5\theta + 204 \cdot \cos^3\theta - 38 \cdot \cos\theta \tag{4.51}$$

$$P_6^3(\cos\theta) = (1 - \cos^2\theta)^{3/2} \cdot (11\cos^3\theta - 3\cos\theta) \tag{4.52}$$

$$\frac{dP_6^3(\cos\theta)}{d\cos\theta} = -3 \cdot (1 - \cos^2\theta)^{\frac{1}{2}} \cdot (11\cos^3\theta - 3\cos\theta) \cdot \cos\theta$$
$$+ (33\cos^2\theta - 3) \cdot (1 - \cos^2\theta)^{\frac{3}{2}} \tag{4.53}$$

$$P_6^4(\cos\theta) = (1 - \cos^2\theta)^2 \cdot (11\cos^2\theta - 1) \tag{4.54}$$

$$\frac{dP_6^4(\cos\theta)}{d\cos\theta} = -4 \cdot (1 - \cos^2\theta) \cdot (11\cos^2\theta - 1) \cdot \cos\theta$$
$$+ 22\cos\theta \cdot (1 - \cos^2\theta)^2 \tag{4.55}$$

$$P_6^5(\cos\theta) = (1 - \cos^2\theta)^{\frac{5}{2}} \cdot \cos\theta \tag{4.56}$$

$$\frac{dP_6^5(\cos\theta)}{d\cos\theta} = 5 \cdot (1 - \cos^2\theta)^{\frac{3}{2}} \cdot \cos\theta + (1 - \cos^2\theta)^{\frac{5}{2}} \tag{4.57}$$

$$P_6^6(\cos\theta) = (1 - \cos^2\theta)^3 \tag{4.58}$$

$$\frac{dP_6^6(\cos\theta)}{d\cos\theta} = -6 \cdot (1 - \cos^2\theta)^2 \cdot \cos\theta \tag{4.59}$$

4.4.2.3 Equations for calculating Q_4

The spherical harmonics for $l = 4$ are given by the following equations:

$$Y_4^0(\theta, \phi) = \frac{3}{16}\sqrt{\frac{1}{\pi}} \cdot (35\cos^4\theta - 30\cos^2\theta + 3) \tag{4.60}$$

$$Y_4^1(\theta, \phi) = -\frac{3}{8}\sqrt{\frac{5}{\pi}} \cdot e^{i\phi} \cdot \sin\theta \cdot (7\cos^3\theta - 3\cos\theta) \tag{4.61}$$

$$Y_4^2(\theta, \phi) = \frac{3}{8}\sqrt{\frac{5}{2\pi}} \cdot e^{2i\phi} \cdot \sin^2\theta \cdot (7\cos^2\theta - 1) \tag{4.62}$$

$$Y_4^3(\theta, \phi) = -\frac{3}{8}\sqrt{\frac{35}{\pi}} \cdot e^{3i\phi} \cdot \sin^3\theta \cdot \cos\theta \tag{4.63}$$

$$Y_4^4(\theta, \phi) = \frac{3}{16}\sqrt{\frac{35}{2\pi}} e^{4i\phi} \cdot \sin^4\theta \tag{4.64}$$

Listed below are the derivatives of the $P_l^m(\cos\theta)$ function. Again, like those in the previous section, $\sin\theta$ has been substituted with the equivalent $(1 - \cos^2\theta)^{\frac{1}{2}}$ for the ease of differentiating w.r.t $\cos\theta$.

$P_l^m(\cos\theta)$, and $\dfrac{dP_l^m(\cos\theta)}{d\cos\theta}$ for $l = 4$ are given by the following equations:

$$P_4^0(\cos\theta) = 35\cos^4\theta - 30\cos^2\theta + 3 \tag{4.65}$$

$$\frac{dP_4^0(\cos\theta)}{d\cos\theta} = 140\cos^3\theta - 60\cos\theta \tag{4.66}$$

$$P_4^1(\cos\theta) = (1 - \cos^2\theta)^{\frac{1}{2}}(7\cos^3\theta - 3\cos\theta) \tag{4.67}$$

$$\begin{aligned}\frac{dP_4^1(\cos\theta)}{d\cos\theta} = &-(1 - \cos^2\theta)^{-\frac{1}{2}} \cdot \cos\theta \cdot (7\cos^3\theta - 3\cos\theta) \\ &+ (1 - \cos^2\theta)^{\frac{1}{2}} \cdot (21\cos^2\theta - 3)\end{aligned} \tag{4.68}$$

$$P_4^2(\cos\theta) = (1 - \cos^2\theta) \cdot (7\cos^2\theta - 1) \tag{4.69}$$

$$\frac{dP_4^2(\cos\theta)}{d\cos\theta} = -28\cos^3\theta + 16\cos\theta \tag{4.70}$$

$$P_4^3(\cos\theta) = (1 - \cos^2\theta)^{3/2} \cdot \cos\theta \tag{4.71}$$

$$\frac{dP_4^3(\cos\theta)}{d\cos\theta} = -3(1 - \cos^2\theta)^{\frac{1}{2}} \cdot \cos^2\theta + (1 - \cos^2\theta)^{\frac{3}{2}} \tag{4.72}$$

$$P_4^4(\cos\theta) = (1 - \cos^2\theta)^2 \tag{4.73}$$

$$\frac{dP_4^4(\cos\theta)}{d\cos\theta} = -4\cos\theta + 4\cos^3\theta \tag{4.74}$$

4.4.2.4 Previous studies using the Steinhardt parameter

Mountain and Brown [275] were one of the first groups to attempt to use the Steinhardt parameters as a means of analysing an MD trajectory. Their study focused on the homogeneous nucleation of a Lennard-Jones liquid, and they used the Q_6 values to track nucleation events in systems modelled with different potential parameters. The calculated Q_6 values successfully indicated when the system moved from being disordered (a Q_6 value below 0.2) to increasingly crystalline (a Q_6 value of approximately 0.4-0.6).

Nosé and Yonezawa [276] followed on from the work of Mountain and Brown [275] and used the Steinhardt parameters to analyse the level of crystallinity in a Lennard-Jones system simulated at different temperatures using MD. They took an 864 atom Lennard-Jones particle starting in the fcc structure, known to be stable below 84 K. They performed simulations starting at 40 K and increased the temperature incrementally by 10 K to 70 K, and then with 5 K increments to 105 K. Simulations were also performed for the reverse scenario, starting from a liquid structure and decreasing the temperature incrementally. The Steinhardt parameters were used as a post-analysis of the simulation trajectories. Nosé and Yonezawa [276] focussed primarily on the Q_6 Steinhardt parameter, where they use a Q_6 value of approximately 0.4 as a general indicator of crystallinity. They found that the softer the interaction between particles, the easier for nucleation or growth to occur.

van Duijneveldt and Frenkel [272] used the umbrella sampling method of Torrie and Valleau [211] to perform biased Monte Carlo simulations of nucleation events, allowing them to estimate the free energy barrier for nucleation. As with the studies mentioned above, van Duijneveldt and Frenkel [272] also chose to use the Q_6 Steinhardt parameter as a representation of the crystalline order in their system. However, in this case the Q_6 parameter was used as the order parameter for biasing the system, and thus for estimating the free energy difference between phases; in previous studies the Q_6 values were calculated solely to analyse the evolution of crystallinity along a trajectory. van Duijneveldt and Frenkel [272] noted that the

Q_6 values are all of the same order of magnitude for the crystalline structures of interest; this makes it a less effective means of distinguishing between crystal structures, but useful as a generic measure of crystallinity in a system. The Q_4 value is then the more useful parameter to distinguish between different crystalline structures. Lynden-Bell *et al.* [277] continued in the same vein as van Duijneveldt and Frenkel [272], but starting using the Steinhardt parameters to study the free energy of nucleation events in ductile metals.

ten Wolde *et al.* [278] used the same regime of van Duijneveldt and Frenkel [272]. However, they were particularly interested in the structure of the precritical, critical and postcritical nuclei - not only the nucleation rate and barrier. They continued to use the Q_6 parameter as the order parameter for the umbrella sampling bias, while they also used the Q_4 parameter and combinations of local order parameters as means to analyse their trajectories. Their simulations showed precritical nuclei were predominantly bcc phase. However, as these grew their internal order, they became increasingly dominated by the fcc phase while leaving a bcc shell.

Radhakrishnan and Trout [279] also implemented the same scheme of umbrella sampling combined with Monte Carlo used by van Duijneveldt and Frenkel [272]. Radhakrishnan and Trout [279] used the Q_4 Steinhardt parameter and tetrahedral order parameter, ζ, as order parameters to bias the system towards nucleation events to investigate the nucleation of ice in liquid water. Complementing these studies were metadynamics simulations performed by Donadio *et al.* [219]. These simulations used the Q_6 Steinhardt parameter and the number of five and six-membered rings as collective variables to investigate the melting of ice.

Studies following the same theme of Radhakrishnan and Trout [279] were performed by Quigley and Rodger [280], where they used MetaD simulations using the Steinhardt parameter to study the nucleation and growth of ice. Quigley and Rodger [281] have also used the Q_4 Steinhardt parameters for exploring the free energy of nanoparticles of calcium carbonate as a function of crystallinity. Very recently Quigley and Rodger [282] have published an overview of using MetaD with multiple collective variables to simulate crystallisation events. The review touches on the works previously mentioned, where the Steinhardt parameter has been used in umbrella sampling Monte Carlo simulations to bias the exploration with respect to different crystalline states.

Our own studies using the Steinhardt parameters combined with MetaD will be discussed later, in Chapter 6. First, we will present our results for the studies using the inertia tensor as a collective variable in the following chapter.

Chapter 5

Exploring the structures of zinc sulfide clusters using the trace of the inertia tensor as a collective variable

5.1 Introduction

Zinc sulfide is a member of the chalcogenide family of materials and exists as two main polymorphs, sphalerite and wurtzite. Recapping from our introductory chapter, sphalerite has a cubic close-packed form with A-B-C-A-B-C stacking sequence, and wurtzite has hexagonal close packing with A-B-A-B stacking. In bulk, sphalerite is the preferred polymorph by approximately 2 kJ mol^{-1}[80]. However, as the size regime is reduced this preference is found to reverse[98]. This has been explained based on the of the surface energy of the two polymorphs; sphalerite is estimated to have a surface energy of 0.86 Jm^{-2}, while for wurtzite the estimated value is lower, 0.57 Jm^{-2}[98]. Experiments have shown that nanoparticles of ZnS (approximately 3.4 nm diameter) suffer from internal strain, most likely due to the surfaces attempting to relax, the effects of which are exaggerated at this scale where there is a high surface to volume ratio[103]. At even smaller sizes, such as clusters of hundreds of atoms in size or less, ZnS is expected to take on shapes that do not resemble the bulk at all, but instead form open or disordered clusters comprised of 4- and 6-membered rings[67, 111, 115, 283].

As introduced in Chapter 1, other groups have investigated the shapes of small clusters of ZnS using computational techniques. For example, genetic algorithms have been used to evolve clusters of ZnS to different structures[115, 116], while others have performed simulated annealing to locate low energy structures[111–113]. These previous studies have determined many low energy configurations for small clusters, most of which favour 3-coordinated atoms over the 4-coordinated atoms found in bulk zinc sulfide. This 3-coordinated environment results in open cage-like or 'bubble' clusters as depicted in Chapter 1. The objective of this work is to examine whether the metadynamics method will offer an efficient means of exploring configurations of zinc sulfide nanoparticles, without an *a priori* bias towards any particular shape. The lack of *a priori* bias is not a feature unique to metadynamics, it is a common feature of other global optimisation techniques previously discussed such as genetic (or evolutionary) algorithms[114, 284] or basin hoppingWales and Scheraga [285]. However, it will be the first time the metadynamics method has been applied to the zinc sulfide system. The results of previous studies will be a useful comparison to test the efficacy of our approach, as many different configurations have already been identified.

As explained in the previous chapter, we have chosen to use two collective variables that are suitable for exploring the configurations of finite systems such as nanoparticles. The first of these is the trace of the inertia tensor, and is the focus of this chapter. At the time of introducing this collective variable as part of our studies, the gyration radius, a closely related variable, was being used by different groups to assist in the study of protein folding[221]. However, the masses of the atoms are usually omitted in the calculation of the gyration radius, while they are retained in the calculation of the trace of the inertia tensor. Additionally, a CV like the gyration radius has not been used for studying transformations in nanoparticles of ionic systems as is done in this study. One of our aims is to examine whether the trace of the inertia tensor can be used to explore the phase space of small particles of zinc sulfide.

In the context of classical mechanics of rigid bodies, there is a physical property known as *inertia*. The inertia is a measure of a system's resistance to change in motion and is directly related to the mass of the object[262]. This property applies for linear motion, but if a body is free to rotate around an axis it also possesses a resistance to rotational motion. This rotational resistance is described by the *moment of inertia*, and it is related not just to the mass, but how the mass of the

system is distributed with respect to that axis. The scalar moment of inertia for
a point with mass m is given by;

$$I = mr^2 \tag{5.1}$$

where r is the distance from the axis of rotation. An illustrative example of the
moment of inertia at work is that of an ice-skater. When the ice-skater crouches
down on one leg and extends the other outwards a sizeable change in the rotational
speed is evident, which is related to the sudden change in the mass distribution
around the rotation axis - and therefore of the moment of inertia of the ice-skater.
The moment of inertia is an additive quality, so if a system can be decomposed
into N subsystems, each of mass m_i and distance r_i from the axis of rotation, the
total moment of inertia is given by the sum of the moments of inertia for each
point:

$$I = \sum_{i=1}^{N} m_i r_i^2. \tag{5.2}$$

If the axis of rotation is not specified, the moment of inertia can be generalised in
the form of a symmetric (3×3) tensor:

$$\mathbf{I} = \begin{bmatrix} I_{11} & I_{12} & I_{13} \\ I_{21} & I_{22} & I_{23} \\ I_{31} & I_{32} & I_{33} \end{bmatrix} \tag{5.3}$$

This definition allows for obtaining the inertia tensor around any axis by
matrix-vector multiplication. The calculation of the components of the inertia
tensor have already been provided in the previous chapter, so here we recall only
the concepts that are important for the present discussion. Firstly, since the
nanoparticles are unconstrained and free to rotate around every axis, a quantity
that depends on the definition of a specific frame of reference (i.e. defining
a specific rotation axis) is clearly inappropriate. We have to consider only
combinations of the elements of the inertia tensor that are rotationally invariant.
The simplest choice we can make is to look at the trace of the inertia tensor;

$$Tr(\mathbf{I}) = I_{11} + I_{22} + I_{33} \tag{5.4}$$

which does not depend on the nanoparticle's orientation in space. For an atomistic system, this quantity is closely related to the radius of gyration:

$$R_g = \sqrt{\frac{1}{2} \cdot \frac{Tr(\mathbf{I})}{\sum_i^N m_i}} = \sqrt{\frac{\sum_i^N m_i \cdot |r_i - r_{CoM}|^2}{\sum_i^N m_i}} \qquad (5.5)$$

The trace of the inertia tensor (and the radius of gyration) gives an indication of the distribution of mass in the system, and as such it has lower values when particles are arranged in a compact spherical distribution and its value increases as the system becomes elongated. The trace of the inertia tensor is an interesting collective variable to use to explore the configurational space of nanoparticles, as there are well known examples of the size-dependence of phases in nanoparticles. A recent example is the work of Johansson *et al.* [286], where InAs nanowires show diameter-dependent phase transitions from wurtzite to zinc-blende structures. Using the trace of the inertia tensor as a collective variable with metadynamics, we should be able to explore the free energy landscape of ZnS nanoparticles and to calculate the relative stability of the various structures.

5.2   Methods

To use the metadynamics method we need a method of calculating and representing the potential energy surface. We have already provided an introduction to two approaches to evaluating the energy of a system in Chapter 2, using quantum mechanics or, alternatively, using force field methods. As we wish to use the metadynamics method to investigate a (hopefully) large portion of phase space of ZnS clusters we are choosing the more efficient, though potentially less accurate, approach. This requires the choice of a suitable force field to model the Zn-S interactions. The force fields we have employed to model ZnS were obtained from the literature[95] and have been summarised in Table 5.1. The form of the Buckingham and torsional potential forms have already been introduced in Chapter 2. The three-body potential in the force field of Wright and Gale [95] is of a harmonic form which exponentially decays, to avoid discontinuity as atoms move between coordination shells. The form is given by;

$$U = \frac{1}{2}k_b(\theta_{ijk} - \theta_0)^2 \exp\left(-\frac{r_{ij}}{\rho_1}\right) \exp\left(-\frac{r_{ik}}{\rho_2}\right) \qquad (5.6)$$

Species	Charge (e)			
Zn core	+2.00			
S core	+1.03061			
S shell	-3.03061			

Buckingham potential	A (eV)	ρ(Å)	C(eV Å^6)	Cut-off (Å)
Zn core - S shell	672.288	0.39089	0.0	12.00
S shell - S shell	1200.0	0.14900	0.0	12.00

Three-body potential	k(eV/rad^2)	θ(°)	ρ_1/ρ_2(Å)	Cut-off (Å)
S shell - Zn core - S shell	9.42834x10^6	109.47	0.3	6.0

TABLE 5.1: Interatomic potentials used for the MetaD simulations of ZnS using the trace of inertia tensor as a CV. These potentials were obtained from Wright and Gale [95]

where k_b is the force constant, θ_0 the equilibrium three-body angle between the bonds *i-j* and *j-k*, while ρ_1 and ρ_2 influence the coupling between angle- and bond-stretching terms[95]. In the context of ZnS all angles relevant to this three-body potential will have the same end-member atom types, so for this material ρ_1 and ρ_2 are constrained to possess the same value.

For bulk ZnS the force field of Wright and Gale [95] gives the sphalerite structure as the most favourable, as is also observed in experiments. We note, however, that the correct description of the subtle energy difference between these two polymorphs ($\sim$2 kJ/mol[80]) is difficult to capture in both force field and quantum mechanical studies. The chosen force field of Wright and Gale [95] achieves this correct order of stability by employing a four-body torsional term between alternating atoms, Zn-S-Zn-S. However, in the case of our nanoparticles we have opted to neglect this torsional term. The potential parameters obtained for modelling ZnS were not originally designed for molecular dynamics studies, rather they were designed for use in lattice dynamics. The energy contribution supplied by the torsional term does not behave cleanly and continuously as the connectivity between atoms is altered. As a result this torsional energy term is not valid when applied to molecular dynamics simulations, where the connectivity between Zn and S atoms is dynamic.

In the second part of this study, we explored the behaviour of ZnS nanoparticles in water. Here we used the same parameters for the Zn-S interactions given in

Table 5.1 while the interactions of ZnS with water were taken from the work of Hamad *et al.* [110]. These potentials are given in Table 5.2.

Buckingham potential	A (eV)	ρ (Å)	C(eV Å^6)	Cut-off (Å)
S - O$_w$	123571	0.25	0.0	12.00
Zn - O$_w$	125	0.4	0.1	12.00
Lennard-Jones	A (eV Å^{12})	C (eV Å^6)	Cut-off (Å)	
S - H$_w$	3.5	0	12.00	

TABLE 5.2: The ZnS-water interactions used for our simulations of ZnS nanoparticles in water. These potentials were obtained from the work of Hamad *et al.* [110].

Species	Charge (e)	
O$_w$	-0.820	
H$_w$	+0.410	
Species	Bond length (Å)	k$_{bond}$ (eV/Å^2)
O$_w$ - H$_w$	0.96	23.44
Species	θ (°)	k$_{angle}$ (eV/rad^2)
H$_w$-O$_w$-H$_w$	104.5	2.17
Lennard-Jones potential	A (eV Å^{12})	C (eV Å^6)	Cut-off (Å)
O$_w$ - O$_w$	27291.75	27.12	12.00
H$_w$ - H$_w$	4×10^{-13}	0.0	12.00

TABLE 5.3: The potential parameters of the CVFF water model of Lau *et al.* [287].

For consistency, we have employed the same water model as that used in the studies performed by Hamad *et al.* [113]. This is a flexible water model known as the consistent valence force field (CVFF) water model and its parameters are reported in Table 5.3

The electrostatic and van der Waals interactions were calculated with a direct sum for the nanoparticles in vacuum while for the simulations in water the Ewald summation scheme was used for the electrostatic interactions.

Our starting configurations were generated by cleaving small clusters from bulk wurtzite using GDIS[288]. All the simulations were performed using a timestep of 1 fs and run for as much as 120 ns simulation time. Small clusters of (ZnS)$_n$ were examined, where $n = 3 - 24$. These cluster sizes were chosen since they

encompass those used in previous studies[111–113, 116] where compact, well ordered, low energy structures were found for similar sized clusters of zinc sulfide using different methods. These starting structures were optimised before being brought to equilibrium, for 10 ps, at 300 K using a Berendsen thermostat.

Metadynamics simulations were then performed in duplicate with different Gaussian parameters; both simulations had a Gaussian width of $0.1 \cdot \text{mass}_{cluster}$ amu $\overset{\circ}{\text{A}}^2$, while one ran with a Gaussian height of 0.2 eV and the other with 0.1 eV, where $\text{mass}_{cluster}$ is the total mass of the cluster in atomic mass units (amu). Structures were then taken at regular intervals from each of the simulation trajectories and optimised using Newton-Raphson methods, with the program GULP[160], to determine if the located structure was stable or not. Only structures with real phonon frequencies were considered stable and included in our tabulations of cluster configurations.

5.2.1   First principles calculations

Optimisation of the low-energy structures found during the above simulations was also performed using first principles methods, with the program SIESTA[138], to evaluate whether the same order of stabilities is seen in both the force field and first principles calculations. This was particularly of interest for the structures found to be most stable for each size to see if there are any discrepancies between the two methods, and to compare these to previous theoretical studies. Additionally, we could compare the relative stabilities of structures using both these methods to the experimental data, such as the work of Kasuya *et al.* [67], which found clusters such as $(\text{ZnS})_{13}$ to be most stable through time-of-flight mass spectrometry.

Throughout the present work the Generalized Gradient Approximation of Perdew *et al.* [289], known as the PBEsol exchange and correlation functional, has been used. This is an improvement on their well known GGA functional PBE[131], where the functional has been optimised for use in solid-state systems. PBEsol has recently been used in a comprehensive study of the two polymorphs of FeS_2, pyrite and marcasite[290]. This study showed that some GGA functionals, such as PBEsol, produce a contraction of the lattice parameters, resulting in the correct prediction of the order of stability of the two polymorphs. As we are interested in investigating the stabilities of the clusters relative to the solid-state, and for a material where there are two polymorphs separated by a small energy difference, it

was important to use a functional which has greater potential to accurately model the relative stabilities of polymorphs.

The first principles SIESTA[138] methodology expands the Kohn-Sham wave functions using a linear combination of atomic orbitals (LCAO). The nuclei and core electrons of atoms are represented through the use of norm-conserving pseudopotentials of the form developed by Troullier-Martins[139], while the valence electrons are treated explicitly. The valence electronic configurations for generating the pseudopotentials were Zn ($3s^23p^63d^{10}$) and S ($3s^23p^4$). The basis sets for sulfur required triple-ζ quality $3s$ and $3p$ orbitals and double-ζ quality $3d$ orbitals, while for zinc double-ζ quality was necessary for the $4s$, $4p$, and $3d$, and single-ζ for the $3s$ and $3p$ semi-core orbitals. A full description of the basis sets used in this study is given in Appendix B. The shape of the basis set was improved following the method introduced by Junquera *et al.* [291], where the pseudoatomic orbitals (PAO) of the isolated atoms are enclosed within a soft-confined spherical potential, removing any discontinuity of the basis function first derivative at the cut-off radius. A split-norm value of 0.15 was used along with 0.02 Ry for the energy shift of radial confinement. An auxiliary real-space Cartesian grid with a cut-off of 400 Ry was used for calculating quantities based on electron density.

5.2.2   Path variables

As will become clear in the following sections, while the trace of the inertia tensor was successful in exploring phase space it turned out to be unsuitable to determine the free energy differences between the various structures found. Hence, we have investigated other collective variables to attempt calculations of free energy differences. Although nanoparticles are small and relatively simple systems, there is no unique CV which is able to differentiate between all the possible shapes and connectivities that are accessible. However, since we have generated long metadynamics trajectories that explored wide portions of the phase space, we can easily extract from them short segments that display the transition between almost any given pair of structures. These short fragments are obviously not enough to extract the free energy profile of the transitions, but they can be used to define a set of CVs that describe the progression of the system along the transition path. In the path variable approach, the Cartesian coordinates of the subset of atoms that are thought to be the most important for the transition are arranged into

a multidimensional array, $\mathbf{R}(t)$, and a sequence of snapshots of their positions is taken in order to form a path that connects the starting point, $\mathbf{R}_A = \mathbf{R}(0)$, to the final one, $\mathbf{R}_B = \mathbf{R}(1)$.

The above is the approach of Branduardi *et al.* [292], who introduced two CVs that utilise the array $\mathbf{R}(t)$. The first CV corresponds to the "position" along the path;

$$s(\mathbf{R}) = \lim_{\lambda \to \infty} \frac{\int_0^1 t e^{-\lambda(\mathbf{R}-\mathbf{R}(t))^2} dt}{\int_0^1 e^{-\lambda(\mathbf{R}-\mathbf{R}(t))^2} dt} \qquad (5.7)$$

while the second CV corresponds to the "distance" orthogonal to the path;

$$z(\mathbf{R}) = \lim_{\lambda \to \infty} -\frac{1}{\lambda} \int_0^1 e^{-\lambda(\mathbf{R}-\mathbf{R}(t))^2} dt \qquad (5.8)$$

s and z are generally referred to as the "path collective variables". In our studies the frequency at which the trajectory had been saved during the metadynamics simulations was not enough to generate a path with sufficient resolution of the transition state region. Therefore, in order to obtain a sufficient number of equally spaced points along the path, we performed an interpolation between the available frames using Cutmull-Rom Cartesian splines[293]. The exact definition of the frames composing the path is not critical to the success of the free energy calculations, provided that the true transition path lies close to one used in the MetaD simulation.

To calculate the free energy difference between two small nanoparticles in vacuum the above method is not necessary, as the same result can be achieved quickly using lattice dynamics, as implemented in GULP[160]. It is possible to calculate the Helmholtz free energy within lattice dynamics using the vibrational partition function. The quasi-harmonic approximation is employed, which assumes that the atoms are vibrating purely harmonically. Under this assumption, the vibrational frequencies can be calculated from the (assumed) harmonic vibrations, and a single point calculation of the free energy is performed on each optimised cluster[160]. Kantorovich [294] introduced analytical derivatives of the free energy, which have also been implemented in a program known as SHELL[295] and in GULP[160]. The variety of methods available and their implementation is beyond the scope of this work, however they are outlined in more detail by Gale and Rohl [160].

The comparison of the values obtained from these two methods (MetaD with the path variables vs. free energy calculation in lattice dynamics) will be an

important proof of concept. Free energy calculations can be performed in different conditions using the path method, which may not be feasible within lattice dynamics. For example, when the presence of solvent plays an important role the path method can be used. However, the free energy calculations performed within the quasi-harmonic approximation for ordered structures are valid only in cases where there is a single dominant local minimum - such as finite nanoparticles or bulk structures.

5.3   Results and Discussion

We initially performed metadynamics simulations using the trace of the inertia tensor as the CV on $(ZnS)_n$ nanoparticles of different sizes ($n = 3-24$) in vacuum and subsequently used the path CV to extract the free energy differences. The complete set of structures and their energies are reported in Appendix A while here we report only the lowest energy structure for each size and a complete description of the $(ZnS)_{12}$ nanoparticle, and associated structures, as a representative example.

5.3.1   Structures

The minimum energy structures obtained for each of the cluster sizes from our MetaD simulations are summarised in Table 5.4. The lowest energy structure obtained from the MetaD simulations of the cluster sizes we have analysed is that of $(ZnS)_{21}$. The energies shown in Table 5.4 are given first as potential energy per formula unit, and secondly as the relative potential energy per formula unit with respect to this lowest energy cluster. A point of interest is that the minimum energy nanoparticle for almost every size has a cage-like structure, and they share the same 4- and 6-membered motifs (with alternating Zn and S atoms). Creating a network of 4- and 6-membered rings appears to be a way reduce the energy of the cluster when in this size range.

First principles calculations of the minimum energy clusters were also performed using SIESTA, and a remarkably similar trend in relative potential energy vs. cluster size was found. The potential energy per formula unit was determined with respect to sphalerite, for the minimum energy structures obtained from both methods, and plotted against the cluster size, as shown in Figure 5.1. This figure
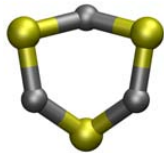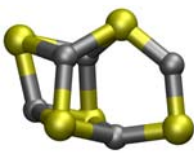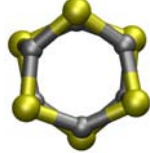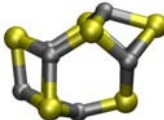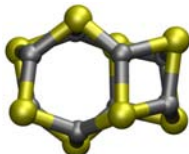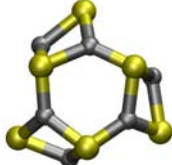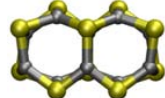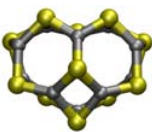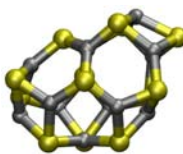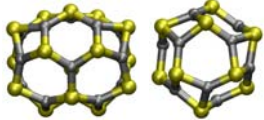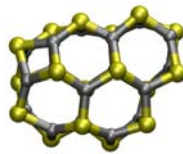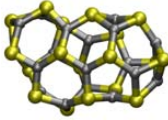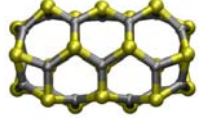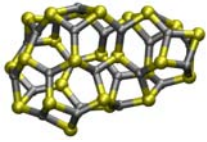
Structure	$(ZnS)_3$	$(ZnS)_4$	$(ZnS)_5$	$(ZnS)_6$
U/ZnS	-3030.9	-3066.6	-3081.5	-3114.5
ΔU/ZnS	140.2	104.5	89.6	56.6
	$(ZnS)_7$	$(ZnS)_8$	$(ZnS)_9$	$(ZnS)_{10}$
U/ZnS	-3118.9	-3135.4	-3142.9	-3143.8
ΔU/ZnS	52.2	35.7	28.2	27.3
	$(ZnS)_{11}$	$(ZnS)_{12}$	$(ZnS)_{13}$	$(ZnS)_{14}$
U/ZnS	-3150.6	-3157.8	-3156.3	-3159.8
ΔU/ZnS	20.5	13.3	14.8	11.3
	$(ZnS)_{15}$	$(ZnS)_{16}$	$(ZnS)_{17}$	$(ZnS)_{18}$
U/ZnS	-3163.1	-3163.0	-3164.7	-3160.0
ΔU/ZnS	8.0	8.1	6.4	11.1
	$(ZnS)_{21}$	$(ZnS)_{22}$	$(ZnS)_{24}$	
U/ZnS	-3171.1	-3170.5	-3166.5	
ΔU/ZnS	0.0	0.6	4.6	-

TABLE 5.4: Summary of compact clusters of zinc sulfide and potential energies, as obtained from forcefield methods. The potential energy per formula unit (U/ZnS) is shown in kJ mol^{-1}. Relative potential energies per formula unit (ΔU/ZnS) with respect to the lowest energy structure in this set of sizes, $(ZnS)_{21}$, are also shown in kJ mol^{-1}.
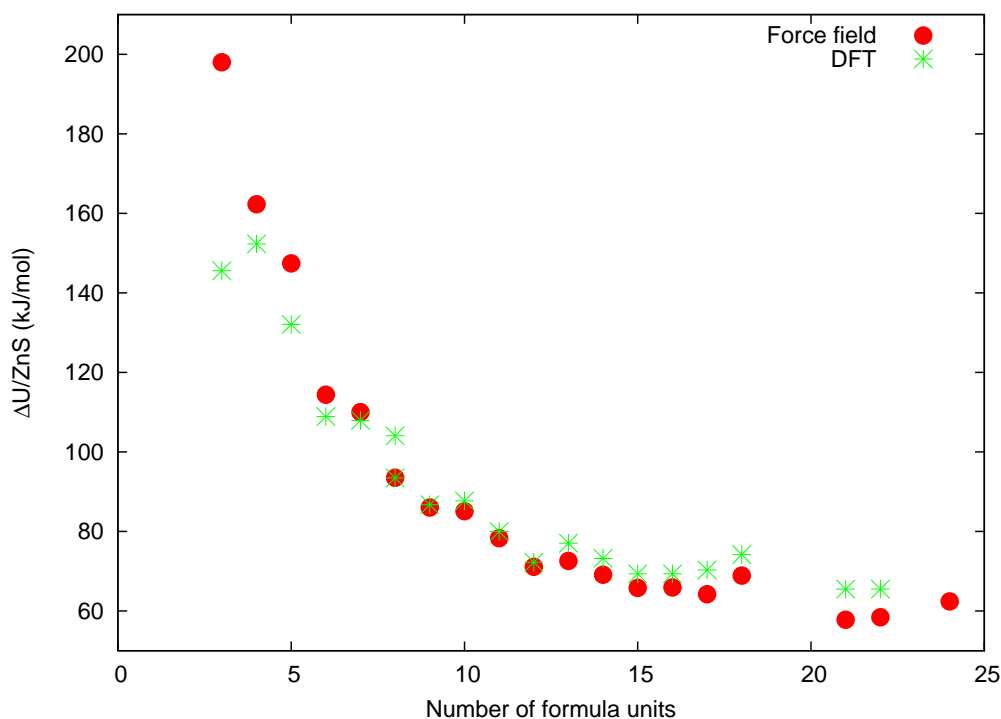
FIGURE 5.1: Plot of potential energy per ZnS formula unit relative to sphalerite (ΔU/ZnS) vs. cluster size, for clusters $(ZnS)_n$, where $n=3\ldots24$. The data obtained from both force field methods and DFT are shown.

also indicates that the smaller cluster sizes are generally higher in energy; as the size of the clusters increases the energy per formula unit decreases, but beyond $n = 10$ the range in variation in energy is much smaller, and must eventually reach a value of 0 (a potential energy equivalent to sphalerite) at larger sizes. The structures contain predominantly 3-fold coordinated atoms, in contrast to the bulk counterparts where the Zn and S atoms are all 4-fold coordinated. We also find that the larger structures can accommodate a greater number of 6-membered rings, which have a geometry close to that found in bulk wurtzite and sphalerite, despite the lower coordination of the atoms. 4-membered rings, which are necessary to close the cage, have a much smaller Zn-S-Zn (and S-Zn-S) angle making them higher in energy than a 6-membered ring. We have investigated the correlation between the energy and the presence of 4- and 6- membered rings, and their connectivity. Figure 5.2 shows where the energy per formula unit vs. the number of 4- and 6-membered rings, and also vs. the number of 4- and 6- membered rings fused together and the number of 4-membered rings fused together. In general the number of 4-membered rings stays constant, with an average of six 4-membered rings present. There appears to be a relationship between the energy and the number of 6-membered rings present, as when there are more 6-membered rings

the U/ZnS decreases. However, the slope of this trend is significantly decreased beyond ten 6-membered rings. The most indicative plots are the lower two plots in Figure 5.2, where the energy per ZnS formula unit is shown with respect to the number of 4-membered rings fused together (sharing a bond), and the number of 4- and 6-membered rings sharing a bond. Excluding the high-energy outliers for the plot of U/ZnS for the 4-membered rings, ($(ZnS)_3$ and $(ZnS)_5$), we find that as the number of 4-membered rings sharing a bond is increased, so does the energy. Conversely, as the number of 4- and 6-membered rings sharing a bond is increased, the energy decreases. These values are inherently related, as a decreasing number of 4-membered rings present generally implies a greater presence of 6-membered rings.

An analogous argument to those above can be used to explain the presence of 8-membered rings in some high energy structures (see Appendix A). The
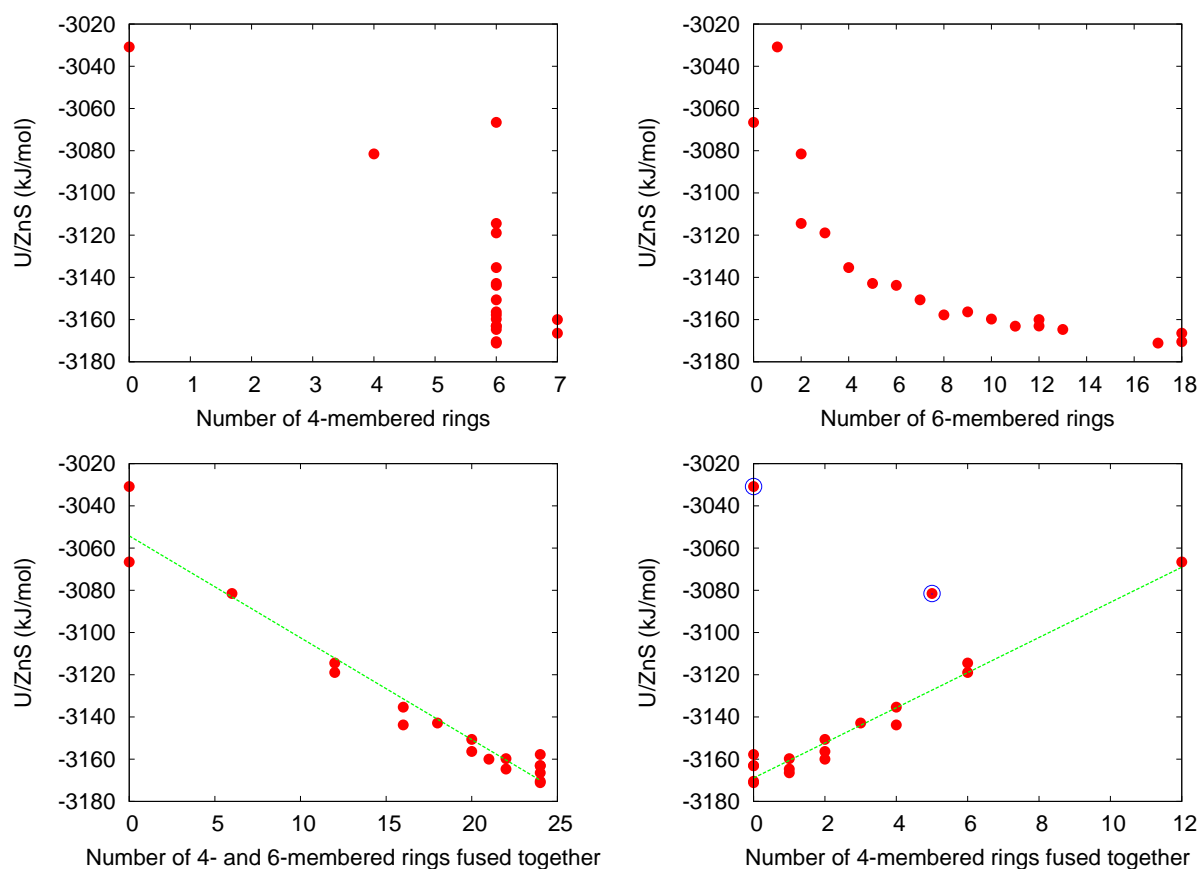
FIGURE 5.2: Plots of U/ZnS vs. number of 4-membered rings present (top left), number of 6-membered rings present (top right), number of 4- and 6-membered rings fused together (bottom left) and number of 4-membered rings fused together (bottom right). The lines are a line of best fit to the data, with any outliers not included in the fit circled.

8-membered rings can easily be rearranged into a combination of 4- and 6-membered rings that have a lower energy. This is highlighted by the fact that we found very few structures with 8-membered rings, and the ones which do have 8-membered rings are generally very high in energy in comparison to other structures for the same cluster. The $(ZnS)_{18}$ and $(ZnS)_{24}$ clusters are clear outliers in Figure 5.1, with higher relative energies than their respective neighbours. Both these clusters are the only minimum-energy clusters in Table 5.4 which have an 8-membered ring present. Based on the clear preference for 4- and 6- membered rings within this size range, it is likely that we have not sufficiently explored the configuration space to locate lower energy structures for these two cluster sizes. There are other examples of high energy structures with 8-membered rings in Appendix A. One example is a structure with two 8-membered rings connected via eight 4-membered rings, found as the highest energy structure for the $(ZnS)_{12}$ cluster. The smallest clusters are also an indication of the ring-preference, for example, the $(ZnS)_4$ cluster, whose lowest energy structure is composed of a fused 4- and 6-membered ring, rather than an 8-membered ring.

In the introductory chapter we presented a literature review of studies performed on zinc sulfide nanoparticles, both experimental and theoretical. A study performed by Kasuya *et al.* [67] using time-of-flight mass spectrometry showed that the $(ZnS)_{13}$ nanoparticle was unusually more stable than surrounding sizes, and the same was observed for $(ZnS)_{33}$ and $(ZnS)_{34}$, two sizes not considered in our current study. Similar results were seen for other materials, CdS and CdSe, in the same work[67]. Our force field and DFT calculations do not indicate the same result for the $n = 13$ cluster. In fact it is slightly higher in energy than the two neighbouring cluster sizes. We should note however that the experimental data obtained from time-of-flight mass spectrometry refers to charged clusters, while our calculations are for neutral clusters. It is possible the relative stabilities of the clusters may be different for charged clusters versus neutral clusters.

Though there is a clear linear relationship between the number of 4-membered rings fused to 6-membered rings, the relationship is less obvious with the other structural parameters we have obtained for each structure. Using multiple linear regression we can obtain a linear combination of these structural terms to estimate the potential energy per ZnS of a given cluster. A general form for a linear fit of

independent variables $x_1, x_2, \ldots, x_n$ is given by:

$$y = m_1 x_1 + m_2 x_2 + \cdots + m_n x_n + c \tag{5.9}$$

In our case each term of the equation will be a contribution to the estimated total energy, E_{total}:

$$
\begin{aligned}
E_{total} \approx \quad & E_{4-ring} + E_{6-ring} + E_{8-ring} + E_{4-4fused} + \\
& E_{4-6fused} + E_{6-6fused} + E_{4-8fused} + E_{6-8fused} + c
\end{aligned}
\tag{5.10}
$$

The terms E_{4-ring}, E_{6-ring} and E_{8-ring} refer to the energy contribution due to the presence of 4-, 6- and 8-membered rings respectively. The values used to fit these three terms will be the number of each of these rings present in our clusters. The final three terms $E_{4-4fused}$, $E_{4-6fused}$ and $E_{4-8fused}$ are the energy contributions due to adjacent ring types sharing a bond or edge, for example a 4- membered ring fused to a 6- membered ring would contribute to the $E_{4-6fused}$ term. The values used to fit these terms will be the number of these fused ring pairs present in each cluster. The final value, c, is a constant.

The dataset used for the multiple linear regression are given in Table 5.5, where the known values are the energies and the unknowns the count of 4-, 6-, 8- membered rings and their shared bonds. The data given in Table 5.5 are not only for the lowest energy minima for each cluster size, but also for additional compact conformations (listed in Appendix A). This was necessary to obtain a better fit to our data, particularly with respect to clusters with 8-membered rings. Had we only used the minimum energy clusters there would only be two entries in the table, $(ZnS)_{18}$ and $(ZnS)_{24}$, with any values to assist in fitting the 8-membered ring parameters.

Fitting our data to Equation (5.10), where each energy term equates to a constant, m, multiplied by an independent variable, *e.g.*, n_{4-ring}, we obtain an approximation to E_{total} in units of kJ/mol;

$$
\begin{aligned}
E_{total} \approx \quad & -61.61 \cdot n_{4-ring} + 64.20 \cdot n_{6-ring} + 59.678 \cdot n_{8-ring} + 32.45 \cdot n_{4-4fused} \\
& +2.11 \cdot n_{4-6fused} - 21.90 \cdot n_{6-6fused} + 7.32 \cdot n_{4-8fused} - 18.40 \cdot n_{6-8fused} - 3095
\end{aligned}
\tag{5.11}
$$

TABLE 5.5:   Table of potential energies (kJ mol^{-1}/ZnS) and structural parameters for $(ZnS)_n$, $n = 3, \ldots, 24$. Here 4-ring, 6-ring and 8-ring are the number of 4-, 6- and 8- membered rings, respectively, and 4-4, 4-6, 6-6, 4-8 and 6-8 fused refer to joins (shared edges) between 4-, 6- and 8- membered rings.

n	U/Zns	4-ring	6-ring	8-ring	4-4 fused	4-6 fused	6-6 fused	4-8 fused	6-8 fused
3	-3030.85	0	1	0	0	0	0	0	0
4	-3066.58	6	0	0	12	0	0	0	0
4	-3035.38	0	0	1	0	0	0	0	0
5	-3081.53	4	2	0	5	6	3	0	0
6	-3114.47	6	2	0	6	12	0	0	0
7	-3118.92	6	3	0	6	12	3	0	0
7	-3115.35	4	4	0	3	10	7	0	0
8	-3135.36	6	4	0	4	16	4	0	0
8	-3116.05	2	6	0	0	8	14	0	0
9	-3142.86	6	5	0	3	18	6	0	0
9	-3133.41	4	6	0	2	12	12	0	0
10	-3143.76	6	6	0	4	16	10	0	0
10	-3132.46	4	7	0	2	12	15	0	0
10	-3126.07	5	5	1	3	9	7	6	6
11	-3150.65	6	7	0	2	20	11	0	0
11	-3142.01	4	8	0	2	12	18	0	0
12	-3157.80	6	8	0	0	24	12	0	0
12	-3150.09	6	8	0	2	20	14	0	0
12	-3146.94	7	6	1	4	16	8	4	4
12	-3151.76	6	8	0	4	16	16	0	0
12	-3134.66	8	4	2	4	16	0	8	8
13	-3156.33	6	9	0	2	20	17	0	0
13	-3148.53	5	8	1	0	18	12	2	6
14	-3159.75	6	10	0	1	22	19	0	0
14	-3151.14	4	11	0	1	14	26	0	0
15	-3163.13	6	11	0	0	24	21	0	0
15	-3156.99	7	9	1	3	20	14	2	6
15	-3154.74	4	12	0	2	12	30	0	0
16	-3163.03	6	12	0	0	24	24	0	0
16	-3162.48	6	12	0	2	20	26	0	0
17	-3164.69	6	13	0	1	22	28	0	0
17	-3157.58	7	11	1	3	20	20	2	6
18	-3160.02	7	12	1	2	21	23	3	5
18	-3159.77	5	13	1	1	18	26	0	8
21	-3171.12	6	17	0	0	24	39	0	0
22	-3170.49	6	18	0	0	24	42	0	0
24	-3166.46	7	18	1	1	24	39	2	6

This fit yields an R^2 value of 0.95, and the energy values obtained from Equation (5.11) are plotted along with the energy values obtained from lattice

dynamics, both shown in Figure 5.3. One possible limitation to this fit is the quantity of data used to fit the parameters. However, we will test the ability of this fit to estimate the energy of new clusters in one of the following sections. A plot of the differences between the estimated data (from Equation (5.11)) and the values obtained from optimisation is given in Figure 5.4. We can see that in general the estimated energy is within 15 kJ/mol per formula unit of the actual value obtained from optimisation.

We should point out that the data we have given in Table 5.5 all relate to the total number of edges, faces and vertices each cluster is composed of. The sum of the number of 4-, 6- and 8- membered rings will give the number of faces, while the sum of the 'fused rings' terms ultimately gives the number of edges. These parameters have been combined in the past to form Euler's characteristic, which has a specialised form for any convex polyhedron[296];

$$V + F = E + 2 \tag{5.12}$$

where V is the number of vertices, F the number of faces and E the number of
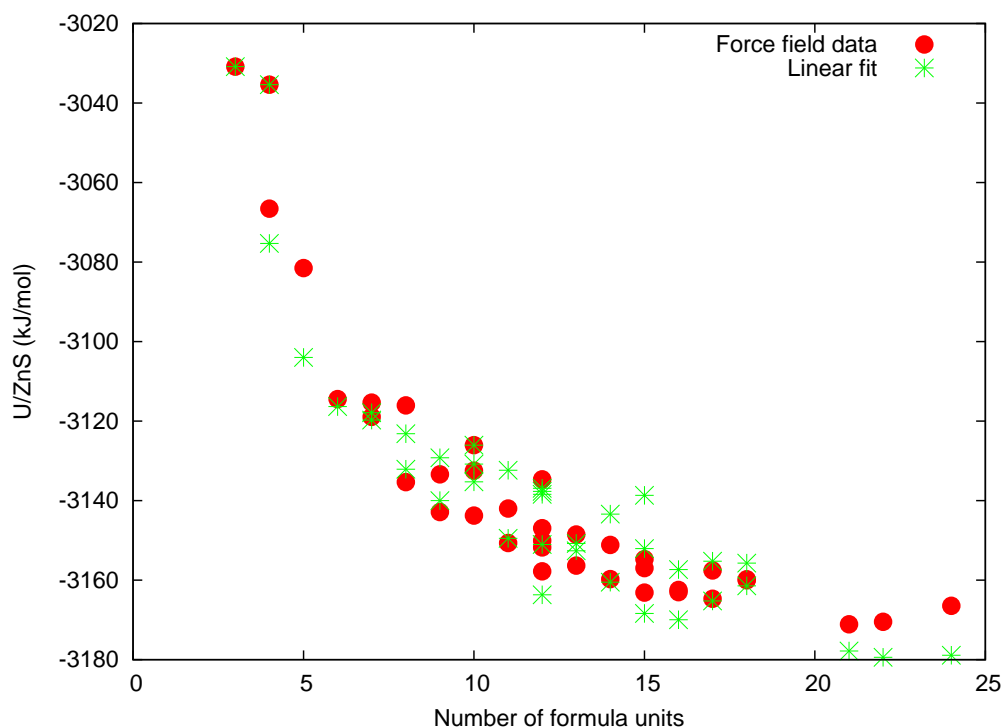
FIGURE 5.3: Energy per formula unit vs. number of formula units. U/ZnS are given from the lattice dynamics simulations and the approximation via Equation (5.11).
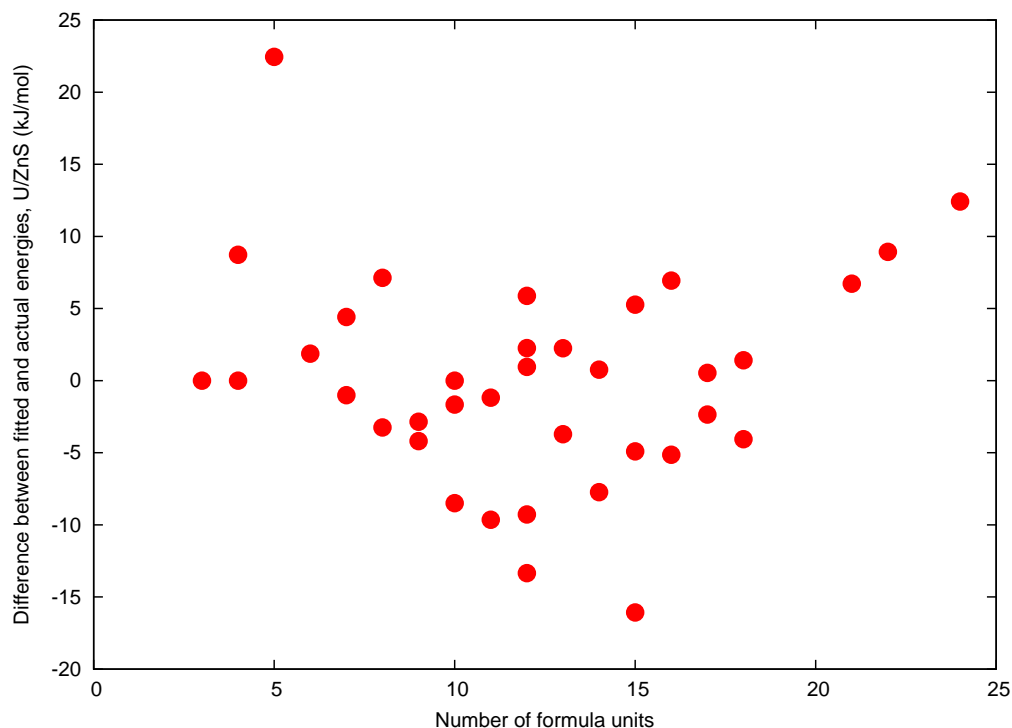
FIGURE 5.4: Difference in energy per formula unit vs. number of formula units. The energy values are the difference between the potential energy obtained from optimisation and the energy values obtained from the linear fit given in Equation (5.11).

edges. This theorem holds for any convex polyhedron, that is, we do not count dangling bonds, or rings which can be considered 'internal' to the cluster (*i.e.*, contained within an outer surface). The structures we have chosen to fit our energies all obey Euler's characteristic. Previous studies into the structures of small ZnS clusters have often referred to this theorem in relation to the low energy clusters obtained. Spanó *et al.* [111] provide two formulae they suggest can be used to predict the number of 4- and 6-membered rings present in a minimum energy cluster:

$$N_{6-ring} = \quad n - 4 - N_{8-ring} \tag{5.13}$$

$$N_{4-ring} = \quad 6 + N_{8-ring} \tag{5.14}$$

This prediction indeed holds true for the majority of the minimum energy clusters we have obtained from $n = 3 - 24$. There are four outliers, $n = 3, 5, 18, 24$. As we already described, $(ZnS)_{18}$ and $(ZnS)_{24}$ are the only minimum energy clusters we found which have 8-membered rings present, and there are likely to be bubble clusters for these sizes formed of only 4- and 6-membered rings which

our simulations have not found. The smallest cluster $n=3$ can be explained as it is not a polyhedron, but a lone 6-membered ring. The $n=5$ cluster can be explained to be an outlier due to the small number of 4-membered rings. According to Equation 5.14 of Spanó *et al.* [111], each low energy cluster should have six 4-membered rings, and more if there are 8-membered rings present. In the case of our low energy $n = 5$ cluster there are only four 4-membered rings present. This relationship of Euler's theorem to small ZnS clusters is also discussed in the work of Burnin *et al.* [116], a work we will consider in more detail in the next section.
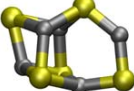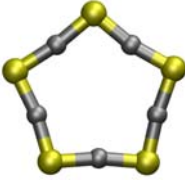
5.3.1.1 Comparison with previous studies

As we mentioned in the introduction, many of the cluster sizes we have chosen to investigate have already been identified in the literature. This means we can compare our structures to those in the literature to compare the efficacy of our method with those of other groups.

One study is particularly relevant and that is the work of Burnin *et al.* [116], as they have investigated small clusters of $(ZnS)_n$, where $n = 1 - 16$. Their work used search and genetic algorithms to locate unique cluster topologies; the clusters were then optimised using DFT. The majority of the lowest energy clusters in this size range correspond our lowest energy minimum clusters. The only structures which do not correspond to theirs are the clusters for $n = 4, 5, 10$. In their study the clusters of size $n = 1 - 5$ do not form any 'bubble clusters'. Instead they form only one and two dimensional structures, such as a simple bond ($n = 1$) or rings for n=2-5, where a 4-, 6-, 8- and 10-membered ring are found for these sizes. In contrast, our our lowest energy cluster for $n = 4$ produced a 'cube' shape of six 4-membered rings, while the $n = 5$ cluster is closely related to the $n = 4$ structure, though with two 2-coordinated atoms protruding from the 'cube' forming a 6-membered ring. These two clusters are shown in the work of Matxain *et al.* [283] as *local* minima, and the n=4 'cube' also appears as a local minimum in the work of Burnin *et al.* [116], while the 8- and 10- membered rings are considered the global minima for these cluster sizes according to the DFT calculations of both of these studies. With our current force field parameters we were unable to optimise these same 8- and 10-membered ring clusters; all attempts to create and optimise these two ring clusters resulted in optimisation down to the two low energy clusters already described and given in Table 5.4.

While we were unable to optimise these larger ring structures using force field methods, we did successfully optimise these clusters using DFT. The difference in these values are given below in Table 5.6.

TABLE 5.6: The relative potential energies obtained for the lowest energy clusters found for $n = 4, 5$, and also the 8- and 10-membered ring clusters cited in other works[116, 283] as the global energy minima at these sizes. The values are given in kJ/mol, as obtained from DFT calculations, and are relative to the energy obtained for bulk ZnS as the sphalerite polymorph.

Structure	ΔU/ZnS (DFT)
$n=4$	
	152.32
	129.16
$n=5$	
	87.67
	130.10

We find that the 8-membered ring structure is in fact lower in energy than the 'cube' form we found in our MetaD simulations. However, the 10-membered ring structure is less stable the 'bubble' like form.

The $(ZnS)_{10}$ cluster given in the work of Burnin *et al.* [116] forms a cluster similar to the sodalite cage structure, a 'bubble' of 4- and 6-membered rings. The low energy $(ZnS)_{10}$ cluster in our work is a well ordered cluster consisting of two layers of two fused 6-membered rings; this has more resemblance to a section of bulk than a bubble cluster. In this case it is possible we have not explored phase space sufficiently to find these bubble-like clusters, or alternatively we are seeing a preference dictated by the force field we are using.

One cluster that is of particular interest is the $(ZnS)_{13}$ cluster which has appeared as an ultra-stable nanoparticle in the mass spectra produced in experiments of

both Kasuya *et al.* [67] and Burnin *et al.* [116]. In the case of Kasuya *et al.* [67], further extended X-ray absorption fine structure experiments showed the average coordination of atoms in their clusters to be approximately 3.2, less than bulk (a coordination of 4) but greater than the coordination of a completely open cage structure. Based on this data they suggest "core-cage" structures as the most stable, with a central core atom surrounded by a cage (or cages). Their suggested ultra-stable cluster for CdSe (and also ZnS) is shown on the left in Figure 5.5. Burnin *et al.* [116] also performed laser ablation experiments on zinc sulfide, using a time-of-flight mass spectrometer to investigate the particles formed, and discovered the same ultra-stable particles as Kasuya *et al.* [67]. The global minimum structure for the neutral $(ZnS)_{13}$ cluster of Burnin *et al.* [116] is shown as the central cluster in Figure 5.5. Our $(ZnS)_{13}$ cluster, viewed from a different direction to that shown in Table 5.4, appears very close in topology to that found in the Burnin *et al.* [116] study. However, the Zn and S atoms appear at alternating positions. We manipulated our structure to resemble that of Burnin *et al.* [116] and optimised it in the same manner as our previous structures. We found our $(ZnS)_{13}$ structure to be of the same energy as that of Burnin *et al.* [116], within the accuracy of our optimisation methods. None of our "global minima" for the cluster sizes explored in our study showed a preference for the "core-cage"-like structure similar to that of Kasuya *et al.* [67]. This could be an effect of limited exploration of phase space, or simply a preference for open-cage structures with the interionic potentials used.
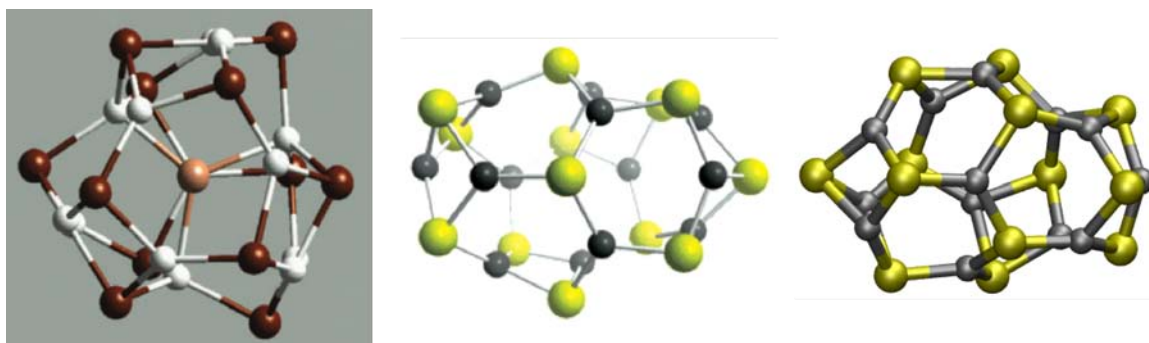
FIGURE 5.5: Suggested cluster formations for the ultra-stable $(ZnS)_{13}$ particle. Kasuya *et al.* [67] (left), Burnin *et al.* [116] (middle) and our studies (right). Images reproduced from Kasuya *et al.* [67] and Burnin *et al.* [116] respectively.

5.3.1.2   Building clusters from the sodalite cage

It is evident from our simulations that the low energy nanoparticles found during the metadynamics for $n = 22$ and $n = 24$ have little, if any, symmetry. However, making an analogy with zeolites, we can easily imagine different structures obtained by fusing together two sodalite cage ZnS nanoparticles and using them as starting configurations for MetaD simulations, as shown in Figure 5.6.
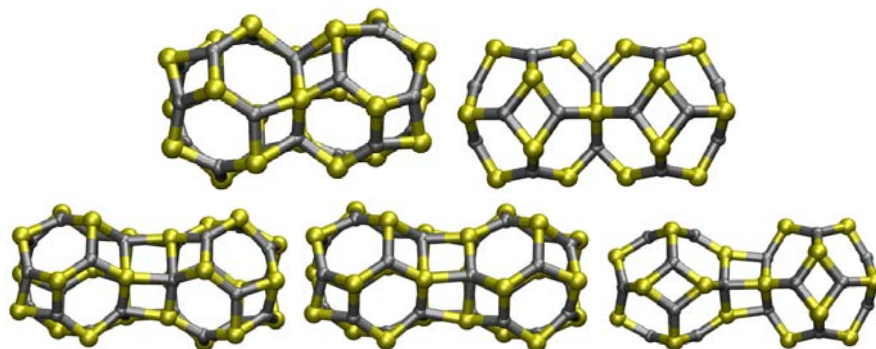
FIGURE 5.6: The five possible ways to join and fuse together two sodalite cage units of ZnS, forming $(ZnS)_{21}$, $(ZnS)_{22}$ and three forms of $(ZnS)_{24}$, shown in order from top left to bottom right.

There are two regions at which the sodalite cages can easily join - at a 4-membered or 6-membered ring. A $(ZnS)_{21}$ structure is formed when two sodalite cages are fused together at a 6-membered ring and an analogous $(ZnS)_{22}$ structure exists with two sodalite cages fused across a 4-membered ring. Three $(ZnS)_{24}$ structures can be formed by allowing bonds to connect two sodalite cages, again either at a 4- or 6-membered ring. The $(ZnS)_{24}$ structure formed by bridging across the four membered ring is unique, while it is possible for $(ZnS)_{24}$ to form two distinct structures when connection occurs at the 6-membered ring, depending on how the two sodalite cages are aligned. This is due to the fact that rotating one of the sodalite cages about the 6-membered ring 'join' by 60 degrees results in three 4-membered rings aligned together, or alternatively two 4-membered rings and a 6-membered ring.

MetaD simulations of these structures were performed with Gaussians of height 0.1 eV and width 50 amu Å^2, and run for between 12 and 24 ns. A number of new cage-like structures were obtained, and these are summarised in Table 5.7 along with the optimised starting structures based on the sodalite cage.
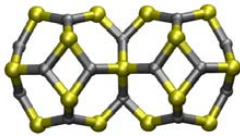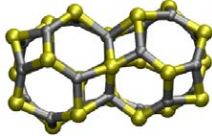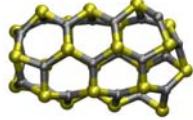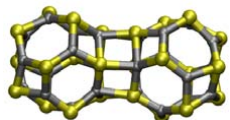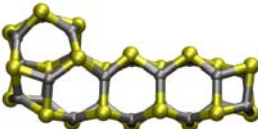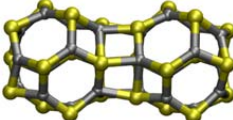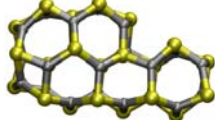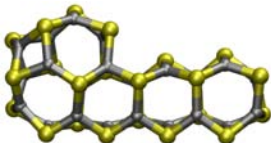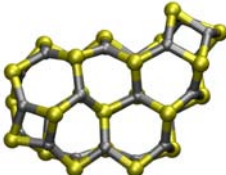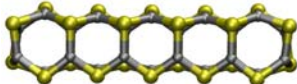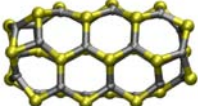
	$(\mathbf{ZnS})_{22}$	$(\mathbf{ZnS})_{21}$	$(\mathbf{ZnS})_{24}$	$(\mathbf{ZnS})_{22}$
U/ZnS	-3159.98	-3163.65	-3163.77	-3164.68
Δ**U**	12.89	9.22	9.10	8.19
	$(\mathbf{ZnS})_{24}$	$(\mathbf{ZnS})_{21}$	$(\mathbf{ZnS})_{24}$	$(\mathbf{ZnS})_{21}$
U/ZnS	-3164.88	-3165.17	-3165.22	-3166.60
Δ**U**	7.99	7.70	7.65	6.27
	$(\mathbf{ZnS})_{22}$	$(\mathbf{ZnS})_{22}$	$(\mathbf{ZnS})_{22}$	$(\mathbf{ZnS})_{24}$
U/ZnS	-3167.10	-3167.83	-3168.56	-3172.87
Δ**U**	5.77	5.04	4.31	0.00

TABLE 5.7: Summary of potential energy values for structures composed of sodalite cages fused or bridged together, along with additional low energy configurations obtained from MetaD simulations initiated from these fused structures. Potential energies per formula unit (U/ZnS) are given in kJ mol^{-1}. Relative potential energies (ΔU) with respect to the lowest energy structure in this set of sizes, $(ZnS)_{24}$, are also given in kJ mol^{-1}.

The highest energy structures were the two clusters comprised of 'fused' sodalite cages - the $(ZnS)_{21}$ and $(ZnS)_{22}$ clusters shown in Figure 5.6. A low energy cage-like cluster was found from the 48 atom simulations, with a potential energy 1.83 kJ/mol (per formula unit) lower in energy than the $(ZnS)_{21}$ cluster found to be the lowest cluster from the original MetaD simulations. The relative potential energies given in Table 5.7 are shown with respect to the new 48 atom cage-like cluster, which is the lowest energy structure found in our studies. All the MetaD simulations for $(ZnS)_{24}$ resulted in a quick transformation to this minimum energy structure, or very similar structures which, when taken from the trajectory and optimised, minimise down to the lowest energy cage-like structure. The MetaD simulations performed on the remaining sizes did result in a variety of new clusters that are given in Table 5.7.

The $(ZnS)_{21}$ simulations did result in some new structures, but none lower in energy than the highly symmetric bubble-like $(ZnS)_{21}$ cluster already obtained in the previous simulations. For $(ZnS)_{22}$ we also found quite a few new clusters, one of which is a highly symmetric long cluster that was found to be the second-lowest energy cluster in these new structures. Again, the lowest energy $(ZnS)_{22}$ cluster was that obtained from the previous set of MetaD simulations.

The above simulations do not prove that we have found the lowest energy structure for $n = 24$, but this process has shown conversely that the structures found in our metadynamics simulation can significantly depend on the starting configuration. This is particularly the case for these larger clusters, where the size of the phase space to be explored goes beyond what can be achieved in the simulation time, even with the assistance of metadynamics. An additional difficulty with these simulations of the largest clusters is that we often found that geometrically different clusters can have the same value of the trace of the inertia tensor, again indicating that this CV is increasingly ineffective for large clusters.

We can use the relevant structural data for these clusters to obtain an estimation of the energy using the fit we obtained in Equation 5.11. The relevant structural parameters are given in Table 5.8, along with the approximation to the energy obtained from the linear fit. The data we have used for the clusters obeys Euler's characteristic (*i.e.*, V+F=E+2), which means we have not counted 'internal' rings, which could be included in the case of the fused sodalite cages.

The data in Table 5.8 has been separated into two groups, the "bubble" clusters obtained from MetaD simulations, and the fused/bridged sodalite cages. The fit of the energy for the bubble clusters is within 15 kJ/mol per ZnS unit of the actual value obtained from our optimisations. This is the same order of error we found in our previous set of estimations. The greatest discrepancies in this new set of data are with our fit of the fused and bridged sodalite cage structures, for which the fused/bridged regions are perhaps not accurately represented by the structural parameters we have given. While we have included the four fused-ring values present for each 4-coordinated atom present at a joining region, we did not count any 'internal' rings which exist between two connected or fused sodalite cages. The energy estimation for these clusters are between 45 and 70 kJ/mol per formula unit less than the values obtained from optimisation.

TABLE 5.8: Table of structural parameters and estimated energies for the $(ZnS)_n$, $n = 21, \ldots, 24$, clusters determined from fused sodalite cages, and subsequent MetaD simulations. Where 4-ring, 6-ring and 8-ring are the number of 4-, 6- and 8- membered rings respectively and 4-4, 4-6, 6-6, 4-8 and 6-8 fused refer to joins (shared edges) between 4-, 6- and 8- membered rings.

n	U/Zns (kJ/mol)	Lin. fit U/ZnS (kJ/mol)	4-ring	6-ring	8-ring	4-4 fused	4-6 fused	6-6 fused	4-8 fused	6-8 fused
				"Bubble" clusters						
21	-3165.17	-3163.22	7	15	1	3	21	31	1	7
21	-3166.60	-3176.58	7	15	1	2	23	32	1	5
22	-3164.68	-3162.31	4	19	0	0	16	49	0	0
22	-3168.56	-3154.15	6	18	0	4	16	46	0	0
22	-3167.83	-3167.73	7	16	1	2	21	35	3	5
22	-3167.10	-3171.11	7	16	1	2	23	33	1	7
24	-3172.87	-3182.56	6	20	0	0	24	48	0	0
				Fused/connected sodalite cages						
21	-3163.65	-3229.14	12	14	0	0	48	18	0	0
22	-3159.98	-3213.61	10	16	0	0	40	28	0	0
24	-3163.77	-3225.70	14	16	0	4	48	25	0	0
24	-3164.88	-3209.38	18	14	0	12	48	18	0	0
24	-3165.22	-3209.38	18	14	0	12	48	18	0	0

The main difference between these structures and the others we have investigated is that we have 4-coordinated atoms present at the bridge or fused region of the sodalite cages. The fitting we performed in the previous section did not have any clusters with 4-coordinated atoms present, and in general the number of n-membered rings or the total number of shared bonds does not inherently indicate the presence of 4-coordinated atoms which may have a significant contribution to the energy. To assist in fitting clusters such as these it may be necessary to include a parameter that reflects at least the number of 4-coordinated atoms, and perform some testing to determine if the fit is significantly better or worse if the 'internal' rings are counted and used in the fitting as well as the 'surface' rings.

We have performed a linear fit of the data including a parameter which indicates simply the number of four-coordinated atoms present. The new linear fit includes data for all of the clusters (those in the previous section, and all the new 42, 44 and 48 atom clusters discussed here). The new equation for approximating the

energy, in units of kJ/mol, is given by:

$$
\begin{aligned}
E_{total} \approx \ & -80.80 \cdot n_{4-ring} + 61.01 \cdot n_{6-ring} + 60.90 \cdot n_{8-ring} + 40.43 \cdot n_{4-4fused} \\
& + 7.97 \cdot n_{4-6fused} - 21.00 \cdot n_{6-6fused} + 11.63 \cdot n_{4-8fused} \\
& - 18.11 \cdot n_{6-8fused} + 4.46 \cdot n_{four-fold} - 3094.41
\end{aligned}
$$

$$(5.15)$$

This fit is slightly less accurate than the previous linear regression attempt, with an R^2 value of 0.92, in comparison to the R^2 of 0.95 obtained for the first linear regression. However, the approximate values obtained from the new linear fit for the fused and connected sodalite cages are much closer to the calculated values. It is possible we could obtain a better fit with a greater dataset of clusters with four-coordinated atoms present; in this case we have only five fused/connected sodalite cages which have four coordinated atoms present and these were included in our linear regression. A plot of the new approximate energy values is given in Figure 5.7, along with the values obtained from force field methods and the approximation obtained from the original linear fit given in Equation (5.11). Additionally, we have plotted the difference between the force field energies and the new set of approximated energies, shown in Figure 5.8. Though there are some outliers in the smaller cluster sizes (where the energy is underestimated by $\sim$27 kJ/mol), in general the linear fit results in an approximation within $\sim$15 kJ/mol of the actual values obtained by force field methods.

5.3.1.3   Zeolite composite building units

The sodalite cage $(ZnS)_{12}$ structure is a composite building unit (CBU) for zeolite structures. This will be introduced in more detail in Chapter 7. Not all of the CBUs listed in the zeolite database[297] can be constructed as ZnS analogues, due to the presence of odd-numbered rings. However, it is interesting that many of the CBUs containing even-numbered rings appeared in our simulations of small clusters. Some of the other symmetrical structures obtained from the MetaD simulations are also composite building units, not just the sodalite cage. The structures explored which overlap with the framework of the composite building units on the International Zeolite Association Structure Commission database[297] are given below in Table 5.9. All but one of these are the minimum energy structure found for the given cluster size. The only one which isn't a low energy structure

is the 'ATN' CBU for $(ZnS)_{12}$ which has only 4- and 8- membered rings, and is the highest energy stable structure found for this cluster size.

The presence of these zeolite motifs in the small clusters of ZnS is something we will return to in Chapter 7.

5.3.2 Efficacy of the trace of the inertia tensor CV

In order to better describe the advantages and disadvantages of this approach we will report in more detail the studies performed on the $(ZnS)_{12}$ cluster. We have chosen to focus on this cluster size as it is not so small that there are very few cluster formations possible (such as $(ZnS)_6$), and it is also not too large, so our metadynamics simulations found a variety of unique cluster shapes within a reasonable simulation time.

In Figure 5.9 we show the time evolution of the trace of the inertia tensor during a metadynamics run performed with a Gaussian height of 0.2 eV and width
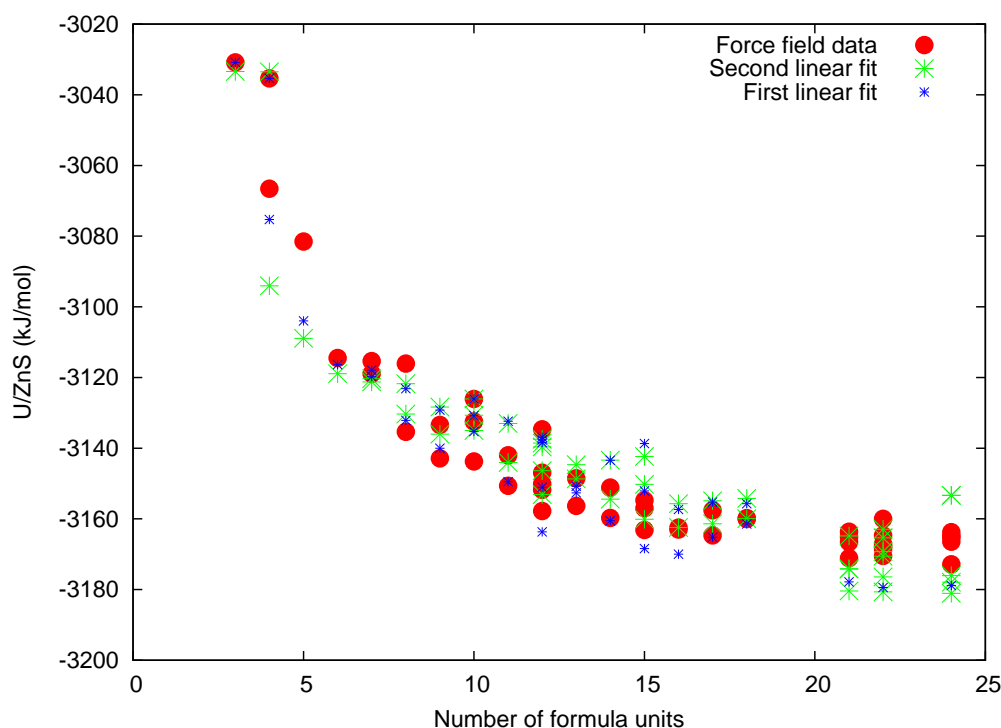
FIGURE 5.7: Energy per formula unit vs. Number of formula units. U/ZnS are given from the lattice dynamics simulations and the energy values approximated from linear regression via Equation (5.15) (Second linear fit) and (5.11) (First linear fit).
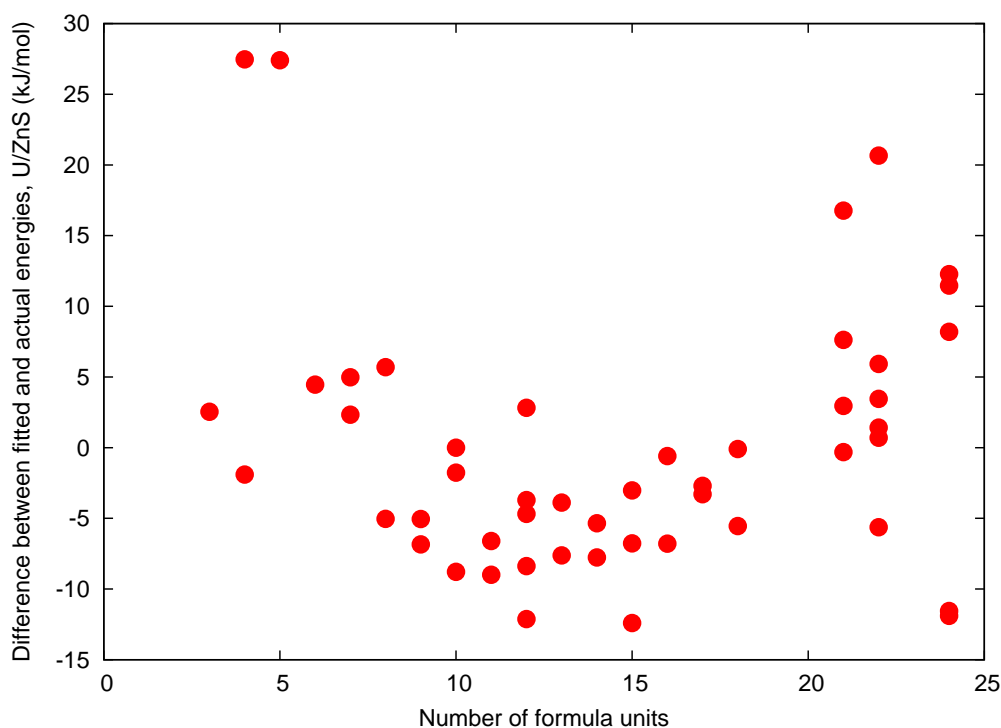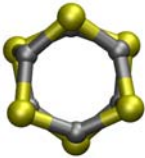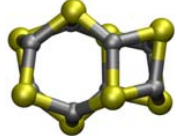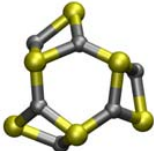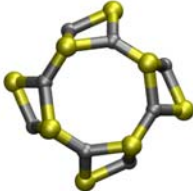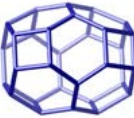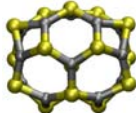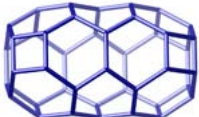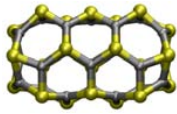
FIGURE 5.8: Difference in energy per formula unit vs. Number of formula units. The energy values are the difference between the potential energy obtained from optimisation and the energy values obtained from the second linear fit given in Equation (5.15).

169 amu Å^2 (one tenth of the total mass of the nanoparticle in amu). The effect of the metadynamics bias potential is clearly shown by the oscillations getting wider and wider until the free energy basin is filled and a transition to a different structure occurs. This plot is significant as it shows the efficacy of metadynamics as a means to enhance the exploration of phase space, and it also demonstrates the limits of the trace of the inertia tensor as a CV. The free energy basin of different clusters, when projected on the trace of inertia tensor, overlap significantly. This makes the estimation of the free energy differences between the structures impossible to calculate. For this size we note that the various minima are somewhat distinct, which makes the trace of inertia tensor useful at least to distinguish the equilibrium structures. However, this is no longer the case for the larger clusters where the trace of inertia tensor has less capacity to differentiate between the (increasingly) large number of configurations.

In order to circumvent the above problem we decided to use the path CV[292] to determine the free energy differences between the ZnS clusters found by using the trace of the inertia tensor. To guarantee the convergence of the MetaD calculation

TABLE 5.9: Zeolite composite building units (CBU) for which $(ZnS)_n$ analogues were found, in the cluster size range $n = 3, \ldots, 24$. The CBU images have been reproduced from the IZA-SC database[297].

CBU	ZnS analogue	CBU	ZnS analogue
D6R	$(ZnS)_6$	AWW	$(ZnS)_8$
CAN	$(ZnS)_9$	ATN	$(ZnS)_{12}$
SOD	$(ZnS)_{12}$	LOS	$(ZnS)_{15}$
LIO	$(ZnS)_{21}$		

with the path CVs we also applied the well-tempered metadynamics scheme[243]. The bias factor was adjusted for each simulation to ensure that the maximum allowed biased potential was enough to overcome the transition barrier. Bias factor values between 5 and 19 were used during the calculations. The simulations were stopped when the Gaussians' heights were smaller than 0.0001 eV throughout the whole free energy landscape of interest.

The results from the above free energy calculations are summarised in Table 5.10, where the free energy differences obtained using lattice dynamics are also provided as a comparison. The values calculated using MetaD are very close to those obtained using minimisation, giving us confidence in the use of this technique for calculating free energy differences even in different conditions where the static approach is not feasible.
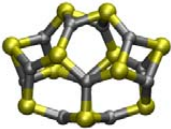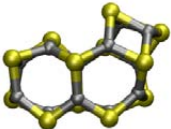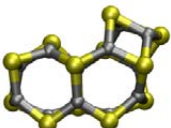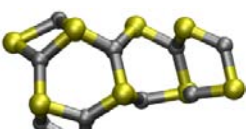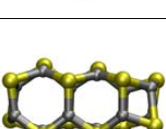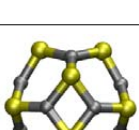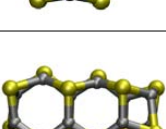
Structures		Lattice Dynamics ΔA/ZnS (kJ/mol)	MetaD Path ΔA/ZnS (kJ/mol)	Lattice Dynamics ΔU/ZnS (kJ/mol)
	→	+2.9	+3.6	+3.2
	→	+3.9	+4.0	+3.8
	→	-10.5	-10.6	-10.9
	→	+18.9	+17.2	+19.5
	→	-5.1	-4.6	-5.2
	→	-6.1	-5.0	-6.0
	→	+14.3	+13.6	+14.7
	→	+1.5	+1.6	+1.7

TABLE 5.10: Free energy differences, shown in kJ/mol per ZnS formula unit, calculated for clusters in vacuum via MetaD using the path variable, and using free energy calculation within lattice dynamics. ΔU/ZnS is also shown, as obtained from optimised structures using interatomic potentials.
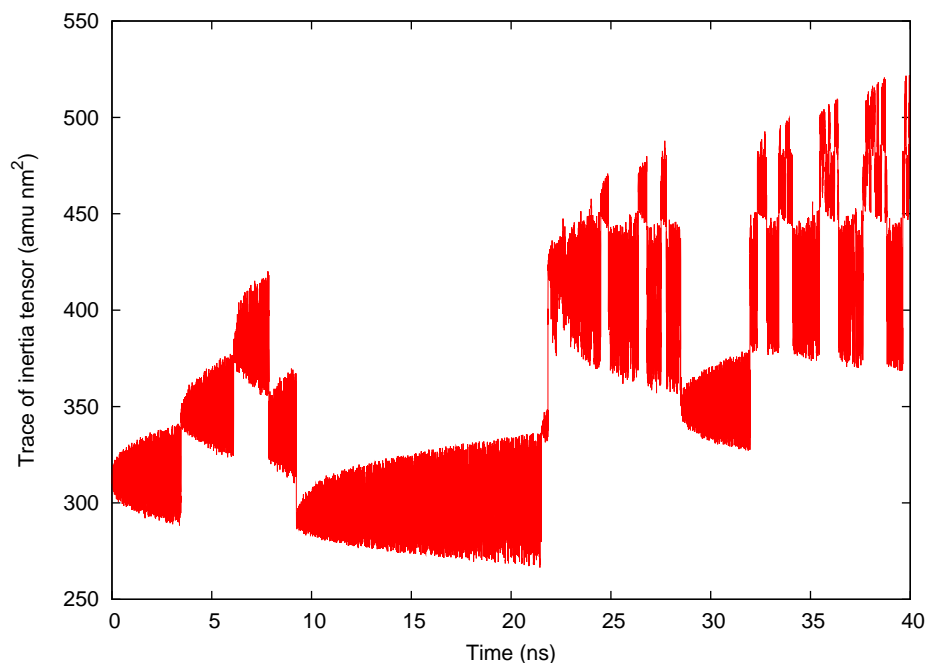
FIGURE 5.9: Evolution of the trace of the inertia tensor over time for the $(ZnS)_{12}$ cluster, obtained from a MetaD simulation performed using the trace of the inertia tensor as the CV; Gaussian height 0.2 eV and width 169 amu Å^2.

The main advantage of the metadynamics simulation is that the free energy over the whole path is obtained and therefore information related to the transition barrier is accessible, which can be harder to achieve from a static calculation. To illustrate this point we have included the 2D free energy profile obtained from the path method for the sixth transition illustrated in Table 5.10 (an elongated structure to the sodalite cage). Figure 5.10 shows a three-dimension plot of the two path variables z and s and the free energy obtained from the path method. We have applied the nudged elastic band method[167, 191] on this free energy profile to show the minimum energy path across this calculated landscape.

A one-dimensional free energy profile of the nudged elastic band progress (plotting only the s variable and the energy at each bead of the nudged elastic band) is given in Figure 5.11. Here we can easily see that there is an activation barrier of approximately 300 kJ/mol, while the free energy difference between the two states is approximately -60 kJ/mol.

A disadvantage of the MetaD calculations is the time necessary to achieve a sufficiently converged free energy profile. Using the path method the simulations took as long as a number of days to complete the calculation to satisfactory convergence, while the calculation of the free energy from the phonons using
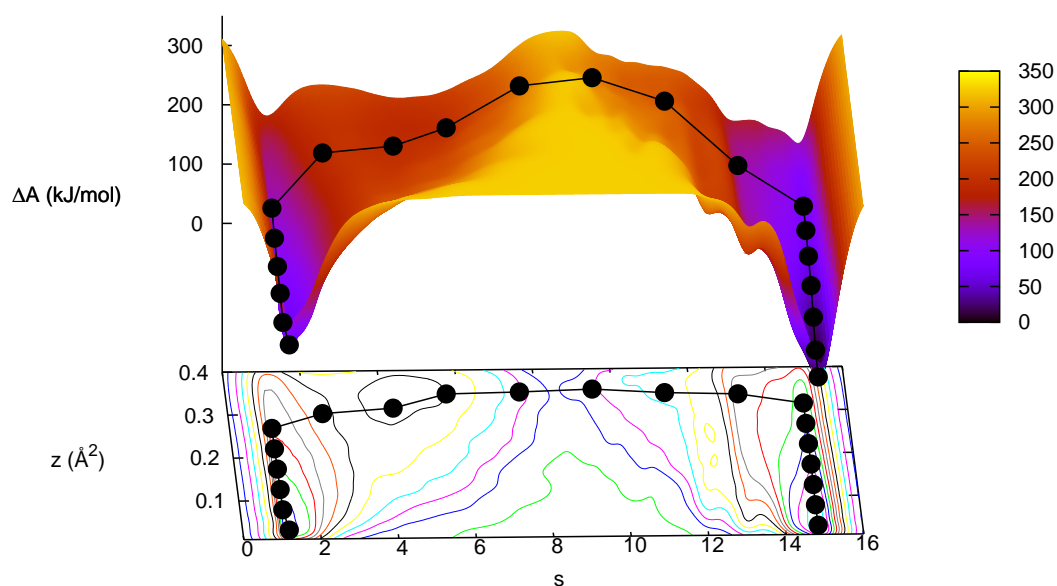
FIGURE 5.10: Plot of free energy vs. the two path CVs z and s. The minimum energy path calculated across this surface between the start (an elongated structure) and final configuration (the sodalite cage) is shown in black across the surface and contour plot.

lattice dynamics requires only a few seconds or minutes. It should be noted that these calculations using the path variables were performed without implementing additional sophisticated MetaD techniques like the use of multiple walkers[298], which could potentially enhance the efficiency of the calculations.

5.3.3 $(ZnS)_{12}$ in water

After investigating the variety of ZnS clusters in vacuum, it is a natural progression of the study to see how these same systems behave in water. Due to the increased computational requirements of the MD simulations of the nanoparticles in water we chose to focus only on the $(ZnS)_{12}$ cluster size.

We ran three different simulations of the $(ZnS)_{12}$ nanoparticle starting from a sodalite cage structure, a 24 atom piece cut from bulk wurtzite and a sodalite cage structure with a water molecule trapped inside. The MetaD runs were performed with Gaussian parameters, height 0.1 eV and width 55 amu Å^2. Each simulation
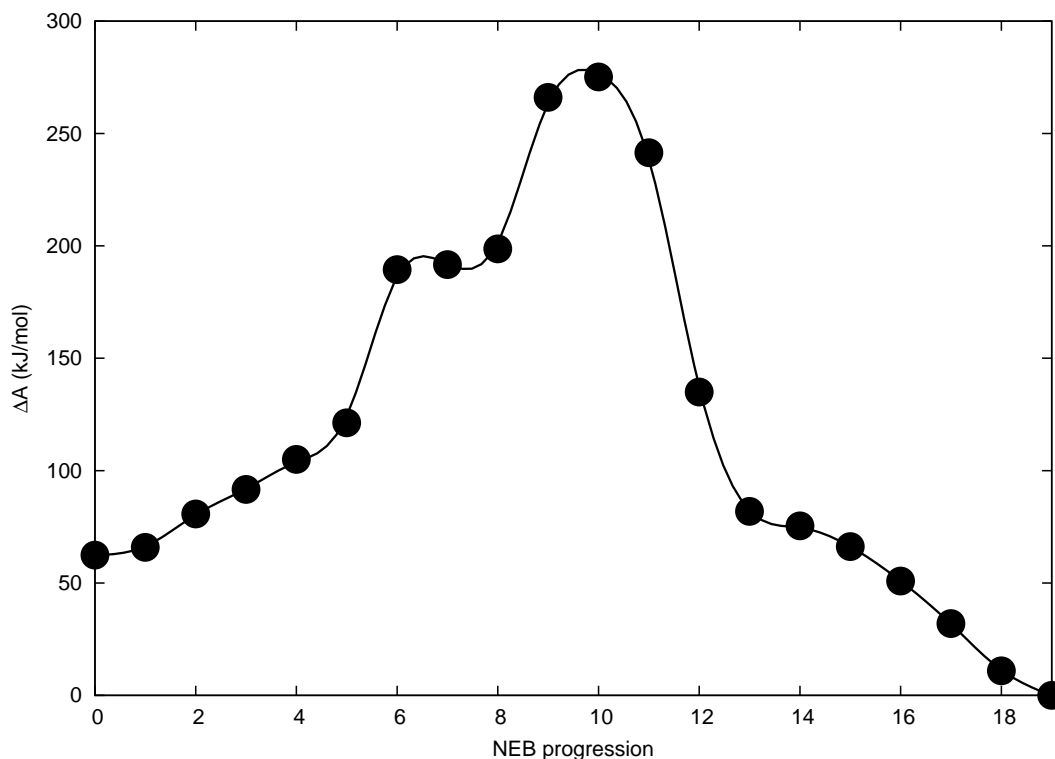
FIGURE 5.11:   The progression of the nudged elastic band across the 2D free-energy profile for the transition between an elongated structure to the sodalite cage-like structure for $(ZnS)_{12}$.

ran for approximately 17 ns. The evolution of these structures during the MetaD simulations in water was quite different to those in vacuum. In particular, the system could clearly adopt more structures, forming sheets and strings of ZnS stabilised by surrounding solvent. Moreover, the free energy barrier between different structures was often so small that few Gaussians were necessary to induce the transitions. The size of the Gaussians was reduced enough to allow the simulations to explore each basin for longer. However transformations from one structure to another occur readily throughout the simulations even with the chosen Gaussian size.

The empty sodalite cage structure in water remained intact for the first 650 ps of the simulation, before it began opening and rearranging into the relatively low energy structure, number 3 shown in Table 5.11. The sodalite cage with a water inside remained intact for only 228 ps before the cage opens up, appearing similar to structure number 3 before transforming into more elongated structures with 2-fold coordinated ions. The structure taken from the bulk takes less than 100 ps to begin transforming to elongated structures with 2-fold coordinated atoms. The progression of the trace of the inertia tensor over time for the simulation of the

'bulk' nanoparticle is given in Figure 5.12. The simulation was performed for a fraction of the time of those performed in vacuum, however it quickly moves from one basin to the next. Overall a much greater region of phase space is explored in comparison to the simulations performed in vacuum.
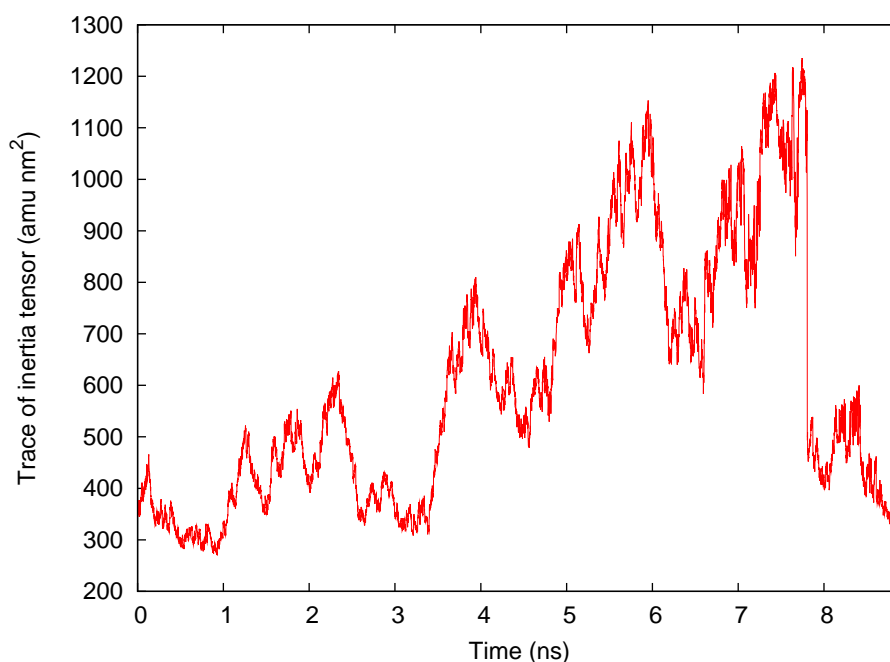

FIGURE 5.12: Plot of the trace of the inertia tensor versus time for the $(ZnS)_{12}$ cluster (cut from bulk wurtzite) and placed in a 30 Å cubic box of water. The Gaussian parameters used were height 0.1 eV and width 55 amu $Å^2$.

Following the same procedure as before, we extracted many different structures for the ZnS nanoparticle from the MetaD trajectory and minimised them in vacuum. Many of the new structures turned out to be much higher in energy than those found during the MetaD in vacuum, due most likely to the significant number of 2-fold coordinated atoms. A select number of these structures are given in Table 5.11 (a more extensive table is included in Appendix A). The reason for the appearance of these structures during the MetaD in water is therefore strictly connected to the strong interaction of ZnS with water, rather than to the stability of the nanoparticle geometry itself. In order to compare the stability of the various structures found we decided to perform a 200 ps long NPT run and calculate the average enthalpy of the system. As all the NPT runs had the same number of water molecules, the differences in enthalpy were directly related to the nanoparticle shape and its interaction with water. The relative enthalpy of each structure is also given in Table 5.11, where it is given relative to the sodalite cage, along with the relative potential energy in vacuo as a comparison. In contrast to the relative
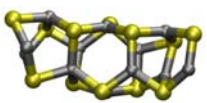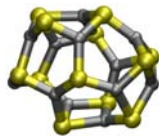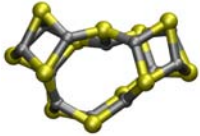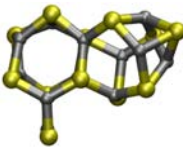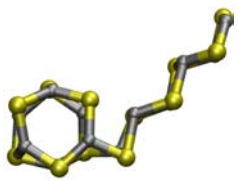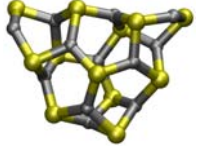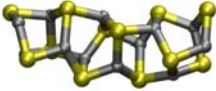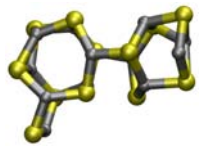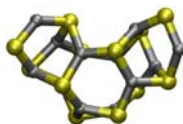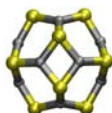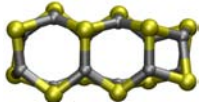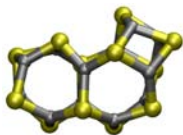
potential energy results obtained for the nanoparticles in vacuum, the enthalpy differences between structures in this case are much smaller, within the range of a few $k_B T$ ($k_B T$=2.4 kJ/mol).

The structures located still possess the 4- and 6-membered ring motifs that are typical of ZnS, and which we observed in the simulations of ZnS in vacuum. The dominant difference between the structures obtained in water, and those in vacuum, is that we find a lar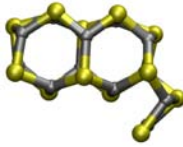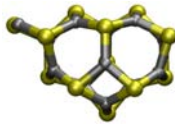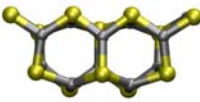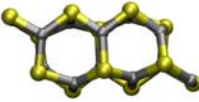ge number of structures with a 'tail' or sheet-like features protruding from the cluster, where a high percentage of 2-fold coordinated ions (by Zn or S atoms) is present. This is more likely to occur in water, as the presence of the solvent can partially compensate for the missing bonds and help stabilise these structures.

Since the enthalpy differences between the nanoparticles in water are so small, we do not expect the difference in free energy between the structures to be very different. Moreover, given the large number of different structures found, the computational time required to perform all the relative free energy differences with the path CV would have been impractically long, so we decided to attempt only a few calculations to extract the free energy differences between the structures found in vacuum when immersed in water. Unfortunately, all the attempts to calculate the free energy between two clusters in water were unsuccessful. In all cases the system preferred to move orthogonal to the path. It is probable that the free energy barrier between clusters in water is actually very low, comparable to the thermal energy, so even if we attempt to use the path method we cannot calculate this very small free energy difference between the two states. This is very different to the path calculations performed in vacuum, where the energy barrier between structures ranged between 50-175 kJ/mol (approximately 4-15 kJ/mol per formula unit). Had the simulations of clusters in water jumped back and forth between basins sufficiently we could have attempted to calculate the free energy difference between the structures directly. However, the clusters in water continued to evolve and take on new shapes throughout each simulation. To achieve sufficient statistics we would need to run the simulations for a prohibitively long period of time.

There are four compact structures in Table 5.11 which overlap with those found from the simulations performed in vacuum, and were also used with the path method discussed in the previous section to approximate the free energy differences between the structures in vacuum. These are shown again in Table 5.12, the first three transitions were calculated directly with the path method and GULP,

TABLE 5.11: Structures obtained from the MetaD simulations of $(ZnS)_{12}$ in water and optimised in vacuo, shown in order of increasing enthalpy. ΔU and ΔH is given with respect to the lowest energy structure in vacuum (the sodalite cage), where ΔH values are obtained from 200 ps NPT simulations in water, and ΔU values obtained in vacuo.
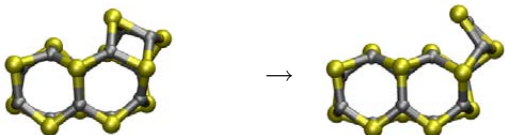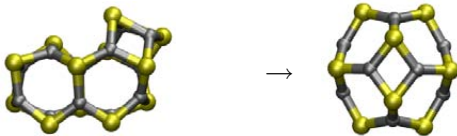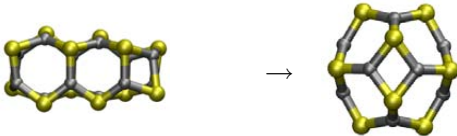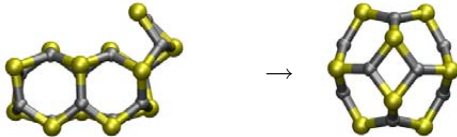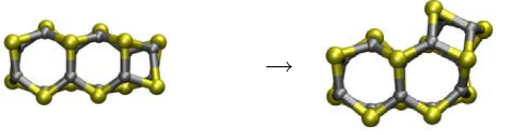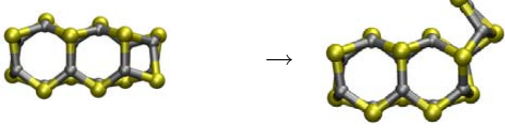
	1	2	3	4
In vacuum $\Delta U/ZnS$	23.3	13.1	21.4	25.8
In water $\Delta H/ZnS$	-7.7	-7.1	-7.1	-7.1
	5	**6**	**7**	**8**
In vacuum $\Delta U/ZnS$	41.1	16.5	26.8	30.7
In water $\Delta H/ZnS$	-6.4	-5.9	-4.3	-4.3
	9	**10**	**11**	**12**
In vacuum $\Delta U/ZnS$	22.2	0.0	6.0	10.9
In water $\Delta H/ZnS$	-4.1	0.0	0.2	0.3
	13	**14**	**15**	**16**
In vacuum $\Delta U/ZnS$	14.7	9.6	17.4	17.3
In water $\Delta H/ZnS$	0.7	2.0	5.1	7.73

while the energy values for the final three transitions can be obtained by taking combinations of the first three 'reactions'. We have tabulated these free energy values again to illustrate the small differences in enthalpy between these structures when solvated.

The relative enthalpy values in both Table A.39 and 5.12 are particularly striking, as the various low enthalpy structures are all within ambient thermal energy of each other. In the case of the path examples we can compare the relative enthalpy (of the simulations in water) to the free energy differences calculated in vacuum, and can already see the enthalpy values are approximately one order of magnitude less than the free energy difference. In comparison to the free energy surface of the ZnS clusters in vacuum, the free energy surface for ZnS solvated is most likely much flatter.

We can see further evidence for this when we compare the plots of the trace of the inertia tensor over time for the $(ZnS)_{12}$ cluster in vacuum and solvated, Figures A.7 and 5.12 respectively. The plot for $(ZnS)_{12}$ in vacuum has distinct basins which are explored for relatively long periods of time (more than 1 ns), while the plot for the same system in water shows that many more basins are explored, however the basins are far less distinct and less time is spent in each 'basin'. Another way to describe this is that the free energy surface being explored in the case of solvated ZnS clusters is essentially flat. This explains also why the metadynamics simulations using the path CVs for the nanoparticles in water were not successful. The path variables are used to describe the transition, or path, between two states A and B. In theory only structures along the pre-defined path should be explored by the metadynamics simulation. However, in the case of our nanoparticles in water, there are many structures with similar trace of inertia tensor values in nearby minima, and there is little or no energy barrier between different states. As the bias is added during the path metadynamics simulation it is very easy for the system to fall into these nearby and easily accessible minima to explore configurations which are not relevant to the transition defined by the path collective variables. With this occurring we found that our metadynamics simulation using the path CV did not obtain sufficient statistics to obtain free energy differences between the desired initial and final configurations.

TABLE 5.12: Free energy differences calculated for clusters in vacuum via MetaD using the path variable, and using lattice dynamics. The differences in enthalpy for the same structural transitions are also given, calculated from the NPT simulations of ZnS in water.

Structures		In vacuum Lattice Dynamics ΔA/ZnS (kJ/mol)	In vacuum MetaD Path ΔA/ZnS (kJ/mol)	In water Average ΔH/ZnS (kJ/mol)
	→	+3.9	+4.0	+0.4
	→	-10.5	-10.6	-0.3
	→	-6.1	-5.0	-0.2
	→	-14.4	-14.6	-0.7
	→	+4.4	+5.6	+0.1
	→	+8.3	+9.6	+0.5

5.4   Conclusions

In this chapter we have investigated very small nanoparticles of ZnS using the trace of inertia tensor as a CV. While this CV was effective for exploring the phase space of nanoparticles and finding new configurations, it does have significant limitations. For example, we found that the basins being explored in the free energy surface

overlap each other, so it is impossible to directly calculate the free energy difference between two basins without employing other free energy methods or other CVs. Another limitation of the CV we have used is that for larger sized nanoparticles, with a great number of degrees of freedom the free energy surface was far more difficult to explore. The larger particles we looked at had a greater tendency to break apart rather than significantly exploring the phase space of the more compact structures. This is in some respects as a result of the overlap between basins; as the particle size increases there are many possible structures that will exist that have the same trace of the inertia tensor value - which makes it difficult, if not impossible, for metadynamics to explore all the structures of interest.

A significant outcome from this first part of our study is the use of the path variable to determine the free energy difference between structures obtained in vacuum. The free energy differences calculated were very close to the values obtained from lattice dynamics, giving us confidence in this approach. Unfortunately the transitions between structures were so facile in water, that it was difficult to use the same method to calculate the free energy differences. We found the structures explored during the path simulation were not only those describing the transformation from state A to state B, but also additional states which should not be explored along the path. This may be a significant side effect of the potential used to model the interactions of ZnS with water, and this will be discussed in later chapters.

Another interesting aspect of the low energy clusters determined is the overlap with the composite building units of zeolite frameworks, and again this will be revisited in later chapters.

In the next chapter we will first attempt to address one of the disadvantages of the trace of the inertia tensor - namely, that it was unsuitable for distinguishing between larger cluster sizes. We will begin using the Steinhardt parameters as introduced in Chapter 4.

Chapter 6

Metadynamics simulation of ZnS phase transitions employing Steinhardt parameters

6.1 Introduction

In the previous chapter we showed that the trace of the inertia tensor can be used as a collective variable (CV) to explore the phase space of small nanoparticles, but was less successful for larger nanoparticles (> 50 atoms). As the size of the system increases there are more structures possible that can have the same value of the trace of the inertia tensor. We found for nanoparticles of 100 atoms or more that the system was more likely to elongate and eventually be pulled apart rather than exploring dense phases of interest with different internal order. Another limitation we experienced is that as the system explored new minima in phase space, the free energy differences between structures were unable to be directly obtained using our metadynamics (MetaD) data as the minima in the free energy surface overlap when projected on to the CV. This implies that another CV orthogonal to the one used would need to be employed to explore the phase space in a way which avoids this overlap.

The trace of the inertia tensor as a CV helps evolve the shape of the system and in turn different structures are also explored. However, this CV is not a descriptor for the internal or crystalline order of the nanoparticles. The purpose of the studies

detailed in this chapter is to investigate a different CV with metadynamics to again explore the phase space of nanoparticles, specifically those of ZnS, to examine whether it may be more effective. We introduced the Steinhardt parameters in Chapter 4. These parameters can be used to determine the local order around a specific atom, or as global parameters that give an indication of the overall crystalline order in a solid. As we have previously mentioned, these parameters have been extensively used to explore the transition from liquid to solid states, and recently have been used to study nucleation of water to form ice[279, 280, 282, 299]. The Steinhardt parameter has also been used in conjunction with MetaD before, but at the time of our investigation it had not been used for inducing phase changes in nanoparticles. Primarily, it had been used to investigate the freezing of water[280]. Concurrently to our studies, Quigley *et al.*[281, 300] did use the Steinhardt parameter to investigate phase changes in calcium carbonate nanoparticles in water.

The aim of this section of our study is to use the Steinhardt parameter as a collective variable in metadynamics to explore phases of zinc sulfide. We aim to first show that this is achievable with periodic zinc sulfide (*i.e.*, bulk), and subsequently in nanoparticles. We have focused on the Q_4 Steinhardt parameter as the values for different crystal structures are distinct enough to distinguish between different crystal structures[272]. An alternative, or complementary, parameter could be the Q_6 parameter. However, the Q_6 values for different phases of ZnS are all of the same order of magnitude, and therefore this quantity is more useful as a measure of overall crystallinity[272]. The following section will cover in more detail some of the methods used to generate our trajectories.

6.2   Methods

A rigid-ion forcefield was used to model zinc sulfide in the present work, as given in Table 6.1. This model was fitted in GULP[160] using the cell parameters and elastic constants, in the same way the ZnS shell model of Wright and Gale [95] was generated. GULP[160] uses a method of fitting known as "relaxed" fitting where the structures are optimised throughout the fitting procedure. The method still uses a sum of squares, as in conventional fitting. However, the displacement of the structural parameters with respect to the given experimental values is used as a means of judging the quality of the fit, rather than using the forces. The relaxed

fitting method is much more computationally expensive than conventional fitting, and is optimal for use once a reasonable set of potential parameters have already been generated.

We decided to use a simplified rigid ion model over a shell model so it would be possible to obtain results from larger nanoparticles in a more timely manner, as a rigid ion model is less computationally expensive. As was discussed in Chapter 2, an ion represented by a shell model is comprised of a central core which has an outer 'shell' attached by a harmonic spring. The outer shell attempts to represent the electron cloud and aims to simulate the polarisability of an atom. The additional computation of the shell's movement throughout a simulation is computationally intensive, and for these reasons makes a shell model more expensive to use.

Species	Charge (e)	
Zn	+1.2534	
S	-1.2534	
Lennard-Jones 12-6	A (eV Å^{12})	B (eV Å^6)
S - S	1003475.3	0.00
Zn - S	5669.3544	0.00

TABLE 6.1: Interatomic potentials used for the MetaD simulations of ZnS using the Steinhardt parameters as collective variables. These parameters were obtained using GULP[160], fitting with the wurtzite and sphalerite structures and physical properties, such as the elastic constants[95].

For the simulations of nanoparticles in water, we have used the same CVFF water of Lau *et al.* [287], and the ZnS-water interactions of Hamad *et al.* [110] as in the previous chapter.

We have already introduced the Steinhardt parameter in Chapter 4, and the specifics of its implementation. One point we have not yet discussed is the need for a smooth switching function to replace the use of a sharp cut-off radius when assessing if one atom is a neighbour of another. The calculation of the Steinhardt parameter, Q_l, requires the definition of which atoms are neighbours of a particle. As we have already introduced, each vector, $\mathbf{r}_{ij}$, that joins a particle i to a neighbouring particle j is considered a 'bond', and a set of values $Y_{lm}(\theta(\mathbf{r}_{ij}), \phi(\mathbf{r}_{ij}))$ is associated with each bond, via the local Steinhardt parameter, $q_{lm}(i)$, given in

Equation 6.1.

$$q_{lm}(i) = \frac{1}{N_b(i)} \sum_{j=1}^{N_b(i)} Y_{lm}(\theta(\mathbf{r}_{ij}), \phi(\mathbf{r}_{ij})) \tag{6.1}$$

Here the m subscript indicates a set of $2l+1$ integer values ranging from $-l$ to $+l$ and $N_b(i)$ is the number of bonds associated with atom i. As also described in Chapter 4, a combination of the local order parameters can give a rotationally invariant global order parameter, given by Equation 6.2;

$$Q_l = \left(\frac{4\pi}{2l+1} \sum_{m=-l}^{l} |\bar{Q}_{lm}|^2 \right)^{1/2} \tag{6.2}$$

where:

$$\bar{Q}_{lm} = \frac{\sum_{i=1}^{N} N_b(i) \; q_{lm}(i)}{\sum_{i=1}^{N} N_b(i)} \tag{6.3}$$

It is important that we calculate the pair distribution functions of the known bulk polymorphs to determine at what radius the first shell of neighbours is located. This first shell of neighbours determines the cut-off required for the definition of a 'bonded neighbour' within the Steinhardt parameter. An appropriate cut-off is found to be approximately 4.5 Å, as this safely includes all of the atoms within the first neighbouring shell. However, for the implementation of the Steinhardt parameter in metadynamics, it is not appropriate to have a discontinuous function for the definition of neighbours. During the simulation the integration of the forces associated with each atom should be a continuous function to ensure that the dynamics are consistent even when atoms are moving across the cut-off region. This problem has been encountered in previous studies using MetaD[219, 261, 280, 301]. For example, the implementation of the coordination number of an atom as the collective variable is similarly problematic - where the definition of a neighbour would ordinarily be considered within a sharp cut-off radius; in MetaD it must be implemented with a switching function that smoothly transitions from 1 (considered a neighbour) to 0 (not considered a neighbour).

We implemented a switching function of the same form used in previous studies, and that is outlined in the article of Bonomi *et al.* [302] which describes the

PLUMED metadynamics plugin[302]. The switching function and the conditions under which it is used are given by Equation (6.4). Above a certain threshold the switching function provides a value within the range of 0 to 1. There is a singularity when $\dfrac{r_{ij} - d_0}{r_0} = 1$, and this is accounted for in the cases below, where the value returned will be $\dfrac{n}{m}$.

$$f(r_{ij}) = \begin{cases} 1 & \text{if } \dfrac{r_{ij} - d_0}{r_0} \leqslant 0 \\[2ex] 0 & \text{if } \dfrac{r_{ij} - d_0}{r_0} \geqslant \text{threshold} \\[2ex] \dfrac{1 - \left(\dfrac{r_{ij} - d_0}{r_0}\right)^n}{1 - \left(\dfrac{r_{ij} - d_0}{r_0}\right)^m} & \text{if } 0 < \dfrac{r_{ij} - d_0}{r_0} < \text{threshold} \\[2ex] \dfrac{n}{m} & \text{if } \dfrac{r_{ij} - d_0}{r_0} = 1 \end{cases} \tag{6.4}$$

In our case the threshold is defined by:

$$\begin{aligned} \text{threshold} &= 0.000001^{1/(n-m)} \\ &= 0.000001^{1/(6-12)} \\ &= 10 \end{aligned} \tag{6.5}$$

Generally the d_0 value is taken as the position of the first peak of the pair distribution function being studied, and r_0 is the maximum width of the peak[302]. The values of n and m define how 'steep' the switching function is. The choice of these parameters will vary dramatically depending on the system being studied, and there is no definitive answer to which are the best parameters to use with any given switching function.

Bulk zinc sulfide was used as a test case for our implementation of the Steinhardt parameter with metadynamics. We expected to observe phase transformations between the two stable polymorphs of zinc sulfide, sphalerite and wurtzite, and hoped to investigate new phases. When investigating phase transformations in bulk phases it is necessary to use a supercell that is commensurate with other expected phases. In this case we are at least hoping to find transitions occurring between sphalerite and wurtzite. As we have discussed in the introductory chapters, sphalerite exists as an A-B-C-A-B-C stacked polymorph and wurtzite an A-B-A-B stacked polymorph. We expected that to force a transition between

the two polymorphs would require shearing of layers of ZnS. The supercell required would need to have a number of layers divisible by 3 and 2, to enable A-B-C and A-B stacking. The supercell we have chosen contains 432 atoms, shown in Figure 6.1, and has 6 layers of atoms in the A-B-C-A-B-C formation. Another comment to make is that the larger the supercell, clearly the more possible polymorphs or phases that can be explored, including the possibility of intergrowths and polytypes, or significant changes in the structure, such as alternate polymorphs or stacking faults.

We have already given the global Steinhardt parameters for a number of simple crystal structures in Chapter 4. The fcc and hcp values are given again in Table 6.2, as these are the values for the like atoms (Zn-Zn or S-S) of the two stable polymorphs of zinc sulfide.

TABLE 6.2: Steinhardt parameters Q_4 and Q_6 for sphalerite and wurtzite crystal structures of zinc sulfide, based on like atom neighbours (Zn-Zn and S-S) which form fcc and hcp layers[272].

Structure	Q_4	Q_6
Sphalerite	0.19094	0.57452
Wurtzite	0.09722	0.48476

6.3   Results and Discussion

There are three distinct sets of results to cover in this section. The first are the results from the MetaD simulations on bulk ZnS, which were performed to test if the Q_4 Steinhardt parameters can be successfully used with MetaD to push the system to different polymorphs. This will be followed by a discussion the results of the same MetaD procedure with the Q_4 parameter CV applied to finite systems, in our case, nanoparticles of ZnS. Finally, the results of MetaD simulations on the same zinc sulfide nanoparticles when solvated by water will be presented.

6.3.1   Bulk zinc sulfide

A 432 atom sphalerite supercell was created by repetition of the sphalerite unit cell using GDIS[288]. As described in the previous section, it is important to

have a multiple of six atomic layers to enable transformation between ABAB and ABCABC stacking of the two ZnS polymorphs by 'shearing' of the atomic layers. The resulting structure was optimised at 0 K, followed by a 100 ps NPT MD run at 300 K and 1 atm, with a 0.1 fs timestep, to determine relaxed cell parameters of the system at this temperature. This was followed by a 500 ps NVT MD run at 300 K with a 1 fs time step to further equilibrate the system before performing any biased MD. The final equilibrated structure from the NVT simulation was taken and used as the starting structure of the MetaD simulations. The starting structure for the sphalerite run is shown in Figure 6.1.

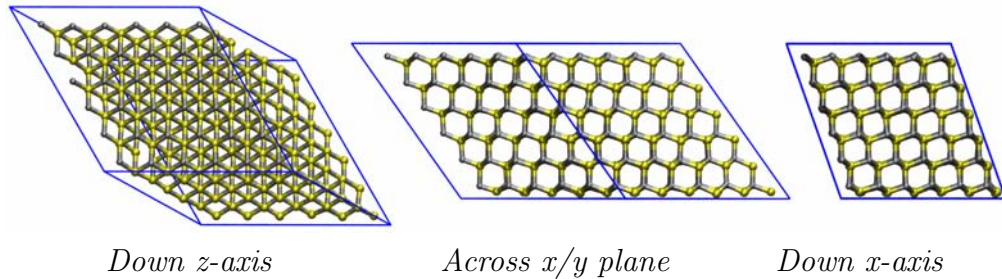*Down z-axis*   *Across x/y plane*   *Down x-axis*

FIGURE 6.1: 432 atom sphalerite starting structure shown from three directions.

The pair distribution functions for sphalerite were calculated for the Zn-Zn and S-S pairs as shown in Figure 6.2. We also calculated the pair distribution functions for the Zn-Zn and S-S pairs for wurtzite, which are shown in Figure 6.3.

The switching function we have chosen for the bulk structures is shown on the pair distribution plots given in Figures 6.2 and 6.3. The switching function parameters are d_0=3.9 Å, r_0=0.25 Å and n=6 and m=12.

$$f(r_{ij}) = \left(\frac{1 - \left(\frac{r_{ij} - 3.9}{0.25} \right)^6}{1 - \left(\frac{r_{ij} - 3.9}{0.25} \right)^{12}} \right) \tag{6.6}$$

Once an appropriate cut-off had been chosen, the calculation of the Q_4 and Q_6 values could be tested for these structures, to demonstrate that the correct values are obtained. The results of the global Q_4 and Q_6 values are given in Table 6.3. The 0 K optimised structure of sphalerite gives exactly the literature Q_4 and Q_6 values for an fcc structure, while the wurtzite values are slightly off from the literature values for an hcp structure. This implies that the wurtzite structure with the forcefield we are using is slightly distorted away from a perfect hcp lattice. This
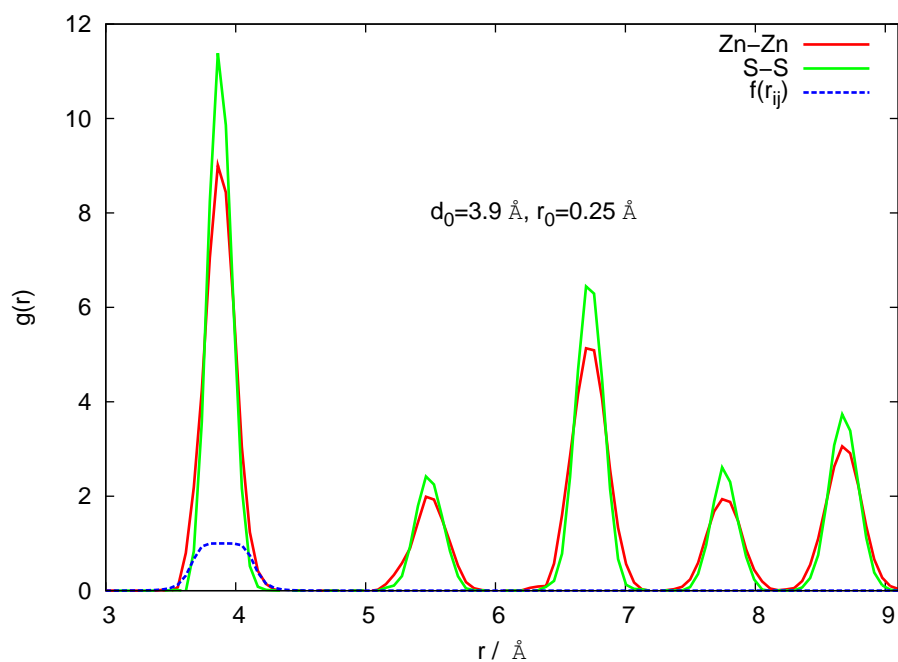
FIGURE 6.2: Pair distribution functions for sphalerite, g(r) for both Zn-Zn and S-S are shown. The switching function used for the neighbour cut-off is defined as $f(r_{ij})$ and is indicated in the figure.
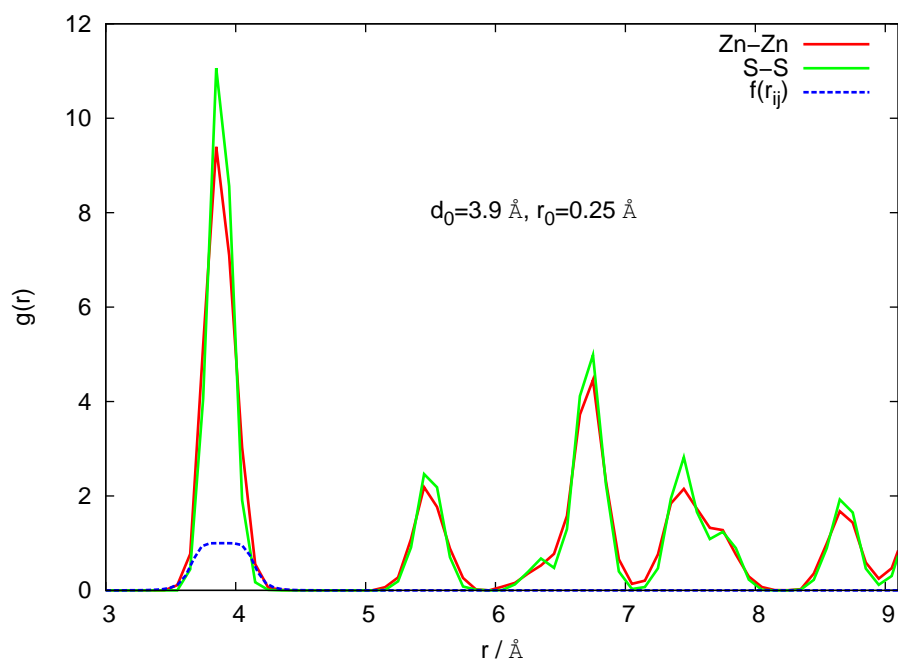

FIGURE 6.3: Pair distribution functions for wurtzite, g(r) for both Zn-Zn and S-S are shown. The switching function used for the neighbour cut-off is defined as $f(r_{ij})$ and is indicated in the figure.

is not surprising as sphalerite has a cubic structure which makes it *isotropic*; the only degree of freedom is one unit cell parameter, so regardless of whether the forcefield makes the unit cell smaller or larger than experiment, the deviation will be the same in all directions. The Steinhardt parameters are *directional*; they do not rely on the distance between particles, only the *orientation*. In the case of wurtzite, the unit cell has two parameters a and c. If the ratio of these deviates from a perfect hcp lattice the Steinhardt parameters will be altered. Though the Q_4 values deviate slightly from the literature value, the deviation is small, being of the order of 1%. A comparison of these values with the 300 K equilibrated structure show this deviation is less than that due to thermal vibrations in the structure, and we can be confident our values are representative of the given crystal structure.

TABLE 6.3: Comparison of global Q_4 and Q_6 for sphalerite (fcc) and wurtzite (hcp). Q_4 and Q_6 values were obtained from like-atoms for the structures obtained after 0 K optimisation and 300 K relaxation runs using the rigid-ion model.

Sphalerite	Q_4	Q_6
Literature fcc[272]	0.19094	0.57452
0 K optimised	0.19094	0.57452
Average over 300 K equilibration	0.18919	0.56456
Wurtzite	Q_4	Q_6
Literature hcp[272]	0.09722	0.48476
0 K optimised	0.09802	0.48494
Average over 300 K equilibration	0.09698	0.47643

Two MetaD simulations were performed on the 432 atom ZnS supercell. One simulation was performed with the Q_4 parameter bias applied only on the Zn-Zn pairs, and another simulation with the bias applied on both the Zn-Zn and S-S pairs. First, we will look at the simulation performed with a bias only applied to the Zn-Zn pairs. The Gaussian parameters for our MetaD runs for this structure all had height W=1.0 eV and width σ=0.01. The plot of the Q_4 values throughout the simulation are given in Figure 6.4. The simulation was run for over 21 ns and explored a wide variety of structures. To analyse the structures explored during this long trajectory, frames were taken at 250 ps intervals and optimised, first using DL_POLY[303] and then refined further using GULP[160]. The optimised structures of interest are given in Table 6.4, along with their Q_4 value and relative
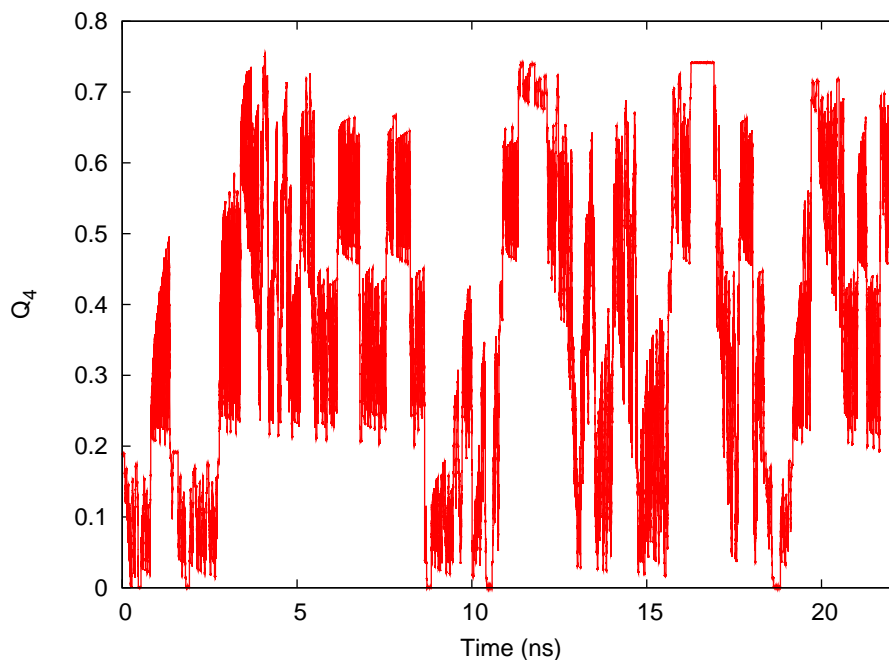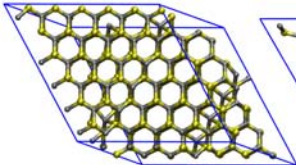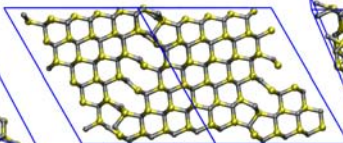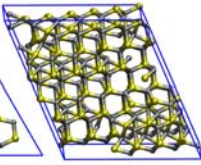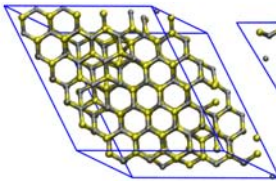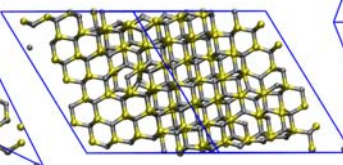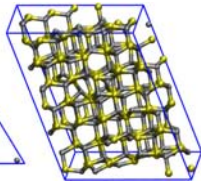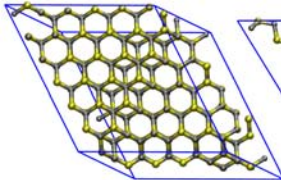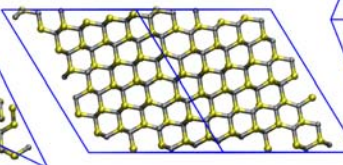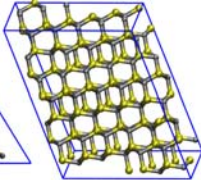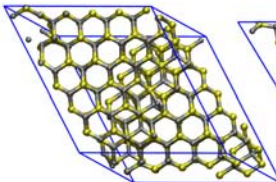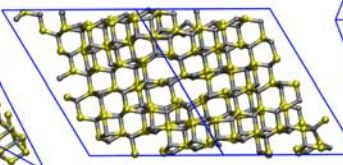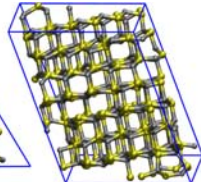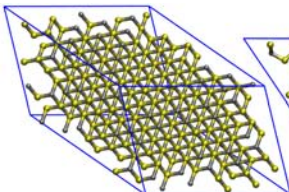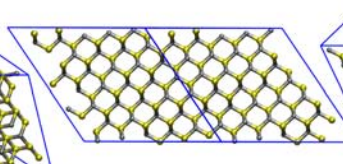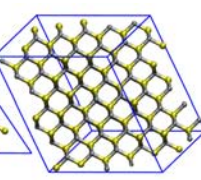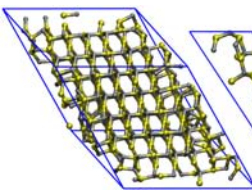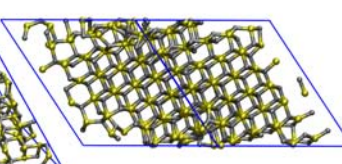
FIGURE 6.4: Plot of Q_4 vs. time for the zinc atoms in a 432 atom supercell of ZnS, initially as sphalerite, simulated using the Q_4 Steinhardt parameter as a CV with MetaD. The Gaussian parameters used were W=1.0 eV and σ=0.01. The MetaD bias was applied only to the Zn-Zn pairs.

energy (ΔU) with respect to sphalerite (kJ/mol per formula unit). The structures were optimised in GULP with constant volume (NVT) and constant pressure (NPT) conditions, to investigate to what extent the fixed volume of the cell may affect the energies of explored phases. The simulation quickly evolved from the starting sphalerite structures to defective wurtzite phases, or structures with mixed phases, while returning to sphalerite again at 7.25 ns, as shown in Table 6.4. In general the ΔU obtained at constant volume is significantly higher than that obtained when the cell is allowed to relax, and this is particularly significant in the case of sphalerite. At 7.25 ns sphalerite is explored again, however the orientation of the crystal within the same cell volume and shape has changed with respect to the starting configuration. As a result, an optimisation at constant volume is significantly higher in energy than the constant pressure calculation. The Q_4 values of the structures explored generally fluctuate around the Q_4 value for wurtzite (approximately 0.0971), supporting the identification of these as partially wurtzite phases. The views in Table 6.4 shown down the z-axis indicate 'incomplete' shearing of the layers across each other - allowing the formation of defective regions of one phase, or for two phases to exist in the same structure.

The second MetaD simulation performed on the sphalerite supercell used a Q_4 bias

TABLE 6.4: Structures found from Zn-Zn biased Q_4 MetaD simulation of 432 atom sphalerite. The relative energies (ΔU) are quoted with respect to sphalerite in kJ/mol per formula unit.

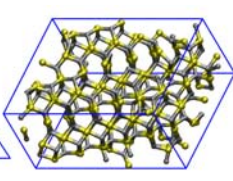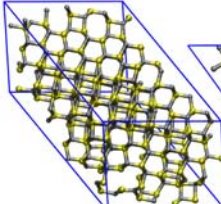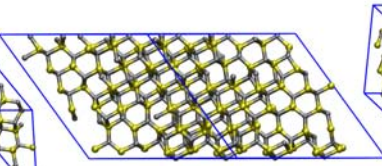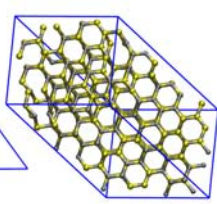| Time (ns)	Structure (Down z-axis)	(Across x/y plane)	(Down x-axis)	ΔU NVT	ΔU NPT	Q_4
4.00				15.7	6.0	0.0788
4.75				16.7	6.4	0.0793
5.25				13.3	3.3	0.0992
5.50				17.4	10.9	0.0909
7.25				21.8	0.0	0.1909 **Spha**
13.00				24.3	29.4	0.1766
18.00				20.1	5.5	0.0847
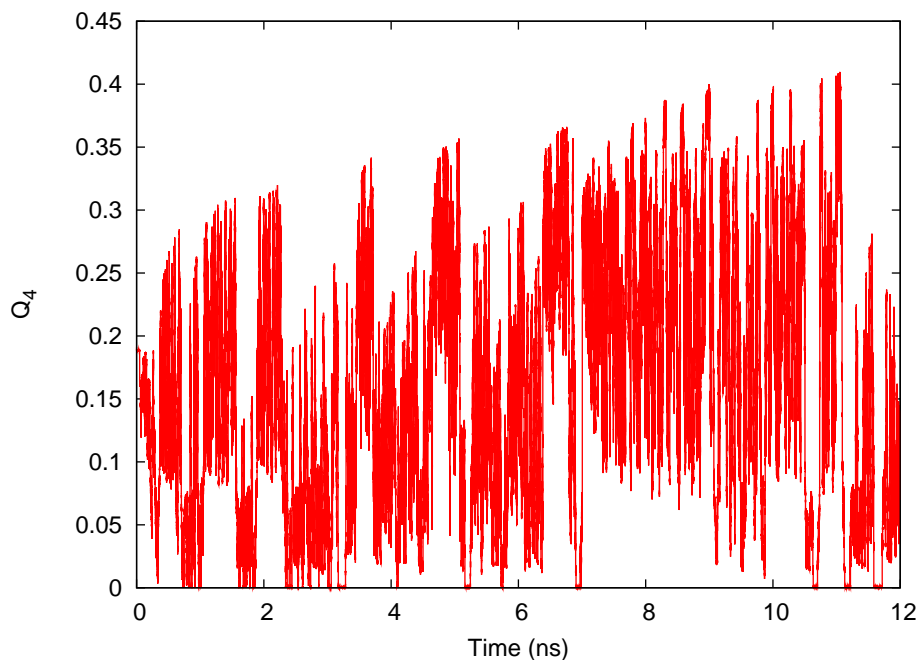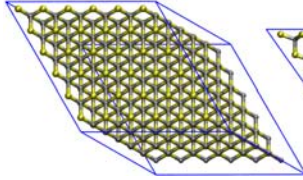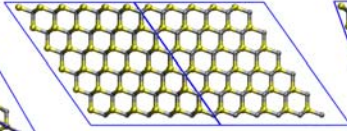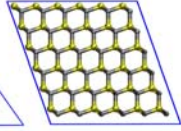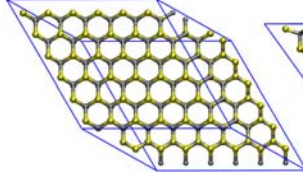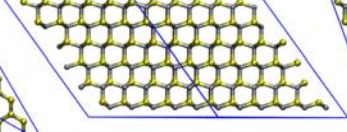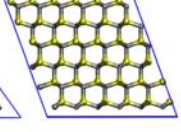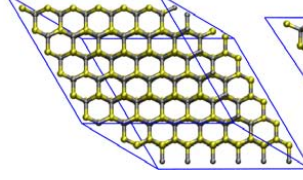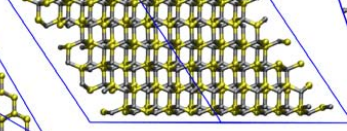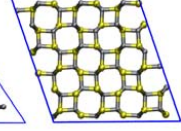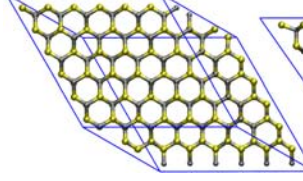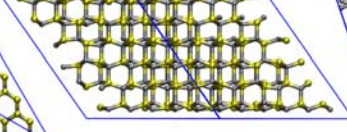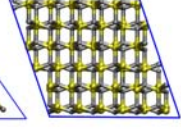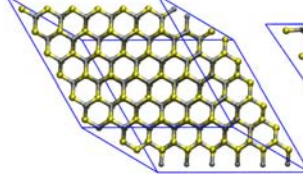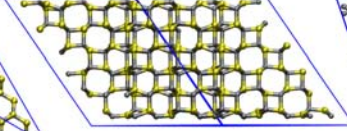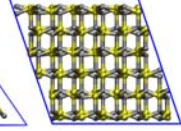
FIGURE 6.5: Plot of Q_4 vs. time for the zinc atoms in a 432 atom supercell of ZnS, initially as sphalerite, simulated using the Q_4 Steinhardt parameter as a CV with MetaD. The Gaussian parameters used were W=1.0 eV and σ=0.01. The MetaD bias was applied both to the Zn-Zn and S-S pairs.

on both the Zn-Zn and S-S pairs. The same Gaussian parameters of W=1.0 eV and σ=0.01 were used for both of the collective variables. The plot of the Q_4 values throughout the simulation are given in Figure 6.5. The simulation was performed using NVT conditions. Structures obtained from this simulation are given in Table 6.5.

The simulation has proceeded very differently to the MetaD simulation performed with a Q_4 bias applied on only the Zn-Zn pairs. Rather than exploring very mixed and defective phases, the simulation performed with a bias on both Zn-Zn and S-S pairs shows very clean transformations resulting from complete shearing of ZnS layers. The relative energies of the explored structures are all also lower in energy than sphalerite, while in the simulation performed with a Q_4 bias only on Zn-Zn pairs all the structures had positive ΔU values with respect to sphalerite. Additionally, the simulation quickly found these distinct phases, with a phase transformation from sphalerite to wurtzite after only 250 ps of simulation. This simulation has also explored another interesting phase formed at 875 ps which has 4- and 8-membered rings along one crystallographic direction. The remaining phases given in Table 6.5 show sections of the crystal comprised of the same 4- and 8-membered ring motifs, though regions of wurtzite and

TABLE 6.5: Structures found from the Zn-Zn and S-S biased Q_4 MetaD simulation of 432 atom sphalerite. The relative energies (ΔU) are quoted with respect to sphalerite in kJ/mol per formula unit.

Time (ps)	Structure (Down z-axis)	(Across x/y plane)	(Down x-axis)	ΔU NVT	ΔU NPT	Q_4
0				0	0	0.1909 **Spha**
250				-3.0	-3.3	0.0894 **Wurtz**
875				-1.6	-2.6	0.0811 **BCT**
1625				-1.2	-1.0	0.0708
1875				-0.7	-1.2	0.0801

sphalerite are still apparent. The implementation of the Q_4 parameter as a CV in metadynamics appears to be very successful for exploring new phases in a bulk system. However, before discussing simulations performed on nanoparticles we should first investigate the phase we found in our bulk simulations with the 4- and 8-membered ring motif.

6.3.1.1 BCT Phase

A phase distinct from either sphalerite or wurtzite was observed at 825 ps in the MetaD simulation performed on bulk ZnS with a bias on both Zn-Zn and S-S pairs, and is shown in Figure 6.6.

Down z-axis   *Across x/y plane*   *Down x-axis*
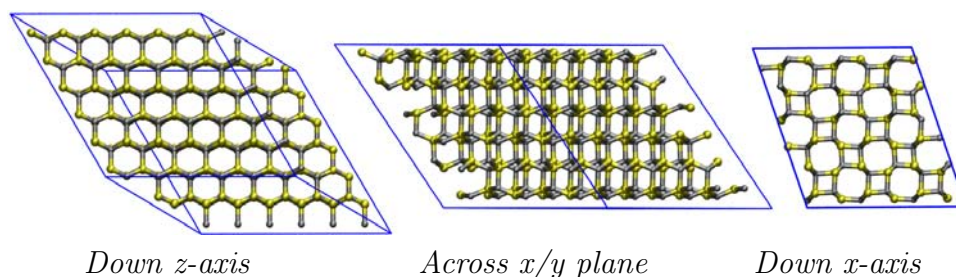
FIGURE 6.6: Structure obtained at 825 ps in MetaD simulation performed with a Q_4 bias on Zn-Zn and S-S pairs. The structure was optimised in GULP using the same rigid ion model and is the body-centered tetragonal (BCT) structure.

After reviewing the literature[304–310] we determined that this phase is known as body-centred tetragonal (BCT) and exists as a zeolite framework of the same name[311]. This phase has been mentioned in the literature in other theoretical studies of the phases of zinc sulfide, in particular in the work of Hamad and Catlow [304]. They observed the BCT phase in ZnS nanoparticles in the size range of 1-4 nm optimised using simulated annealing methods[304]; two examples from their study are shown in Figure 6.7. So far this phase has not been identified experimentally for ZnS. A literature review into the BCT phase reveals the phase has also been studied recently as a possible polymorph of ZnO[305–308], and suggested as a new allotrope of carbon[309] and silicon[310].
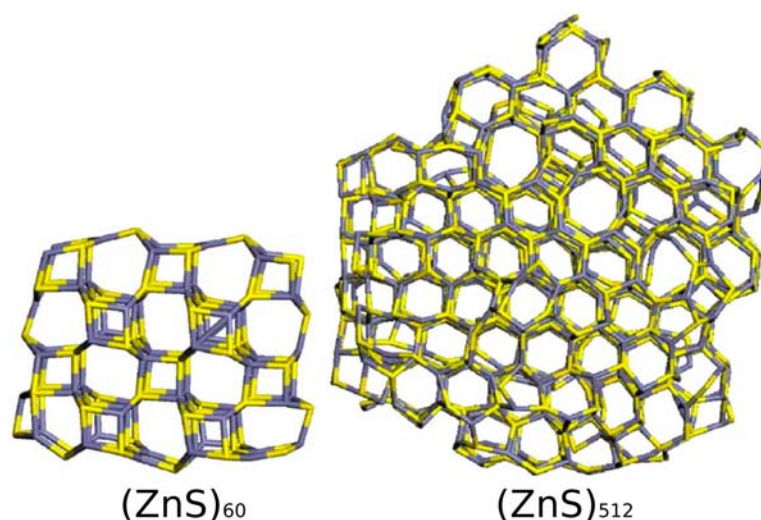
$(ZnS)_{60}$ $(ZnS)_{512}$

FIGURE 6.7: Nanoparticles of size $(ZnS)_{60}$ and $(ZnS)_{512}$ showing regions of the BCT phase, obtained via simulated annealing by Hamad and Catlow [304]. Image reproduced from Hamad and Catlow [304].

Our method uses the nearest neighbours to determine the crystallinity in the system, so it is interesting to analyse the structure in terms of nearest neighbours, and compare this to the literature. To the best of our knowledge the Q_4 and

Q_6 values have not been quoted in the literature for the BCT zeolite framework phase we have found in our simulations. First, if we consider the pair distribution function of Zn-Zn and S-S pairs given in Figure 6.8, we can see there are two peaks indicating the nearest neighbours, below a cut-off of approximately 4.5 Å. This corresponds to the like atoms in our BCT structure having a coordination number of 11, and is supported by the tetragonal packing of equal spheres introduced by Baur [267]. A comparison of our 11 coordinated cluster, and that of Baur [267] is given in Figure 6.9. One important point to make is that though the structure has been referred to as the "body-centred tetragonal" phase, here, and in previous literature already mentioned, this phase corresponds to the BCT zeolite framework, and is distinct from another form of tetragonal packing known as body-centred tetragonal, in which there is a coordination number of 10[267, 312].

The distinction between these two forms is also given in Baur [267], in a comparison of density of packing in terms of the space occupied by the spheres, as given in Table 6.6.

TABLE 6.6: Comparison of the coordination number and density of different packed structures. Table reproduced from Baur [267].

Packing of equal spheres	Coordination Number	Density (fractional)
Close packing (hcp and fcc)	12	0.7405
Tetragonal packing	11	0.7187
Body-centred tetragonal	10	0.6981

The cut-off we have used for calculating the local q_4 and q_6 values for each atom in our BCT ZnS structure gives 11 neighbours. S-S and Zn-Zn clusters of nearest neighbours are given in Figure 6.10, with some of the angles indicated on both of the clusters. Though the clusters appear superficially very similar, there are slight distortions in the angles between the neighbours, which results in a shift in the Q_4 and Q_6 values obtained for the BCT phase. The Steinhardt values obtained are given in Table 6.7, and imply that the Zn-Zn neighbours have slightly different environments to the S-S clusters. This distortion is a result of the forcefield we are using, and not due to problems with the optimisation of an initially distorted structure. We tested this with a 'reference' BCT structure, taking the zeolite framework from the International Zeolite Association structure database[297]. The BCT topology was taken from the zeolite database and transformed into a zinc sulfide form, where each of the T sites are alternating Zn and S atoms. Optimising this structure using the same rigid ion forcefield yielded a structure with the same
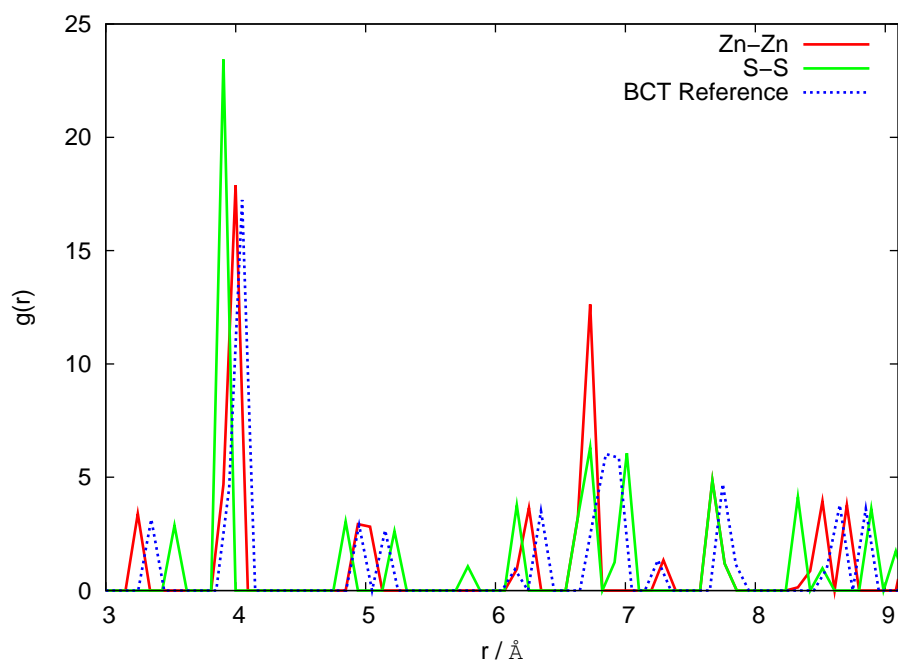
FIGURE 6.8: Pair distribution functions (PDF) for the BCT phase calculated from a 432 atom periodic ZnS structure obtained from a MetaD run followed by optimisation. g(r) for both Zn-Zn and S-S are shown. A "reference" PDF for the BCT framework is also shown, which has been calculated from the BCT zeolite framework[297].
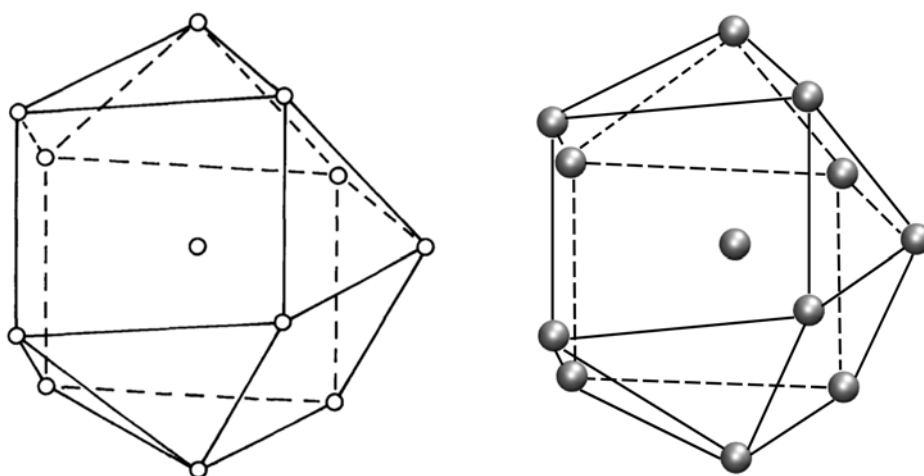
FIGURE 6.9: Baur [267] identified a new way of packing equivalent spheres known as tetragonal packing, in which the coordination number is 11, this cluster is shown on the left and the image is reproduced from their work [267]. The image on the right is a Zn-Zn nearest neighbour cluster taken from our optimised BCT phase, and clearly correlates with that of Baur [267].

distortion of the angles in the tetragonal packed cluster of 11 neighbours. We also determined the Q_4 and Q_6 values for this reference (unoptimised) BCT framework to compare it to the values obtained from our optimised structure. These are also given in Table 6.7. Despite the differences in the Q_4 and Q_6 values obtained using Zn-Zn or S-S pairs in our zinc sulfide BCT structure, the global values are very close to the 'reference' values. These values for the BCT phase are not currently reported in the literature, so we have compared these to the values obtained from the BCT topology obtained from the IZA database[297].
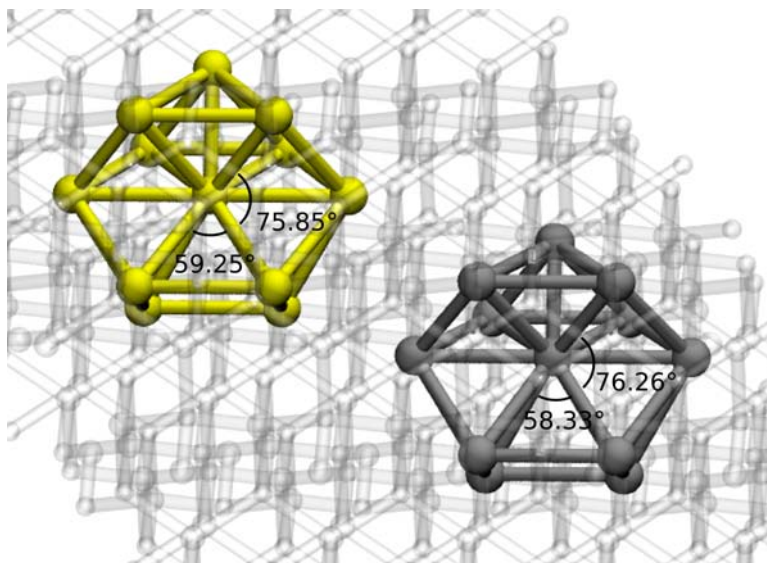
FIGURE 6.10: Clusters of nearest neighbours for Zn-Zn (grey) and S-S (yellow) pairs in the BCT form of ZnS. Two angles are indicated on the figure, showing there is some slight variation in the orientation of sulfur neighbours and zinc neighbours.

TABLE 6.7: Comparison of global Q_4 and Q_6 for the BCT phase. Q_4 and Q_6 values were obtained by calculating neighbours between like atoms (Zn-Zn and S-S neighbours) for structures optimised using the rigid-ion model. The reference BCT values were obtained from the BCT topology in the IZA database[297].

	Q_4	Q_6
Zn-Zn	0.07029	0.43247
S-S	0.12612	0.47020
Global	0.08106	0.44363
Reference BCT framework	0.08250	0.44124

Using bulk zinc sulfide as a test case, we have shown that the Q_4 Steinhardt parameters are very effective collective variables for driving phase transitions using
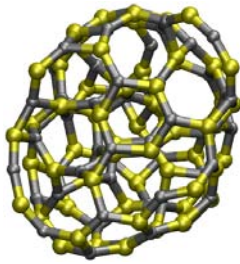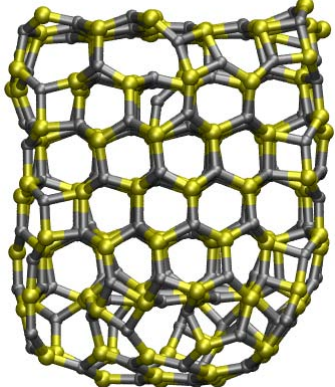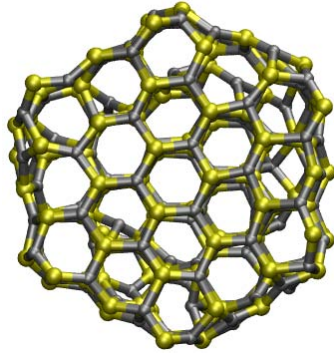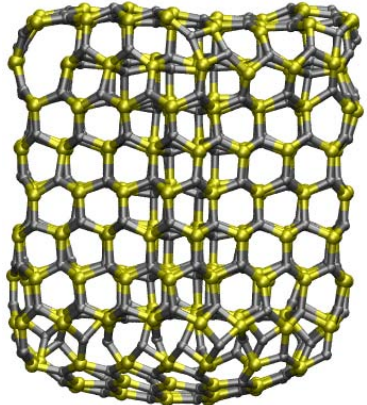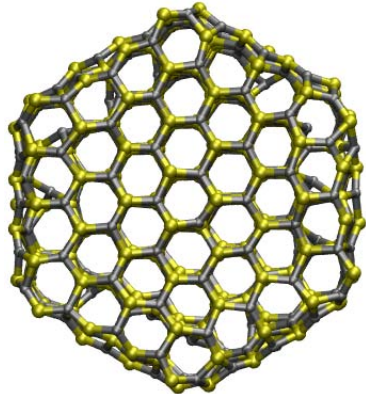
the metadynamics method, particularly when biasing both Zn-Zn and S-S pairs. In the next section we will use the same method discussed here to drive phase transitions in nanoparticles of zinc sulfide.

6.3.2 Finite particles of ZnS in vacuum

The starting structures for the nanoparticle runs were generated in the same way as for the previous chapter, where structures of different sizes were cut from bulk wurtzite using the program GDIS[288]. We chose nanoparticles of 120, 360 and 840 atoms, and these structures were optimised at 0 K followed by a 100 ps NVT MD run at 300 K with a 0.1 fs timestep. The final structures from these equilibration runs were used as the starting structures for our biased MetaD runs, and are shown from two directions in Table 6.8. As described in previous sections the Steinhardt parameters are relevant for bulk systems, as their values are calculated using the orientation of neighbouring atoms. For these studies we required larger nanoparticles, with lower surface to bulk atom ratios, for our CV to be of use. The motivation for the sizes chosen was to have a range of nanoparticles which bridge from the sizes of nanoparticles used in the previous chapter, to particles that are (in relative terms) much larger, with many more internal 'bulk' atoms, and of a comparable size to those used in previous studies[106, 108].

There are already some interesting features in the above nanoparticles before starting the biased simulations. The 120 atom cluster has already lost much of the bulk structure, and 4- and 8- membered rings can be seen, particularly at the edges of the nanoparticle. The 360 atom cluster has maintained the bulk-like structure, much more so than the smaller 120 atom particle. However, the surface layers show some 4- and 8- membered rings not seen in the bulk polymorphs. The two larger clusters we have investigated show internal strain, where the 'core' appears to have a different structure. This has also been observed in a theoretical study performed by Morgan and Madden [313], where they find internal strain present in relaxed wurtzite nanocrystals. They actually found interfaces in which 4- and 8- membered rings are formed; a cross section of one of their relaxed nanoparticles which shows these interfaces is given in Figure 6.11. They suggest that the internal strain compensates for the highly polar {0001} surfaces at either end of the hexagonal rod[313].

TABLE 6.8: Structure of the equilibrated 120, 360 and 840 atom nanoparticles cut out of bulk wurtzite, optimised at 0 K and then equilibrated at 300 K. With increasing particle size there is internal strain that can be seen in the side view images of the relaxed nanoparticles.

Size, Approx. Diam.	Viewed across ab plane	Viewed down c axis
120 atom, ≈ 1.2 nm		
360 atom, ≈ 1.6 nm		
840 atom, ≈ 2.5 nm		
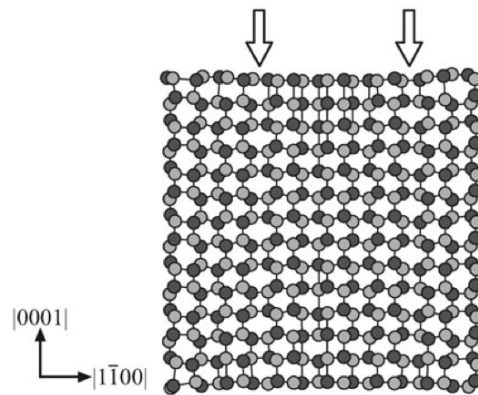
FIGURE 6.11: Image of the midsection of a relaxed wurtzite nanoparticle obtained by Morgan and Madden [313]. They found that after relaxing their 3724 atom wurtzite nanoparticle two interfaces, constructed of alternating 4- and 8- membered rings, were formed (these are indicated with an arrow). Image reproduced from Morgan and Madden [313].
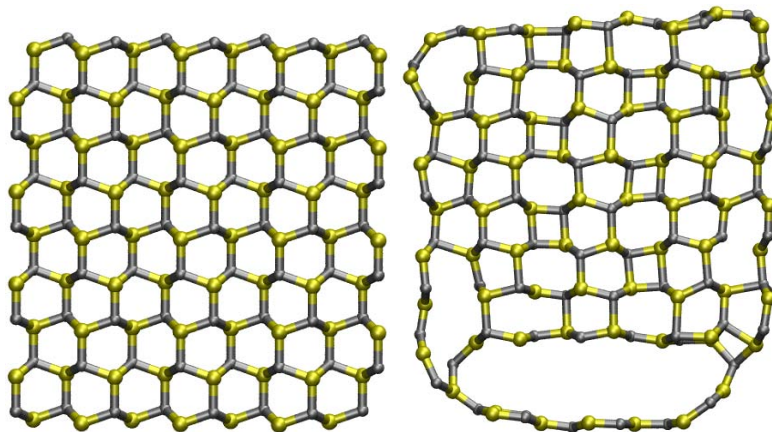
FIGURE 6.12: Cross-section taken from the 840 atom nanoparticle before any relaxation (left) and after optimisation at 0 K and 100 ps equilibration at 300 K (right). The equilibrated structure has clearly changed to form interfaces with 4- and 8- membered rings.

We took images of the cross-sections of our 840 atom relaxed nanoparticle to compare it to the findings of Morgan and Madden [313]. Relaxation of this nanoparticle was performed in DL_POLY as a 0 K optimisation run; the time step was small, 0.1 fs, and the structure was optimised after approximately 5.3 ps. The cross section is given in Figure 6.12 and shows the same cross-section region of the nanoparticle before and after relaxation. The formation of the core is initiated by relaxation of the two polar surfaces of the hexagonal nanoparticle 'rod'. There is significant flattening of the surface layer of atoms at each end of the nanorod, and rearrangement of the atoms at the corners and edges of the structure. The relaxation of the surface layers appears to initiate further rearrangement of the

nanoparticle, particularly in the core where we see inversion of wurtzite, exactly as described in the relaxation run of Morgan and Madden [313]. Morgan and Madden [313] describe the mechanism of the wurtzite nanoparticle relaxation in terms of the underlying crystal structure inducing a surface reconstruction. In our case we first observe some surface reconstruction, which in turn induces internal strain in the nanoparticle. Agrawal *et al.* [314] performed theoretical studies to explore the transformation of ZnO nanowires from wurtzite to BCT under strain. They also found the transformation to BCT was initiated at the surface, before layers below transformed. Figure 6.13 shows the breaking and forming of bonds down the c axis of the nanoparticle, producing a wurtzite region with the reverse orientation of the starting crystal - and where these layers connect is the 4- and 8-membered ring motif of the BCT phase.
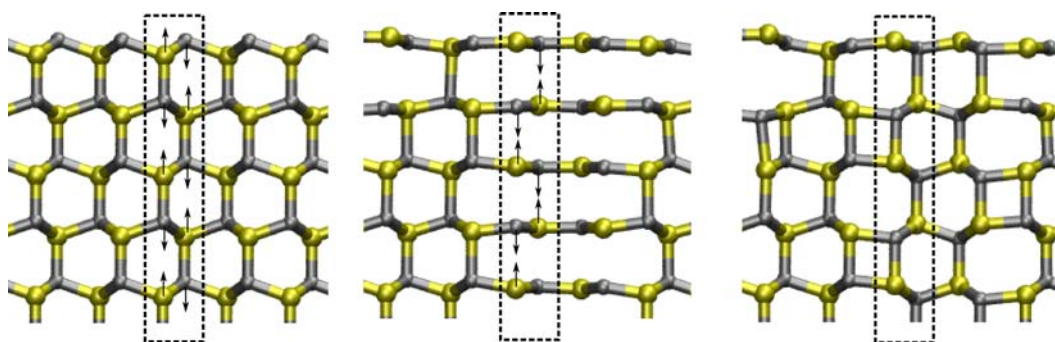
FIGURE 6.13: Closer view of the mechanism of the transformation at the core of the 840 atom nanoparticle. A sequence of atoms transforming from wurtzite to 4- and 8- membered rings of the BCT phase are highlighted. The sulfur anions are shifting up and zinc cations shifting downwards. The result is two wurtzite sections oriented in opposite directions, forming a BCT-like region between them.

For the MetaD simulations of the nanoparticles of ZnS we also require an appropriate switching function to define the neighbour cut-off range for the Steinhardt parameter. We have calculated the pair distribution function (PDF) for the 360 atom nanoparticle, shown in Figure 6.14. Overlaid on the PDF we have shown the switching function used for the bulk simulations, and two new switching functions we have based on the nanoparticle PDF. The parameters for the first "nanoparticle switching function" are d_0=3.8 Å, r_0=0.17 Å, n=6 and m=12. This function is fitted on the first pair of nearest neighbours in the PDF obtained from the nanoparticle. The second switching function is based on the bulk parameters. However the steepness of the switching region has been reduced by decreasing the
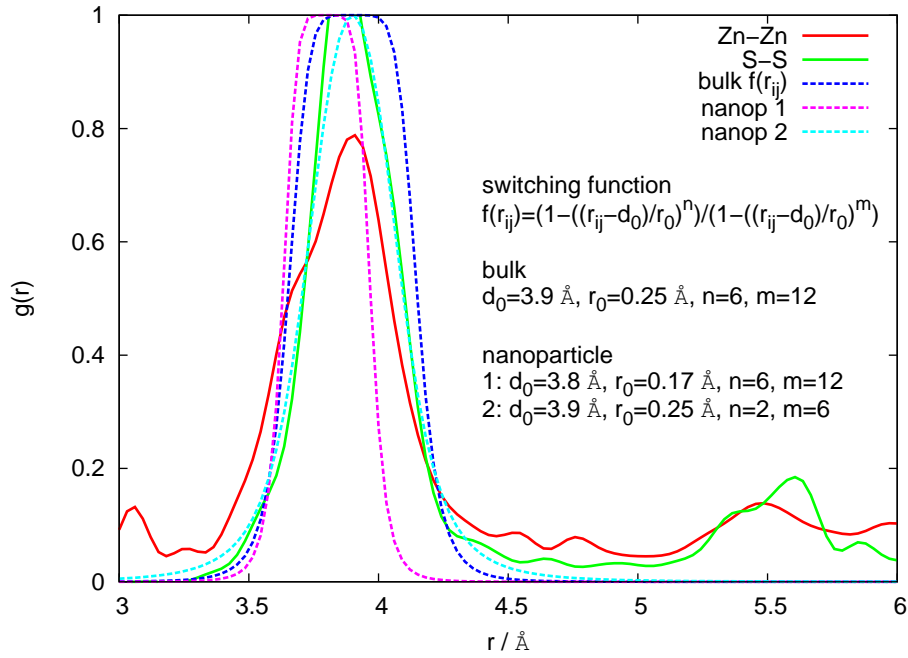
FIGURE 6.14: Pair distribution function for S-S and Zn-Zn pairs in the relaxed 360 atom ZnS nanoparticle. The switching function used for the bulk structure is shown for a comparison with the switching functions used for the nanoparticle systems.

exponents n and m; the parameters for this function are: d_0=3.9 Å, r_0=0.25 Å, n=2 and m=6.

6.3.2.1   120 atom ZnS nanoparticle in vacuum

Four MetaD simulations were performed for the 120 atom nanoparticle in vacuum. Two simulations were performed with Q_4 biases applied to only Zn-Zn pairs, and two others with the Q_4 bias applied to both Zn-Zn and S-S pairs. The differences between these simulations were the switching functions used to determine the neighbouring atoms in the calculation of the Steinhardt parameter, as explained in the previous section. All of the simulations performed using the Q_4 Steinhardt parameter as a CV explored new structures of the 120 atom nanoparticle. The 120 atom system was also a small enough system that significantly longer trajectories could be obtained within a reasonable time frame. In this case we have trajectories spanning at least 30 ns of simulation time. To perform an effective analysis of the long trajectories produced, we have taken frames at every 250 ps of the simulation and optimised these at 0 K using DL_POLY[303], followed by an optimisation using GULP[160]. We have taken the lowest energy structures from these simulations

and included them in Tables 6.9-6.12. The relative energies (ΔU) are given with respect to sphalerite. In the case of this smaller sized nanoparticle all but one of the simulations tended to explore bubble-like cages.

The MetaD method using the Q_4 Steinhardt parameter has enabled configurations of similar sizes and shapes to be explored much more efficiently than the method examined in the previous chapter, i.e. the trace of inertia tensor. The structures explored for the 120 atom structure are generally 'cage-like' or 'bubble' clusters, formed of hexagonal nets, with occasional 4- and 8- membered rings present. The final simulation performed on the 120 atom nanoparticle used the switching function based on the bulk PDF, and has a bias on both Zn-Zn and S-S pairs. This simulation is distinct from the rest, with 'bubble' clusters forming as two layers of hexagonal sheets, reminiscent of planes of graphite. These structures are an interesting outcome from these simulations, as Freeman *et al.* [315] have suggested that graphitic nanofilms are precursors to wurtzite films. In their study they were looking at ZnO, but the same could occur for ZnS. They found wurtzite films transform to graphitic films to remove the dipole of the [0001] surfaces.

At this nanoparticle size there appears to be little effect from the different switching functions, and more variation is seen between the simulations run with a bias only on the Zn-Zn pairs and the bias on both Zn-Zn and S-S pairs. An additional point to make is that the configurational space of these 120 atom nanoparticles is significantly larger than the smaller nanoparticle sizes explored in the previous chapter. It is possible for many structures to exist with very similar energies, and this is reflected in the ΔU of the structures explored.

6.3.2.2   360 atom ZnS nanoparticle in vacuum

The structures obtained from the MetaD simulation of a medium sized nanoparticle, 360 atoms, in our study gave starkly different results to the 120 atom nanoparticle.

For the 360 atom nanoparticle the same set of simulations were performed - MetaD simulations with the Q_4 Steinhardt parameter used to bias either Zn-Zn pairs or both the Zn-Zn and S-S pairs in the nanoparticle. The Gaussian parameters used were height W=0.5 eV and width σ=0.01. The simulations performed with a bias on both Zn-Zn and S-S pairs were significantly different depending on which

TABLE 6.9: Low energy structures obtained from simulation of 120 atom nanoparticle using Q_4 bias on only Zn-Zn pairs. The switching function parameters were d_0=3.8 Å, r_0=0.17 Å, n=6 and m=12. The relative energies (ΔU) are quoted with respect to sphalerite in kJ/mol per formula unit.

Time (ns)	1.50	27.00	33.50	56.00
$\Delta U/ZnS$ (kJ/mol)	37.0	36.6	37.5	37.2

TABLE 6.10: Low energy structures obtained from simulation of 120 atom nanoparticle using Q_4 bias on only Zn-Zn pairs. The switching function parameters were d_0=3.9 Å, r_0=0.25 Å, n=2 and m=6. The relative energies (ΔU) are quoted with respect to sphalerite in kJ/mol per formula unit.

Time (ns)	5.25	22.25	30.00	32.25
$\Delta U/ZnS$ (kJ/mol)	36.7	34.9	36.2	32.4

switching function was used for the selection of neighbouring atoms. Similar structures were explored in the simulations performed with only a bias on the Zn-Zn pairs - again the main difference between the simulations seems due to the switching function used. For this reason we will focus only on the simulations performed with Zn-Zn and S-S pairs, and discuss the differences with respect to the switching function. Tabulations of the structures obtained from the simulations performed with a bias only on the Zn-Zn pairs are listed in Appendix C.

The simulation performed with a switching function based on that used for the bulk briefly explored the bulk phases before evolving to double-bubble-like clusters, with

TABLE 6.11: Low energy structures obtained from simulation of 120 atom nanoparticle using Q_4 bias on both Zn-Zn and S-S pairs. The switching function parameters were d_0=3.8 Å, r_0=0.17 Å, n=6 and m=12. The relative energies (ΔU) are quoted with respect to sphalerite in kJ/mol per formula unit.

Time (ns)	3.50	5.50	32.75	37.75
$\Delta U/ZnS$ (kJ/mol)	37.3	37.2	35.4	36.4
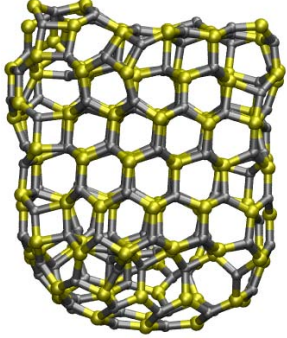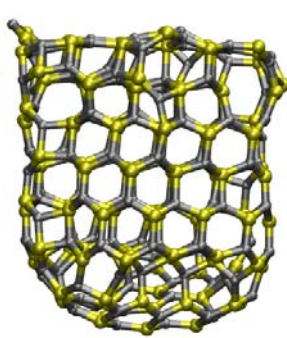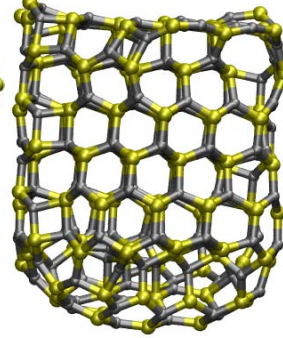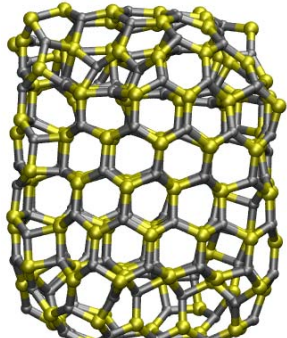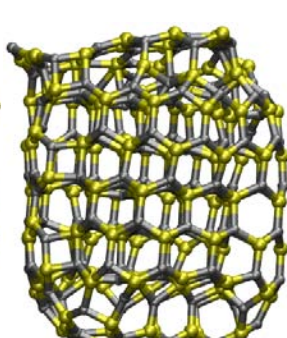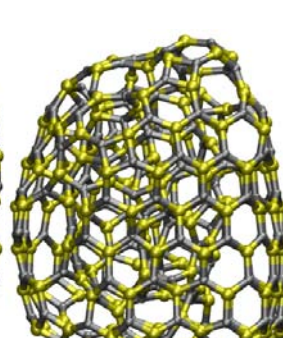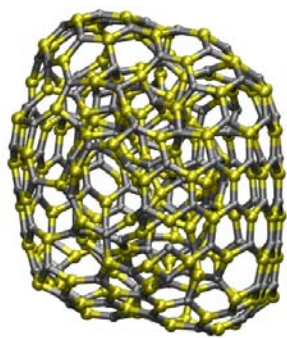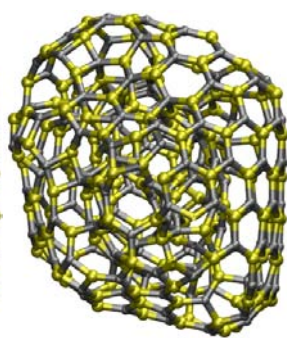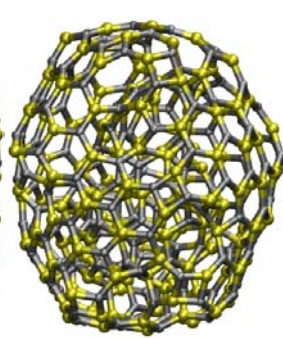
TABLE 6.12: Low energy structures obtained from MetaD simulation of 120 atom nanoparticle using Q_4 bias on both Zn-Zn and S-S pairs. The switching function parameters were d_0=3.9 Å, r_0=0.25 Å, n=2 and m=6. The relative energies (ΔU) are quoted with respect to sphalerite in kJ/mol per formula unit.

Time (ns)	8.75	14.50	36.50	72.25
$\Delta U/ZnS$ (kJ/mol)	30.7	32.0	31.5	32.6

a distinct centre and outer layer. A number of the low energy structures obtained throughout this simulation performed with a bias on the Zn-Zn and S-S pairs are given in Table 6.13. The double-bubble-like clusters explored in this simulation were all generally higher in energy than the starting state. These structures are quite amorphous, and a preference for 3-coordinated atoms is retained. As already mentioned, a similar evolution of the structure - from well ordered to 'amorphous' or bubble-like - was also observed in the simulation performed with a bias only on the Zn-Zn atoms.

The structures obtained in the second simulation with a bias on both Zn-Zn and S-S pairs used a switching function based on the PDF of the 840 atom nanoparticle. The evolution of the structures of the nanoparticle in this simulation

TABLE 6.13: Low energy structures obtained from MetaD simulation of 360 atom nanoparticle using Q_4 bias on both Zn-Zn and S-S pairs. The switching function parameters were d_0=3.9 Å, r_0=0.25 Å, n=2 and m=6. The relative energies (ΔU) are quoted with respect to sphalerite in kJ/mol per formula unit.

Time (ns)	0.75	1.50	2.00
$\Delta U/ZnS$ (kJ/mol)	29.4	29.2	29.1
Time (ns)	2.25	3.00	5.75
$\Delta U/ZnS$ (kJ/mol)	29.5	30.1	29.1
Time (ns)	7.50	7.75	9.00
$\Delta U/ZnS$ (kJ/mol)	29.9	29.8	29.3
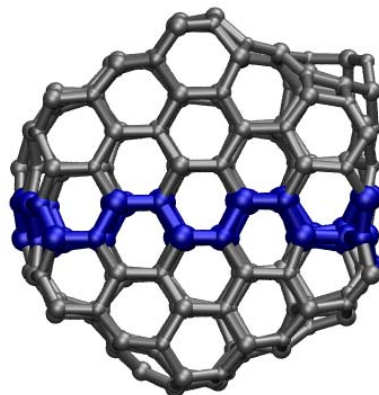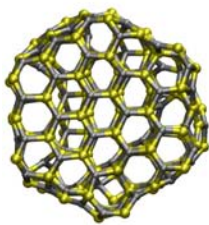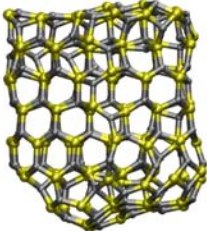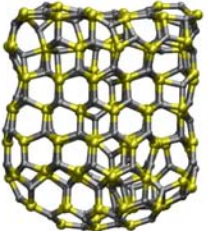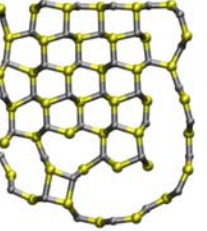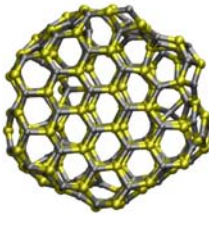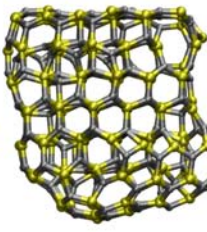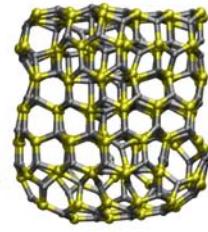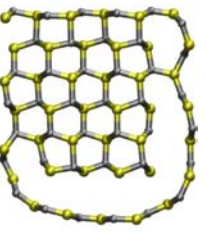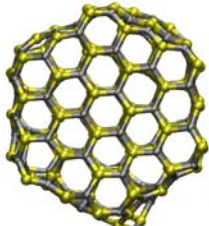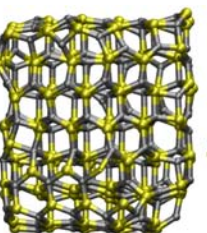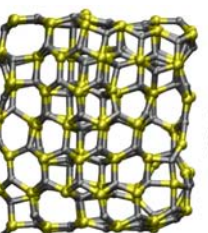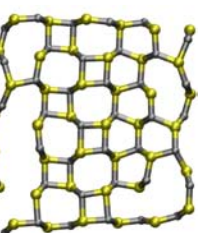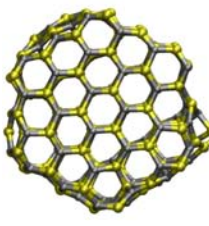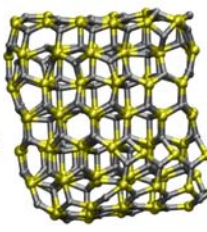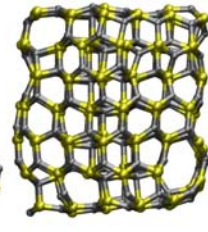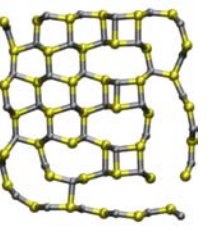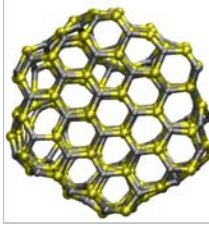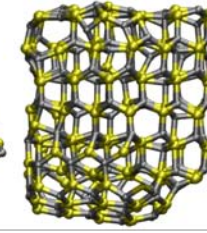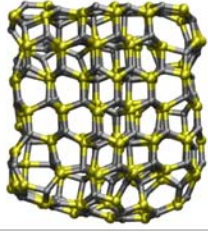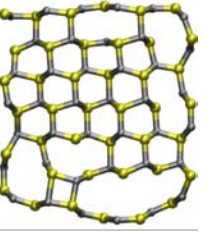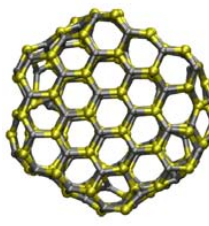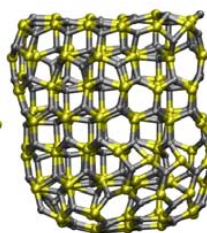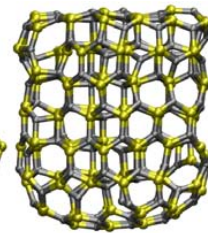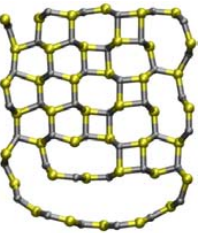
FIGURE 6.15: Image showing the top-down view of the 360-atom nanoparticle. The region where the cross-section of the optimised nanoparticle structures has been taken is indicated in blue.

were more subtle, with disorder appearing at the core and surface of the structures. This simulation investigated many structures that were lower in energy than the starting structure, and bubble-like clusters were not explored. Again structures were taken at 250 ps from the trajectory and optimised in the same manner as the previous structures. Low energy structures, or those of particular interest, have been included in Table 6.14. Each structure has been shown from three different perspectives, and the fourth perspective is a cross-section slice taken across the middle of the nanoparticle. Figure 6.15 has been provided to show the reader where the cross-section slice has been taken.

The structures from this simulation were predominantly bulk-like, with a large proportion of 4-coordinated atoms present. The structures explored were not bubble or cage-like structures, and the starting structure is more or less maintained, with more 4- and 8- membered ring formations appearing within the core of the nanoparticles. The lowest energy structure obtained is the final structure given in Table 6.14 and has been included with three views in Figure 6.16. The lowest energy structure has formed 4- and 8- membered rings in the core, while the lower surface is a cap that is almost entirely detached from the nanoparticle.

The simulations performed with the switching function modelled on the 840 atom nanoparticle show the system taking on structures with 8-membered ring channels through the structure. We have already found the core of the nanoparticles significantly altering to take on 4- and 8- membered ring motifs. As the MetaD simulation progresses we find the 8- membered ring motif continuing throughout

TABLE 6.14: Low energy structures obtained from a MetaD simulation using the Q_4 Steinhardt parameter as a CV bias on both the Zn-Zn and S-S pairs. The switching function used had parameters d_0=3.8 Å, r_0=0.17 Å, n=6 and m=12. The relative energies (ΔU) are quoted with respect to sphalerite in kJ/mol per formula unit.

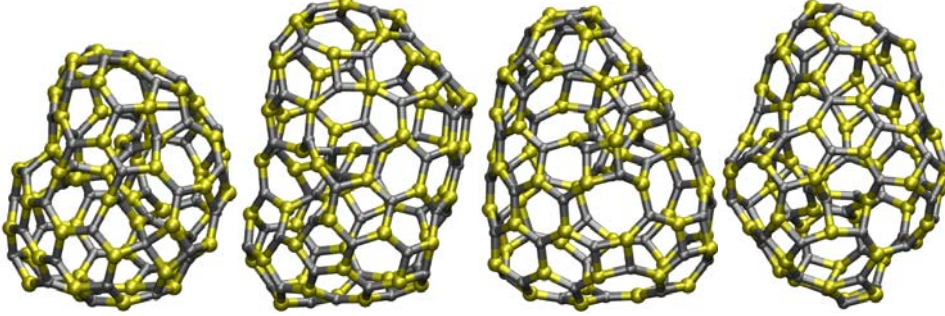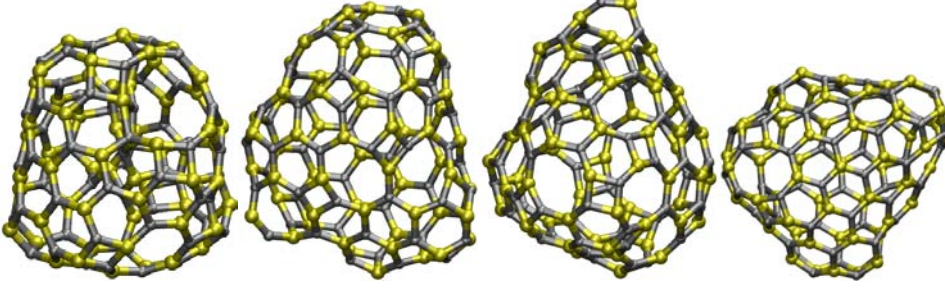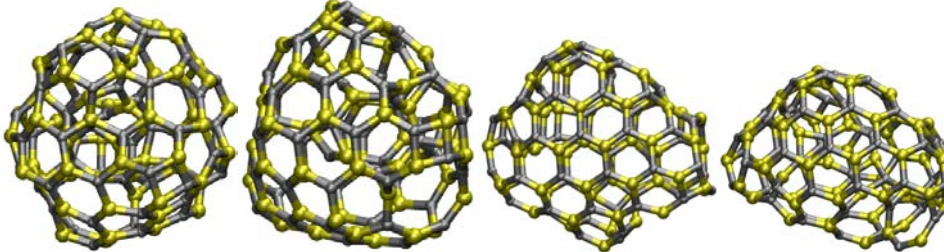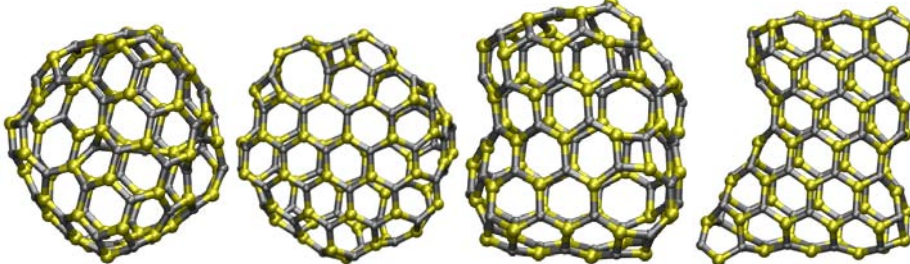| Time (ns)	Structure	ΔU
7.50		28.3
13.25		28.0
14.75		28.6
16.75		28.0
17.50		27.7
18.00		27.1
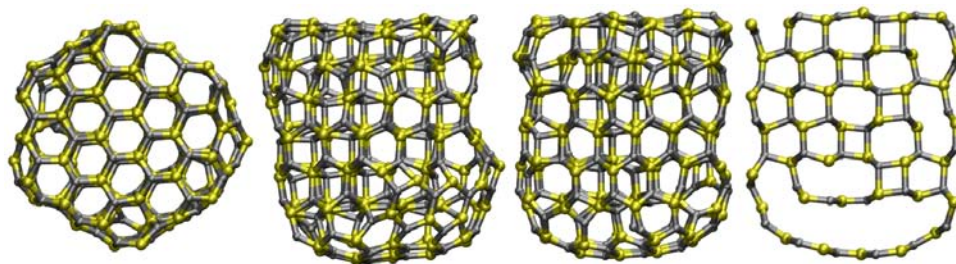
FIGURE 6.16: Lowest energy structure obtained for the 360 atom zinc sulfide nanoparticle. Structure obtained from the MetaD simulation using Q_4 as the CV. The bias was applied on both Zn-Zn and S-S pairs, with a switching function of d_0=3.8 Å, r_0=0.17 Å, n=6 and m=12.
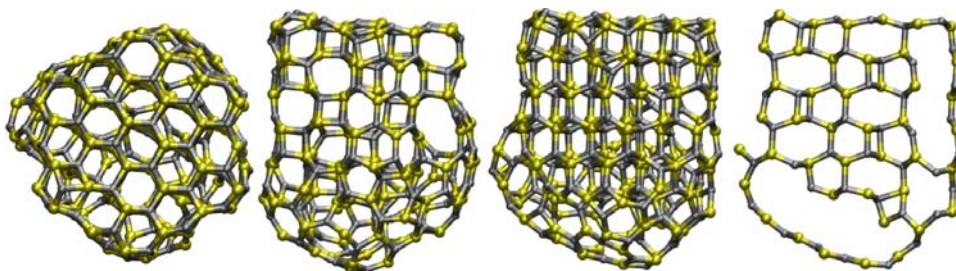
FIGURE 6.17: Structure taken at 13500 ps of the MetaD performed with a bias only on Zn-Zn pairs with switching function parameters d_0=3.8 Å, r_0=0.17 Å, n=6 and m=12. The structure obtained here shows the 8-membered ring channels forming through the entire nanoparticle. ΔU with respect to sphalerite is approximately 33.4 kJ/mol per formula unit.

the structure to form a nanoporous structure with 8-membered ring channels. This is shown as a larger image in Figure 6.17.

6.3.3   Finite particles of ZnS in water

Four simulations were performed on a 360 atom nanoparticle in water. The simulation parameters were as described in the previous section for the 360 atom nanoparticle in vacuum, where the bias is only applied to the atoms of the nanoparticle, either the Zn-Zn pairs or both the Zn-Zn and S-S pairs. The same 360 atom nanoparticle obtained from the relaxation runs in vacuum was used to create the starting configuration for this simulation. A box of 2686 molecules of water was prepared around the 360 atom ZnS nanoparticle and equilibrated using a 1 ns run under the NPT ensemble to obtain a cubic supercell with sides 45 Å in length.
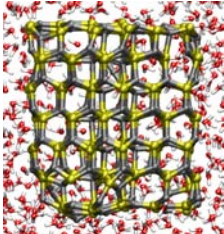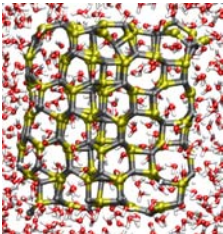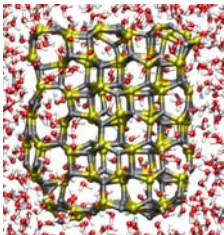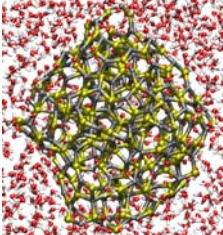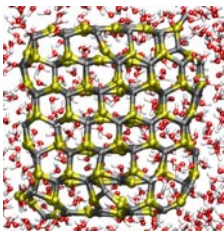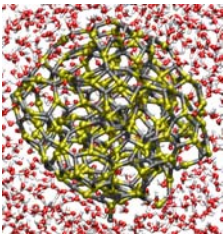
The simulations of the 360 atom nanoparticle in water behaved similarly to the equivalent simulations performed in vacuum. The two simulations performed with a bias applied to both Zn-Zn and S-S pairs behaved most like the simulations in vacuum with a switching function parameter of the 'bulk', d_0=3.8 r_0=0.17 n=6 m=12. These simulations showed limited transformations of the nanoparticle, where only the core of the nanoparticle underwent transitions similar to those shown in Table 6.14. The two simulations performed with the Q_4 bias applied to the Zn-Zn only pairs both investigated the widest variety of structures. In these cases we found the simulation explored more crystalline phases, with significant regions acquiring the BCT phase. However, as the simulation progressed, the system evolved into more amorphous double-bubble clusters. We will focus on the simulation performed with a Q_4 bias on Zn-Zn pairs with switching function parameters d_0=3.8 r_0=0.17 n=6 m=12, where the widest variety of structures were explored.

A transformation from a wurtzite cluster to a predominantly BCT phase cluster occurs in approximately 1.5 ns and further transition to amorphous phases occurs by approximately 6 ns of simulation. While we did see transformations to amorphous phases in our simulations performed in vacuum within similar periods of simulation time using the same switching function, we did not find the same range of crystalline and amorphous structures explored in the one simulation. In vacuum, the simulations which did explore amorphous phases spent very little time exploring compact and crystalline configurations before significantly deforming into 'bubble-clusters' or totally disordered phases.

We have taken selected frames from the MetaD simulation and performed 20 ps of NPT runs to obtain an average enthalpy to compare the relative stability of these structures to those found in the previous chapter. The frames, and the time at which they occur in the MetaD simulation are given in Table 6.15, along with the relative enthalpy per formula unit. We detailed similar information for the much smaller clusters of $(ZnS)_{12}$ in Chapter 5.

The relative enthalpy differences per formula unit for the more compact, crystalline clusters are very small and comparable to the level of accuracy we would expect for these enthalpy calculations. In contrast, the amorphous nanoparticles have enthalpies approximately an order of magnitude larger than the crystalline clusters. This contrasts to our observations in the previous chapter for the small clusters of ZnS in water, where the relative enthalpy of the nanoparticles was lower

TABLE 6.15: Structures taken from the MetaD simulation of the 360 atom wurtzite nanoparticle in water, with Q_4 bias only on Zn-Zn pairs and switching function parameters d_0=3.8 Å, r_0=0.17 Å, n=6 and m=12. NPT simulations were performed to obtain the average enthalpy values for each state, and the enthalpy is given relative to the structure with the lowest enthalpy from the set, at 2.12 ns. The number of water molecules, coordinated with Zn, in the first hydration shell (within 3 Å) of the nanoparticle are given as Zn-O_w coord.

Time (ns)	Structure	ΔH/ZnS (kJ/mol)	Zn-O_w coord.	Time (ns)	Structure	ΔH/ZnS (kJ/mol)	Zn-O_w coord.
0.12		0.4	21.1	5.50		0.4	25.1
1.50		0.2	25.2	6.25		9.8	22.1
2.12		0.0	23.8	6.88		11.2	22.4

for the less ordered clusters, and higher for the well ordered, compact clusters. In the previous chapter the small, disordered clusters with low enthalpy values tended to have a higher proportion of 2-fold coordinated atoms present, made energetically favourable by coordination with surrounding water molecules. For these larger nanoparticles the surface to volume ratio is much smaller, resulting in far less strained clusters which appear to favour maintaining the crystalline, predominantly 4-fold coordinated phase. We calculated the average number of water molecules within 3 Å of a Zn atom and found very similar values for each cluster, these values are also shown in Table 6.15. There is no appreciable trend between the average number of water molecules coordinated to Zn and the enthalpy for these larger nanoparticles of ZnS, which suggests that at this cluster size the solvation of the surface plays a less significant role than for the smaller clusters as

expected. Based on these studies it appears that solvated clusters at this size will prefer to maintain their crystalline form rather than adopting an amorphous state which will be higher in enthalpy.

As with our previous simulations of zinc sulfide nanoparticles in water (see Chapter 5), we find the water plays a stabilising role for the nanoparticles. A wider variety of clusters are explored in the simulations performed in water, even if they are seen for a relatively short simulation time. We will investigate the ZnS-water interactions we have used throughout our work in a later chapter.

6.4 Conclusions

We have shown the Q_4 Steinhardt parameter can be successfully used as a CV in metadynamics to explore the phase space of nanoparticles. The method described in this chapter helped overcome one of the problems found with the inertia tensor, that is, we were able to explore the phase space of larger nanoparticles. The theme of zeolite motifs from the previous chapter has continued into the results of these phase investigations of larger nanoparticles. Using the Steinhardt Q_4 parameter as a collective variable we have been able to push bulk zinc sulfide, and nanoparticles, to the BCT phase which exists as a zeolite framework.

There are a number of implementation aspects which could significantly affect the results obtained from this method. These include:

- The parameters of the switching function

- The size of the system

It is important to determine 'good' switching function parameters - values which will sufficiently include the nearest neighbours in the calculation of the Steinhardt parameter. However, when the system begins to transform during the metadynamics simulation, it is possible that the nearest neighbours in the new structures will be beyond the switching function region, giving Steinhardt parameter values which do not accurately represent the alignment of neighbouring atoms and rendering the metadynamics ineffective.

Throughout the simulations we have discussed we have continued the theme of zeolite motifs in zinc sulfide structures, with the BCT phase occurring in our larger nanoparticles. Following this trend, we have decided to investigate the phase stability of zeolite-like zinc sulfide structures in a methodical way in the next chapter.

Chapter 7

Nanoporous zinc sulfide

7.1 Introduction

Our previous studies and those of others[111–113] have shown that ZnS has a preference for open cage-like structures, in the case of small clusters, and, at larger cluster sizes, networks with open channels are found. Both of these features are reminiscent of motifs found in zeolites, a well-studied group of aluminosilicate minerals. In this chapter we will continue to explore the possible phases of zinc sulfide, with a focus on the possibility of forming zeolitic framework analogues. Though ZnS structures with zeolite motifs have been found in theoretical studies, they have not yet been found experimentally. Before delving into the methods and results, we should introduce some background relating to zeolites and how this large set of frameworks is constructed and defined.

The term zeolite refers to crystalline structures of naturally occurring aluminosilicate materials[316]. These minerals have complex three-dimensional networks comprised of corner-linked tetrahedra of $[SiO_4]^{4-}$ or $[AlO_4]^{5-}$; an example of a generic TO_4 tetrahedron is shown in Figure 7.1. An International Zeolite Association (IZA) was formed in 1973 to promote the development of zeolite science and technology, and four years later a Structure Commission (IZA-SC) was formed as part of this association. The IZA-SC evaluates zeolite structural data present in the literature and compiles this data to make it available for the public from one localised source, known as the Zeolite Structure Database[297]. The IZA-SC has authority from IUPAC to assign framework codes (of three letters) to unique and confirmed framework topologies[317]. To date there are

197 frameworks listed in the zeolite structure database[297]. The structures of
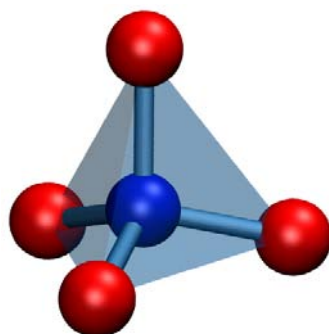
FIGURE 7.1: TO$_4$ tetrahedron, where T is the central atom shown in blue and the oxygen atoms shown in red. This tetrahedral structure is the building block for traditional zeolite frameworks, where T is usually Si or Al and the tetrahedra connect by corner-sharing oxygens.

zeolite frameworks are so diverse that secondary building units (SBU) are often used to assist in describing different frameworks[318]. Zeolites can be depicted as a simplified framework where each bond shown is actually a T-O-T connection. When viewed in this way, zeolites have repeating motifs that can be easily described as n-membered rings or three dimensional units. These motifs are SBUs, and have been documented by the IZA-SC. The SBUs currently known are shown in Figure 7.2.
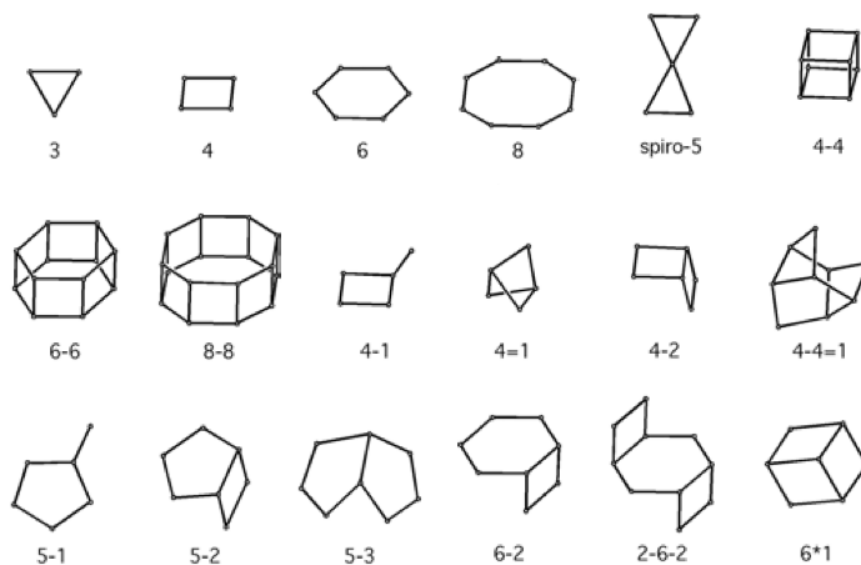
FIGURE 7.2: Secondary Building Units (SBU) found in current zeolite frameworks, as documented in the Atlas of Zeolite Frameworks[319]. Each line represents a T-O-T connection, making each corner of an SBU a tetrahedral (T) atom. Image reproduced from Baerlocher *et al.* [319].

A comparison of the different ways zeolite structures can be represented is shown in Figure 7.3, where different representations of the sodalite cage are shown. The first image shows an all atom representation; the middle image shows how the interconnected TO_4 tetrahedra can be connected as polyhedra; the final image is a 'framework' representation, where each line indicates a T-O-T connection. This final representation is the one we will focus on throughout our later discussions, as it is this topology that we can 'convert' to a hypothetical ZnS form.
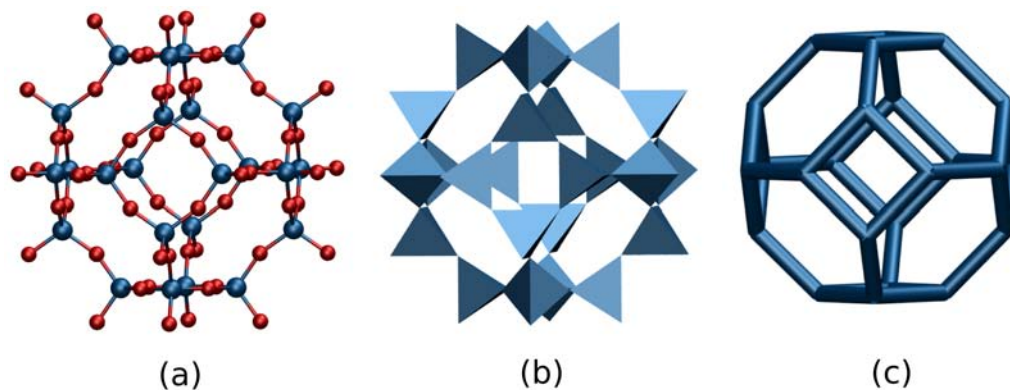
FIGURE 7.3: Different representations of a silicate (SiO_4) sodalite cage, (a) full atom representation, with oxygen shown in red and silicon in blue; (b) polyhedral representation, SiO_4 tetrahedra shown; (c) framework, where connectivity between the Si atoms is considered.

Zeolite frameworks have open porous structures, with channels and cavities that can adsorb molecules and contain cations. The quantity of cations incorporated in a zeolite structure is dependent on the number of $[AlO_4]^{5-}$ tetrahedra present in the framework, as these provide the framework with a residual negative charge that counter-ions must compensate[316]. Zeolites can be very effective ion-exchange materials - the cations are not part of the intrinsic framework, and in some cases can be readily exchanged with other cations in solution[316]. Their regular arrays of channels with specific apertures means zeolites can be used as molecular sieves to selectively allow molecules of only certain dimensions to pass through them[316, 320]. This defining feature of zeolites has made them the subject of intense studies for a number of decades[321]. Hundreds of zeolitic frameworks have been studied and defined, both naturally occurring and synthetic[319, 321].

As an example, a well-known zeolite structure, ZSM-5, is shown in Figure 7.4 using two different representations, to give the reader an idea of how the corner-sharing TO_4 tetrahedra connect to form a complex three-dimensional network. The representation on the left shows all of the bonds between Si and O, and also the
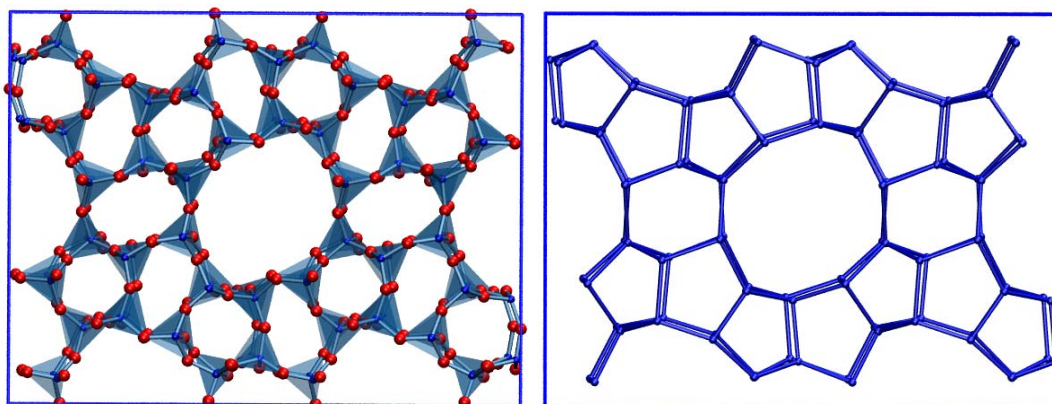
FIGURE 7.4: Two representations of the framework for the ZSM-5 zeolite, viewed along [010]. Full representation with the $[SiO_4]^{4-}$ tetrahedra (left) with oxygen atoms shown in red. Framework structure (right), where the oxygens are not depicted and each line represents a Si-Si connection.

$[SiO_4]^{4-}$ tetrahedra. The representation on the right is the same structure shown on the left; however, it has been simplified by considering only the connections between tetrahedral centres to represent the framework, as shown in the sodalite example in Figure 7.3. These figures also clearly show the porous nature of the structure, with a channel comprised of 10-tetrahedra present in the middle of the cell.

Zeolites such as ZSM-5 have long been used for acid catalysis, where bridging Al-O-Si oxygens are protonated, providing the acid species for catalysis[323]. The product of zeolite catalysis is also size-controlled due to the size-selective nature of the zeolite pores. An example of this is the catalytic formation of xylene (dimethylbenzene) from toluene (methylbenzene). The *ortho-*, *meta-* and *para-*isomers of xylene can be formed and inter-converted via acid catalysis. However, if the catalysis is performed in ZSM-5 zeolite, the predominant product
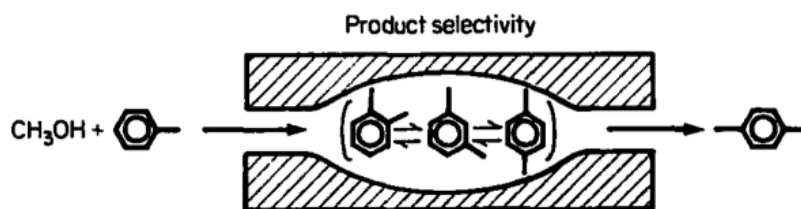
FIGURE 7.5: Depiction of the acid catalysed inter-conversion of the isomers of xylene within the zeolite pores, and the size-selective nature of the pores allowing only one isomer, the more linear *para-*isomer, to pass through. Image reproduced from Csicsery [322].

is the *para-* form, as illustrated in Figure 7.5. The preference for the *para*-isomer can be explained by its shape; its linear nature means it can more readily diffuse through the pores of the zeolite, while the remaining isomers remain trapped until they also convert to the *para-* isomer[323].

Another means of simplifying the representation of a zeolite network is to consider the structure as comprised of 'composite building units'. These are also listed on the IZA-SC website, and are more complex building blocks comprised of the SBUs. The example sodalite cage given in Figure 7.3 shows the formation of a complex building unit from the SBUs. The sodalite cage motif is common to many zeolite frameworks, and we have already seen this motif in previous chapters as it is the lowest energy cluster found for a $(ZnS)_{12}$ cluster. For example, there are three different frameworks 'SOD', 'FAU' and 'LTA' which are composed of sodalite cages connected in different ways. A summary of the composite building blocks for these three common zeolite frameworks are shown in Table 7.1, along with an example of the zeolite framework.

TABLE 7.1: Three well-known zeolite frameworks, SOD, LTA and FAU. All of these frameworks consist of the sodalite cage interconnected in different ways. The SOD framework has no additional connecting units, while the LTA framework has a 'D4R', double-four-membered-ring connection, and the FAU network has a 'D6R', double-six-membered-ring connection. Only a portion of the FAU framework is shown to better illustrate the connectivity of the sodalite cages. The composite building block images (bottom row) are reproduced from the IZA-SC website[317].

SOD	LTA	FAU
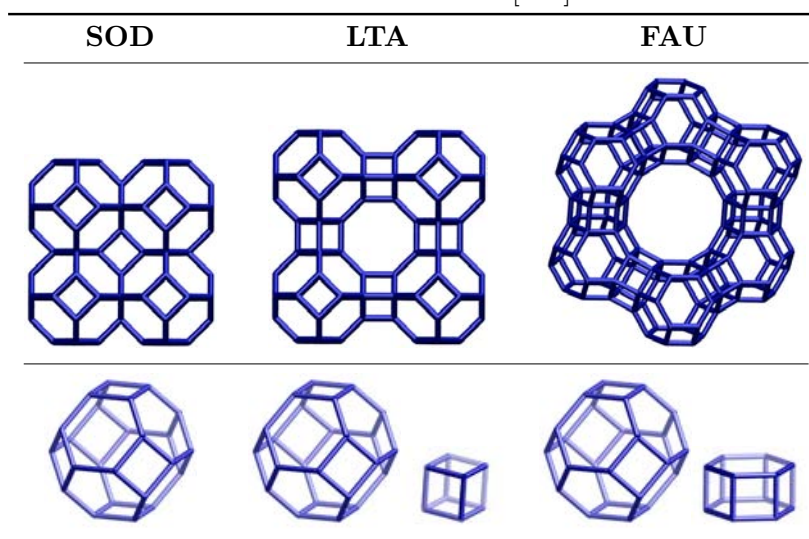
The SOD framework has no connecting unit between the sodalite cages; they are simply fused together via the 4-membered rings of each cage. The LTA framework connects the sodalite cages via the 4-membered rings of adjacent sodalite cages,

producing an additional double four-membered ring 'D4R' building block. The FAU framework has the sodalite cages connected via the 6-membered rings of adjacent sodalite cages, producing an additional double six-membered ring 'D6R' building block. These images indicate how diverse the zeolite frameworks can be, even if the primary building unit is the same and only the means of connection between units is altered.

The zeolite framework codes (such as SOD, LTA and FAU) and their associated building units were traditionally only used in the context of alumino-silicate compounds, to help classify the large number of structures that exist. However, other materials, such as ionic sulfides and oxides, can also show the same structural motifs as zeolites, and be classified in the same way[67, 283, 324, 325]. We have already seen the formation of cage-like clusters in our own results in the previous chapters, and in our literature review of nanoscale structures[111–113]. Some groups, such as that of Bromley and Flikkema [326], have dedicated their research to investigating possible zeolite-like networks in novel materials as well as traditional silicates. They first investigated likely ground-state clusters for $(SiO_2)_N$, where $N = 7 \ldots 12$[327]. The same group later took the lowest energy clusters from this work and studied theoretical zeolite frameworks by using "magic" clusters of $(SiO_2)_8$ as the SBU of different frameworks[328]. They also applied the underlying concept of this work to other materials. Of particular relevance to our work, Carrasco *et al.* [325] looked at low density structures of metal oxides, MgO and ZnO. Previous MgO studies have also found 'magic numbers' for some stable structures via mass spectra[329]. Carrasco *et al.* [325] took these stable cluster structures as the building blocks for larger frameworks. The open-structure polymorphs proposed by Carrasco *et al.* [325] have yet to be reported for any other metal oxide material, but have topological links with silicate-based zeolite structures. For both MgO and ZnO, they used the sodalite cage as the main SBU, with different interconnecting units. Examples of how they built different frameworks using the sodalite cage are shown in Figure 7.6. The framework codes are related to the zeolite frameworks FAU, LTA and SOD, which we have already introduced.

Woodley *et al.* [330] have very recently performed similar theoretical studies where they built microporous frameworks from small ZnO cages. To expand on the studies performed previously by Carrasco *et al.* [325], Woodley *et al.* [330] considered not only the $(ZnO)_{12}$ sodalite cage structure as a building block,
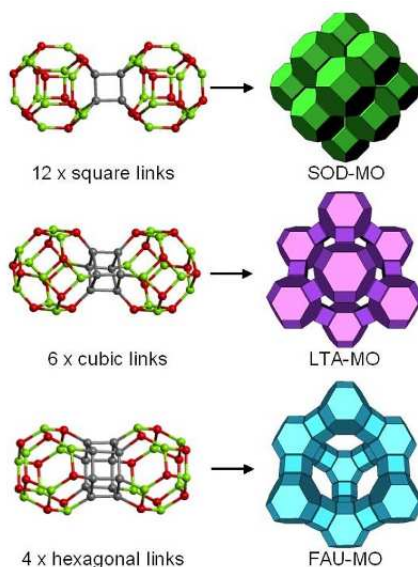
FIGURE 7.6: $(MO)_{12}$ nanocage used as a building block for creating nanoporous zeolitic frameworks of MgO and ZnO in Carrasco *et al.* [325]. Image reproduced from Carrasco *et al.* [325]

but also attempted to build frameworks from other stable structures known for ZnO. They used clusters of $(ZnO)_n$ where n=4, 12, 16, 24, 28, 36, 48 and 64, shown in Figure 7.7. Their studies were repeated in the same year on a different material, SiC[331]. In these studies, each of the building blocks were considered as octahedra, and the larger frameworks constructed by the sharing of corners between these octahedra.
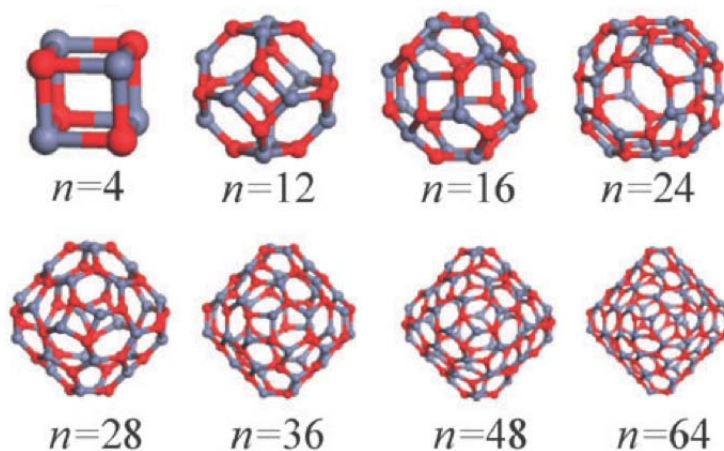
FIGURE 7.7: $(ZnO)_n$ nanocages used as building blocks for creating nanoporous zeolitic frameworks of ZnO in studies of Woodley *et al.* [330]. Image reproduced from Woodley *et al.* [330]

Another recent study is that of Zwijnenburg *et al.* [332], which predicts for tetrahedrally coordinated 1:1 binary solids many low density polymorphs, such as those based on zeolitic frameworks, are likely to exist. They suggest that this phenomena is probably not confined to the tetrahedral 1:1 binary solids, but may apply to all simple solids.

Motivated by these previous studies for other MX systems we want to apply the same approach to zinc sulfide. The aim of the work performed in this chapter is to investigate the relative stabilities of hypothetical nanoporous materials consisting of zinc sulfide. This is a logical step from the results in the previous chapters, where we have seen zeolite motifs appear in our simulations of nanoparticles and bulk ZnS. How we will perform this systematic study will be presented in the next section.

7.2   Methods

To compare the stabilities of different zeolitic frameworks of ZnS, it was first necessary to build the appropriate frameworks. As mentioned in the introduction, the IZA-SC makes the topologies of zeolite frameworks freely available. We first went through this database and sourced all of the structures that have only even-membered rings. This restriction exists for ZnS frameworks, since Zn and S atoms must strictly alternate (*i.e.*, we cannot have Zn-Zn or S-S connections, which would occur if the frameworks had odd-numbered rings). There are 91 structures found to be appropriate, and these are given in Table 7.2.

The structures in the IZA-SC database are comprised of generic TO_4 units, where T is usually aluminium or silicon. To generate the frameworks of a ZnS composition a program was developed to automate the assignment of Zn or S type to each T atom. First, the framework structures were taken from the IZA-SC website and the oxygens removed. The remaining 'T' atoms provide the zeolite-like network we need to convert to a ZnS form. The program developed then takes the generic framework file and loops over the atoms to generate a network where the 'T' sites have been replaced by alternating Zn-S pairs. This is done by first generating a nearest-neighbour list for each atom, and then starting from the first atom assigning arbitrarily the atom type Zn and its neighbouring atoms the atom type S. This assignment is continued iteratively through neighbouring atoms until

each atom in the network has been assigned the correct atom type, producing a network of alternating Zn-S atoms. We have grouped the allowed structures obtained from the IZA-SC database based on the rings present in the structure. For example SOD, comprised only of interconnected sodalite cages, has only 6- and 4- membered rings, so this is listed under '6-4 frameworks' in Table 7.2. Likewise, the LTA framework we have also discussed, has 8-, 6- and 4- membered rings, so this is listed under the heading '8-6-4 frameworks'.

Once the zeolite structures had been transformed to an equivalent ZnS structure, these were then optimised based on a number of different force fields using the program GULP[160]. The force fields we have used are the rigid-ion model introduced in the previous chapter, the shell model of Wright and Gale [95], the same shell model of Wright and Gale [95] without its torsional term, a rigid-ion version of the Wright and Gale [95] model with the torsional term and finally the shell model force field of Hamad *et al.* [94]. The parameters for the aforementioned force fields are given in Tables 7.3-7.6. The Wright and Gale [95] model has been referred to as 'Shells/Tors' in our plots, as we used this entire force field, including the torsional term, which enables the correct order of sphalerite and wurtzite to be modelled. The same model without the torsional term is referred to as 'Shells/NoTors' in our plots, and the rigid-ion version of the Wright and Gale [95] model is referred to as 'Rigid/Tors'.

The functional form for the non-bonded interactions of the Hamad *et al.* [94] model is a mixture of the Buckingham and Lennard-Jones 9-6 potential, given by Equation (7.1):

$$V_{ij} = A \exp(-\frac{r_{ij}}{\rho}) + B r_{ij}^{-9} - C r_{ij}^{-6} \tag{7.1}$$

The three-body potential of the Wright and Gale [95] model is given by the form:

$$U_{ijk}^b = \frac{1}{2} k_b (\theta_{ijk} - \theta_0)^2 \exp\left(-\frac{r_{ij}}{\rho_1}\right) \exp\left(-\frac{r_{jk}}{\rho_2}\right) \tag{7.2}$$

This is a harmonic potential with exponential decay, reducing the chance of a discontinuity as atoms transfer between coordination shells.

With many studies having referred to the presence of "bubble-clusters" of zinc sulfide and magic-number clusters that resemble zeolite structures[111–113], it

TABLE 7.2: Tabulation of the 91 zeolite frameworks obtained from IZA-SC that possess only even-numbered rings.

6-4 Frameworks

AFG	AST	FAR	FRA	GIU	LIO
LOS	MAR	MSO	SOD	TOL	
UOZ					

8-4 Frameworks

ACO	EDI	MER	PHI	SIV	THO

8-6-4 Frameworks

ABW	AEI	AEN	AFN	AFT	AFX
AFY	ANA	APC	APD	ATN	ATT
ATV	AWO	AWW	BCT	CHA	DFT
EAB	ERI	GIS	GOO	JBW	KFI
LEV	LIT	LTA	LTN	OWE	PAU
RHO	SAS	SAT	SAV	TSC	UEI
ZON					

10-6-4 Frameworks

AEL	AFO	AHT	JRY	LAU	PON

10-8-6-4 Frameworks

CGS	CGF	WEN

12-6-4 Frameworks

AFI	ATO	ASV	ATS	CAN	EMT
FAU	OSI	SAO			

12-8-6-4 Frameworks

AFR	AFS	BPH	EZT	GME	ITW
LTL	MOZ	OFF	SBE	SBS	SBT
SFO					

Larger Frameworks

CZP	ETR	USI	AET	VFI
(12-8-4)	(18-8-6-4)	(12-10-6-4)	(14-6-4)	(18-6-4)

TABLE 7.3: Rigid-ion model for ZnS. These parameters were obtained using GULP[160], fitting to the wurtzite and sphalerite structures, cell parameters and physical properties, such as the elastic constants[95].

Species	Charge (e)		
Zn	+1.2534		
S	-1.2534		
Lennard-Jones (12-6) Potential	A (eV $Å^{12}$)	B (eV $Å^6$)	Cut-off (Å)
S - S	1003475.3	0.00	12.00
Zn - S	5669.3544	0.00	12.00

seems relevant to investigate how the force fields being used perform for these structures. The rigid-ion model we have used throughout our studies has been fitted using the same experimental data used to derive the Wright and Gale [95] shell model.

We have previously described shell model force fields in Chapter 2, where we introduced the computational methods to be used throughout our studies. To briefly recap, a 'shell model' force field attempts to take into account the

TABLE 7.4: Wright and Gale [95] model for ZnS. The torsional term enables this force field to reproduced the experimental observation that sphalerite is the preferred polytype of ZnS.

Species	Charge (e)		
Zn core	+2.00		
S core	-1.03061		
S shell	-3.03061		
Buckingham potential	A (eV)	ρ (Å)	C (eV $Å^6$)	Cut-off (Å)
Zn core - S shell	672.288	0.39089	0.0	12.00
S shell - S shell	1200.0	0.14900	0.0	12.00
Core-shell potential	k (eV/$Å^2$)	Cut-off (Å)		
S core - S shell	13.302743	0.8		
Exponential three-body potential	k (eV/rad^2)	θ_0 (°)	ρ_1/ρ_2 (Å)	Cut-off (Å)
S shell - Zn core - S Shell	9.42834 x 10^6	109.47	0.3	6.0
Torsional Potential	k_1 (eV)	m/n	r_{min} (Å)	r_{max} (Å)
Zn cor - S shel - Zn cor - S shel	0.005	+1/+3	2.5	3.0

TABLE 7.5: Rigid-ion version of the Wright and Gale [95] model for ZnS. The torsional term is retained, and enables this force field to reproduced the experimental observation that sphalerite is the preferred polytype of ZnS.

Species	Charge (e)			
Zn core	+2.00			
S core	-2.00			
Buckingham potential	A (eV)	ρ (Å)	C (eV Å^6)	Cut-off (Å)
Zn core - S core	672.288	0.39089	0.0	12.00
S core - S core	1200.0	0.14900	0.0	12.00
Exponential three-body potential	k (eV/rad^2)	θ_0 (°)	ρ_1/ρ_2 (Å)	Cut-off (Å)
S core - Zn core - S core	9.42834 x 10^6	109.47	0.3	6.0
Torsional Potential	k_1 (eV)	m/n	r_{min} (Å)	r_{max} (Å)
Zn core - S core - Zn core - S core	0.005	+1/+3	2.5	3.0

TABLE 7.6: Hamad *et al.* [94] model for ZnS. Cut-offs of 15 Å were used for all the short-range potentials.

Species	Charge (e)			
Zn core	+2.00			
S core	-1.357			
S shell	-3.357			
General potential	A (eV)	ρ (Å)	B (eV Å^9)	C (eV Å^6)
Zn core - S shell	213.20	0.475	664.35	10.54
S shell - S shell	11413.09	0.153	0.0	129.18
Core-shell potential	k (eV/Å^2)			
S core - S shell	27.690			
Exponential Three-body potential	k (eV/rad^2)	θ_0 (°)		
S shell - Zn core - S shell	0.778	109.47		

polarisability of one or all of the ions being modelled. This is accomplished by representing the ion as being comprised of a central core, and a 'shell' surrounding it, attached via a spring, which represents a polarisable cloud of electrons. We have also already discussed that the shells can be implemented using two different approaches, either modelling the shells with or without a mass. Both of these approaches are more computationally intensive than a rigid-ion model, where the time step can be relatively large. A balance between accuracy and the speed of computation needs to be found when deciding which approach and force field to use. One disadvantage of the rigid-ion model is that the representation of the system may be less accurate by not taking into consideration the polarisability of the ions, and ultimately this is why we have chosen to explore a number of different models.

The complete shell model of Wright and Gale [95] includes a torsional potential. In sphalerite, the torsional angle is in a staggered conformation, while in wurtzite the less stable eclipsed form is present. The energetic penalty imposed by this torsional term enables the force field to obtain the correct order of stability for the bulk polymorphs of zinc sulfide. The final model we have considered is the force field of Hamad *et al.* [94]. This force field has been used for many previous studies of nanoscale zinc sulfide, and includes some of the first theoretical studies showing "bubble-clusters" and nano-onions of ZnS. Hamad *et al.* [94] focussed primarily on the energy of different surfaces for determining their interatomic parameters.

The sulfur anion is much more polarisable than zinc, and as such both the shell model of Wright and Gale [95] and that of Hamad *et al.* [94] represent the sulfur anion using the core-shell representation, while the zinc cations are only modelled in a rigid manner.

After all of the framework structures had been optimised with each of the force fields a subset consisting of the low-energy structures was further optimised using first principles methods with the program SIESTA[138]. Investigating the relative energies of the structures with both first principles methods and force field methods enables us to evaluate whether any of the force fields we are using reproduce the order of stabilities given by first principles methods. This is especially important as none of the classical force fields were designed with the purpose of modelling ZnS in these open zeolitic frameworks, and given these are theoretical frameworks we have no experimental data with which to validate our results.

Throughout the present work the Generalized Gradient Approximation of Perdew *et al.* [289], known as the PBEsol exchange and correlation functional, has been used. This is an improvement on their well known GGA functional PBE[131], where the functional has been optimised for use in solid-state systems. PBEsol has recently been used in a comprehensive study of the two polymorphs of FeS_2, pyrite and marcasite[290]. This study showed that recently developed GGA functionals, such as PBEsol, produced a contraction of the lattice parameters, resulting in the correct prediction of the order of stability of the two polymorphs. As we are investigating a solid-state system, and in particular a material where there are two polymorphs separated by a small energy difference, it was important for us to use a functional which has greater potential to accurately model the relative stabilities of polymorphs.

The first principles SIESTA[138] methodology expands the Kohn-Sham wave functions using a linear combination of atomic orbitals (LCAO). The nuclei and core electrons of atoms are represented through the use of norm-conserving pseudopotentials of the form developed by Troullier-Martins[139], while the valence electrons are treated explicitly. The valence electronic configurations for generating the pseudopotentials were Zn ($3s^2 3p^6 3d^{10}$) and S ($3s^2 3p^4$). The basis sets for sulfur required triple-ζ quality for the $3s$ and $3p$ orbitals and double-ζ quality $3d$ orbitals, while for zinc double-ζ quality was necessary for the $4s$, $4p$, and $3d$, and single-ζ for the $3s$ and $3p$ orbitals. A full description of the basis sets used in this study is given in Appendix B. The shape of the basis set was improved following the method introduced by Junquera *et al.* [291], where the pseudoatomic orbitals (PAO) of the isolated atoms are enclosed within a soft-confined spherical potential, removing any discontinuity of the basis function first derivative at the cut-off radius. A split-norm value of 0.15 was used and 0.02 Ry for the energy shift of radial confinement. An auxiliary real-space Cartesian grid with a cut-off of 400 Ry was used for calculating quantities based on electron density and the Brillouin zone was sampled using a mesh with resolution controlled by using a K-grid cut-off of 12 Å[142].

In the following section we will present our results from the optimisations of the theoretical nanoporous ZnS frameworks performed using the force field methods and first principles techniques described above.

7.3 Results and Discussion

Before applying the different force fields to optimise the hypothetical ZnS frameworks, we have first optimised the bulk polymorphs to determine how well each force field reproduces the experimental data for zinc sulfide. The results obtained from each force field are tabulated for sphalerite and wurtzite in Tables 7.7 and 7.8, respectively.

The shell model of Hamad *et al.* [94] reproduces the physical properties of sphalerite very accurately, with the cell parameters and elastic constants all very close to the experimental values. However, its representation of wurtzite is less successful, with the lattice parameter c being underestimated by approximately 3% of the experimental value. Additionally, the force field of Hamad *et al.* [94] is unable to predict the small energy difference between sphalerite and wurtzite, with a ΔU of approximately 0.073 eV or 7.04 kJ/mol, and favouring wurtzite rather than sphalerite. As we discussed in our introduction to the properties of bulk zinc sulfide in Chapter 1, the energy difference between the two polymorphs has been listed in thermodynamic tables[333] as approximately 13 kJ/mol. However, more recent experiments have suggested it may be much smaller, of the order of 2 kJ/mol[80] with sphalerite being the more stable polymorph.

TABLE 7.7: Calculated structure and properties of sphalerite. The results from five force fields are shown, along with experimental values where available.

Observable	Shell/Tors	Shell/NoTors	Rigid	Rigid/Tors	Hamad *et al.* [94]	Expt. [334, 335]
$a(\text{Å})$	5.4506	5.4506	5.4574	5.4506	5.4117	5.4093
Volume (Å^3)	161.93	161.93	162.54	161.93	158.49	158.34
U/ZnS (eV)	-33.466	-33.466	-14.374	-33.466	-33.220	-
C_{11} (GPa)	107.71	107.06	100.71	107.72	105.37	104.62
C_{12} (GPa)	59.40	59.82	63.00	59.42	67.45	65.34
C_{44} (GPa)	33.70	32.97	55.59	66.47	42.83	46.13
K (GPa)	75.5	75.6	75.6	75.5	80.1	77.1
ϵ_{11}^{0}	6.49	6.97	2.96	4.35	6.23	8.3
ϵ_{11}^{∞}	4.76	4.90	1.00	1.00	3.35	5.2

TABLE 7.8: Calculated structure and properties of wurtzite. The results from five force fields are shown, along with experimental values where available.

Observable	Shell/Tors	Shell/NoTors	Rigid	Rigid/Tors	Hamad *et al.* [94]	Expt. [334]
a(Å)	3.8922	3.8945	3.8802	3.8863	3.8762	3.8230
c(Å)	6.1973	6.1906	6.2293	6.2151	6.0877	6.2565
Volume (Å^3)	81.31	81.31	81.22	81.29	79.21	80.75
U/ZnS (eV)	-33.442	-33.533	-14.408	-33.442	-33.293	-
C_{11} (GPa)	111.04	110.71	126.80	136.48	124.72	124.20
C_{12} (GPa)	55.69	55.72	56.08	46.16	60.09	60.15
C_{44} (GPa)	37.76	37.55	35.54	45.48	37.40	28.64
C_{13} (GPa)	58.00	58.71	45.12	42.07	59.09	45.54
C_{33} (GPa)	126.01	124.27	135.81	157.36	113.21	140.00
K (GPa)	76.5	76.5	75.8	76.6	79.7	74.0
ϵ_{11}^0	6.71	6.80	2.86	4.47	6.06	-
ϵ_{33}^0	6.91	7.60	3.20	4.58	6.66	-
ϵ_{11}^∞	4.79	4.82	1.00	1.00	3.32	-
ϵ_{33}^∞	4.91	5.09	1.00	1.00	3.41	-

TABLE 7.9: Calculated structure and properties of the hypothetical ZnS BCT phase. The results from five force fields are shown.

Observable	Shell/Tors	Shell/NoTors	Rigid	Rigid/Tors	Hamad *et al.* [94]
a(Å)	6.6571	6.6597	6.6132	6.6627	6.5258
c(Å)	3.8675	3.8649	3.8659	3.8622	3.8746
Volume (Å^3)	171.3983	171.4174	169.0727	171.4544	165.9947
U/ZnS (eV)	-33.280	-33.471	-14.401	-33.28	-33.245
C_{11} (GPa)	79.06	78.19	93.71	108.00	88.87
C_{12} (GPa)	70.16	71.44	51.59	55.96	66.26
C_{44} (GPa)	28.81	28.95	29.81	39.31	32.77
C_{13} (GPa)	57.80	57.34	52.36	45.14	59.98
C_{33} (GPa)	125.82	126.55	138.42	147.95	136.49
K (GPa)	72.1	72.1	69.9	72.3	75.3
ϵ_{11}^0	6.81	6.92	3.23	4.76	6.26
ϵ_{33}^0	5.39	5.29	2.22	3.45	5.11
ϵ_{11}^∞	4.52	4.54	1.00	1.00	3.23
ϵ_{33}^∞	4.31	4.27	1.00	1.00	3.14
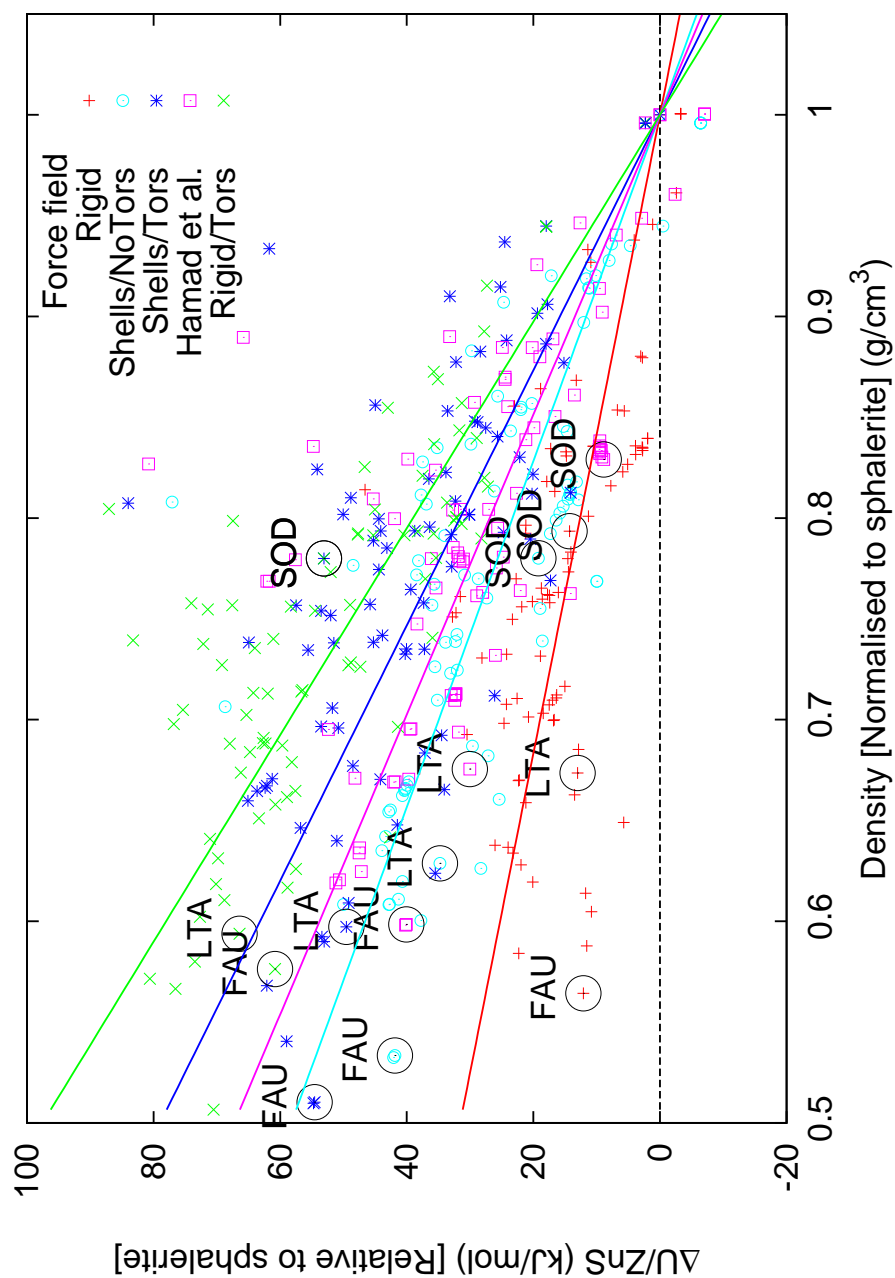
FIGURE 7.8: Plot of energy *vs.* density for the zeolitic ZnS frameworks optimised using five different force fields. Energies are given with respect to sphalerite, and the densities have also been normalised with respect to sphalerite for each of the force fields. Lines of best fit for each set of data are shown, along with the three common zeolite frameworks FAU, SOD and LTA, indicated on the plot by circling and labelling of the relevant data points.

7.3.1   Optimisations of the zeolite frameworks

A total of 91 zeolite structures were optimised using the five different force fields. Images of the optimised structures for all of these frameworks can be found in the Appendix D. Only two structures from the set of 91 were unable to be successfully optimised; these were the PAU and LTN frameworks. While these structures were successfully optimised with four of the five force fields used, neither could be successfully optimised using the Shells/Tors model of Wright and Gale [95]. These two structures have the largest unit cell of any of the frameworks investigated, with the PAU framework consisting of 672 and the LAU framework of 768 atoms. Taking any of the optimised structures (obtained from the Rigid, Rigid/Tors, Hamad *et al.* or Shells/NoTors) and attempting to optimise these using the complete shell model of Wright and Gale [95] resulted in distortion of these large structures, with the resulting final structure possessing a large number of imaginary vibrational modes and a failure to converge.
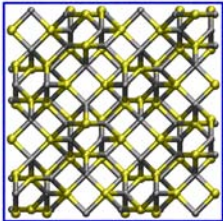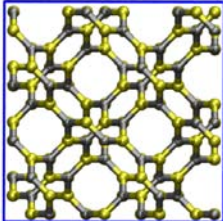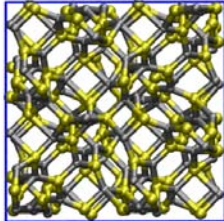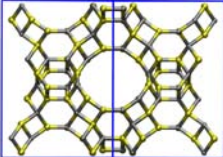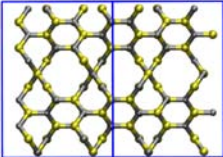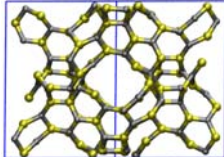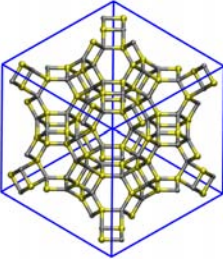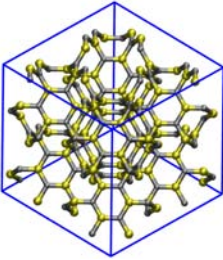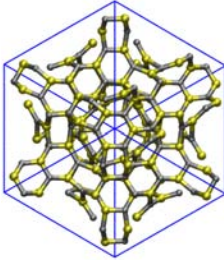
While these are the only two outliers in our optimisations, there are some structures that do clearly deviate from the starting structure/topology after optimisation. Here we will summarise some of these deviations, while also investigating any significant trends in the energies obtained from the different force fields. When comparing a large variety of structures, such as our hypothetical ZnS frameworks, it is useful to create scatter plots of energy vs. density. These plots have been used in the past when studying the relationship between the energy and the density in silicate frameworks[336], where it was found there was a correlation between the two - the less dense the structure, the less stable. We would expect a similar trend for our own frameworks, where the less dense structures become increasingly unstable in comparison to the stable bulk polymorphs.

The scatter plot of energy vs. density for the optimised frameworks is given in Figure 7.8. All of the framework energies have been calculated with respect to sphalerite, which experimentally is shown to be the lowest energy bulk polymorph[80, 334]. The densities have also been normalised to the density for sphalerite obtained for the different force fields. Here it can be seen that the rigid-ion model exhibits a somewhat lower spread in the values than the other models, with the structures all generally having lower relative energies than those obtained using the shell models. Figure 7.8 includes the FAU, LTA and SOD points indicated with a circle. Something else that stands out about the rigid-ion model

is that the FAU, LTA, and SOD structures appear to have their energies of the same order of magnitude, with only a slight decrease with decreasing density. This is the reversal of the expected trend, and the trends shown for the other models. The Rigid/Tors model also has a similar discrepancy, with the FAU structure appearing lower in energy than the denser LTA framework.

Looking at the optimised geometries we have obtained for these structures, we note that the FAU framework optimised with both the rigid-ion models has optimised to a structure which deviates from the FAU topology, while the remaining shell models maintain the FAU topology after optimisation. Three different views of the FAU structure are shown in Table 7.10 for a better comparison of how the optimised structures differ from the starting FAU configuration. With both of the structures obtained via rigid ion models there is a loss of the connectivity between the sodalite cages.

TABLE 7.10: FAU zeolitic framework viewed along [100], [110] and [111] before and after optimisation with the two rigid-ion models used.

View	Before optimisation	Rigid	Rigid/Tors
viewed along [100]			
viewed along [110]			
viewed along [111]			

It appears that the Hamad *et al.* [94] model and the Wright and Gale [95] model ('Tors') have similar trends with regard to the scattering of the data points in Figure 7.8. A particular point of interest with the Wright and Gale [95] model is

that this force field gives much higher energies for the SOD and BCT frameworks in comparison to the other models used. The 'Shells/NoTors' Wright and Gale [95] model without the torsional term results in the energies of the SOD and BCT frameworks appearing similar to the rigid-ion model. The torsional term is clearly playing a significant role in the determination of energies of these dense frameworks.

The low energy and high density structures are significant, as these are more likely to appear as stable polymorphs of ZnS. The low-energy and high density region of the scatter plot given in Figure 7.8 has been enlarged in Figure 7.9, for better clarity in this region. The predicted stabilities of sphalerite and wurtzite from the different force fields are of particular interest. As mentioned in the introduction to the properties of zinc sulfide, sphalerite is the preferred polymorph for bulk ZnS. However, three of the force fields predict wurtzite to be the more stable polymorph, while only the two force fields with the torsional term present, the shell model of Wright and Gale [95] and our modified rigid version of this model, predict sphalerite to be more stable.
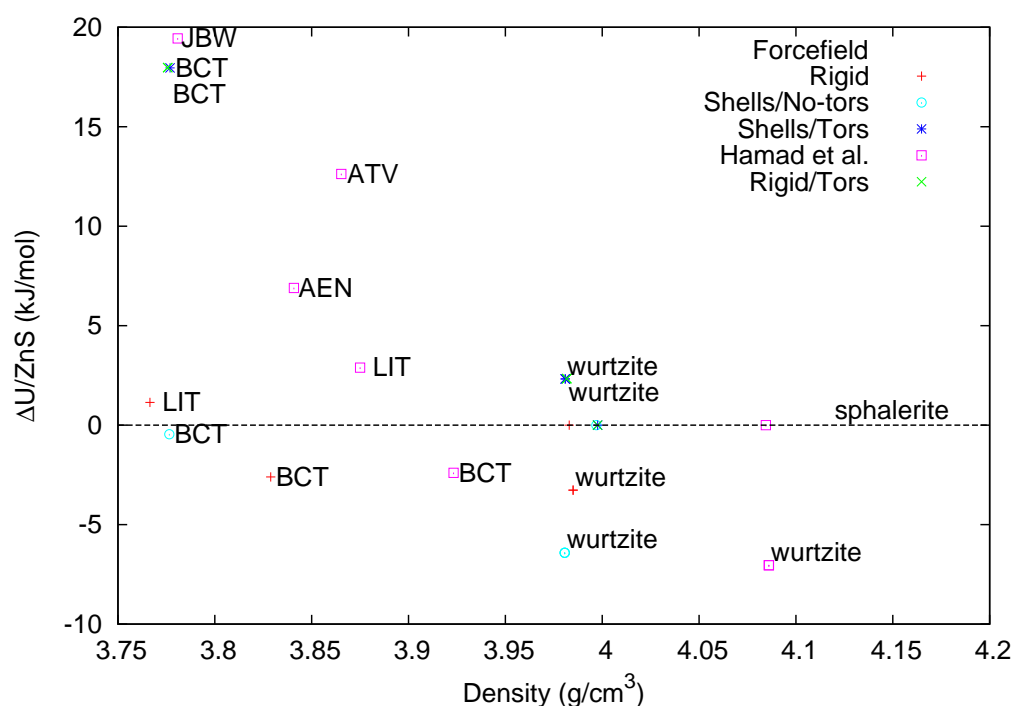
FIGURE 7.9: High-density region of the relative potential energy per formula unit vs. density plot of zeolitic ZnS frameworks optimised using five different force fields. Sphalerite is used as the reference point for calculation of the relative energies, and is indicated on the graph by a dotted line.

Removing the torsional term from the Wright and Gale [95] model results in a reversal of this trend, rendering the energy difference between sphalerite and wurtzite of the same order as that between these phases when modelled by the force field of Hamad *et al.* [94]. One of the other important differences between these models is the placement of the body-centred tetragonal (BCT) phase that we covered in detail in the previous chapter. The BCT framework also exists as zeolitic framework. It is interesting that the BCT structure appears to have such a low energy with three of the force fields, and is only disfavoured by the two models with a torsional term present, the shell model of Wright and Gale [95] and the rigid version of this same model. Recent studies have shown the BCT phase appears in other materials such as ZnO[305, 306, 337], and has even been suggested as a stable allotrope of carbon[309].

As there are significant discrepancies in the relative energy of the BCT phase using different force fields we decided to take the structures in the high-density region of the scatter plot and optimise these using first principles methods. These structures are all hypothetical so we do not have any experimental data to compare against, so first principles calculations should offer another perspective on the expected energy difference between BCT and the stable polymorphs.

Before delving into our discussion about how the BCT phase is modelled by our own QM calculations, we should first mention the results of the first principles calculations on the bulk polymorphs of ZnS. The parameters we have used with SIESTA[138] have managed to reproduce the correct order of stability between sphalerite and wurtzite. Sphalerite is approximately 0.0041 eV more stable than wurtzite according to the physical properties given in Table 7.11. This equates to approximately 0.39 kJ/mol per formula unit more stable, which is slightly less than the 2 kJ/mol predicted by experiment[80], however the precise value will depend on the functional used. The cell parameters obtained from DFT also correlate remarkably well with the those of experiment.

The high-density frameworks are given in Table 7.12, where the density is greater than 3.5 g/cm^3 as modelled by the rigid ion force field. QM calculations using SIESTA[138] were performed on these structures. It is interesting that all the frameworks in this table are in the '8-6-4' category. Figure 7.10 shows an energy vs. density scatter plot for the structures optimised using first principles methods, along with the values obtained using the rigid ion force field and the shell force field of Wright and Gale [95] with the torsional term. The potential energies per

TABLE 7.11: Calculated structure and energy of sphalerite obtained from first principles calculations. The experimental values are shown where available.

Structure	Observable	First principles	Expt. [334]
Sphalerite	a(Å)	5.4001	5.4093
	Volume (Å^3)	157.47	158.34
	U/ZnS (eV)	-6430.0486	-
Wurtzite	a(Å)	3.8215	3.8230
	c(Å)	6.2569	6.2565
	Volume (Å^3)	78.83	80.75
	U/ZnS (eV)	-6430.0446	-

formula unit for the wurtzite and BCT phases relative to sphalerite for each of the five force fields are also given in Table 7.13. One of the important features of Figure 7.10 is that the BCT phase is shown to be approximately 10 kJ/mol less stable than wurtzite or sphalerite according to our first principles calculations; a feature that was only reproduced by the force fields with a torsional term, these being the complete shell model of Wright and Gale [95] and the rigid ion version of this force field (Rigid/Tors). Interestingly the remaining three force fields without a torsional term, Rigid, Shells/NoTors and that of Hamad *et al.* [94] all obtain the same order of stabilities for the dense polymorphs - wurtzite the lowest in energy, followed by BCT and finally sphalerite.

TABLE 7.12: High density structures ($\rho > 3.5$ g/cm^3) obtained using the rigid ion model

8-6-4 Frameworks						
ABW	AEN	ATV	AWO	BCT	JBW	LIT

TABLE 7.13: Potential energies of high-density structures relative to sphalerite obtained using the five different force fields and first principles calculations. All values are given in units of kJ/mol per formula unit.

Structure	Shell/Tors	Shell/NoTors	Rigid	Rigid/Tors	Hamad *et al.* [94]	DFT
Sphalerite	0.00	0.00	0.00	0.00	0.00	0.00
Wurtzite	2.32	-6.41	-3.27	2.34	-7.04	0.39
BCT	17.96	-0.46	-2.61	17.97	-2.40	10.69
Hyp.	33.19	11.17	3.04	27.17	9.11	24.46

The BCT phase has been mentioned in the context of ZnS in one of the previous works of Hamad and Catlow [304], where they noticed the 4- and 8- ring
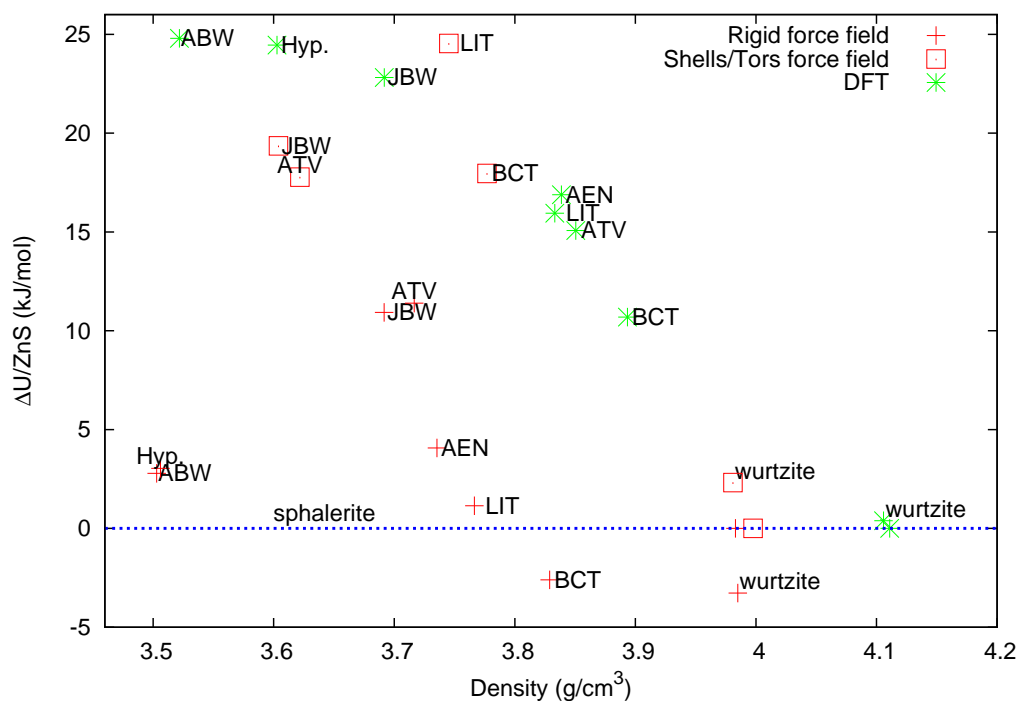
FIGURE 7.10: Plot of potential energy relative to sphalerite vs. density for the high density zeolitic structures and known polymorphs of ZnS optimised using first principles methods, the rigid ion model with no torsional term and the shell model of Wright and Gale [95] with a torsional term present. The framework codes for all structures are shown. The structure labelled "Hyp." is a hypothetical structure we found in previous simulations.

characteristics of the BCT phase in their nanoparticles of ZnS optimised using simulated annealing methods. They performed optimisations using both classical and QM methods on both finite clusters and periodic systems. The appearance of the BCT phase in their simulations of ZnS nanoparticles is somewhat unsurprising when we consider Figure 7.9, where BCT is the second most stable phase, next to wurtzite, when using the Hamad *et al.* [94] force field. What is surprising is that their study from 2006 states that for the bulk structures the BCT phase is 69.1 kJ/mol less stable than the sphalerite phase. This value is alarmingly large for a polymorph of any material[338–340], and it is possible that these DFT calculations did not fully converge. The work of Hamad and Catlow [304] also describes the relative energies of sphalerite, wurtzite and the BCT phase using the same force field. According to their calculations[304] their force field should yield the BCT phase 1.1 kJ/mol less stable than sphalerite, and 7.16 kJ/mol less stable than wurtzite; implying wurtzite should be the most stable phase, followed by sphalerite and finally the BCT the least stable. Our calculations using their

force field do find wurtzite to be the lowest energy phase, however the BCT phase is still 2.40 kJ/mol per formula unit lower in energy than sphalerite. It is not clear why there is a discrepancy between our values obtained using their force field and the values given in their work. One possible explanation is that there may be some force field parameters missing from the paper outlining the force field[94].

One main result from these comparisons is that the force fields with a torsional term present manage to reproduce a similar energy difference between the BCT phase and the bulk phases as that obtained from our first principles calculations. However, none of the five different force fields we have used stand out as managing to reproduce all of the results obtained from our first principles calculations on the high-density structures selected. As none of these force fields were developed specifically to model these nanoporous zeolite-type structures this result is perhaps unsurprising.

7.3.2   A hypothetical zeolite structure

From some of our MetaD simulations performed with a Q_4 and Q_6 Steinhardt parameter bias in the previous chapter we found a 'new' zeolite structure. This was found from the 360 atom nanoparticles in vacuum, where the core structure took on BCT-like phases. We attempted to extract portions of the BCT-like core and create a bulk structure, which we have labelled 'Hyp.' in our energy vs. density plots. The structure is shown from different crystallographic directions along with the BCT phase in Table 7.14, and the potential energies obtained relative to sphalerite are given in Table 7.13. The structure appears to have similarities with the BCT phase, in that one direction has the same array of 4- and 8- membered rings, and another direction has an array of hexagons. However, it is clear when viewing the structure as a three-dimensional object that they are indeed composed of different composite building units. The BCT phase is composed of connected 'LAU' units, while our hypothetical structure is composed of 'double crankshaft chain' (DCC) CBUs, also shown in Figure 7.14.

Of the 91 structures from the IZA structure database[297] containing even number rings there are 14 frameworks which contain, or solely composed of, the double crankshaft chain CBU, these are: APC, ATT, AWO, GIS, GME, LTL, MER, OFF, OWE, PHI, SAO, SIV, UEI, WEN. The structure which most closely resembles our hypothetical structure is the 'APC' framework, and we have included this in

TABLE 7.14: Our hypothetical zeolite framework found in simulations in Chapter 5, along with those of the BCT and APC framework. The CBUs for these structures are also shown.

View	Hypothetical	APC	BCT
viewed along [100]			
viewed along [010]			
viewed along [001]			
CBU	DCC	DCC	LAU
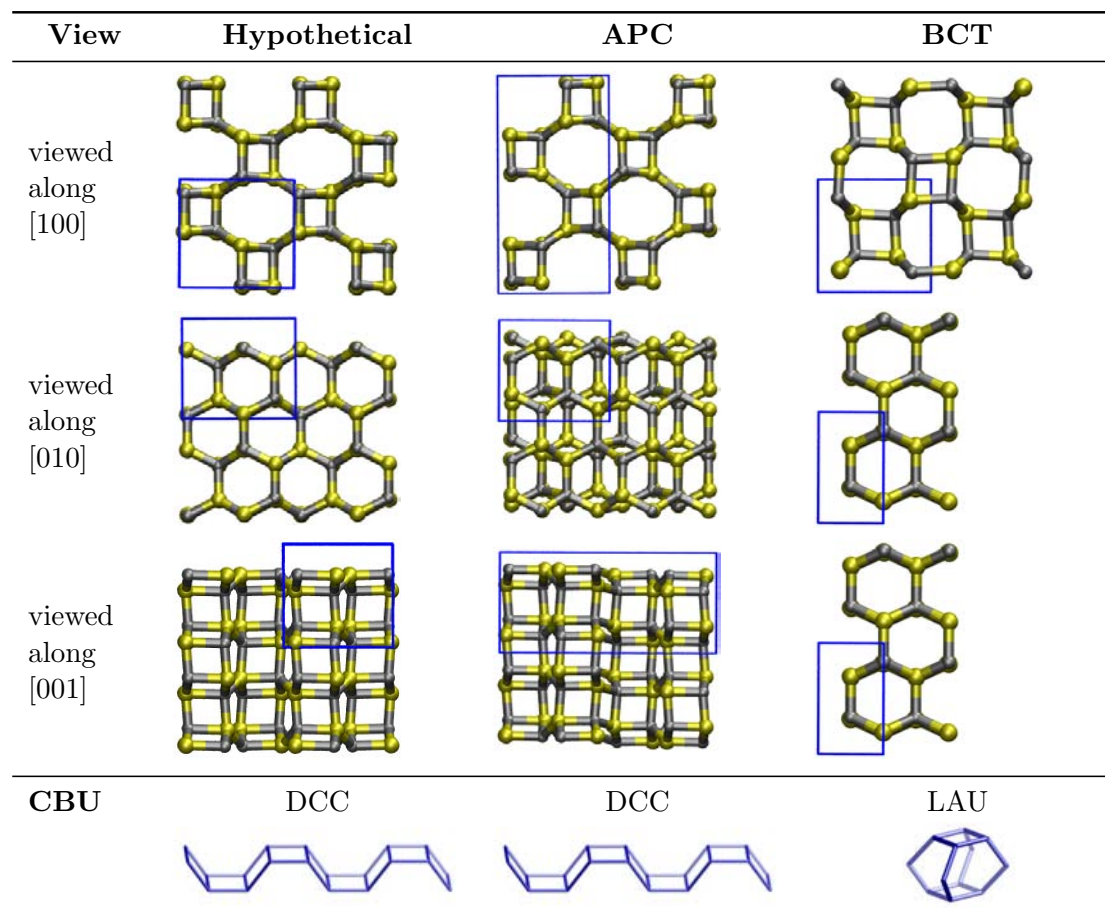
TABLE 7.15: Potential energies of our hypothetical structure and the APC framework relative to sphalerite, obtained using the five different force fields and first principles calculations. All values are given in units of kJ/mol per formula unit.

Structure	Shell/Tors	Shell/NoTors	Rigid	Rigid/Tors	Hamad *et al.* [94]	DFT
Hyp.	33.19	11.17	3.04	27.17	9.11	24.46
APC	33.81	26.16	10.51	48.97	21.18	35.31

Table 7.14. It is difficult to clearly visualise the structural differences between our hypothetical phase, and the BCT and APC frameworks, so we have attempted to highlight the building units of the different structures to better illustrate the differences, shown in Table 7.16. In these figures we have highlighted the double crankshaft chain CBUs in different colours; equivalent layers are shown in the same colour. From Table 7.16 we can clearly see our zeolite has a repeating sequence of two layers, while the APC structure has repeating unit of four layers of these

CBUs. Additionally, the first two layers of the APC phase has the DCC units aligned in the same way as our hypothetical phase, while the final two layers have the DCC units present as mirror images of the top two layers. The BCT phase is entirely different to either our hypothetical phase or the APC framework, and is comprised solely of LAU CBUs. We have highlighted only the top four LAU building blocks for the BCT phase in Table 7.16. The view along [100] and the off-axis view down [010] of the BCT phase are perhaps the best illustrations, where any four-membered ring actually indicates a 'stack' of LAU CBUs, including the

TABLE 7.16: Our hypothetical zeolite framework and the APC and BCT frameworks shown from four different directions. The CBUs for our hypothetical structure and the APC indicated in the same colour are equivalent layers, while the LAU units of the BCT are shown in different shades only to clarify individual units.

View	Hypothetical	APC	BCT
viewed along [100]			
viewed along [010]			
viewed along [001]			
Slightly off-axis down [100] and [010] (far right)			
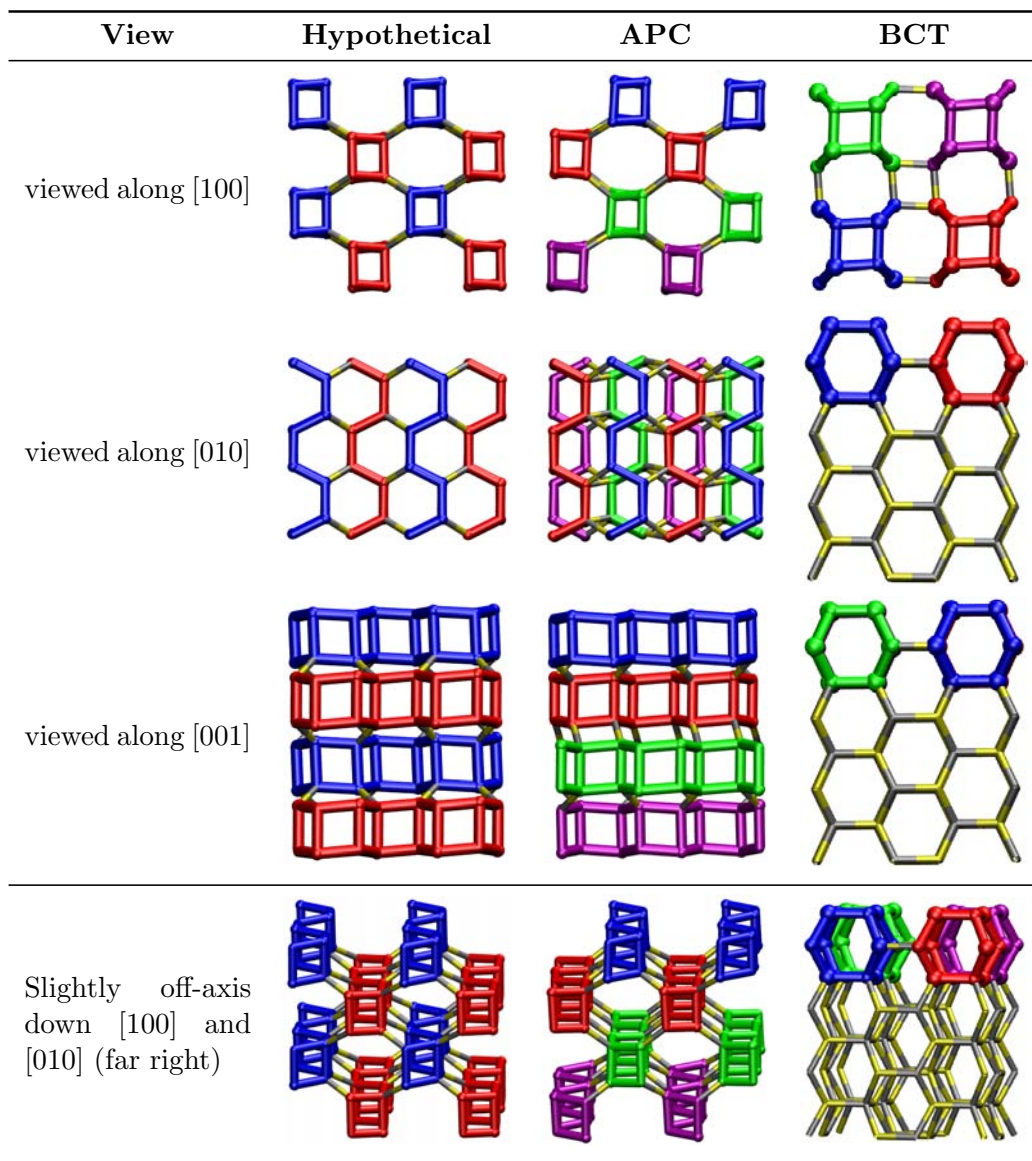
central four-membered ring. The relative potential energies given in Table 7.15 show that all the five force fields find the APC phase to be higher in energy than our hypothetical phase, in agreement with the values obtained from our first principles calculations. The Wright and Gale [95] force field gives the lowest energy difference between the two hypothetical polymorphs, less than 1 kJ/mol, while the other force fields yield a ∼7-15 kJ/mol difference between the two phases, not far from the ∼9 kJ/mol found via DFT.

7.4   Conclusions

One of the issues involved with predicting stabilities of a system using computational methods, whether it be finite or periodic, is first determining a good force field. Our studies into hypothetical zeolitic ZnS frameworks have highlighted this, where many of the force fields aren't capable of predicting the correct stabilities for the known bulk polymorphs. An additional failure is taking into account the stabilities of other phases, such as the BCT phase, as predicted by QM methods. If classical methods are desired to model these nanoporous structures in the future it seems valuable to develop a new zinc sulfide force field which is fitted not only to experimental data for the bulk polymorphs wurtzite and sphalerite, but also considers data relevant to the BCT phase. It is possible the simulations of nanoparticles of ZnS from previous chapters would have obtained very different structures had the energy of the BCT phase been considered in the parameterisation of the force field.

As mentioned in the earlier chapters, we will now investigate the parameters used to model the ZnS-water interactions.

Chapter 8

Interaction of zinc sulfide with water

8.1 Introduction

The interactions of ZnS with water are particularly relevant for investigating 'real-world' problems, where ZnS is generally not present in vacuum. In Chapter 1 we introduced some of the reasons why we are studying the material zinc sulfide, such as its technological applications as a semiconducting material[51]. However, perhaps more significant is the means of obtaining ZnS or other sulfide materials from the Earth. The processing of sulfide ores is usually performed via leaching with highly acidic or alkaline solutions, and large quantities of waste materials are produced. These wastes can break down when exposed to air and water, generating sulfuric acid and potentially releasing heavy metals from the remaining ore, which can wash into surface or ground water supplies[70]. This process is known as acid mine drainage (AMD) which we introduced in Chapter 1, and has been extensively studied in the literature[341–344]. Sulfide minerals can also be formed naturally by sulfate reducing bacteria in anoxic environments, and the biomineralisation of ZnS via biofilms is also of significant interest[345]. It is the nature of these mineral surfaces, and their reactivity, which in effect controls all of these processes and therefore there is a significant impetus for understanding the interfacial interactions between sulfide materials and water. Many studies have been performed investigating the surface stabilities of zinc sulfide[70, 89, 94],

however there is still not much data available on the binding of water to these surfaces.

In this chapter we will focus on the investigation of the ZnS-water interactions, with the aim of validating the force field(s) we have used throughout the works detailed in the previous chapters. In addition to comparing the results obtained from the different force fields we have used, we will also employ first principles calculations as another means of validation.

8.2 Methods

8.2.1 Force field parameters

We will use the same five force fields for modelling ZnS outlined in the previous chapter, Chapter 7. These are the force fields of Hamad *et al.* [94], Wright and Gale [95] (Shells/Tors), Wright and Gale [95] without the torsional term (Shells/NoTors), a rigid-ion version of the Wright and Gale [95] model (Rigid/Tors) and finally a rigid-ion model (Rigid) used in our metadynamics simulations described in Chapters 5 and 6. These models have already been tabulated in Chapter 7, in Tables 7.3-7.6, and will not be repeated here.

Species	Charge (e)		
O_w	-0.820		
H_w	+0.410		
Species	Bond length (Å)	k_{bond} (eV/Å^2)	
O_w - H_w	0.96	23.44	
Species	θ (°)	k_{angle} (eV/rad^2)	
H_w-O_w-H_w	104.5	2.17	
Lennard-Jones potential	A (eV Å^{12})	C (eV Å^6)	Cut-off (Å)
O_w - O_w	27291.75	27.12	12.00
H_w - H_w	4x10^{-13}	0.0	12.00

TABLE 8.1: The potential parameters of the CVFF water model of Lau *et al.* [287].

For consistency, we have employed the same water model as that used in the studies performed by Hamad *et al.* [113]. This is a flexible water model known

as the consistent valence force field (CVFF) water model and its parameters are reported in Table 8.1.

We note that the bond-stretching and angle-bending terms in the CVFF force field have the form:

$$E_{bond} = k_r(r_{OH} - r_{OH}^0)^2 \tag{8.1}$$

$$E_{angle} = k_\theta(\theta_{HOH} - \theta_{HOH}^0)^2 \tag{8.2}$$

The equivalent forms implemented in GULP[160] or DL_POLY_2.0[303] both use $\frac{1}{2}k$ rather than k as the multiplier. When employing the above potential parameters in GULP or DL_POLY_2.0 the k values given in Table 8.1 therefore need to be doubled.

8.2.2   First principles calculations

As described in the preceding chapters, the first principles SIESTA[138] methodology expands the Kohn-Sham wave functions using a linear combination of atomic orbitals (LCAO). The nuclei and core electrons of atoms are represented through the use of norm-conserving pseudopotentials of the form developed by Troullier-Martins[139], while the valence electrons are treated explicitly. We have used the same pseudopotentials and basis sets for the zinc and sulfur as used in the previous chapters (Chapters 5 and 7), which we will repeat below for completeness. However, additional pseudopotentials and basis sets were required for modelling the hydrogen and oxygen atoms of water.

The valence electronic configurations for generating the pseudopotentials were Zn $(3s^23p^63d^{10})$, S $(3s^23p^4)$, O $(2s^22p^4)$ and H $(1s^1)$. As described previously, the basis sets for sulfur required triple-ζ quality $3s$ and $3p$ orbitals and double-ζ quality $3d$ orbitals, while for zinc double-ζ quality was necessary for the $4s$, $4p$, and $3d$, and single-ζ for the $3s$ and $3p$ orbitals. The basis sets for oxygen required triple-ζ quality $2s$ and $2p$ orbitals, and double-ζ $3d$ orbitals; hydrogen required triple-ζ quality $1s$ and double-ζ $2p$ orbitals. A full description of the basis sets used in this study is given in Appendix B.

The shape of the basis set was improved following the method introduced by Junquera *et al.* [291], where the pseudoatomic orbitals (PAO) of the isolated atoms

are enclosed within a soft-confined spherical potential, removing any discontinuity of the basis function first derivative at the cut-off radius. A split-norm value of 0.15 was used and 0.02 Ry for the energy shift of radial confinement. An auxiliary real-space Cartesian grid with a cut-off of 400 Ry was used for calculating quantities based on electron density.

8.2.3   Calculating binding energies

In the next section we will begin to report the binding energies between clusters of zinc sulfide and water molecules. However, before we delve into these results it is necessary to briefly outline how binding energies are calculated.

In general the binding energy between two or more molecules is calculated by taking the difference between the total energy of the complex and the sum of the energies obtained from the individual non-interacting components[119]. Ordinarily the energy of the complex is lower than the sum of its individual components, but it is conventional to describe the binding energy as a positive value (*i.e.*, the negative of the heat of formation).

In our case our 'complex' is a cluster of zinc sulfide and one or more bound water molecules, which makes the individual non-interacting components to consider the zinc sulfide cluster and the water molecule(s). This calls for three optimisation calculations; one of the complex, the individual zinc sulfide cluster and finally of a water molecule. The binding energy for this system is defined by:

$$U_{binding} = -[U_{complex} - (U_{ZnS\ cluster} + n \cdot U_{H_2O})] \qquad (8.3)$$

where n is the number of water molecules bound to the complex. In our tabulations we have also divided the binding energy by the number of water molecules, to obtain a binding energy per water molecule that can be easily compared between different clusters.

When performing first principles calculations to determine binding energies there is an added complication as a result of using finite atom-centred basis sets[119]. Computation of the energies for the individual components using first principles methods will employ only the basis sets relevant to each component, while the calculation for the whole complex enables 'sharing' of the orbitals between the

individual components as orbitals from all the components are present. Taking the difference between these values to obtain the binding energy results in a binding energy that is greater in magnitude than the calculation should yield. This phenomenon is known as the basis set superposition error (BSSE). Fortunately we can attempt to correct for this over-estimation of the binding energy. One method to overcome BSSE is known as the counterpoise method introduced by Boys and Bernardi [346]. There are however a number of methods available, and these are compared elsewhere[347] and are beyond the scope of this chapter. We also direct the reader to van Duijneveldt *et al.* [348] who have reviewed the applications of counterpoise theory and other methods to determine the BSSE correction.

Once the potential energy for the complex has been obtained, this relaxed structure can be used to perform a number of single point calculations, to obtain the BSSE correction value. The BSSE correction value can be defined by[348]:

$$U_{BSSE} = U^{A\{AB\}} - U^A + U^{B\{AB\}} - U^B \tag{8.4}$$

Where $U^{A\{AB\}}$ and $U^{B\{AB\}}$ indicate the energy of A and B calculated separately via single-point calculations, however with the basis sets of both A and B present in each calculation. The values U^A and U^B are the values obtained from single-point calculations for each component separately, with only the basis sets relevant to each component present. The value of U_{BSSE} calculated in this way should be a negative value, usually within the range of 0 to -10 kJ/mol, to be added to the (positive) binding energy calculated via (8.3). In the context of our study the A and B components are the ZnS cluster and the bound water(s), respectively. In the next section both the binding energy calculated via Equation (8.3) and the BSSE corrected binding energy will be tabulated.

8.3 Results and Discussion

8.3.1 Clusters and binding energies

The ability of the different forcefields to describe the ZnS-water interaction has been investigated, first by looking at the binding energy of a water molecule to the sodalite cage $(ZnS)_{12}$ structure, shown in Table 8.2. We have chosen this cluster as it is consistently the lowest energy cluster for this size using all the force fields.

Clusters such as this, with a water molecule (or many water molecules) coordinated to a zinc or sulfur atom, were used by Hamad *et al.* [110] to parameterise their ZnS-water interactions.

The binding energies of water to sodalite are also given in Table 8.2. The force field which obtains a binding energy closest to our first principles calculation is the "Rigid/Tors" force field - a rigid version of the force field of Wright and Gale [95], where the binding energy is 52.3 kJ/mol and the DFT calculation yields 58.0 kJ/mol. The Zn-O$_w$ distance is also the closest, 2.22 Å for the Rigid/Tors model and 2.18 Å for the DFT results.
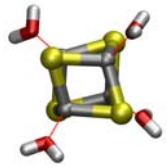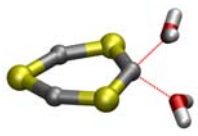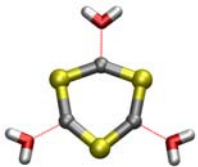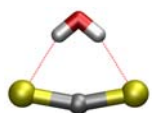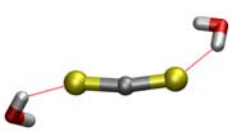
TABLE 8.2: Binding energies for water to a ZnS sodalite cage as obtained using six different force fields and first principles calculations.

Structure	Binding energy (kJ/mol)	O$_w$-Zn Distance (Å)
Force field		
Shells/Tors	40.1	2.36
Shells/NoTors	39.9	2.37
Rigid/Tors	52.3	2.22
Rigid	21.7	2.66
Hamad *et al.* [94]	39.6	2.37
Rigid/Tors (Mod.)	153.7	1.81
DFT	57.7	2.18
DFT (BSSE corr.)	48.8	2.18

The ZnS-water interactions we have used are those of Hamad *et al.* [110]. Referring back to their work we can investigate how they developed their potential parameters. They used the energies obtained via first principles calculations of six different ZnS clusters coordinated with differing numbers of water molecules to derive their potentials. These clusters are given in Table 8.3, along with the binding energy per water molecule obtained via six force fields, our own DFT calculations and also the values given in the original paper of Hamad *et al.* [110]. The sixth force field given in Tables 8.2 and 8.3, "Rigid/Tors (Mod.)", uses the Rigid/Tors model with a modified version of ZnS-water potential, which we will discuss in the following section. Here we will first discuss the five force fields we have already become familiar with from the previous chapters.

We have included the values listed in the original paper of Hamad *et al.* [110] in Table 8.3. We can see some discrepancies in our binding energies calculated using

TABLE 8.3: Binding energies and the cluster configurations used in the work of Hamad *et al.* [110] to derive their ZnS-water potential parameters. Binding energies from the literature[110] are shown, from interatomic potential (IP) and first principles (DFT) methods, along with those from the six force fields we have used and our own DFT calculations, BSSE corrected values are shown in parentheses. All values are given in units of kJ/mol per bound water molecule.

Cluster	IP Ref.[110]	Force field		Dist. Å	DFT Ref.[110]	DFT (BSSE)	Dist. Å
	60.3	Hamad *et al.* [110]	62.9	2.15	65.1	63.0 (55.4)	2.11
		Shells/Tors	65.3	2.11			
		Shells/NoTors	65.4	2.11			
		Rigid/Tors	83.9	2.03			
		Rigid	30.8	2.46			
		Rigid/Tors (Mod.)	192.9	1.79			
	57.9	Hamad *et al.* [110]	63.9	2.20	48.2	55.3 (48.4)	2.13
		Shells/Tors	68.3	2.14			
		Shells/NoTors	68.1	2.14			
		Rigid/Tors	76.2	2.12			
		Rigid	35.4	2.48			
		Rigid/Tors (Mod.)	96.9	1.80			
	48.2	Hamad *et al.* [110]	50.3	2.32	53.1	61.6 (53.1)	2.17
		Shells/Tors	43.7	2.34			
		Shells/NoTors	44.7	2.37			
		Rigid/Tors	43.7	2.28			
		Rigid	26.9	2.61			
		Rigid/Tors (Mod.)	146.9	1.84			
	57.9	Hamad *et al.* [110]	61.5	2.23	48.2	51.0 (44.5)	2.17
		Shells/Tors	67.4	2.13			
		Shells/NoTors	67.2	2.13			
		Rigid/Tors	75.1	2.13			
		Rigid	34.4	2.49			
		Rigid/Tors (Mod.)	177.3	1.81			
	86.8	Hamad *et al.* [110]	78.9	2.68	106.1	4.1 (1.6)	2.99
		Shells/Tors	116.4	2.43			
		Shells/NoTors	116.4	2.43			
		Rigid/Tors	101.5	2.59			
		Rigid	30.8	3.11			
		Rigid/Tors (Mod.)	106.5	2.51			
	86.8	Hamad *et al.* [110]	78.0	2.49	100.8	19.2 (16.9)	2.42
		Shells/Tors	83.86	2.43			
		Shells/NoTors	83.82	2.43			
		Rigid/Tors	93.71	2.46			
		Rigid	47.95	2.79			
		Rigid/Tors (Mod.)	96.87	2.57			

their potential, and those given from the literature. As we described in the previous chapter, it is possible there are some potential parameters missing from their ZnS potential given in the literature[94], as we also could not reproduce the relative potential energies between the bulk polymorphs of ZnS - sphalerite, wurtzite and BCT. It is likely the discrepancy we find in our binding energies is due to some differences (or missing parameters) in our implementation of the Hamad *et al.* [94] ZnS potential. The difference in binding energy is overestimated by up to 5 kJ/mol per water molecule where binding occurs between zinc and oxygen, and underestimated by approximately 8 kJ/mol per water molecule where the binding occurs between sulfur and hydrogen.

Overall the rigid-ion model (Rigid) consistently offers binding energies which are much lower than those obtained from the other force fields, and the DFT calculations, with the exception of our DFT calculations where water is coordinated to sulfur. The shell model of Wright and Gale [95], both with and without the torsional term (Shells/Tors and Shells/NoTors), is neither significantly better nor worse than the shell model of Hamad *et al.* [94]. In some cases the binding energy is slightly larger or slightly less than the binding energy obtained via the Hamad *et al.* [94] model but there does not appear to be a clear overall trend. However, the binding energies for S-H$_w$ using Shells/Tors, Shells/NoTors and Rigid/Tors are somewhat closer to the values obtained from the DFT calculations of Hamad *et al.* [94].

The values obtained for the final structure in Table 8.3 are the least 'consistent', in the sense that many of the optimisations performed located a minimum which appears to be slightly different to that depicted in Hamad *et al.* [110], with the water molecules finding different orientations to coordinate with the sulfur atoms. The water molecules tended to rotate such that both the hydrogen atoms of the water molecules are coordinated with the end-group sulfur atoms of the S-Zn-S cluster. A similar minimum was obtained from the DFT optimisation, where one water molecule has rotated and both the hydrogen atoms would be considered coordinated to a sulfur atom, while the second water molecule remained with one hydrogen atom coordinated. However, the image for the cluster in Hamad *et al.* [110] implies that the water molecules and cluster are all oriented in the same plane, with only one hydrogen atom of each water molecule coordinating with the sulfur atoms of the cluster. The starting configurations for the optimisation calculations were adjusted in an attempt to obtain the minima shown in the paper

of Hamad *et al.* [110], with all the molecules oriented in the same plane, with little success.

The second last cluster in Table 8.3 also yields a very low binding energy with our DFT calculations. We have repeated this calculation with different starting configurations, with the water molecule closer to the ZnS cluster, in an attempt to locate a minimum which obtains a more reasonable binding energy with no success. In all instances, either the water molecule was too close and the cluster was found to be completely unstable and the optimisation fails to converge, or alternatively the same minimum was found with a binding energy of approximately 2 kJ/mol after BSSE correction. The binding energy as obtained from our DFT calculations for the final cluster in the table also has a very low binding energy of approximately 17 kJ/mol after BSSE correction. While this may appear more reasonable than the 2 kJ/mol of the second last cluster, it is still significantly lower than the binding energies obtained using any of the other force fields, or the DFT calculation of Hamad *et al.* [94]. The force fields used and the DFT calculations of Hamad *et al.* [94] all find the binding between S-H_w to be greater than the binding energy between Zn-O_w. Its not clear if our DFT calculations, which show a small H_w-S interaction, is a discrepancy, or if all the other models are overestimating the binding energy.

8.3.2 Free Energy Perturbation

A more accurate way of modelling the interactions between a material and water is firstly to consider its properties when in contact with bulk water, rather than the coordination of a cluster with only a few water molecules, which essentially behaves as a cluster in *in vacuo* rather than a 'solvated' cluster. Secondly, one of the properties of ions in bulk water is the solvation free energy, and this can be used to enhance the accuracy of a model of a material's interaction with water[349, 350].

The value of the solvation free energy can be obtained theoretically via a method we introduced in Chapter 3 known as free energy perturbation (FEP), an idea that was originally proposed by Zwanzig [227]. He introduced a means of calculating the free energy difference between two systems described by two different Hamiltonians, $\mathscr{H}_a(\mathbf{p}^N, \mathbf{q}^N)$ and $\mathscr{H}_b(\mathbf{p}^N, \mathbf{q}^N)$. This technique is commonly used to perform "alchemical" transformations, where one species is transformed into another and the free energy difference associated with the transformation

is calculated. As mentioned in Chapter 3, solvation free energies of ions can be calculated using FEP, whereby an ion in solvent is iteratively 'perturbed' to disappear, leaving only the solvent. In the context of our work we can investigate performance of the ZnS-water potential by calculating the free energy of solvation of the Zn^{2+} and S^{2-} ions using free energy perturbation (FEP) and compare these values to those obtained from experiment.

FEP calculations use a procedure known as staging, where a number of intermediate states are introduced between the two states of interest and the system is progressively perturbed from one to the next, until the final state is reached[228]. This procedure ensures that every perturbation is small and therefore that the sampling will be accurate and the overall free energy difference can be obtained as the sum of all the intermediate contributions. We can write the potential energy as a linear combination of U_a and U_b;

$$U_{\lambda_i} = (1 - \lambda_i)U_b + \lambda_i U_a \qquad (8.5)$$

where λ_i is called the perturbation parameter and $\lambda_i = 1$ corresponds to state a and $\lambda_i = 0$ to state b. The FEP equation can then be rewritten as;

$$\Delta A_{a \to b} = \sum_{i=0}^{N-1} \Delta A_{\lambda_i \to \lambda_{i+1}} = \sum_{i=0}^{N-1} -k_B T \ln \langle e^{-\beta \Delta U_{\lambda_i, \lambda_{i+1}}} \rangle_{\lambda_i}. \qquad (8.6)$$

where λ_i identifies the intermediate stages of the perturbation. The optimal number of intermediate states depends on the problem; generally the greater the difference between the starting and final state the more intermediate states are necessary[228]. λ_i can be seen as a perturbation parameter which allows for going from state a to state b. In our case λ is simply a scaling factor that perturbs to zero the interactions between the ion and the solvent.

In practice, to achieve satisfactory convergence it is necessary to treat the electrostatic and long-range interactions separately, such that[351]:

$$U_{solute-solvent} = U_{\lambda_C}^{elec}(r) + U_{\lambda_{LJ}}^{vdw}(r) \qquad (8.7)$$

The electrostatic portion can be treated via:

$$U_{\lambda_C}^{elec}(r) = \sum_i \sum_j \lambda_c \frac{q_i q_j}{r_{ij}} \qquad (8.8)$$

However, the long-range interactions, such as Lennard-Jones 12-6 interactions, have a discontinuity in the force field as r tends to zero, due to the $1/r^{12}$ term[351]. To avoid this problem a 'soft-core' potential can be implemented, a λ-dependent variant of the Lennard-Jones potential, which tends to a finite a value at $r=0$. The concept of using a soft-core potential to avoid this discontinuity when perturbing the Lennard-Jones interactions to zero was originally introduced by Beutler *et al.* [352], and an example of a soft-core potential is illustrated in Figure 8.1. The use of
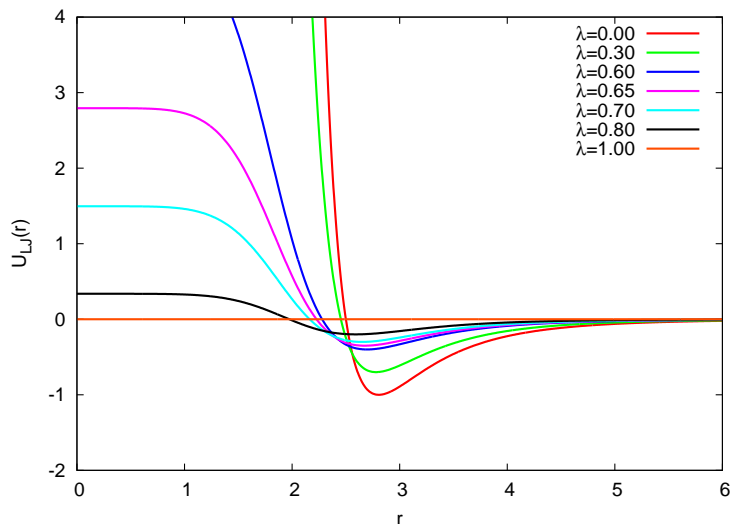
FIGURE 8.1: Example of a λ-dependent soft-core Lennard-Jones potential. At $\lambda=0$ the potential has the original Lennard-Jones form, going to infinity as r tends to zero. As λ increases to one, the potential form changes to reach a finite value at small values of r. Image adapted from Beutler *et al.* [352].

soft-core potentials to avoid discontinuities in FEP calculations has been recently discussed in the literature[351, 353, 354]. We have used the parameterisation of the soft-core Lennard-Jones term as used by Hess and van der Vegt [355];

$$U_{LJ\ soft-core} = (1 - \lambda_{LJ})U_{LJ}([\alpha_{LJ}\sigma_{LJ}^6\lambda_{LJ} + r^6]^{(1/6)}) \qquad (8.9)$$

where the paramater α_{LJ} controls the 'soft-core' behaviour of the Lennard-Jones potential at r values close to zero, and depends on the system being explored[351]. The parameter σ_{LJ} in Equation (8.9) defines a soft-core interaction radius[353, 355]. In our case we have used an α_{LJ} value of 0.6 and σ_{LJ} of 2.8 Å, as used in the study of Hess and van der Vegt [355]. The potential U_{LJ} is the 'ordinary' hard-core potential form used (*i.e.*, the not λ-dependent LJ potential). In contrast to the variation of the Coulombic interaction given in Equation (8.8), in Equation (8.9) a λ_{LJ} value of 0 indicates a full LJ interaction, while a value of

1 indicates the interaction has been 'turned off'. While Equation (8.9) gives one possible form of a λ-dependent LJ potential, and is the form used in the present study, other forms can be found in the literature[351, 354]. We used a version of the DL_POLY[303] molecular dynamics program modified to perform these FEP simulations in the manner we described above. It is worth noting that when implementing the free energy perturbation method the calculation of long-range electrostatics interactions are unchanged; they are handled in the same manner as in our previous MD studies in water - using the Ewald summation.

Experimentally all ions exist with full integer charges, the only reason partial charges are used in force field models is to better reproduce the nature of the bulk material. For our investigation of the free energy of solvation it is necessary to use ions of full integer charge to make a meaningful comparison to experimental values. Later this essentially limits us to those ZnS potentials with full +2/-2 charges on the Zn and S ions, respectively, when using the derived ZnS-water interactions to perform simulations of clusters coordinated with water. This leaves us with the Rigid/Tors model (the rigid-ion version of the Wright and Gale [95] model), as we have removed the shells from the model, and the ions possess integer charges. FEP calculations were performed using the ZnS-water interactions of Hamad *et al.* [110] to determine the solvation free energy of S^{2-} and Zn^{2+} ions. In theory it is possible to perform FEP calculations using a shell model where the sum of the charges on the core and shell add to an integer value. However, we have not yet implemented the capability for perturbation of the shells in our version of DL_POLY[303] and we leave this for future studies.

The starting configurations for our simulations were a 25.4 Å sided box of 520 water molecules, with either the Zn^{2+} or S^{2-} ion positioned at the centre of the box. Twenty evenly spaced values of λ were used (1.00,0.95,...,0.05) to remove the charges on the ions, followed by another twenty values of λ (0.00,0.05,...,0.90,0.95) to progressively reduce the Lennard-Jones interactions to zero. Raiteri *et al.* [349] demonstrated that removing each interaction separately in this way improves the accuracy of the FEP calculations, where they used the FEP method to investigate the free energy of solvation of Ca^{2+} ions. In their work they have successfully used a $\delta\lambda = 0.1$ spacing, while in our work we have chosen a more conservative value of $\delta\lambda = 0.05$ spacing to confidently achieve convergence. As was shown in the same study, evenly spaced λ values are effective for calculating the free energy perturbation of an ion 'disappearing', however the reverse (a particle appearing)

can be problematic if a soft-core potential is not implemented. In these cases logarithmic spacing of λ values can be used instead. Each simulation (performed at a specific λ value) was performed for 1 ns, with an initial 200 ps of equilibration.

TABLE 8.4: Calculated and literature values for the solvation free energy of Zn^{2+} and S^{2-}. The FEP calculation was performed using the Rigid/Tors ZnS potential and the ZnS-water interactions of Hamad *et al.* [110].

Species	Calculated value (kJ/mol)	Experiment[356] (kJ/mol)
Zn^{2+}	-1450 ± 1	-1955
S^{2-}	-1285 ± 2	-1315

The free energies obtained are given in Table 8.4 along with the values listed in the literature from experiment[356]. The free energy of solvation of Zn^{2+} is significantly higher (less exothermic) than the value found experimentally, with a difference between the values of approximately 505 kJ/mol, while the difference for the free energy of solvation of S^{2-} is only 30 kJ/mol. We have devised a new set of potential parameters for the ZnS-water interactions in an attempt to better model the free energy of solvation. The parameter that obviously needs major alteration is the interaction of water with the Zn^{2+} ion. For this parameter we began with the interactions for the Mg^{2+} ion with water, which members of the group have been investigating for other studies[357]; these are listed in Table 8.5. This was a convenient starting point as Mg^{2+} has an experimental solvation free energy of -1830 kJ/mol[356], not far from the value for Zn^{2+}, -1955 kJ/mol, and both ions have a double positive charge. The Mg-water interactions already developed use the Lennard-Jones form given in Equation (8.10).

TABLE 8.5: $Mg-O_w$ potential parameters[357] used as a starting point for refitting the $Zn-O_w$ interactions.

Lennard-Jones 12-6	ϵ (eV)	σ (Å)
Mg core - O_w core	0.048385	2.238

$$U_{LJ} = \epsilon \left[\left(\frac{\sigma}{r_{ij}} \right)^{12} - \left(\frac{\sigma}{r_{ij}} \right)^{6} \right] \tag{8.10}$$

The free energy of solvation for Zn^{2+} is more exothoermic than Mg^{2+}, and much more than the free energy of solvation obtained using the parameters of Hamad *et al.* [110]. To correct this we need to bring the water molecules closer to the

zinc ion, which can be achieved by decreasing the value of σ in the Lennard-Jones 12-6 potential in Equation (8.10). The potential parameters we have obtained by modifying the parameters in Table 8.5 are given in Table 8.6. Using these new potential parameters to perform the same free energy perturbation simulation of Zn^{2+} and S^{2-} in water we obtained new values of the solvation free energies, and these are listed in Table 8.7. For Zn^{2+} we obtained a solvation free energy of -1956 $\pm$ 2 kJ/mol, much closer to the experimentally determined value than the value obtained using the Hamad *et al.* [110] parameters (-1450 kJ/mol). The free energy of solvation for S^{2-} is also improved.

TABLE 8.6: ZnS-water interactions derived to obtain more accurate values of the free energy of solvation. These were parameterised using the Rigid/Tors force field for the ZnS interactions.

Lennard-Jones 12-6	ϵ (eV)	σ (Å)	
Zn core - O_w core	0.048385	1.96	
Buckingham potential	A (eV)	ρ (Å)	C (eV Å^6)
S core - O_w core	123571	0.2465	0.00

TABLE 8.7: Calculated and literature values for the solvation free energy of Zn^{2+} and S^{2-}. The FEP calculation was performed using the Rigid/Tors ZnS potential and the ZnS-water interactions given in Table 8.6.

Species	Calculated value (kJ/mol)	Experiment[356] (kJ/mol)
Zn^{2+}	-1956 $\pm$ 2	-1955
S^{2-}	-1314 $\pm$ 2	-1315

The Zn^{2+} and S^{2-} ions were also run for 2 ns of simulation time with the same starting configurations to determine the coordination number of water around the ions, and the pair distribution function (PDF) of water with the ions in bulk water. These simulations were performed both with the Hamad *et al.* [110] potential and our modified potential given in Table 8.6. The PDF and coordination number plots for the original and modified water interactions are shown in Figure 8.2. We can see that the changes to the Zn-O_w interaction have resulted in a slightly shorter Zn-O_w distance, with an average distance for the first coordination shell of water molecules at 1.90 Å, shortened from approximately 2.05 Å in the original Zn-O_w interactions of Hamad *et al.* [110]. This value is slightly lower than that estimated from experiment, 2.093 Å[358, 359]. The number of water molecules coordinated
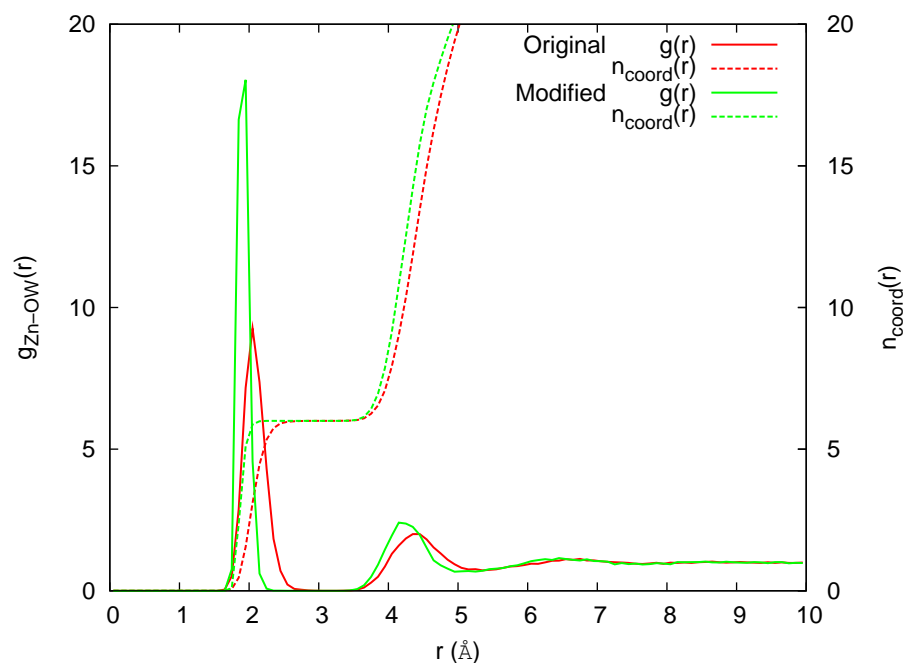
FIGURE 8.2: Pair distribution function for Zn-O_w as obtained in bulk water using the original ZnS-water interactions of Hamad *et al.* [110] (red) and our modified force field (green). The number of water molecules coordinated to the ion with respect to distance from the ion is also shown (dashed lines).

around the Zn^{2+} ion is the same for both force fields, with a value of 6. This is the coordination number experimentally found[358], and is illustrated in Figure 8.4. Throughout the 2 ns simulation of the Zn^{2+} ion in water we did not observe any of the water molecules from the solvation shell exchanging with waters in the bulk solvent. This is unsurprising considering the very exothermic value for the free energy of hydration, and is consistent with experimental observations[360, 361] where exchanges are expected to occur with a frequency at least on the order of tens of nanoseconds.

For sulfur we have measured the pair distribution functions for both the S-O_w and S-H_w distances, and the number of water molecules coordinating with sulfur, these are all shown in Figure 8.3. The difference between the original force field and our modified version is minimal, as expected due to the small alterations we made to the S-O_w interactions. The shift in S-O_w distance is from approximately 3.35 Å to 3.30 Å and approximately 2.40 Å to 2.35 Å for S-H_w. The number of water molecules coordinated to the S^{2-} ion is 11; the same number is obtained when using both force fields. The sulfur ion and surrounding 11 water molecules are shown in Figure 8.4
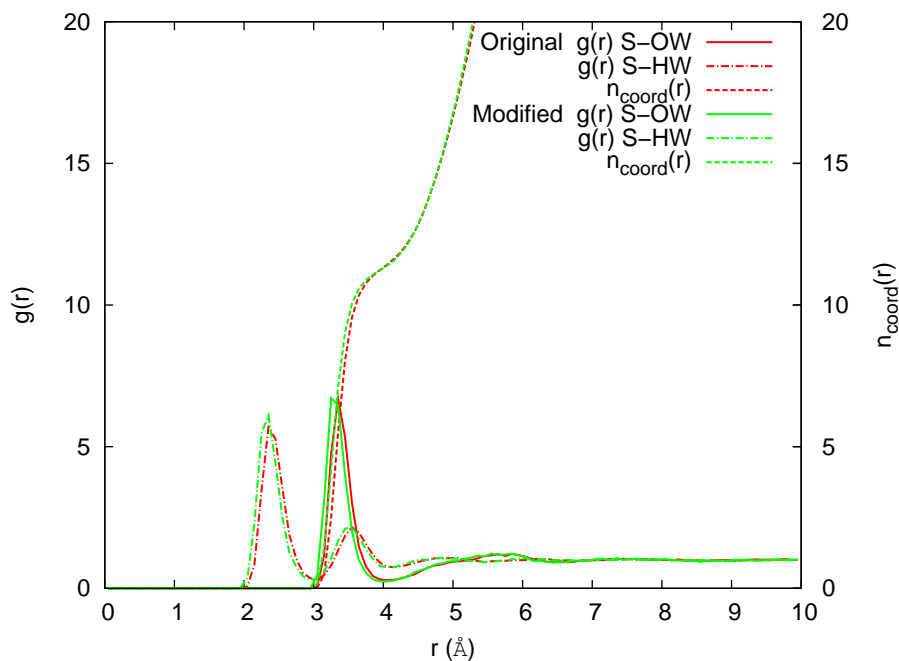
FIGURE 8.3: Pair distribution functions for S-O_w (bold lines) and S-H_w (dot-dash lines) as obtained in bulk water using the original ZnS-water interactions of Hamad *et al.* [110] (red) and our modified force field (green). The number of water molecules coordinated to the ion with respect to distance from the ion is also shown (dashed lines).
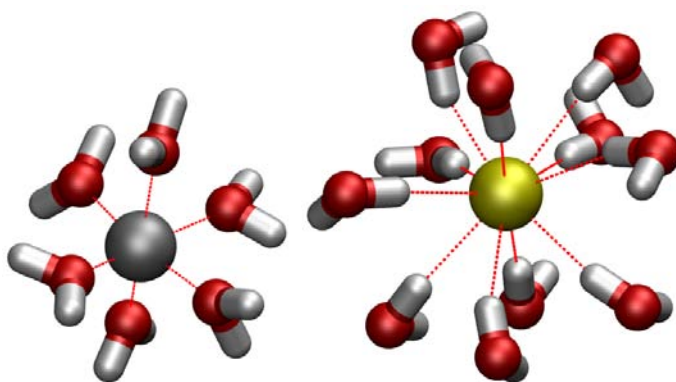
FIGURE 8.4: Coordination of water with zinc (left) and sulfur (right) ions. Six oxygen atoms (O_w) coordinate with zinc while eleven hydrogen atoms of water coordinate with sulfur. The same coordination was observed using the 'original' rigid ion model, and the version modified to obtain the correct free energy of solvation.

We have also re-run the calculations of the small clusters coordinated with water with these new ZnS-water potentials. The values of the binding energies obtained per water molecule are given in Table 8.3, along with the binding energies obtained using the five other force fields. We have labelled this newly fitted force field as 'Rigid/Tors (Mod.)' to indicate we used the Rigid/Tors model and a modified ZnS-water interaction. With our modified force field we generally find higher binding energies for the clusters involving Zn-O_w interactions, while the clusters involving S-H_w interactions have binding energies of the same order of magnitude as obtained via the original force field. Neither of these outcomes is surprising as we made significant changes to the Zn-O_w interactions but few changes to the S-H_w interactions for the ZnS-water potential. What is surprising is the magnitude of the binding energy for water coordinated with Zn. The binding energies using our modified ZnS-water potential are generally 2-3 times the values obtained using the other force fields and DFT calculations. The Zn-O_w distance is also much smaller, with an average Zn-O_w distance of 1.81 Å, at least 0.3 Å shorter than the distances obtained using the other models.

While the significant changes made to the Zn-O_w parameter reproduce the experimentally determined free energy of solvation, it is possible that the ZnS-water parameters we have produced are not suitable for estimating the binding energy of water to small clusters of ZnS. The parameters may be more suitable for calculations involving bulk water interacting with ZnS.

8.3.3 Water interaction with surface

The binding energy of a water molecule on the (110) surface of sphalerite has been investigated using the six different forcefields already discussed. A variety of starting configurations were generated, with a water molecule positioned at different sites across the surface. In this way we hoped to probe how many distinct surface binding sites exist for sphalerite, and how these differ between the models.

The (110) surface was chosen because it is a perfect cleavage surface[70] for sphalerite-type crystal structures and for ZnS it is predicted to be the most stable surface[89, 94]. Due to its existence as a cleavage surface for many semi-conductor materials it is also one of the most well-studied surfaces, and there are a variety of experimental and theoretical studies in the literature to compare against our results.
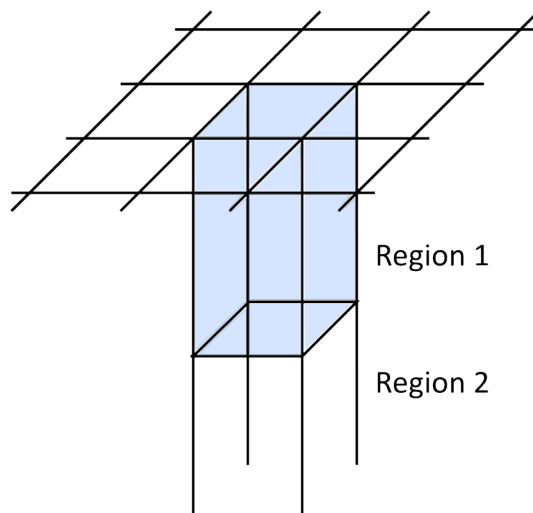
FIGURE 8.5: Schematic of a surface 'super cell' set-up for optimisation. Atoms in region 1 (shaded) are allowed to relax, while those below in region 2 remain fixed. Image adapted from Gay and Rohl [362].

Before we can investigate the interaction of water with the (110) surface we first need to generate the surface and relax it with each of the five force fields. Surface relaxation calculations are generally performed by allowing a top layer of a given surface slab to relax (region 1), while the lower layers of the surface are fixed (region 2), as depicted in Figure 8.5 and described in the work of Gay and Rohl [362].

Prior to performing our relaxation runs we first needed to determine an adequate thickness of both region 1 and 2 which allows convergence of the surface energy (*i.e.*, the surface energy obtained is not affected by either of the regions being too thin). We first tested the required thickness of region 2, keeping region 1 at a thickness of one layer. We created 6 different surfaces with region 2 ranging from 1 to 6 layers in thickness. Our results show that the surface energy converges with a thickness of four layers in region 2. The process was repeated, this time keeping region 2 at a thickness of four layers, and increasing the thickness of region 1 from 1 to 6 layers. We found convergence of the surface energy also with a thickness of four layers. A larger surface was constructed, again with 8 total layers depth (4 layers for region 1 and 4 layers for the fixed region 2), and with approximate surface of dimensions 20 Å x 20 Å. The actual surface 'cell' parameters varied depending on the force field used, as these all relax sphalerite with slightly different dimensions and configurations. The surfaces were created with this larger super cell with the aim in mind of investigating the binding energy of one water molecule on the surface. We required the surface to be large enough
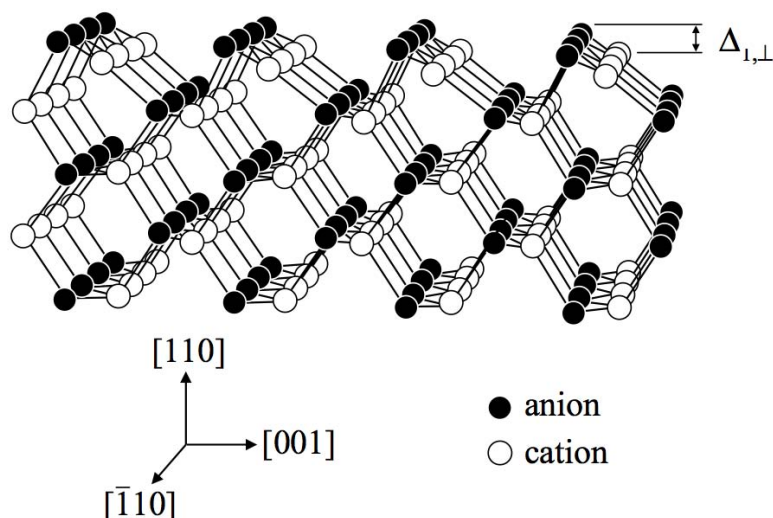
FIGURE 8.6: An example of a relaxed (110) sphalerite surface. The main structural parameter which indicates surface rearrangement, $\Delta_{1,\perp}$, is indicated. Image reproduced and adapted from Rosso and Vaughan [70], originally adapted from Duke [93, 363].

such that neighbouring mirror images of the water molecules do not interact with each other, as we have considered only an individual water molecule interacting with the surface.

The (110) cleavage surface of sphalerite is a charge neutral surface, and relaxation generally involves a displacement of the first layer of ions. Specifically the anion, in this case sulfur, is displaced upwards and the cation, zinc in our case, moves downwards upon relaxation[70, 364]. The perpendicular shear of the surface, $\Delta_{1,\perp}$, is one of the main structural parameters which describes the degree of surface relaxation[70]. This parameter essentially indicates the difference in the vertical positions of the anions and cations in the top 'layer' of the surface, as indicated in Figure 8.6 for the example of a relaxed (110) sphalerite surface.

The surface energy obtained using the Hamad *et al.* [94] force field accurately replicates the value of 0.53 J/m^2 as described in their paper[94]. We have given a complete listing of the surface energies and $\Delta_{1,\perp}$ parameters obtained from the relaxed surfaces in Table 8.8, along with a tabulation of data obtained from the literature.

Before considering the calculations performed to investigate the binding of water to these relaxed (110) surfaces there are some points of interest to discuss from these results obtained from the relaxed (110) surfaces. A clear point of interest is the inability of either of the rigid-ion models to replicate the experimentally

TABLE 8.8: Surface energies, and structural parameter $\Delta_{1,\perp}$ for the relaxed (110) sphalerite surface, using five different force fields. Data obtained from the literature is also tabulated.

Force field	Surface energy (J/m^2)	$\Delta_{1,\perp}$ $(\mathring{A})$
Hamad *et al.* [94]	0.5304	0.355
Shells/Tors[95]	0.4535	0.517
Shells/NoTors	0.4389	0.531
Rigid/Tors	0.8917	0.002
Rigid	0.4100	0.134
Experimental [365]	-	0.59
Wright *et al.* [89]	0.65	0.28
Steele *et al.* [364] (DFT)	0.35	0.52
Steele *et al.* [364]	0.53	0.25
Zhang *et al.* [98]	0.39	-

determined distortion of the (110) surface upon relaxation. Both of the rigid ion models have very small values for $\Delta_{1,\perp}$, in comparison to the other three force fields we have used, where Rigid/Tors has barely any distortion at all, 0.002 Å, and Rigid a small distortion of 0.134 Å. It seems the surface distortion of ZnS is reliant on the polarisability of the sulfur anions. Another outcome from these results is that of the models investigated, the shell model of Wright and Gale [95] manages to replicate the surface distortion of the same order as the experimental value. The Wright and Gale [95] model with (Shells/Tors) and without the torsional term (Shells/NoTors) obtain similar $\Delta_{1,\perp}$ values, 0.517 and 0.531 Å, respectively, close to the experimental value of 0.59 Å[365] and the value obtained from first principles calculations of Steele *et al.* [364].

Once we had obtained these relaxed surfaces for the five force fields we began investigating the binding energy of one water molecule to the relaxed (110) sphalerite surface. We generated six different starting configurations, with the water molecule located at different positions on the (110) surface. In all cases our optimisations located essentially only one unique minimum. This is illustrated in Figures 8.7 and 8.8, where the water molecule is located in the same position across the surface. The optimisations performed using the Rigid/Tors ZnS model in conjunction with the Hamad *et al.* [110] ZnS-water potential were the only calculations which yielded a slightly different minimum, shown in Figure 8.8, where the water molecule oriented itself parallel to the plane of the ZnS surface. All the other potential models (including the Rigid/Tors model with our ZnS-water

potential generated in the previous section) yielded the water in the orientation shown in Figure 8.7, essentially perpendicular to the (110) surface.
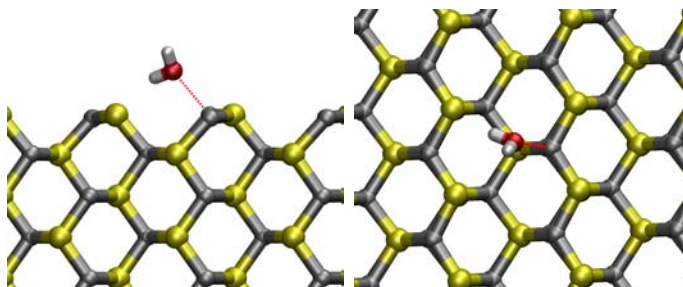
FIGURE 8.7: Sphalerite (110) surface with one adsorbed water molecule after relaxation; the same position for water was obtained using all the force fields except the Rigid/Tors model. Images show views across the (110) plane (left) and viewed perpendicular to the (110) plane (right).
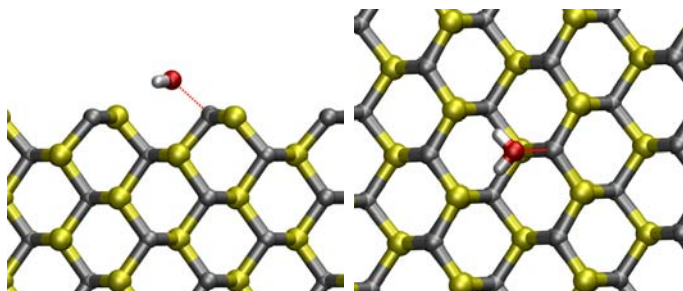
FIGURE 8.8: Sphalerite (110) surface with one adsorbed water molecule after relaxation with the rigid ion model. Images show views cross the (110) plane (left) and viewed perpendicular to the (110) plane (right).

The binding energies for all the optimised surfaces with one adsorbed water molecule are given in Table 8.9. The binding energies obtained for a water molecule to the (110) surface are of the same order of magnitude of those found for the ZnS clusters of Hamad *et al.* [110] shown in Table 8.3. Again, the Rigid/Tors model with the modified ZnS-water interaction yields the greatest outlier in the binding energies, with a binding energy approximately 2-3 times greater than any of the other force fields.

8.4 Conclusions

We have performed a variety of calculations to investigate the binding energy of water with small ZnS clusters and the (110) sphalerite surface. The initial studies

TABLE 8.9: Binding energies of one water molecule to an optimised (110) sphalerite surface, using six different force fields. The first five values listed in the table used the ZnS-water potential of Hamad *et al.* [110], while the final entry used the Rigid/Tors ZnS potential and the modified ZnS-water potential introduced in the previous section and given in Table 8.6.

Force field	Binding energy (kJ/mol)	Zn-O_w Dist. (Å)
Hamad *et al.* [94]	52.1	2.35
Shells/Tors	49.1	2.37
Shells/NoTors	48.3	2.37
Rigid/Tors	70.7	2.38
Rigid	28.9	2.71
Rigid/Tors (Mod.)	166.5	1.82

of the clusters showed that many of the force fields yielded binding energies of the same order as those obtained via DFT. In general, the rigid-ion model offered binding energies that were lower than the other force fields and the first principles calculations. Significant discrepancies were observed from the DFT calculations for the clusters with the hydrogen of water bound to sulfur atoms, where very low binding energies were obtained in comparison to all the force fields and the results of Hamad *et al.* [110]. It is possible the binding energies obtained via the force fields and Hamad *et al.* [110] are over-estimates of the actual value. This may be due in part to the use of the CVFF water force field, which was originally parameterised to model bulk water[287]. The use of this water model to calculate binding energies of clusters in the gas phase (with very few bound water molecules) may not be entirely valid, and may explain the significant discrepancies between some of the binding energies obtained using force field methods and those of the DFT calculations.

Free energy perturbation simulations were performed to determine how the ZnS-water interactions of Hamad *et al.* [110] would reproduce the experimental solvation free energy of Zn^{2+} and S^{2-}. We found the solvation free energy of Zn^{2+} was approximately 500 kJ/mol less exothermic than the experimental value. Re-fitting the ZnS-water interactions of Hamad *et al.* [110] did result in the experimental free energy of solvation being reproduced. However, repeating the binding energy calculations for the small ZnS clusters resulted in binding energies significantly larger than that found with any of the other force fields we studied. The main outcome from these calculations is that its likely a new ZnS-water potential is required for investigating the stability of ZnS clusters in bulk water.

While the binding energies obtained for the individual water molecules to the small clusters of zinc sulfide may be accurate, they are not necessarily suitable for fitting the potentials which will dictate the behaviour of zinc sulfide in *bulk* water. It is well known that there exist many-body effects in intermolecular forces that cannot be ignored if an accurate description of a system is desired[366]. In the context of our studies this means the water-water interactions for multiple water molecules surrounding a ZnS cluster are likely to be appreciable. Additionally, the water model we have used does not allow for polarisability of the water molecule; this is another factor which may significantly hinder accurate representations of the systems we have studied[367, 368]. Implementation of polarisable force fields for both the solute and solvent may enable accurate values of binding energies and the free energy of solvation to be modelled. Based on our results presented in this chapter the development of a fully polarisable force field for ZnS, optimised to be employed in bulk water, may be a wise direction for future studies.

Chapter 9

Conclusions

Throughout this work we have employed a variety of computational techniques, with the initial aim of investigating the size and shape of nanoparticles of zinc sulfide. We began with a focus on the nano-scale, which led us to investigate bulk nanoporous zinc sulfide (zeolite analogues), and finally to an evaluation of the ZnS-water potential used in our study of nanoparticles in water.

One of the objectives of this thesis was to study the application of accelerated dynamics for exploring the structures of nanoparticles. The trace of the inertia tensor was the first collective variable we implemented for use with the metadynamics approach. This collective variable proved useful in exploring the phase space of small clusters of $(ZnS)_n$ (where $n = 3, \ldots, 24$). However, the efficacy was clearly reduced as the number of degrees of freedom increased, with limitations in the exploration of phase space as $n > 18$. Additionally, we found it was not possible to directly calculate free energy differences from these simulations as there is significant overlap between the free energy basins of different minima when projected onto the trace of the inertia tensor. Instead, we required additional collective variables, such as the path variables, in order to calculate the free energy differences. The additional metadynamics simulations we performed using the path variables gave comparable free energy differences for clusters *in vacuo* as calculated using lattice dynamics within the quasi-harmonic approximation. To our knowledge this is the first time the free energy values obtained using the metadynamics method with the path variables have been validated using an alternative means of obtaining the free energy. The second set of collective variables implemented were the Steinhardt bond order parameters, Q_4 and Q_6.

We focussed on the Q_4 Steinhardt parameter as the Q_4 values for the fcc and hcp phases (the two bulk polymorphs of ZnS) were more uniquely identifying than the Q_6 values. Prior to performing the metadynamics simulations using the Q_4 collective variable we found interesting deformations through the central 'core' of the larger ZnS wurtzite nanoparticles upon relaxation. The deformed core has been seen in the literature by other studies using different force fields[313]. This internal strain is driven by a need to compensate the highly polar {0001} surfaces at either end of the nanoparticle. The metadynamics simulations performed on larger clusters (360 and 840 atom nanoparticles of ZnS cleaved from wurtzite) showed the formation of clusters with 8-membered ring channels, a structure identified as an analogue of the BCT zeolite framework. Many of the minima obtained for the different cluster sizes in the trace of the inertia studies were also shown to be analogues of composite building units of zeolite structures.

The common structural theme of zeolite motifs in both our small ($(ZnS)_n$ where $n = 3, \ldots, 24$) and large (360 and 840 atom) nanoparticles led us to investigate more generally zinc sulfide zeolite analogues. Our study highlighted the differences between five different ZnS force fields. We found that many of the force fields did not accurately model the experimental difference in energy between the two polymorphs of ZnS, wurtzite and sphalerite. Only the full shell model of Wright and Gale [95] and the rigid-ion version of this, where both include a torsional term, correctly modelled sphalerite as the lower energy polymorph. In addition to this, the BCT phase we observed in our simulations of ZnS nanoparticles is also modelled with very different results using the five different force fields. As there is currently no experimental data for a BCT phase of ZnS, we performed first principles calculations on the low energy polymorphs to offer another means of comparing the force field results. We found that only those force fields with a torsional term accurately modelled the BCT phase as higher in energy than either wurtzite or sphalerite, consistent with the order of stability obtained from our DFT calculations. The relaxed core of the 840 atom ZnS nanoparticle from our Steinhardt parameter studies was used to create a 'hypothetical' zeolite structure which has similarities with the 'APC' zeolite framework. This hypothetical framework has double crankshaft chains layered in 'ABABAB...' stacking while APC has 'ABCABC...' stacking of the same composite building unit. In all cases our new hypothetical zeolite structure was higher in energy than the bulk polymorphs, sphalerite and wurtzite, and the BCT phase.

Overall, this study highlighted that there may be significant issues using these force fields to investigate clusters of ZnS, particularly when using them to infer the stability of one cluster over another when the bulk the stabilities obtained by a given force field are contrary to experiment and first principles calculations. In the future it may be desirable to develop new force fields for zinc sulfide that take into account the energy difference of the BCT phase as obtained via first principles calculations. The lack of an appropriate force field for investigating ZnS is also highlighted by our investigation of small clusters. Our calculations did not show an unusually stable $(ZnS)_{13}$ cluster, despite the fact that this cluster size appears to be ultra-stable via laser ablation experiments and mass spectrometry[67, 115]. It is possible that the phase space was insufficiently explored to find a lower minimum for the $(ZnS)_{13}$ cluster, or that the force field we used is not capable of accurately modelling the energies of these clusters.

The final portion of the present study was an investigation into the ZnS-water interactions. The ZnS-water clusters used by Hamad *et al.* [110] to calculate binding energies and generate their ZnS-water potentials were investigated using all the ZnS force fields used throughout this work and first principles calculations. The rigid-ion models were the least capable of reproducing the values obtained via first principles methods. However, the clusters involving S-H_w bonds were found to have significantly lower binding energies using our first principles calculations, much less than those obtained from any of the force fields or the DFT calculations of Hamad *et al.* [110]. Free energy perturbation calculations using the Rigid/Tors model combined with the Hamad *et al.* [110] ZnS-water potential showed that the free energy of solvation of Zn^{2+} ions is approximately 500 kJ/mol less exothermic than the value obtained experimentally, while the solvation free energy of S^{2-} was only 30 kJ/mol more exothermic. We generated a new set of ZnS-water interactions, with the aim of enabling the free energy of solvation to be modelled more accurately. The re-fitted ZnS-water potentials were also used to calculate the binding energies of the clusters of Hamad *et al.* [110] and we found that the new force field combined with the Rigid/Tors model yielded the largest binding energies, which are consistently 2-3 times the magnitude of those obtained using other force fields and DFT methods.

One aspect of our work which we didn't investigate was the use of both of the CVs simultaneously (ie. using both the moment of inertia tensor and the Q_4 Steinhardt parameter). The metadynamics method allows the implementation of more than

one CV, and the use of both our parameters would drive the internal order and shape of the system simultaneously. This would be an interesting focus for future studies as size and shape dependent phase transitions in nanoparticles are known to exist[63, 68, 369].

It is clear from our investigation and comparison of ZnS and ZnS-water interactions that there is the need for improved force fields. The ZnS force fields could be improved by including the the data obtained by first principles methods for the BCT phase in the fitting process. It would be interesting to repeat the evaluation of the energies for ZnS zeolite analogues, performed in Chapter 7, using a ZnS force field which is designed for nanoporous ZnS structures or at least included the BCT phase during parameterisation. Ultimately a new ZnS force field is required which enables accurate modelling of bulk phases through to finite clusters, and with improved interactions with water. A reactive force field, such as those of the ReaxFF methodology[370, 371], would also allow the modelling of water dissociation at the surface of cluster. This would be particularly relevant for the sulfur anions which generally form SH^- in water[372]. In addition, the use of variable charges computed "on-the-fly" would capture some of the many-body effects missing in existing models.

In conclusion, our work has demonstrated that the use of metadynamics has potential for exploring nanostructures. Not only were many clusters and structures explored, but the metadynamics simulations performed helped highlight any deficiencies in the force fields used. Our work has shown that future studies of zinc sulfide nanoclusters, in vacuum or solvent, will be greatly assisted by the development of more accurate force fields.

Appendix A

Metadynamics using the trace of the inertia tensor

This appendix contains tabulations for all of the unique structures found from the metadynamics simulations performed, using the trace of the inertia tensor as the collective variable, on small clusters of $(ZnS)_n$, where $n = 3, \ldots, 24$. The force field used to optimise all of the structures was the shell model of Wright and Gale [95] without the torsional term. This is the same force field we used for our metadynamics simulations of the same clusters. In addition to the structures and potential energies of the different structures, we have also included the plots of the trace of the inertia tensor value over time for the metadynamics simulations from which the structures were obtained.

TABLE A.1: Structures obtained from the MetaD simulations of $(ZnS)_3$, optimised using lattice dynamics.

$(ZnS)_3$ structures

1

TABLE A.2: Potential energy for the structure obtained for $(ZnS)_3$, shown in Table A.1.

$(ZnS)_3$ potential energies (kJ mol^{-1})

Structure	U	ΔU	U/ZnS	ΔU/ZnS
1	-9092.6	0.0	-3030.9	0.0

TABLE A.3: Structures obtained from the MetaD simulations of $(ZnS)_4$, optimised using lattice dynamics.

$(ZnS)_4$ structures

| **1** | **2** |

TABLE A.4: Potential energies for the structures found for $(ZnS)_4$, shown in Table A.3.

$(ZnS)_4$ potential energies (kJ mol^{-1})

Structure	U	ΔU	U/ZnS	ΔU/ZnS
1	-12266.3	0.0	-3066.6	0.0
2	-12141.6	124.7	-3035.4	31.2

TABLE A.5: Structure obtained from the MetaD simulations of $(ZnS)_5$, optimised using lattice dynamics.

$(ZnS)_5$ structure

| **1** |
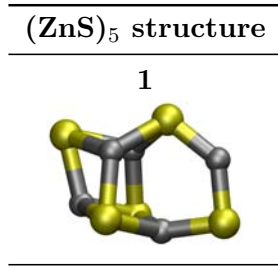
TABLE A.6: Potential energy for the structure found for $(ZnS)_5$, shown in Table A.5.

$(ZnS)_5$ potential energies (kJ mol^{-1})

Structure	U	ΔU	U/ZnS	ΔU/ZnS
1	-15407.6	0.0	-3081.5	0.0

TABLE A.7: Structure obtained from the MetaD simulations of $(ZnS)_6$, optimised using lattice dynamics.
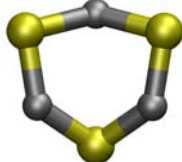
$(ZnS)_6$ structures

| **1** |

TABLE A.8: Potential energy for the structure obtained for $(ZnS)_6$, shown in Table A.7.

$(ZnS)_6$ potential energies (kJ mol^{-1})

Structure	U	ΔU	U/ZnS	ΔU/ZnS
1	-18686.8	0.0	-3114.5	0.0
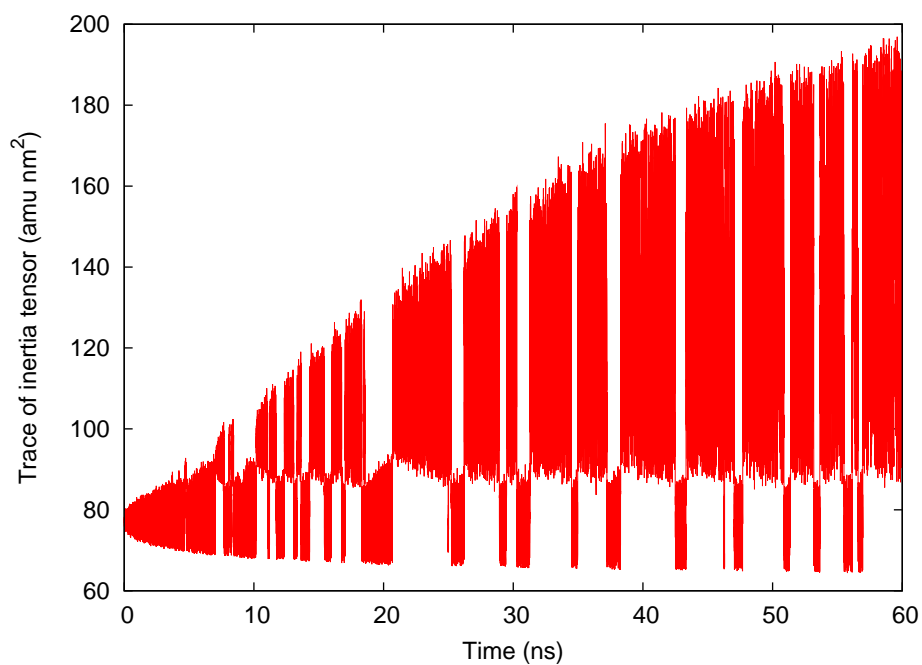
FIGURE A.1: Evolution of the trace of the inertia tensor over time for the $(ZnS)_6$ cluster
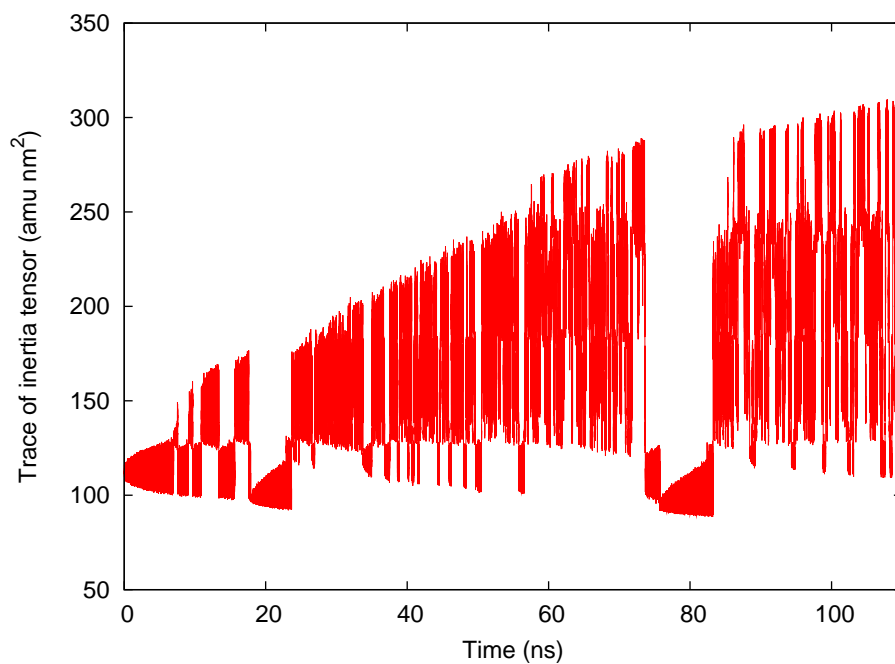
FIGURE A.2: Evolution of the trace of the inertia tensor over time for the 14 atom ZnS cluster

TABLE A.9: Structures obtained from the MetaD simulations of $(ZnS)_7$, optimised using lattice dynamics.

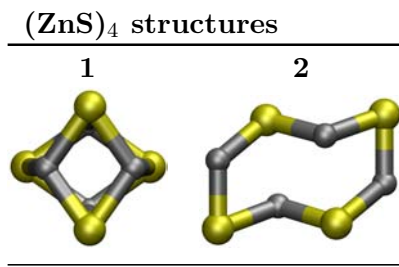| $(ZnS)_7$ structures |
|:---:|
| **1**   **2** |
| |
| **3** |
| |

TABLE A.10: Potential energies for the structures obtained for $(ZnS)_7$, shown in Table A.9.

$(ZnS)_7$ potential energies (kJ mol^{-1})				
Structure	**U**	**ΔU**	**U/ZnS**	**ΔU/ZnS**
1	-21832.4	0.0	-3118.9	0.0
2	-21807.4	25.0	-3115.3	3.6
3	-21646.8	185.7	-3092.4	26.5

TABLE A.11: Structures obtained from the MetaD simulations of $(ZnS)_8$, optimised using lattice dynamics.

$(ZnS)_8$ structures
1   **2**
3   **4**
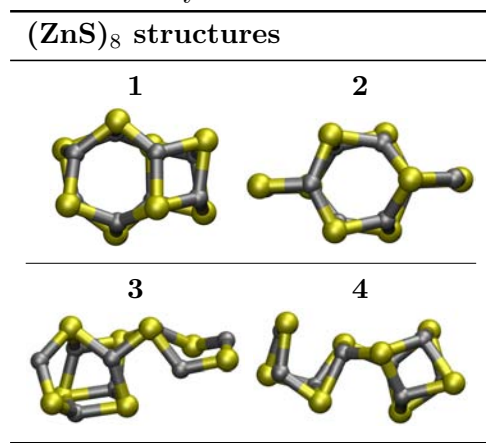
TABLE A.12: Potential energies for the structures obtained for $(ZnS)_8$, shown in Table A.11.

$(ZnS)_8$ potential energies (kJ mol^{-1})				
Structure	**U**	**ΔU**	**U/ZnS**	**ΔU/ZnS**
1	-25082.9	0.0	-3135.4	0.0
2	-24928.4	154.4	-3116.1	19.3
3	-24820.7	262.1	-3102.6	32.8
4	-24811.6	271.3	-3101.4	33.9
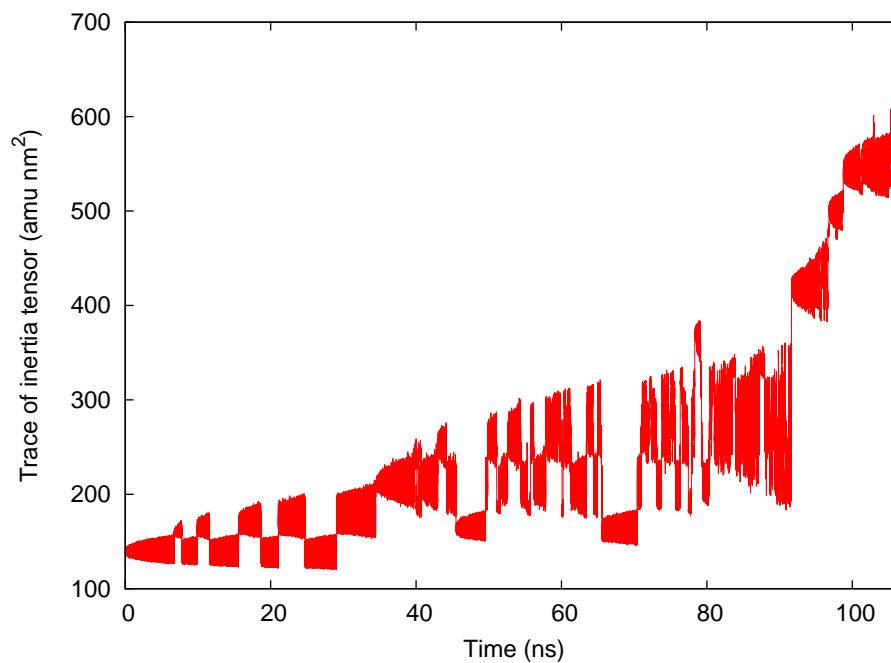
FIGURE A.3: Evolution of the trace of the inertia tensor over time for the $(ZnS)_8$ cluster

TABLE A.13: Structures obtained from the MetaD simulations of $(ZnS)_9$, optimised using lattice dynamics.
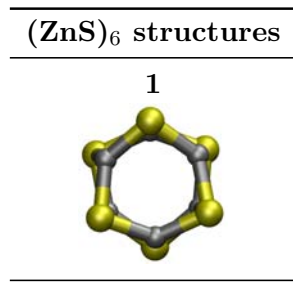
$(ZnS)_9$ structures
1 2
3
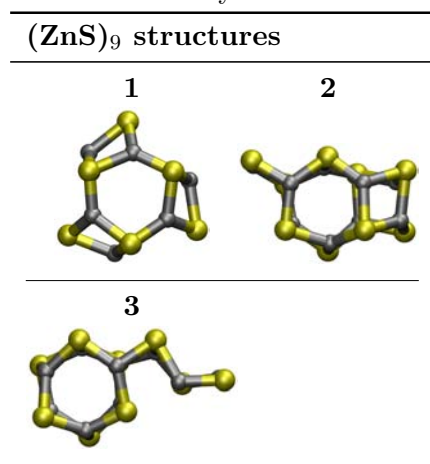
TABLE A.14: Potential energies for the structures obtained for $(ZnS)_9$, shown in Table A.13.

| $(ZnS)_9$ potential energies (kJ mol^{-1})				
Structure	U	ΔU	U/ZnS	ΔU/ZnS
1	-28285.7	0.0	-3142.9	0.0
2	-28200.7	85.0	-3133.4	9.4
3	-28079.6	206.1	-3120.0	22.9

FIGURE A.4: Evolution of the trace of the inertia tensor over time for the $(ZnS)_9$ cluster

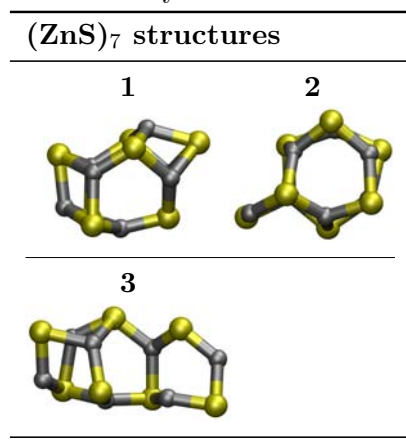TABLE A.15: Structures obtained from the MetaD simulations of $(ZnS)_{10}$, optimised using lattice dynamics.

$(ZnS)_{10}$ structures
1 **2**
3 **4**
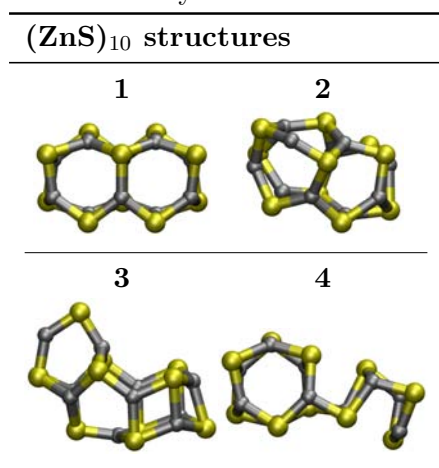
TABLE A.16: Potential energies for the structures obtained for $(ZnS)_{10}$, in Table A.15

$(ZnS)_{10}$ potential energies (kJ mol^{-1})			
Structure	**U**	**ΔU**	**U/ZnS**	**ΔU/ZnS**
1	-31437.6	0.0	-3143.8	0.0
2	-31324.6	113.0	-3132.5	11.3
3	-31260.7	176.9	-3126.1	17.7
4	-31245.7	191.9	-3124.6	19.2
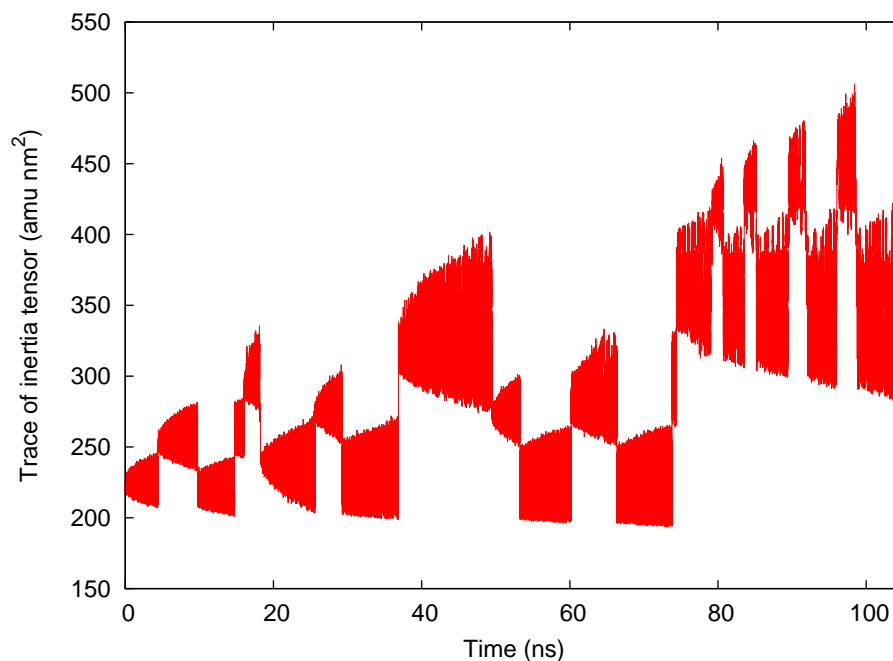
FIGURE A.5: Evolution of the trace of the inertia tensor over time for the $(ZnS)_{10}$ cluster.

TABLE A.17: Structures obtained from the MetaD simulations of $(ZnS)_{11}$, optimised using lattice dynamics.

$(ZnS)_{11}$ structures
1 2

| 3 4 |
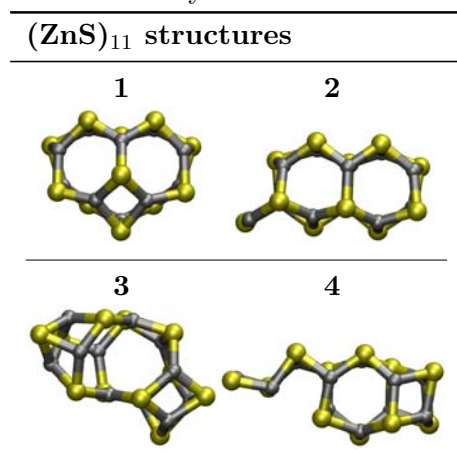
TABLE A.18: Potential energy for the structure obtained for $(ZnS)_{11}$, in Table A.17

| $(ZnS)_{11}$ potential energies (kJ mol^{-1})				
Structure	U	ΔU	U/ZnS	ΔU/ZnS
1	-34657.1	0.0	-3150.6	0.0
2	-34562.1	95.0	-3142.0	8.6
3	-34525.0	132.1	-3138.6	12.0
4	-34464.9	192.2	-3133.2	17.5

FIGURE A.6: Evolution of the trace of the inertia tensor over time for the $(ZnS)_{11}$ cluster.

TABLE A.19: Structures obtained from the MetaD simulations of $(ZnS)_{12}$, optimised using lattice dynamics.

(ZnS)₁₂ structures
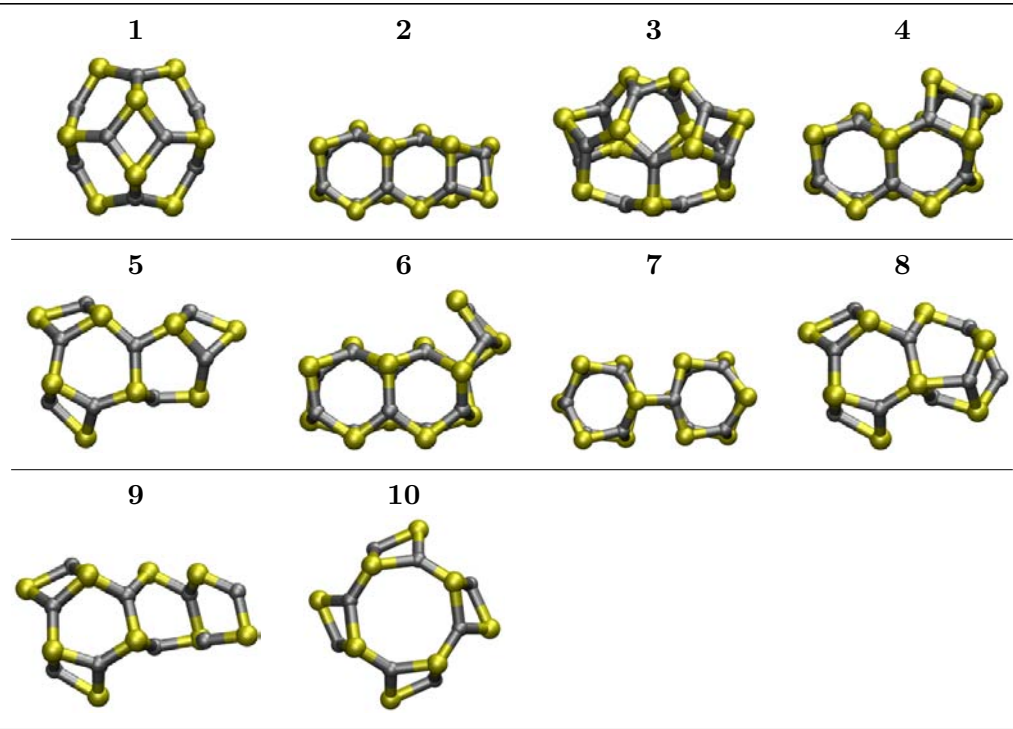
TABLE A.20: Potential energy for the structure obtained for $(ZnS)_{12}$, in Table A.19

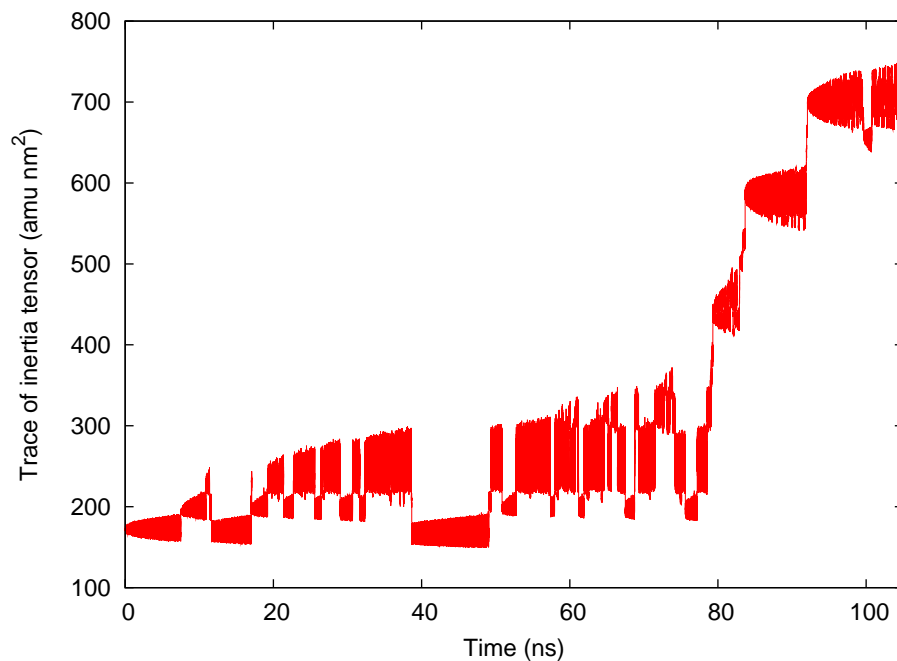| $(ZnS)_{12}$ potential energies (kJ mol^{-1})			
Structure	**U**	**ΔU**	**U/ZnS**	**ΔU/ZnS**
1	-37893.6	0.0	-3157.8	0.0
2	-37821.2	72.5	-3151.8	6.0
3	-37801.2	92.5	-3150.1	7.7
4	-37763.3	130.4	-3146.9	10.9
5	-37722.0	171.6	-3143.5	14.3
6	-37717.7	175.9	-3143.1	14.7
7	-37717.1	176.5	-3143.1	14.7
8	-37662.5	231.1	-3138.5	19.3
9	-37659.2	234.4	-3138.3	19.5
10	-37615.9	277.7	-3134.7	23.1
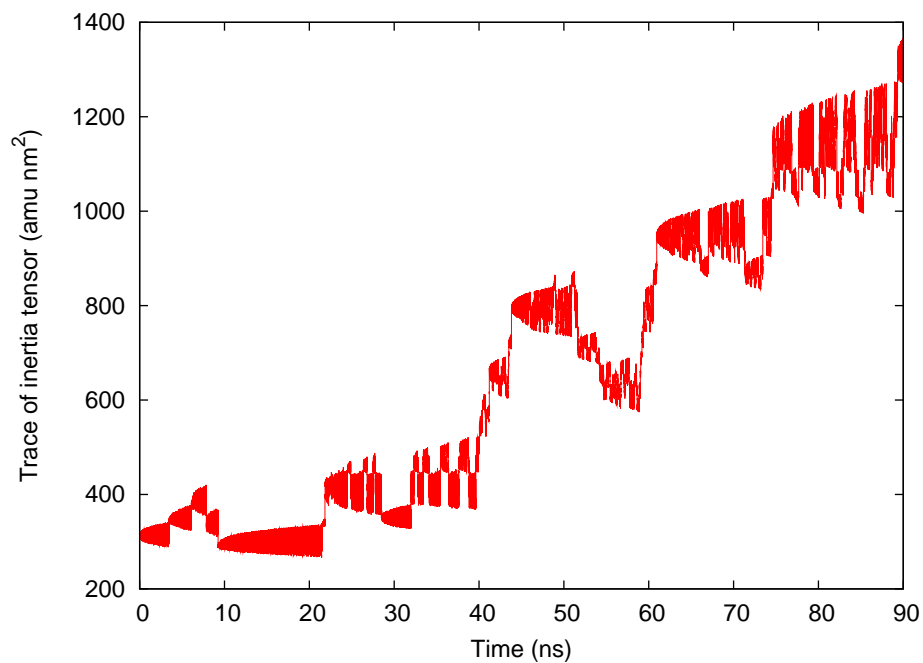
FIGURE A.7: Evolution of the trace of the inertia tensor over time for the $(ZnS)_{12}$ cluster

TABLE A.21: Structures obtained from the MetaD simulations of $(ZnS)_{13}$, optimised using lattice dynamics.
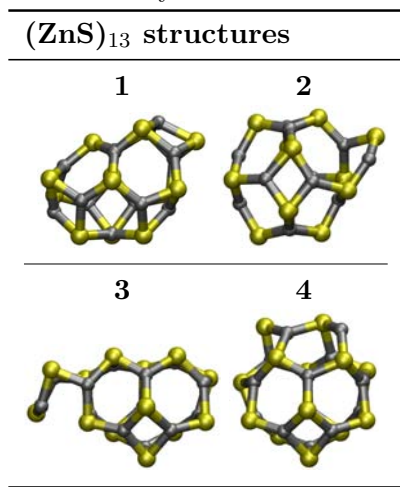
$(ZnS)_{13}$ structures

TABLE A.22: Potential energies for the structures obtained for $(ZnS)_{13}$, shown in Table A.21

| $(ZnS)_{13}$ potential energies (kJ mol^{-1})				
Structure	**U**	**ΔU**	**U/ZnS**	**ΔU/ZnS**
1	-41032.3	0.0	-3156.3	0.0
2	-40930.9	101.4	-3148.5	7.8
3	-40922.3	110.0	-3147.9	8.5
4	-40918.6	113.7	-3147.6	8.7

FIGURE A.8: Evolution of the trace of the inertia tensor over time for the $(ZnS)_{13}$ cluster

TABLE A.23: Structures obtained from the MetaD simulations of $(ZnS)_{14}$, optimised using lattice dynamics.

$(ZnS)_{14}$ structures

TABLE A.24: Potential energies for the structures obtained for $(ZnS)_{14}$, shown in Table A.23.

$(ZnS)_{14}$ potential energies (kJ mol^{-1})				
Structure	U	ΔU	U/ZnS	ΔU/ZnS
1	-44236.5	0.0	-3159.8	0.0
2	-44115.9	120.6	-3151.1	8.6
3	-44113.5	123.1	-3151.0	8.8
4	-44101.8	134.7	-3150.1	9.6
5	-44085.5	151.0	-3149.0	10.8
6	-44032.6	203.9	-3145.2	14.6
7	-44031.8	204.7	-3145.1	14.6
8	-43990.2	246.4	-3142.2	17.6
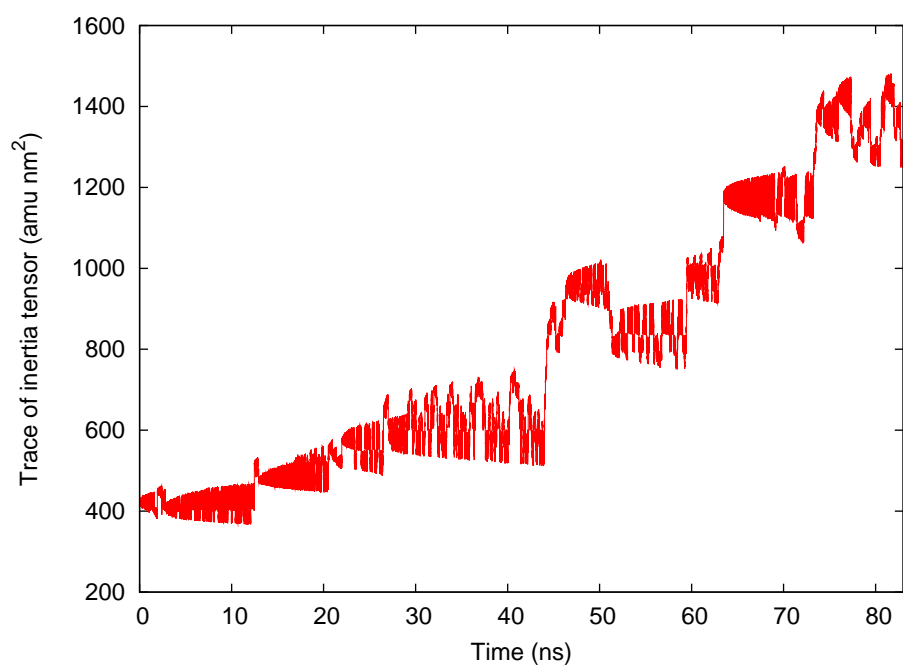
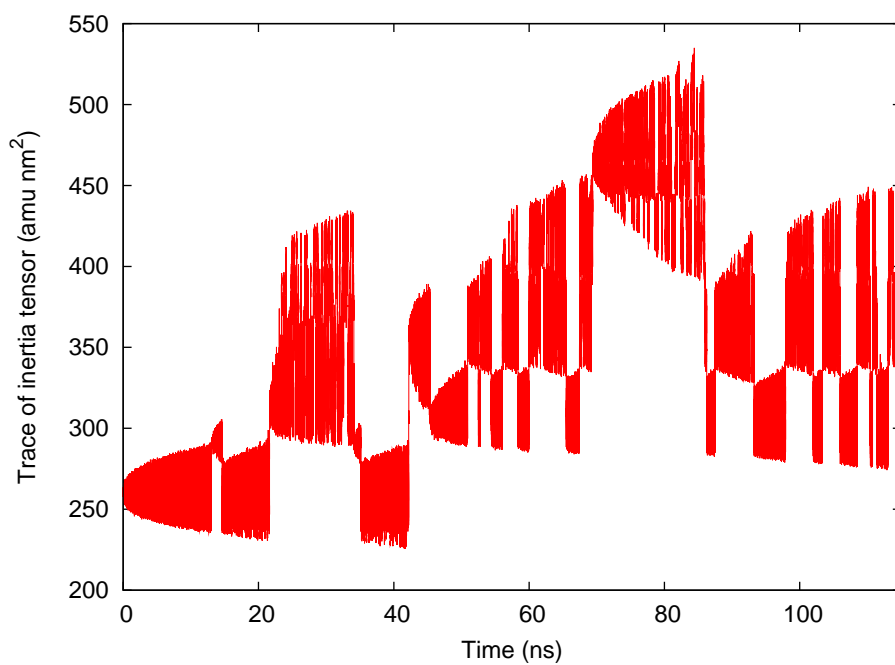FIGURE A.9: Evolution of the trace of the inertia tensor over time for the $(ZnS)_{14}$ cluster

FIGURE A.10: Evolution of the trace of the inertia tensor over time for the $(ZnS)_{15}$ cluster

TABLE A.25: Structures obtained from the MetaD simulations of $(ZnS)_{15}$, optimised using lattice dynamics.


$(ZnS)_{15}$ structures

TABLE A.26: Potential energies for the structures obtained for $(ZnS)_{15}$, shown in Table A.25.

| Structure	U	ΔU	U/ZnS	ΔU/ZnS
$(ZnS)_{15}$ potential energies (kJ mol^{-1})				
1	-47446.9	0.0	-3163.1	0.0
2	-47354.8	92.2	-3157.0	6.1
3	-47321.1	125.9	-3154.7	8.4
4	-47262.9	184.0	-3150.9	12.3
5	-47222.7	224.3	-3148.2	15.0
6	-47211.7	235.3	-3147.4	15.7
7	-47203.4	243.5	-3146.9	16.2
8	-47169.5	277.4	-3144.6	18.5
9	-47141.8	305.2	-3142.8	20.3
10	-47108.8	338.1	-3140.6	22.5

FIGURE A.11: Evolution of the trace of the inertia tensor over time for the $(ZnS)_{16}$ cluster

TABLE A.27: Structures obtained from the MetaD simulations of $(ZnS)_{16}$, optimised using lattice dynamics.

$(ZnS)_{16}$ structures				
1	**2**	**3**	**4**	**5**
6	**7**	**8**	**9**	

TABLE A.28: Potential energies for the structures obtained for $(ZnS)_{16}$, shown in Table A.27

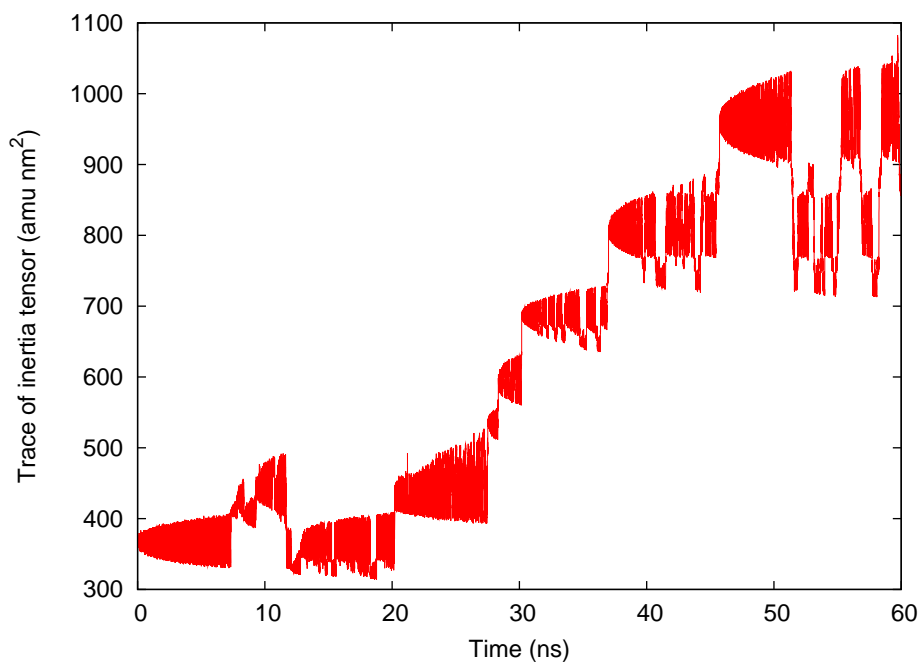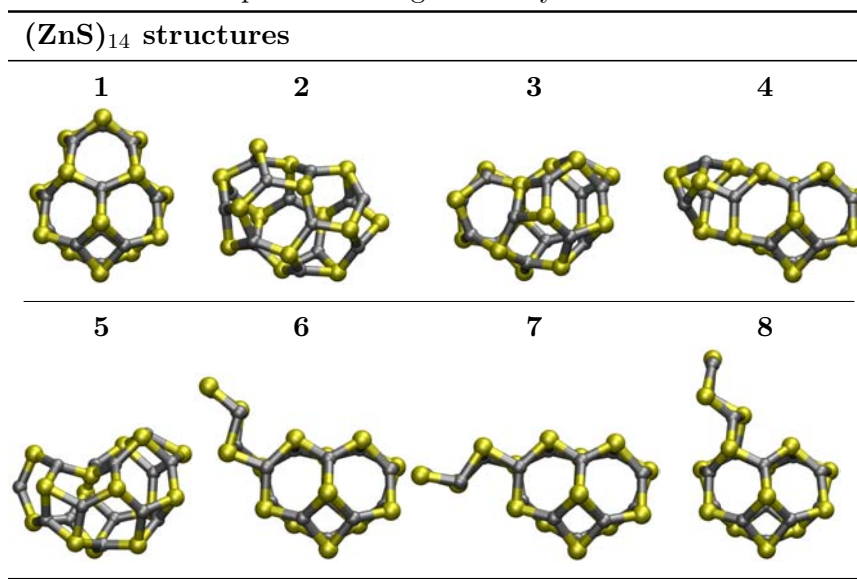| $(ZnS)_{16}$ potential energies (kJ mol^{-1})			
Structure	**U**	**ΔU**	**U/ZnS**	**ΔU/ZnS**
1	-50608.5	0.0	-3163.0	0.0
2	-50599.7	8.8	-3162.5	0.6
3	-50529.4	79.2	-3158.1	4.9
4	-50507.7	100.9	-3156.7	6.3
5	-50496.4	112.1	-3156.0	7.0
6	-50473.9	134.7	-3154.6	8.4
7	-50467.0	141.5	-3154.2	8.8
8	-50441.6	166.9	-3152.6	10.4
9	-50394.1	214.4	-3149.6	13.4

FIGURE A.12: Evolution of the trace of the inertia tensor over time for the $(ZnS)_{17}$ cluster

TABLE A.29: Structures obtained from the MetaD simulations of $(ZnS)_{17}$, optimised using lattice dynamics.

$(ZnS)_{17}$ structures

1	2	3	4	5

6	7	8	9	10

TABLE A.30: Potential energies for the structures obtained for $(ZnS)_{17}$, shown in Table A.29.

(ZnS)$_{17}$ potential energies (kJ mol^{-1})			
Structure	U	ΔU	U/ZnS	ΔU/ZnS
1	-53799.7	0.0	-3164.7	0.0
2	-53678.9	120.8	-3157.6	7.1
3	-53663.5	136.3	-3156.7	8.0
4	-53659.7	140.1	-3156.4	8.2
5	-53640.9	158.8	-3155.3	9.3
6	-53616.6	183.1	-3153.9	10.8
7	-53616.2	183.6	-3153.9	10.8
8	-53609.6	190.1	-3153.5	11.2
9	-53572.1	227.6	-3151.3	13.4
10	-53467.8	331.9	-3145.2	19.5

TABLE A.31: Structures obtained from the MetaD simulations of $(ZnS)_{18}$, optimised using lattice dynamics.

(ZnS)$_{18}$ structures

TABLE A.32: Potential energies for the structures obtained for $(ZnS)_{18}$, shown in Table A.31.

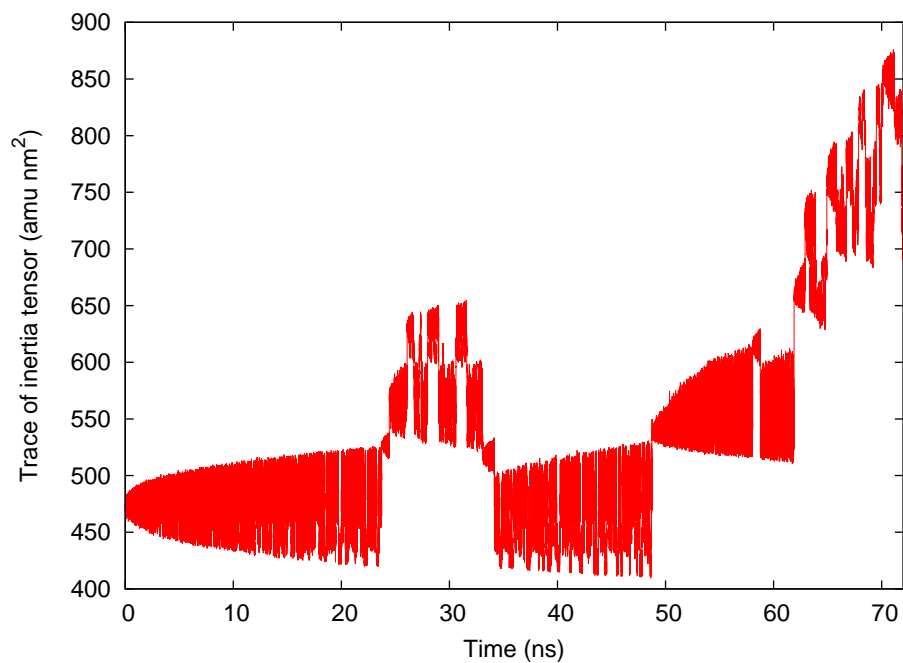| (ZnS)$_{18}$ potential energies (kJ mol^{-1})			
Structure	U	ΔU	U/ZnS	ΔU/ZnS
1	-56880.3	0.0	-3160.0	0.0
2	-56875.8	4.6	-3159.8	0.3
3	-56857.8	22.6	-3158.8	1.3
4	-56838.9	41.4	-3157.7	2.3
5	-56824.5	55.8	-3156.9	3.1
6	-56777.9	102.4	-3154.3	5.7
7	-56760.8	119.5	-3153.4	6.6
8	-56752.2	128.1	-3152.9	7.1
9	-56749.6	130.8	-3152.8	7.3
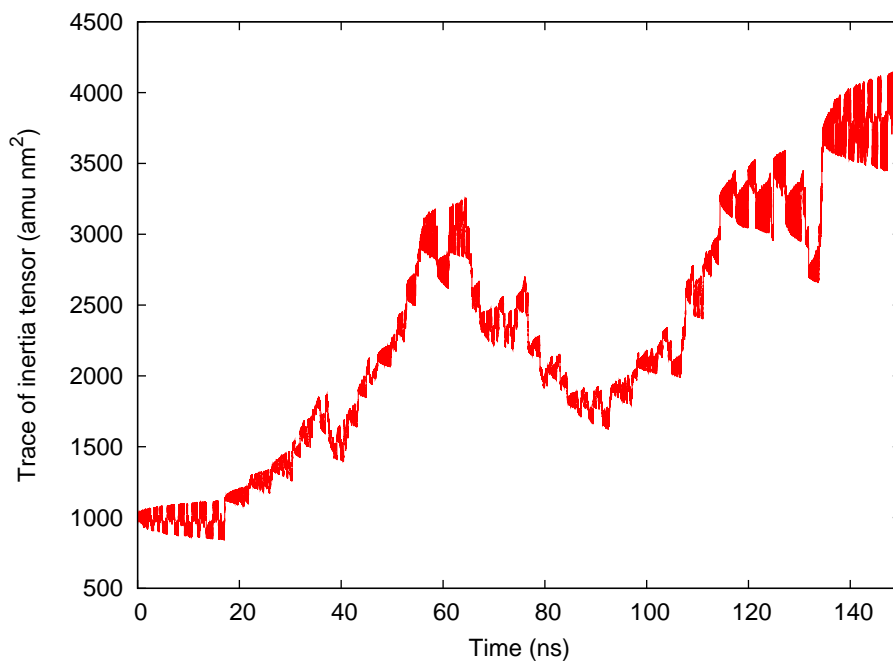
FIGURE A.13: Evolution of the trace of the inertia tensor over time for the $(ZnS)_{22}$ cluster
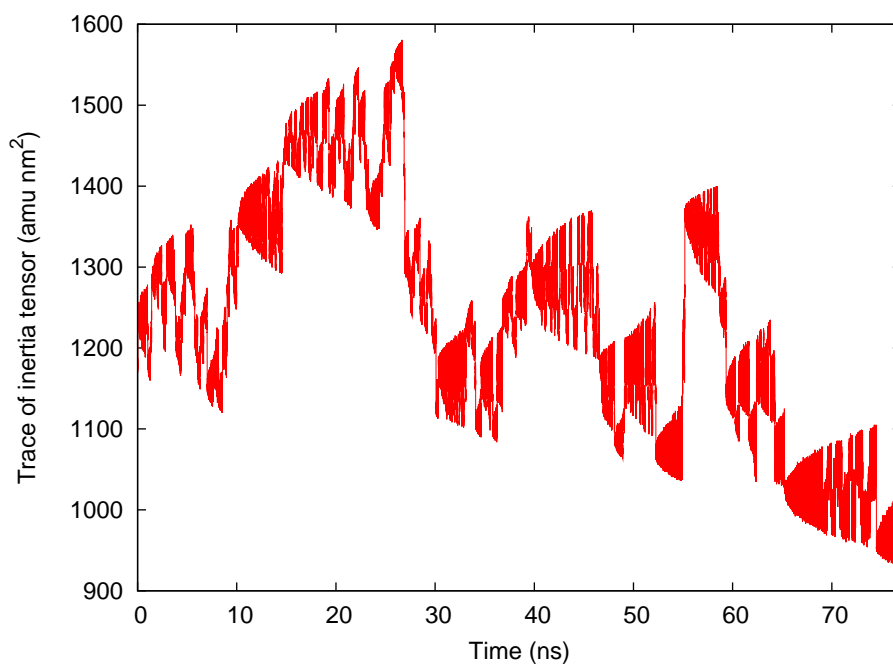
FIGURE A.14: Evolution of the trace of the inertia tensor over time for the $(ZnS)_{24}$ cluster.

TABLE A.33: Structures obtained from the MetaD simulations of $(ZnS)_{21}$, optimised using lattice dynamics.

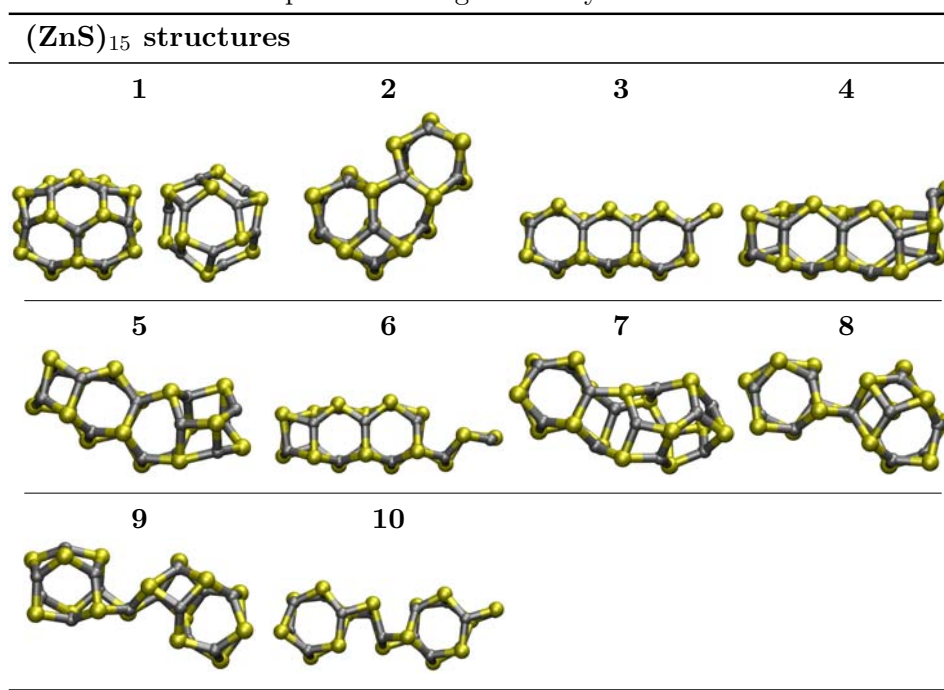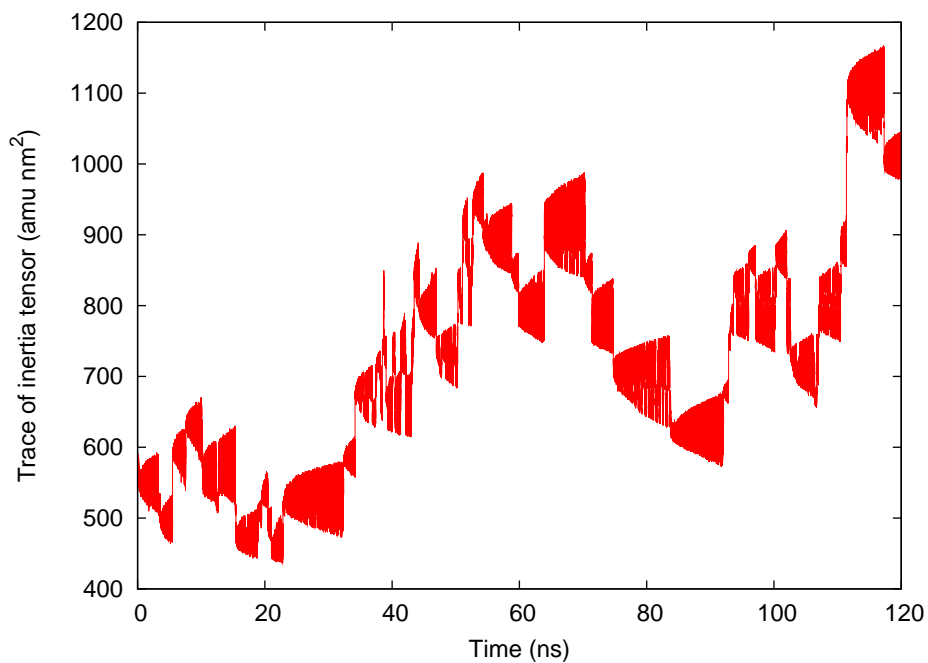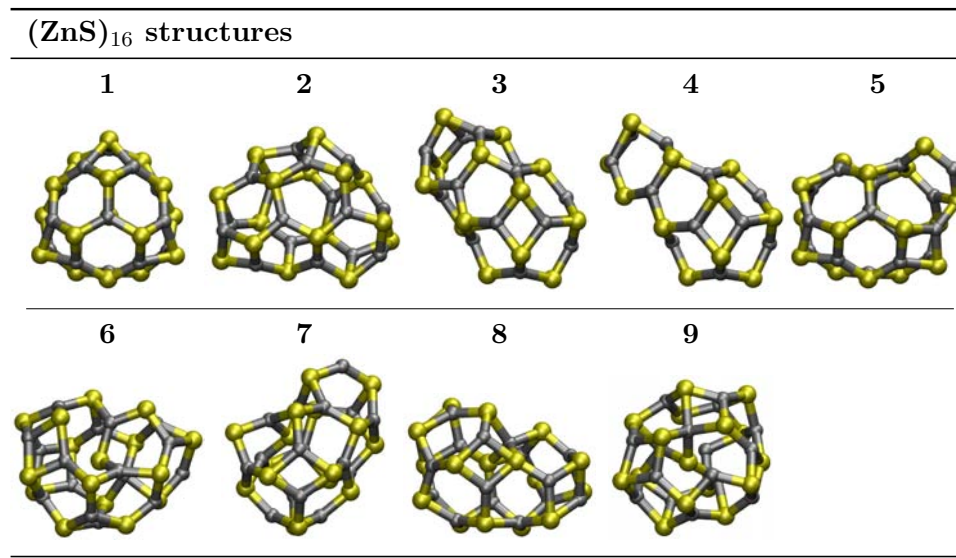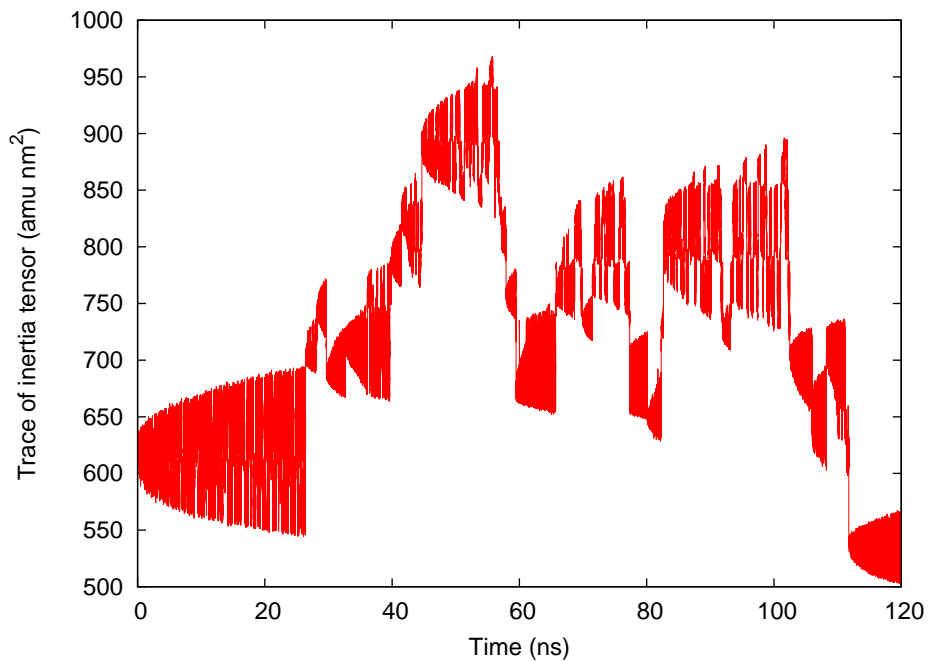| $(ZnS)_{21}$ structures			
1	**2**	**3**	**4**

5	**6**	**7**	
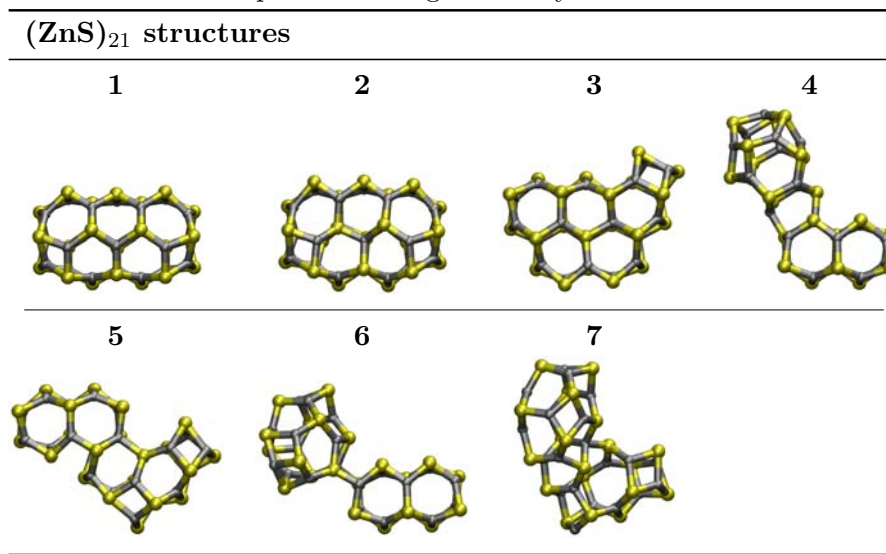
TABLE A.34: Potential energies for the structures obtained for $(ZnS)_{21}$, shown in Table A.33.

$(ZnS)_{21}$ potential energies (kJ mol^{-1})				
Structure	**U**	**ΔU**	**U/ZnS**	**ΔU/ZnS**
1	-66593.5	0	[-3171.1]	[0.0]
2	-66578.7	14.7	[-3170.4]	[0.7]
3	-66473.7	119.7	[-3165.4]	[5.7]
4	-66317.3	276.1	[-3158.0]	[13.2]
5	-66310.9	282.6	[-3157.7]	[13.5]
6	-66310.7	282.8	[-3157.7]	[13.5]
7	-66249.9	343.5	[-3154.8]	[16.4]

TABLE A.35: Structures obtained from the MetaD simulations of $(ZnS)_{22}$, optimised using lattice dynamics.
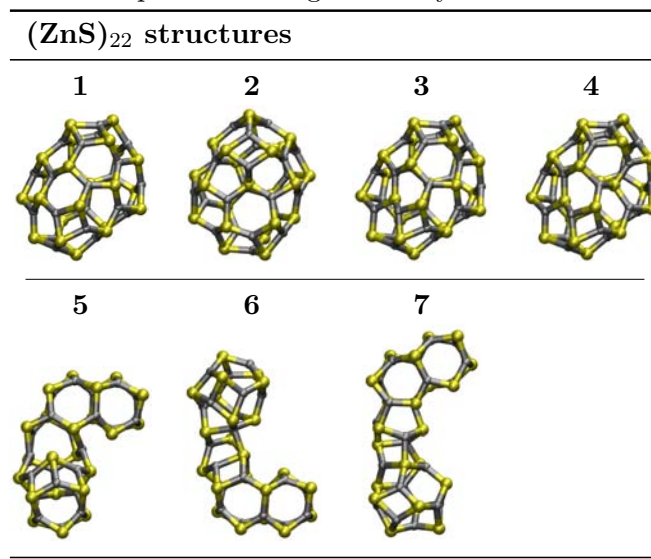
$(ZnS)_{22}$ structures

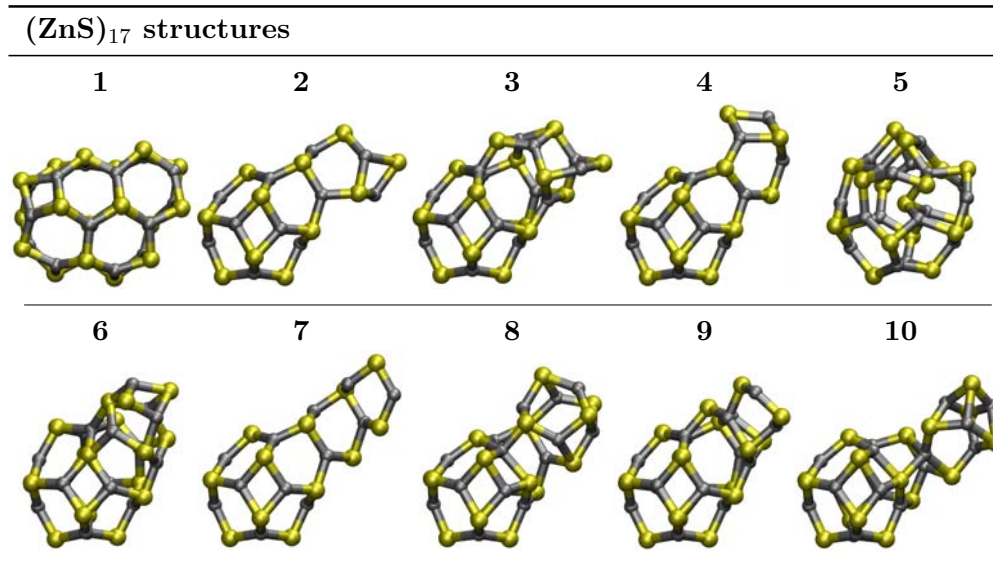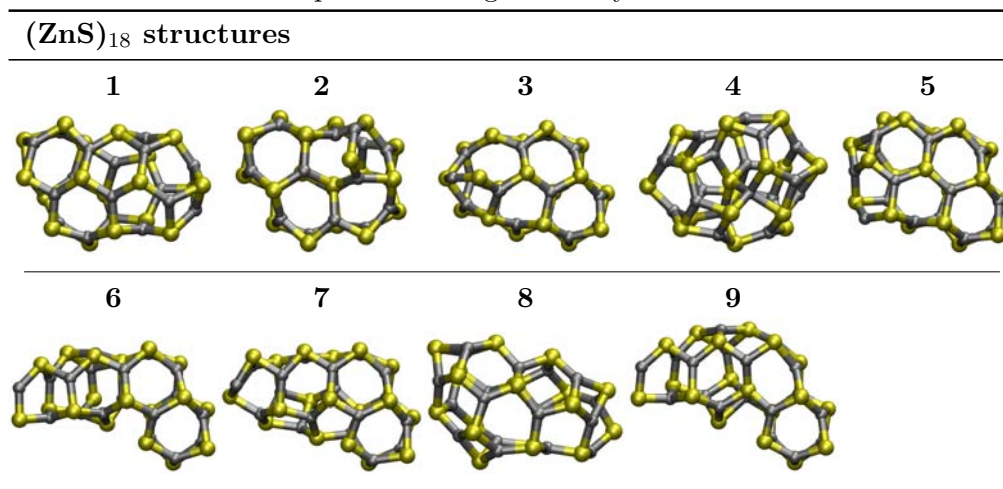

TABLE A.36: Potential energies for the structures obtained for $(ZnS)_{22}$, shown in Table A.35.

$(ZnS)_{22}$ potential energies (kJ mol^{-1})				
Structure	**U**	**ΔU**	**U/ZnS**	**ΔU/ZnS**
1	-69750.8	0.0	-3170.5	0.0
2	-69743.5	7.3	-3170.2	0.3
3	-69742.5	8.3	-3170.1	0.4
4	-69736.2	14.6	-3169.8	0.7
5	-69511.6	239.2	-3159.6	10.9
6	-69504.1	246.7	-3159.3	11.2
7	-69494.8	256.0	-3158.9	11.6

TABLE A.37: Structures obtained from the MetaD simulations of $(ZnS)_{24}$, optimised using lattice dynamics.
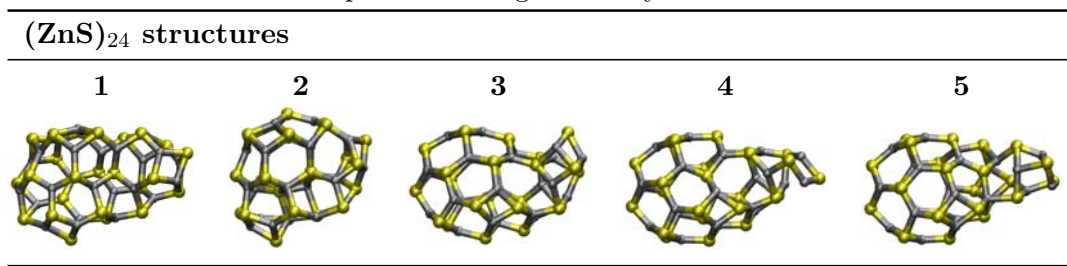
$(ZnS)_{24}$ structures

TABLE A.38: Potential energies for the structures obtained for $(ZnS)_{24}$, shown in Table A.37.

(ZnS)$_{24}$ potential energies (kJ mol^{-1})				
Structure	**U**	**ΔU**	**ΔU**	**ΔU/ZnS**
1	-75994.9285	0	-3166.46	0.0
2	-75970.3810	24.5475	-3165.43	1.0
3	-75896.4475	98.481	-3162.35	4.1
4	-75895.7680	99.1605	-3162.32	4.1
5	-75833.5140	161.414	-3159.73	6.7

TABLE A.39: Structures obtained from the MetaD simulations of $(ZnS)_{12}$ in water, optimised *in vacuo* using lattice dynamics.

TABLE A.40: Energies and enthalpies of the structures obtained from the MetaD simulations of $(ZnS)_{12}$ in water, shown in Table A.39. The potential energy values were obtained by minimising the structures in vacuum using lattice dynamics, and the average enthalpies were obtained from 200 ps NPT MD simulations. The relative potential energy and enthalpy are given with respect to the sodalite cage structure (Structure 1).

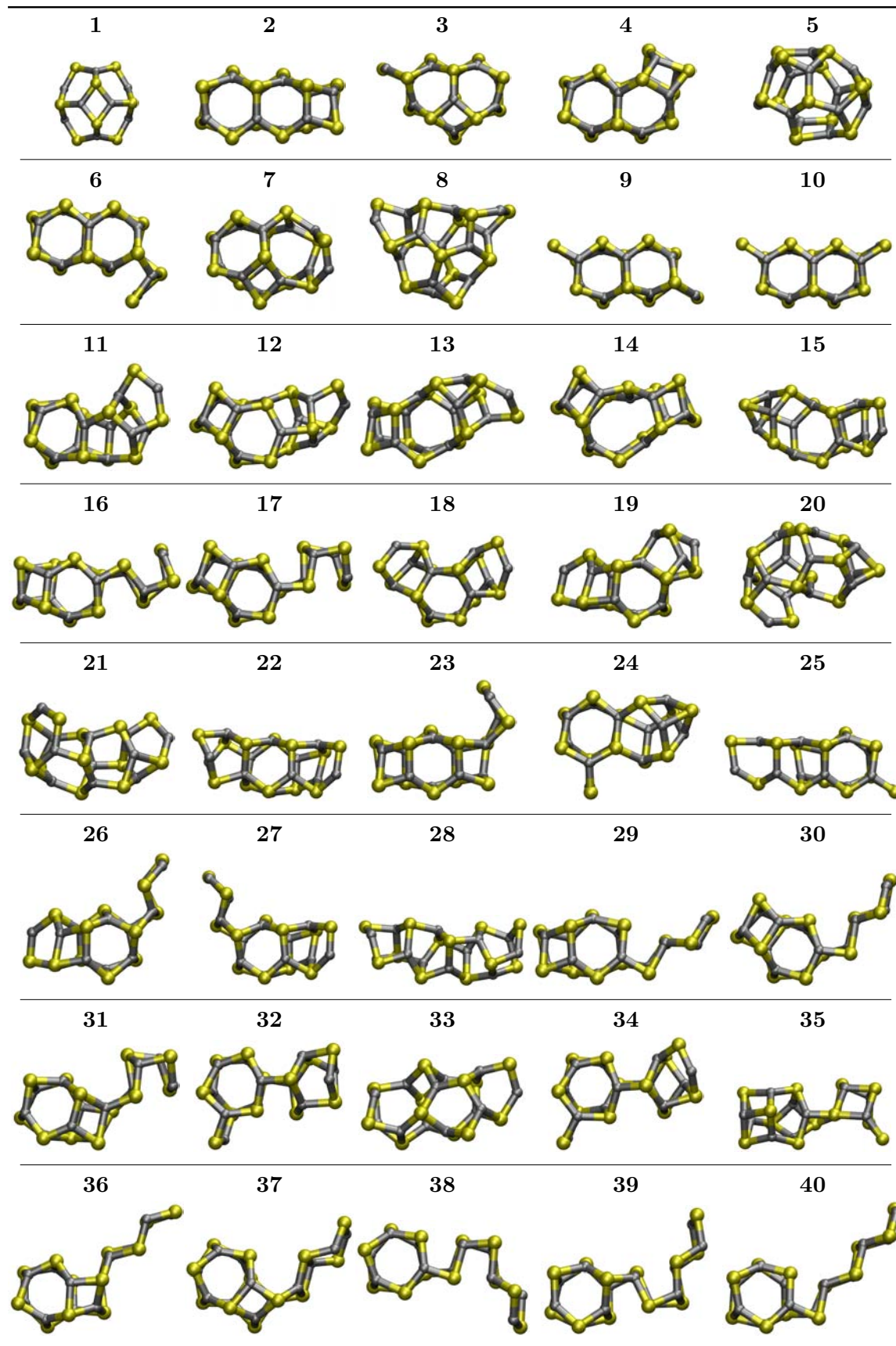| $(ZnS)_{12}$ potential energies and enthalpies (kJ mol^{-1})						
Structure	U	ΔU	U/ZnS	ΔU/Zns	H/ZnS	ΔH/ZnS
1	-37893.6	0.0	-3157.8	0.0	-5229.43	0
2	-37821.2	72.5	-3151.8	6.0	-5229.23	0.2
3	-37778.0	115.6	-3148.2	9.6	-5227.41	2.02
4	-37763.3	130.3	-3146.9	10.9	-5229.08	0.35
5	-37736.1	157.5	-3144.7	13.1	-5236.54	-7.11
6	-37717.7	175.9	-3143.1	14.7	-5228.68	0.75
7	-37706.3	187.3	-3142.2	15.6	-5226.69	2.74
8	-37695.4	198.2	-3141.3	16.5	-5235.31	-5.88
9	-37685.9	207.7	-3140.5	17.3	-5221.65	7.78
10	-37685.3	208.3	-3140.4	17.4	-5224.29	5.14
11	-37673.5	220.2	-3139.5	18.3	-5225.48	3.95
12	-37665.3	228.3	-3138.8	19.0	-5223.05	6.38
13	-37651.0	242.6	-3137.6	20.2	-5225.44	3.99
14	-37636.4	257.2	-3136.4	21.4	-5236.47	-7.04
15	-37633.0	260.6	-3136.1	21.7	-5231.66	-2.23
16	-37630.4	263.2	-3135.9	21.9	-5228.57	0.86
17	-37626.6	267.0	-3135.6	22.2	-5225.07	4.36
18	-37627.5	266.1	-3135.6	22.2	-5233.49	-4.06
19	-37626.1	267.5	-3135.5	22.3	-5231.41	-1.98
20	-37624.9	268.7	-3135.4	22.4	-5231.03	-1.6
21	-37615.5	278.2	-3134.6	23.2	-5228.72	0.71
22	-37613.5	280.1	-3134.5	23.3	-5237.19	-7.76
23	-37587.8	305.8	-3132.3	25.5	-5226.11	3.32
24	-37583.5	310.1	-3132.0	25.8	-5236.47	-7.04
25	-37584.3	309.3	-3132.0	25.8	-5230.87	-1.44
26	-37580.2	313.4	-3131.7	26.1	-5231.62	-2.19
27	-37575.3	318.3	-3131.3	26.5	-5226.36	3.07
28	-37572.0	321.6	-3131.0	26.8	-5233.65	-4.22
29	-37569.8	323.9	-3130.8	27.0	-5220.91	8.52
30	-37562.9	330.7	-3130.2	27.6	-5230.97	-1.54
31	-37536.6	357.0	-3128.1	29.8	-5222.7	6.73
32	-37525.2	368.4	-3127.1	30.7	-5233.65	-4.22
33	-37513.3	380.4	-3126.1	31.7	-5221.57	7.86
34	-37506.0	387.6	-3125.5	32.3	-5233.31	-3.88
35	-37504.0	389.6	-3125.3	32.5	-5227.8	1.63
36	-37484.4	409.2	-3123.7	34.1	-5232.1	-2.67
37	-37478.0	415.6	-3123.2	34.6	-5233.31	-3.88
38	-37436.5	457.1	-3119.7	38.1	-5225.85	3.58
39	-37436.5	457.2	-3119.7	38.1	-5226.3	3.13
40	-37399.9	493.7	-3116.7	41.1	-5235.75	-6.32

Appendix B

SIESTA

Basis set example from .fdf file

PAO.SplitNorm 0.15

PAO.SplitNormH 0.50

PAO.SoftDefault true

PAO.SoftPotential 100.0 Ry

PAO.SoftInnerRadius 0.95

%block PAO.Basis

Zn_pbesol 5

n=3 0 1

6.0

1.0

n=3 1 1

6.0

1.0

n=4 0 2

8.0 0.0

1.0 1.0

n=4 1 2

9.0 0.0

1.0 1.0

n=3 2 2

8.0 0.0

1.0 1.0

S_pbesol 3

n=3 0 3

8.0 0.0 0.0

1.0 1.0 1.0

n=3 1 3

8.0 0.0 0.0

1.0 1.0 1.0

n=3 2 2 E 100.0 0.00

6.0 0.0

1.0 1.0

O_pbesol 3

n=2 0 3

7.0 0.0 0.0

1.0 1.0 1.0

n=2 1 3

7.0 0.0 0.0

1.0 1.0 1.0

n=3 2 2 E 120.0 0.00

7.0 0.0

1.0 1.0

H_pbesol 2

n=1 0 3

7.0 0.0 0.0

1.0 1.0 1.0

n=2 1 2 E 70.0 0.0

3.5 0.0

1.0 1.0

%endblock PAO.Basis

Appendix C

Metadynamics using Steinhardt parameter Q_4

This appendix contains tabulations of the structures obtained from metadynamics simulations performed on a 360 atom wurtzite ZnS nanocluster using the Q_4 parameter. For the structures given in Tables C.1 and C.2 the bias was applied to the Zn-Zn pairs only. The results from the simulations performed with the bias applied to both Zn-Zn and S-S pairs are detailed in Chapter 6, along with the remainder of the simulations performed using the Q_4 Steinhardt parameter.

Table C.1: Low energy structures obtained from MetaD simulation of 360 atom nanoparticle using Q_4 bias on the Zn-Zn pairs. The switching function parameters were d_0=3.9 Å, r_0=0.25 Å, n=2 and m=6. The relative energies (ΔU) are quoted with respect to sphalerite in kJ/mol per formula unit.
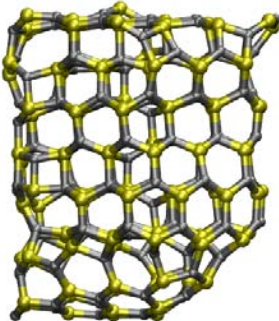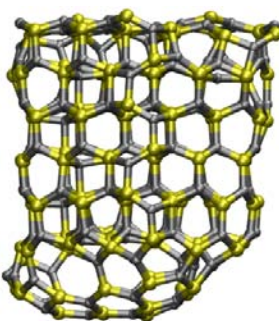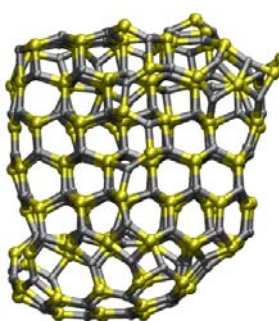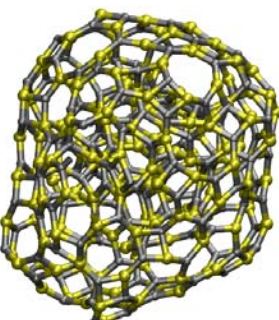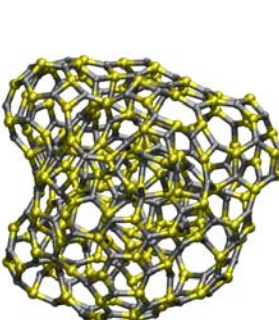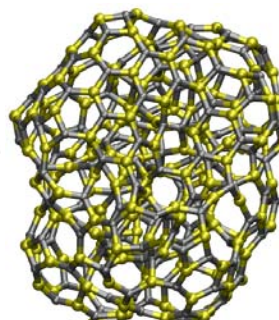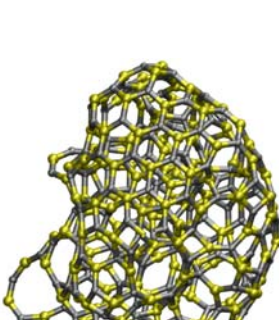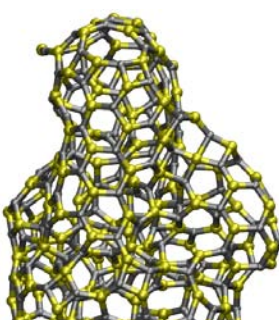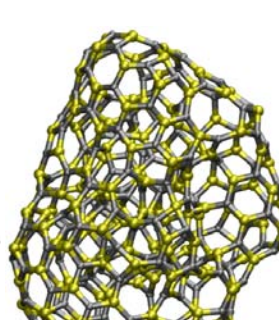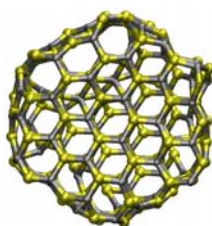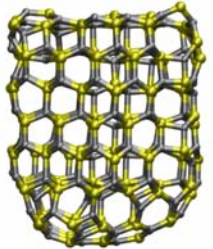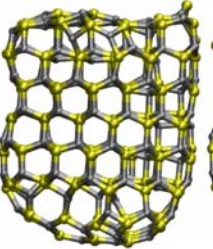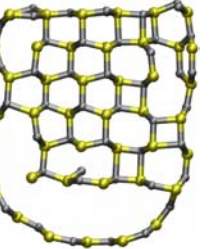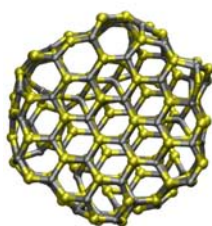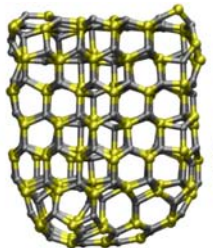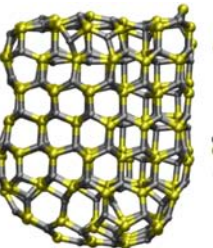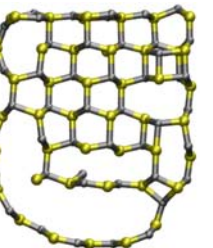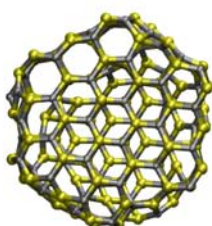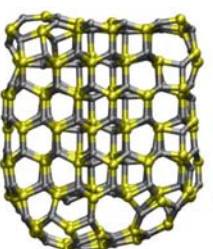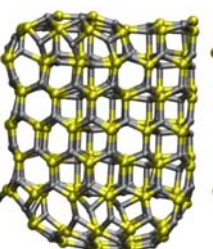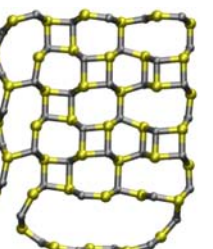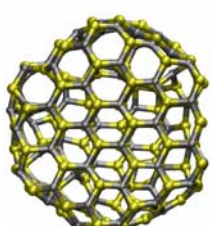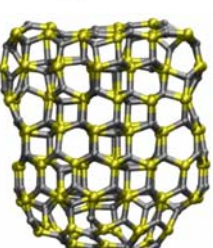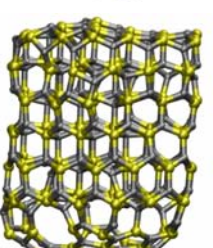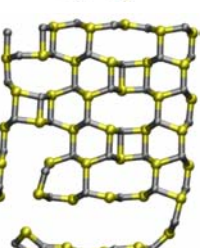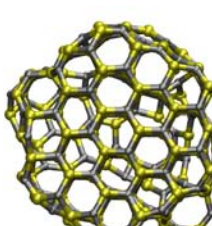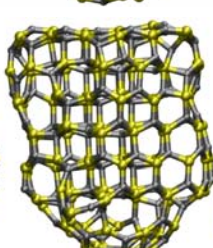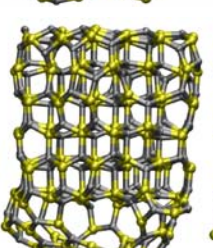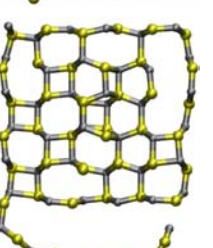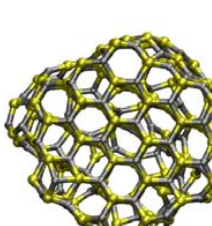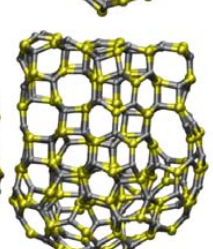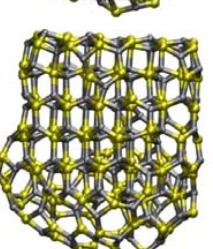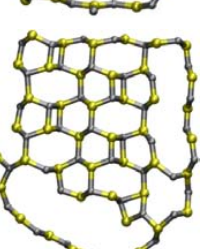
Time (ns)	0.50	1.75	2.00
ΔU (kJ/mol)	28.8	28.6	30.3
Time (ns)	5.50	6.50	8.75
ΔU (kJ/mol)	34.6	34.8	33.4
Time (ns)	14.25	20.00	21.25
ΔU (kJ/mol)	34.9	34.5	32.5

TABLE C.2: Low energy structures obtained from a MetaD simulation using the Q_4 Steinhardt parameter as a CV bias on the Zn-Zn pairs. The switching function used had parameters d_0=3.8 Å, r_0=0.17 Å, n=6 and m=12. The relative energies (ΔU) are quoted with respect to sphalerite in kJ/mol per formula unit.
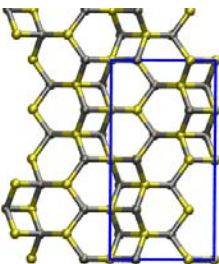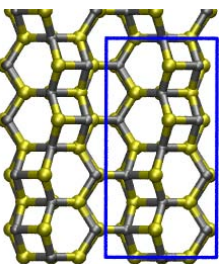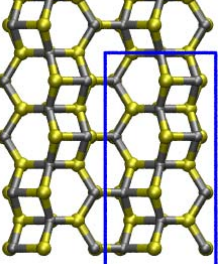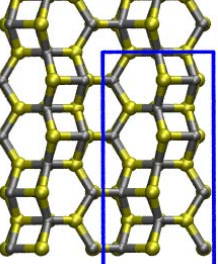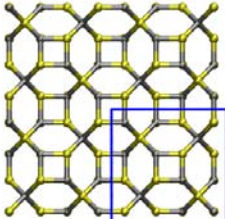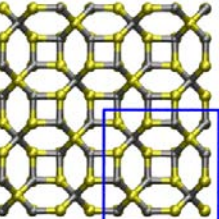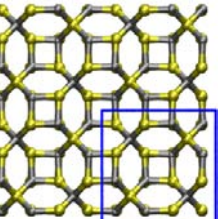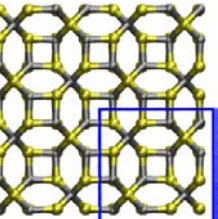
Time (ns)	Structure	ΔU
3.25		27.2
3.50		27.1
4.00		28.2
8.25		27.6
9.25		28.7
13.50		30.5

Appendix D

Hypothetical nanoporous ZnS

This appendix contains tabulations for all of the optimised zeolite frameworks
detailed in Chapter 7. The starting topologies are shown, along with topologies
resulting from optimisation with three force fields, the rigid ion model used in
Chapter 6 (referred to as 'Rigid' throughout Chapter 7), and the Wright and Gale
[95] model with a torsional (Shells/Tors), and the same model without a torsional
term (Shells/NoTors).

TABLE D.1: Zeolite frameworks with 6- and 4-membered rings. Images for the
starting topology and the resulting topologies after minimisation using three
different forcefields (Rigid, Shells/NoTors and Shells/Tors) are shown.

Table D.1: 6-4 Frameworks optimised with different forcefields – Continued

Frame	Start	Rigid	No-Tors	Tors
FAR viewed normal to [001]				
FRA viewed normal to [001]				
GIU viewed along [100]				
LIO viewed normal to [001]				

Continued on Next Page...

Table D.1: 6-4 Frameworks optimised with different forcefields – Continued

Frame	Start	Rigid	No-Tors	Tors

LOS viewed normal to [001]

MAR viewed normal to [001]

MSO viewed normal to [001]

SOD viewed along [100]

TOL viewed normal to [001]

Table D.1: 6-4 Frameworks optimised with different forcefields – Continued

Frame	Start	Rigid	No-Tors	Tors
UOZ viewed along [100]				
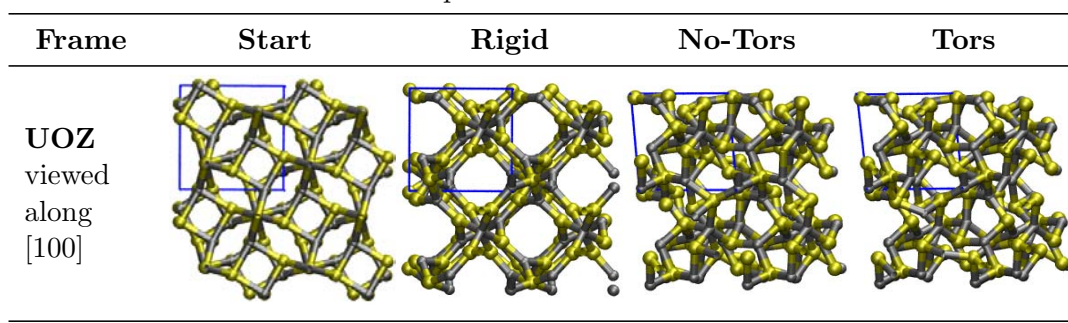
TABLE D.2: Zeolite frameworks with 8- and 4-membered rings. Images for the starting topology and the resulting topologies after minimisation using three different forcefields (Rigid, Shells/NoTors and Shells/Tors) are shown.

Frame	Start	Rigid	No-Tors	Tors
ACO viewed along [100]				
EDI viewed along [001]				
MER viewed along [100]				
PHI viewed along [001]				
SIV viewed along [100]				
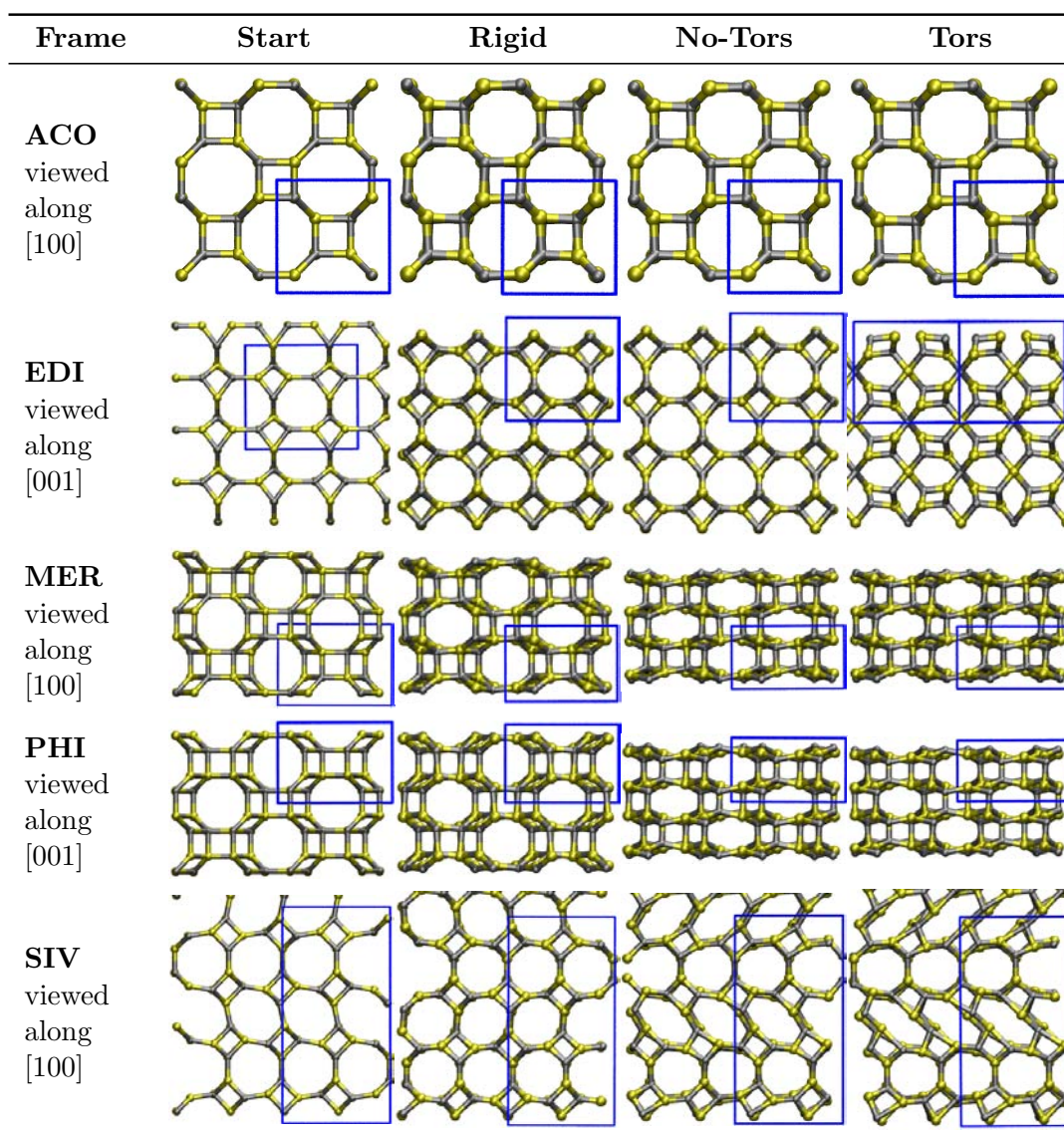
Continued on Next Page. . .

Table D.2: 8-4 Frameworks optimised with different forcefields – Continued

Frame	Start	Rigid	No-Tors	Tors
THO viewed along [010]				
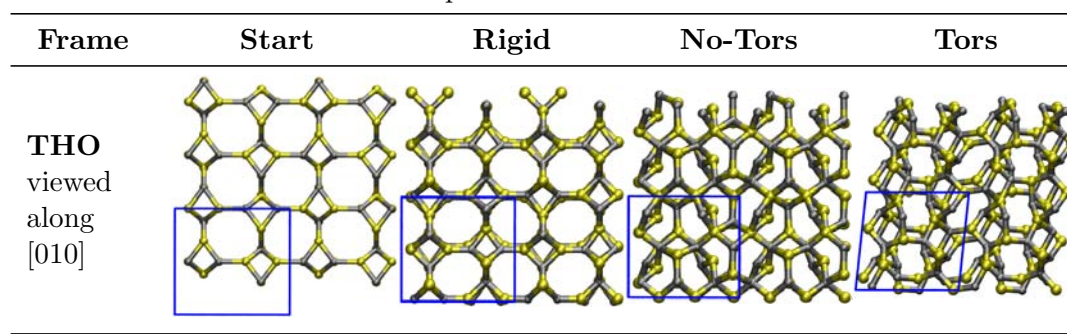
TABLE D.3: Zeolite frameworks with 8-, 6- and 4-membered rings. Images for the starting topology and the resulting topologies after minimisation using three different forcefields (Rigid, Shells/NoTors and Shells/Tors) are shown.

Frame	Start	Rigid	No-Tors	Tors
ABW viewed along [010]				
AEI viewed along [001]				
AEN viewed along [001]				

Continued on Next Page. . .

Table D.3: 8-6-4 Frameworks optimised with different forcefields – Continued

Frame	Start	Rigid	No-Tors	Tors
AFN viewed along [010]				
AFT viewed normal to [001]				
AFX viewed normal to [001]				
AFY proj down [001]				
ANA viewed along [001]				

Continued on Next Page. . .

Table D.3: 8-6-4 Frameworks optimised with different forcefields – Continued

Frame	Start	Rigid	No-Tors	Tors

Frame	Start	Rigid	No-Tors	Tors
APC viewed along [100]				
APD viewed along [100]				
ATN viewed along [001]				
ATT viewed along [010]				

Continued on Next Page. . .

Table D.3: 8-6-4 Frameworks optimised with different forcefields – Continued

Frame	Start	Rigid	No-Tors	Tors
ATV viewed along [100]				
AWO viewed along [100]				
AWW viewed along [100]				
BCT viewed along [100]				
CHA viewed along [100]				

Continued on Next Page. . .

Table D.3: 8-6-4 Frameworks optimised with different forcefields – Continued

Frame	Start	Rigid	No-Tors	Tors
DFT viewed along [100]				
EAB viewed normal to [001]				
ERI viewed normal to [001]				
GIS viewed along [100]				

Continued on Next Page. . .

Table D.3: 8-6-4 Frameworks optimised with different forcefields – Continued

Frame	Start	Rigid	No-Tors	Tors
GOO viewed along [110]				
JBW viewed along [100]				
KFI viewed along [100]				

Continued on Next Page. . .

Table D.3: 8-6-4 Frameworks optimised with different forcefields – Continued

Frame	Start	Rigid	No-Tors	Tors
LEV viewed normal to [001]				
LIT viewed along [100]				
LTA viewed along [100]				
OWE viewed along [100]				

Continued on Next Page. . .

Table D.3: 8-6-4 Frameworks optimised with different forcefields – Continued

Frame	Start	Rigid	No-Tors	Tors
RHO viewed along [100]				
SAS viewed along [001]				
SAT viewed normal to [001]				
SAV viewed along [001]				
TSC viewed along along [001]				
UEI viewed along [010]				

Continued on Next Page. . .

Table D.3: 8-6-4 Frameworks optimised with different forcefields – Continued

Frame	Start	Rigid	No-Tors	Tors
ZON viewed along [010]				

TABLE D.4: Zeolite frameworks with 10-, 6- and 4-membered rings. Images for the starting topology and the resulting topologies after minimisation using three different forcefields (Rigid, Shells/NoTors and Shells/Tors) are shown.

Frame	Start	Rigid	No-Tors	Tors
AEL viewed along [010]				
AFO viewed along [001]				
AHT viewed along [001]				
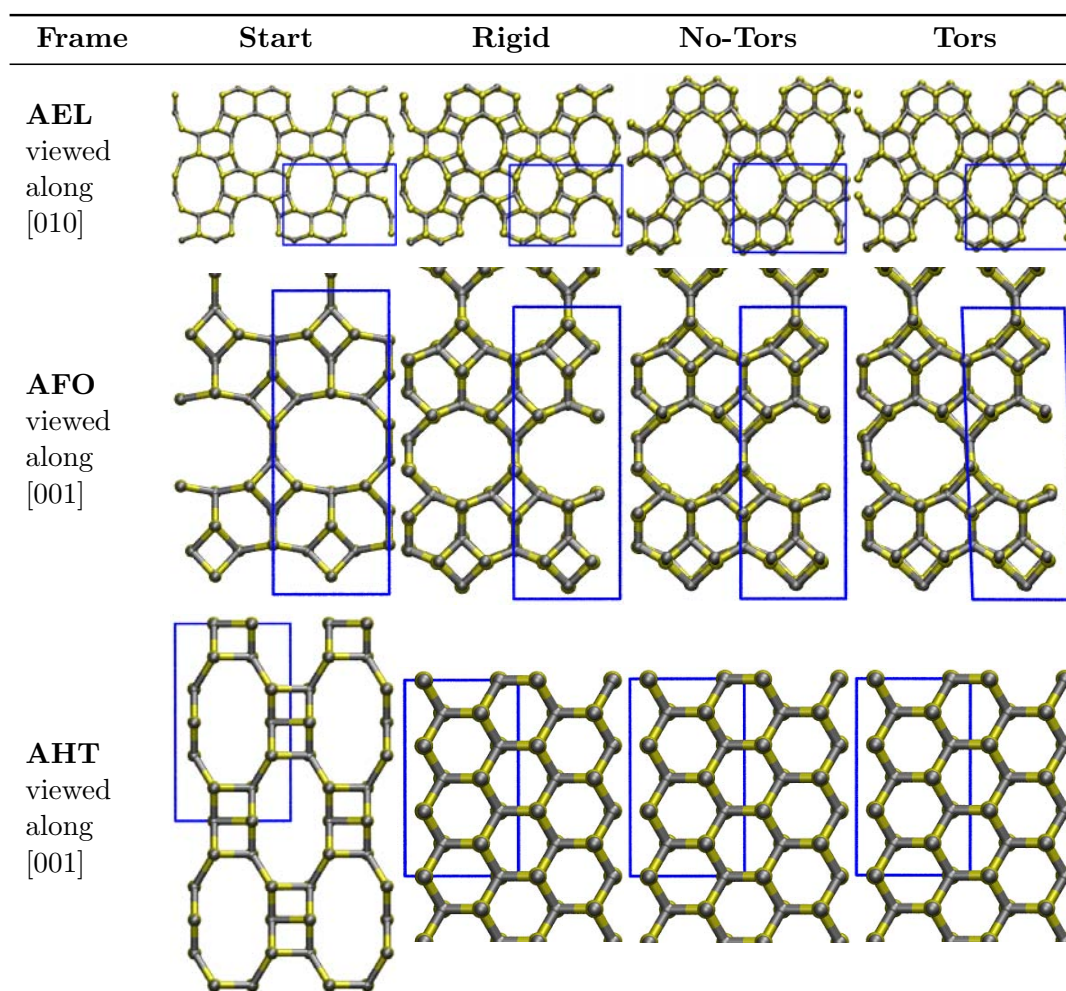
Continued on Next Page. . .

Table D.4: 10-6-4 Frameworks optimised with different forcefields – Continued

Frame	Start	Rigid	No-Tors	Tors
JRY viewed along [100]				
LAU viewed along [001]				
PON viewed along [100]				
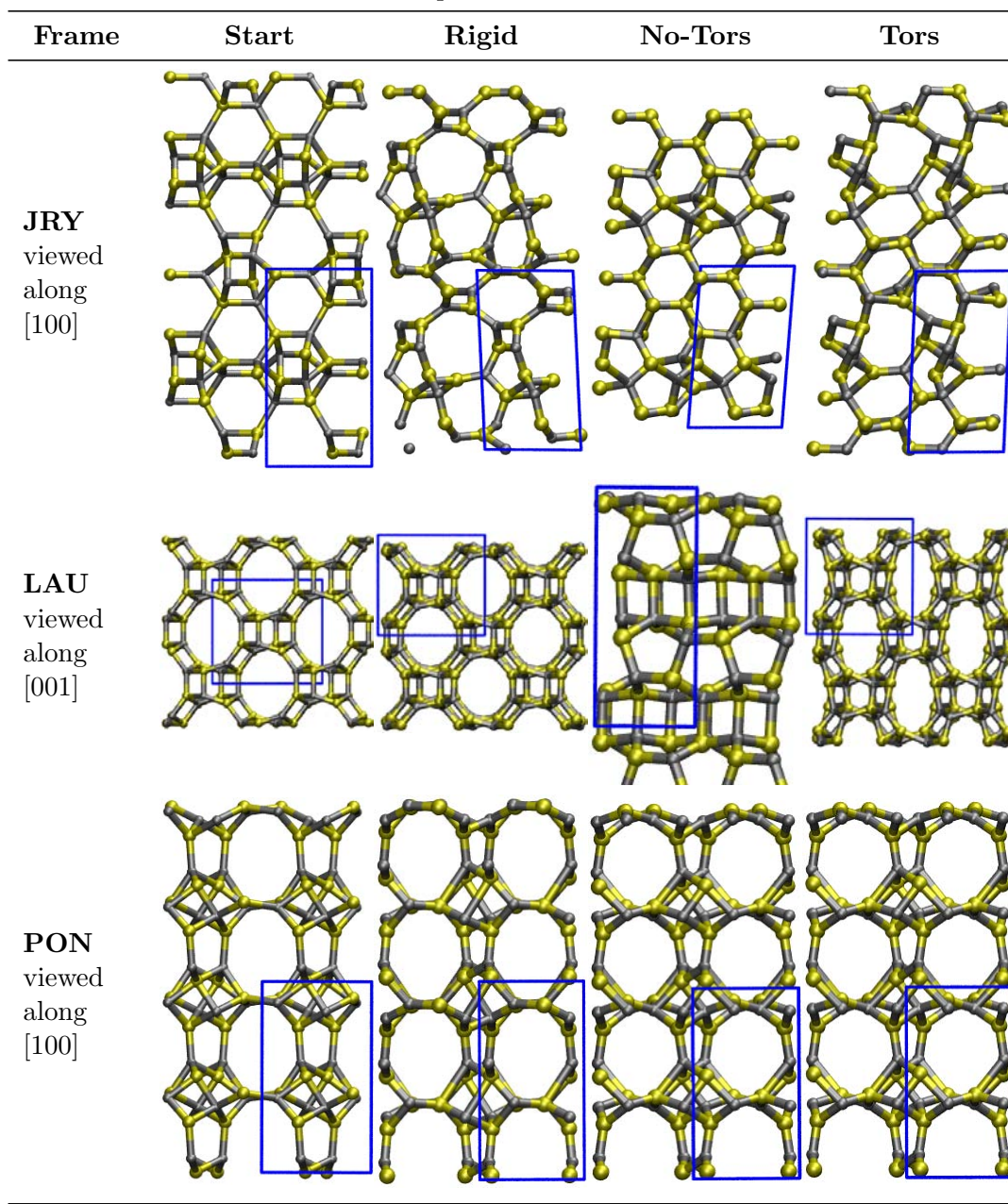
TABLE D.5: Zeolite frameworks with10-, 8- 6- and 4-membered rings. Images for the starting topology and the resulting topologies after minimisation using three different forcefields (Rigid, Shells/NoTors and Shells/Tors) are shown.

Frame	Start	Rigid	No-Tors	Tors
CGS viewed along [100]				
CGF viewed along [001]				
WEN viewed normal to [001]				
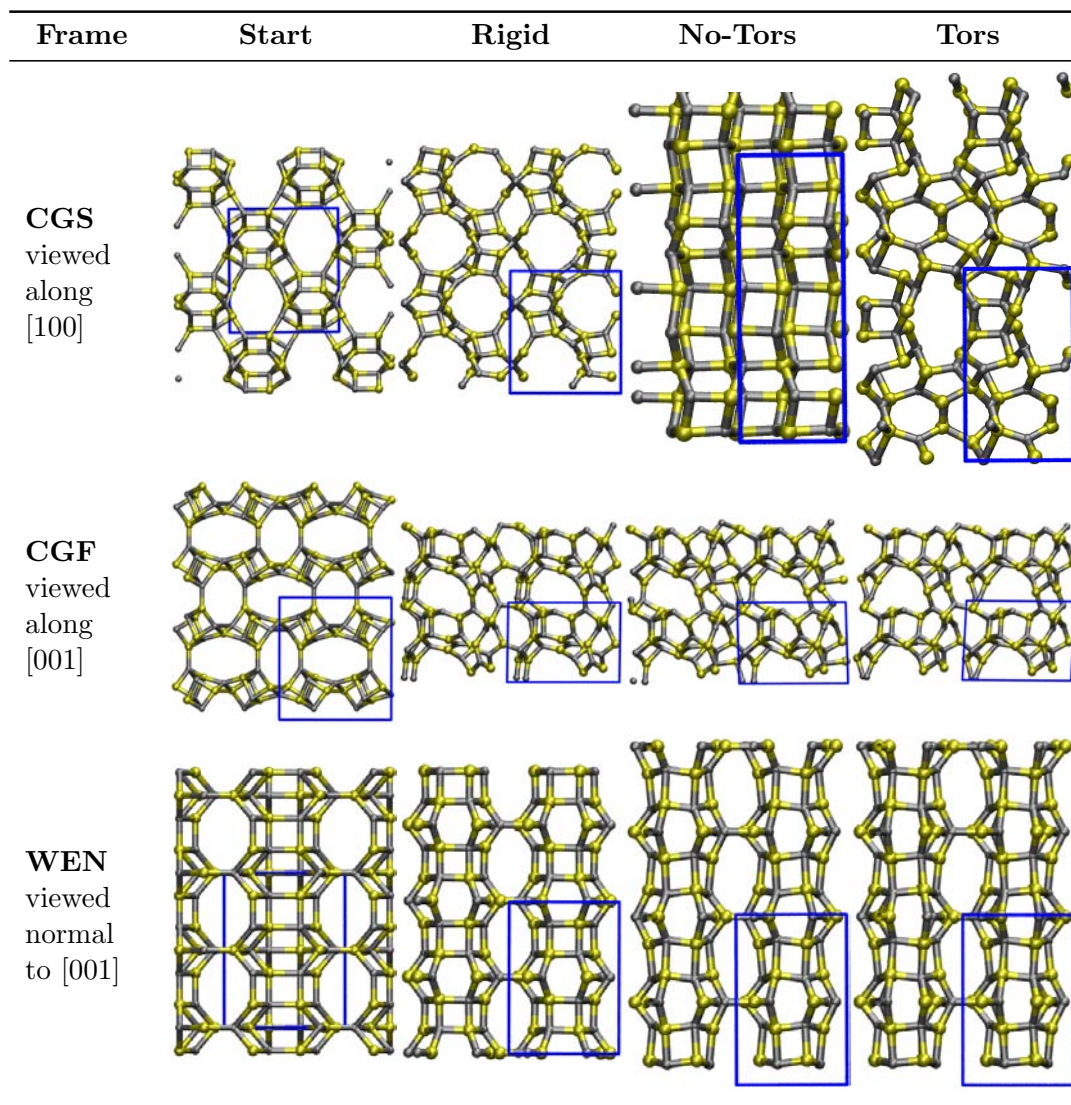
TABLE D.6: Zeolite frameworks with 12-, 6- and 4-membered rings. Images for the starting topology and the resulting topologies after minimisation using three different forcefields (Rigid, Shells/NoTors and Shells/Tors) are shown.

Frame	Start	Rigid	No-Tors	Tors
AFI viewed along [001]				
ATO viewed along [001]				
ASV viewed along [001]				
ATS viewed along [001]				
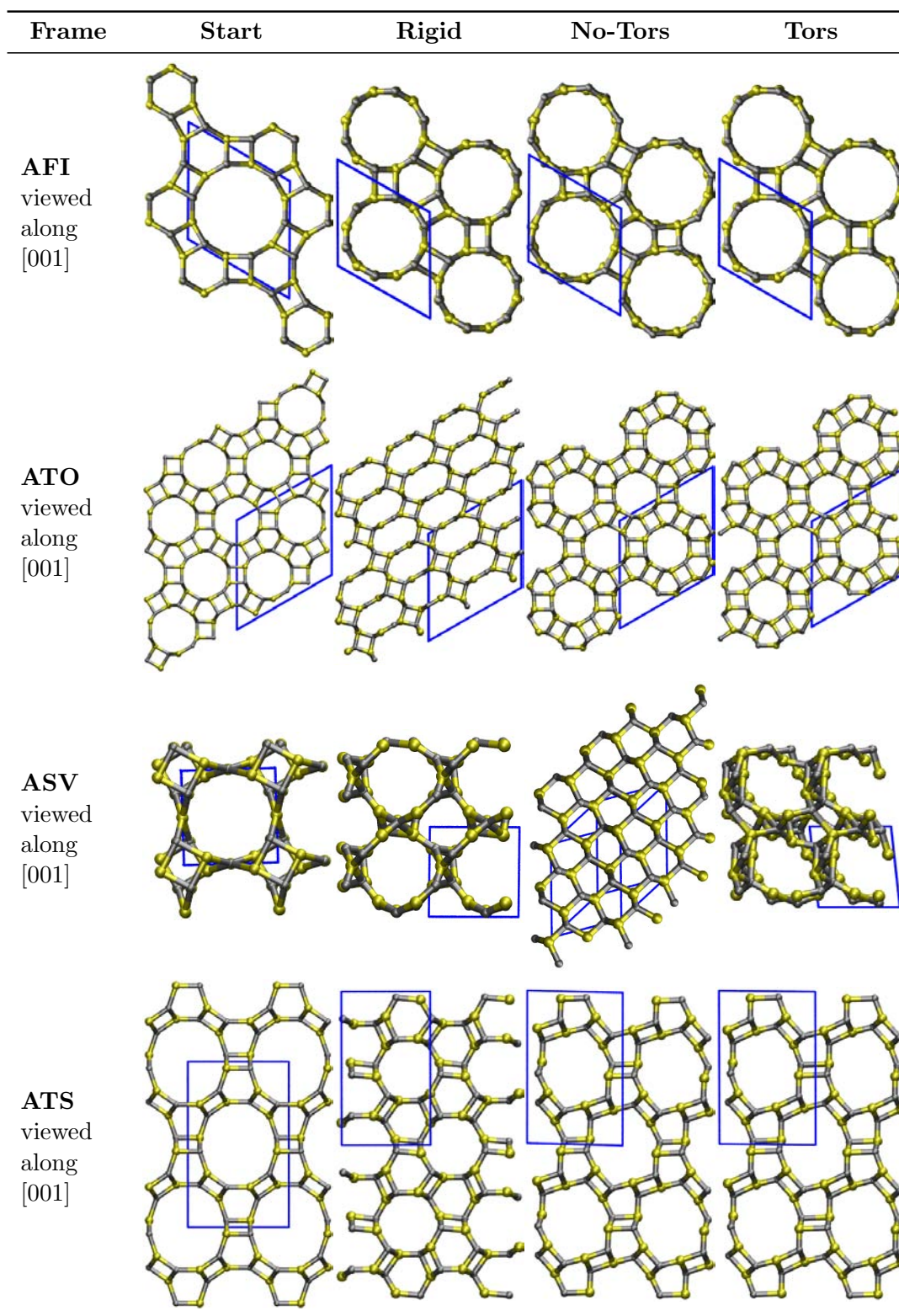
Continued on Next Page...

Table D.6: 12-6-4 Frameworks optimised with different forcefields – Continued

Frame	Start	Rigid	No-Tors	Tors
CAN viewed along [001]				
EMT viewed along [001]				
FAU viewed along [100]				
OSI viewed along [001]				
SAO viewed along [100]				
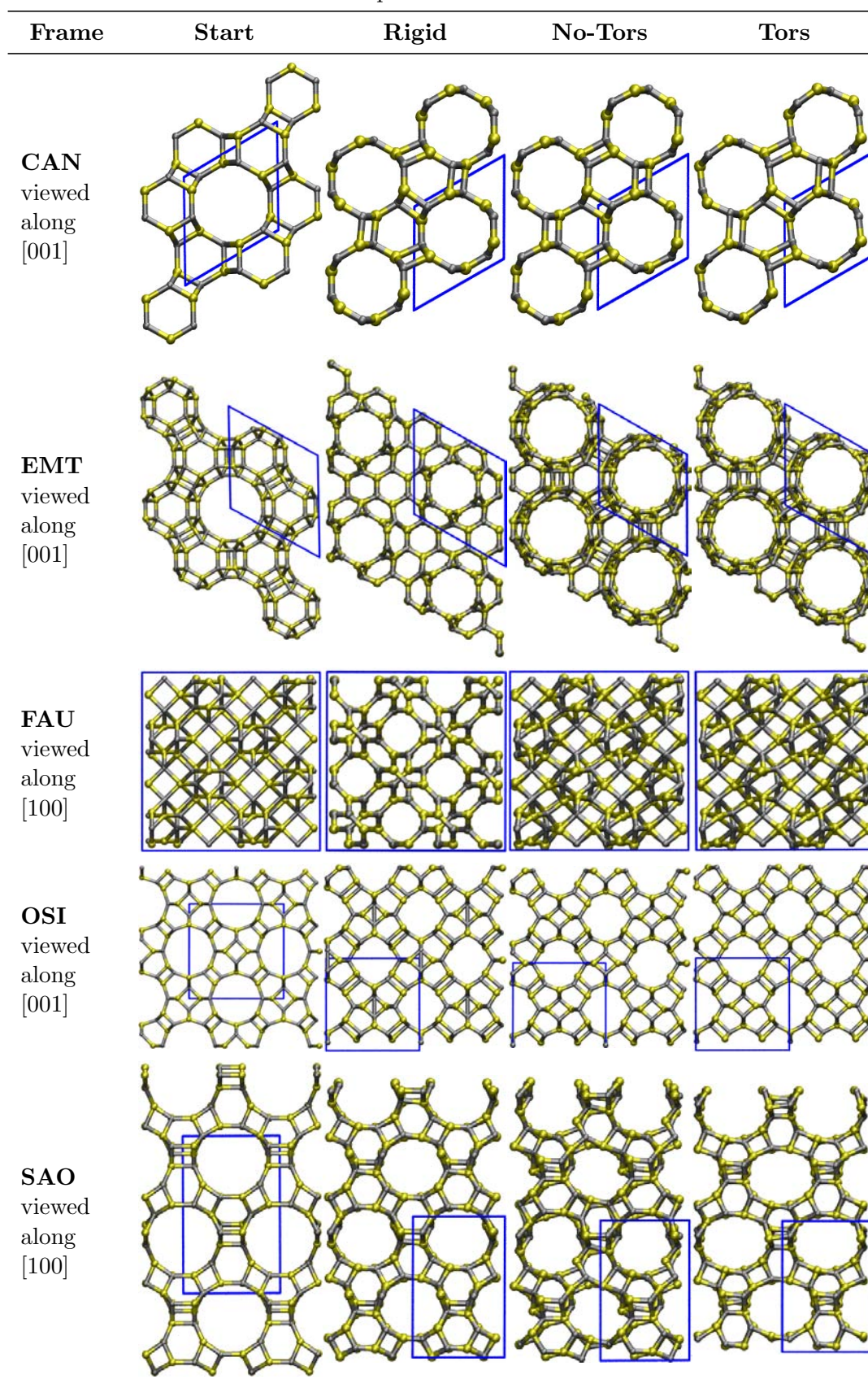
TABLE D.7: Zeolite frameworks with 12-, 8-, 6- and 4-membered rings. Images for the starting topology and the resulting topologies after minimisation using three different forcefields (Rigid, Shells/NoTors and Shells/Tors) are shown.

Frame	Start	Rigid	No-Tors	Tors
AFR viewed along [010]				
AFS viewed along [100]				
BPH viewed normal to [001]				
EZT viewed along [100]				
GME viewed normal to [001]				

Continued on Next Page. . .

Table D.7: 12-8-6-4 Frameworks optimised with different forcefields – Continued

Frame	Start	Rigid	No-Tors	Tors
ITW viewed along [001]				
LTL viewed normal to [001]				
MOZ viewed normal to [001]				
OFF viewed normal to [001]				

Continued on Next Page. . .

Table D.7: 12-8-6-4 Frameworks optimised with different forcefields – Continued

Frame	Start	Rigid	No-Tors	Tors
SBE viewed normal to [001]				
SBS viewed normal to [001]				
SBT viewed normal to [001]				
SFO viewed normal to [001]				
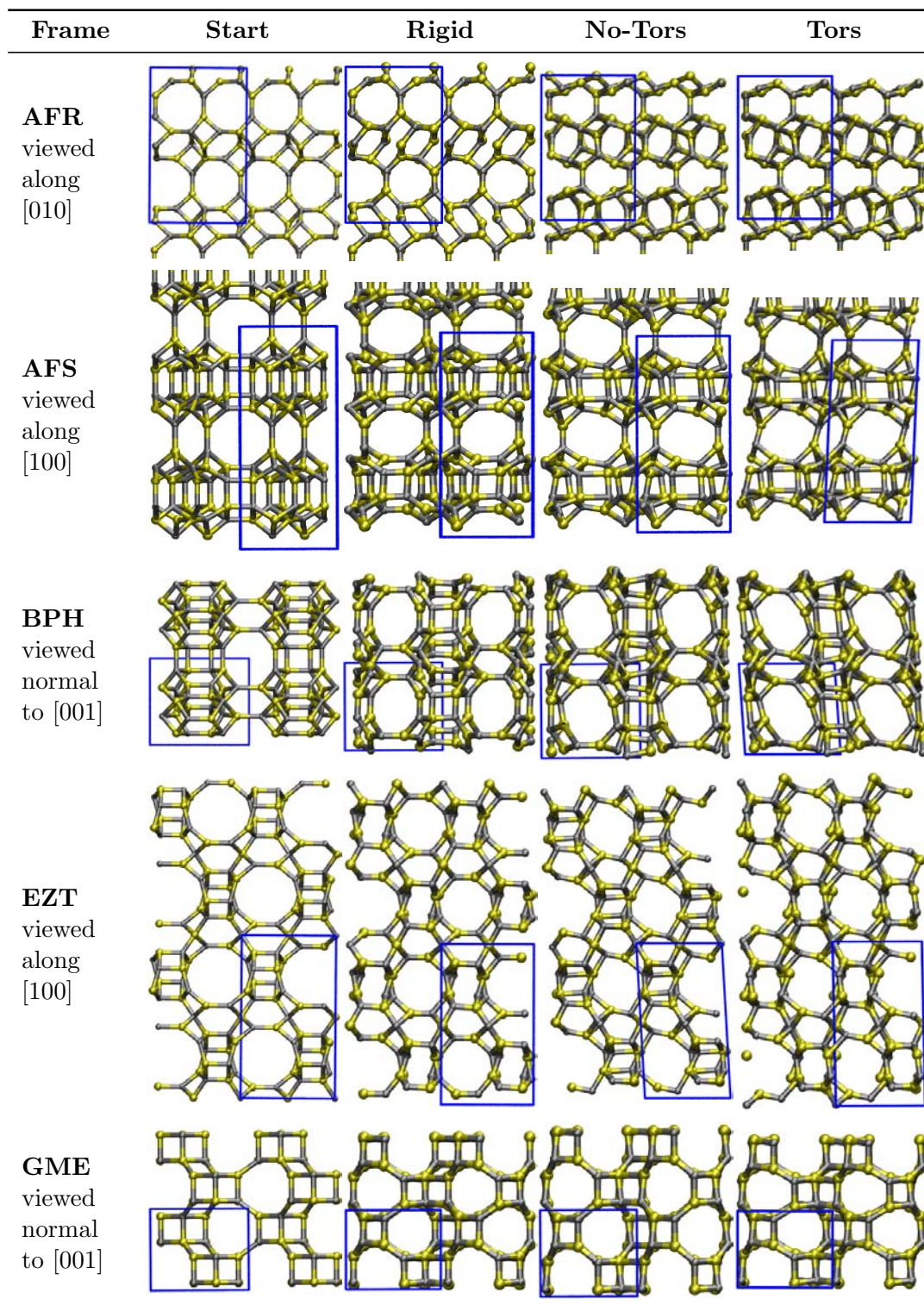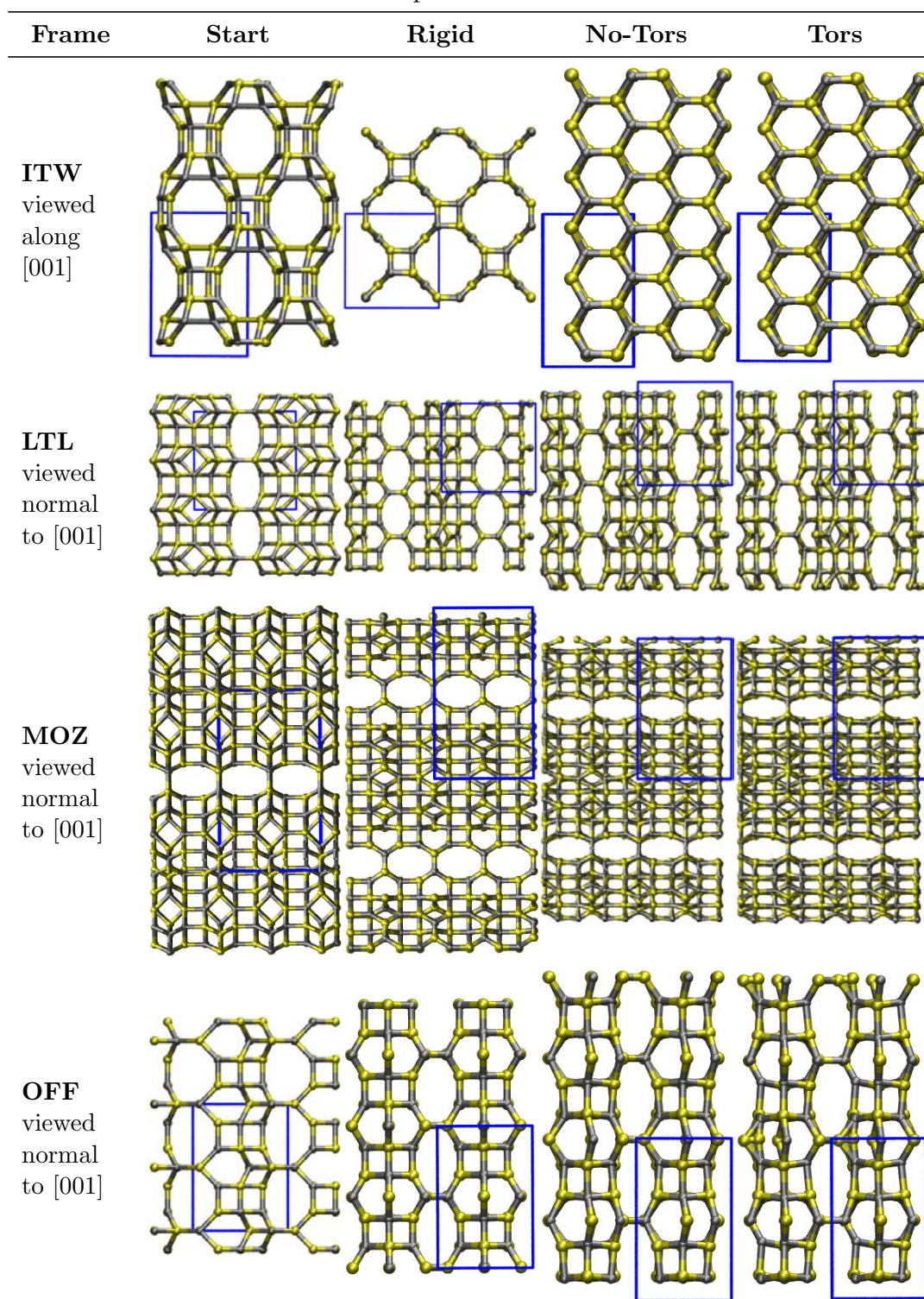
Continued on Next Page. . .

Table D.7: 12-8-6-4 Frameworks optimised with different forcefields – Continued

Frame	Start	Rigid	No-Tors	Tors

Table D.8: Zeolite frameworks with larger membered rings - 18-, 14-, 12-membered rings. Images for the starting topology and the resulting topologies after minimisation using three different forcefields (Rigid, Shells/NoTors and Shells/Tors) are shown.

Frame	Start	Rigid	No-Tors	Tors

CZP 12-8-4 viewed normal to [001]

ETR 18-8-6-4 viewed along [001]

USI 12-10-6-4 viewed along [001]
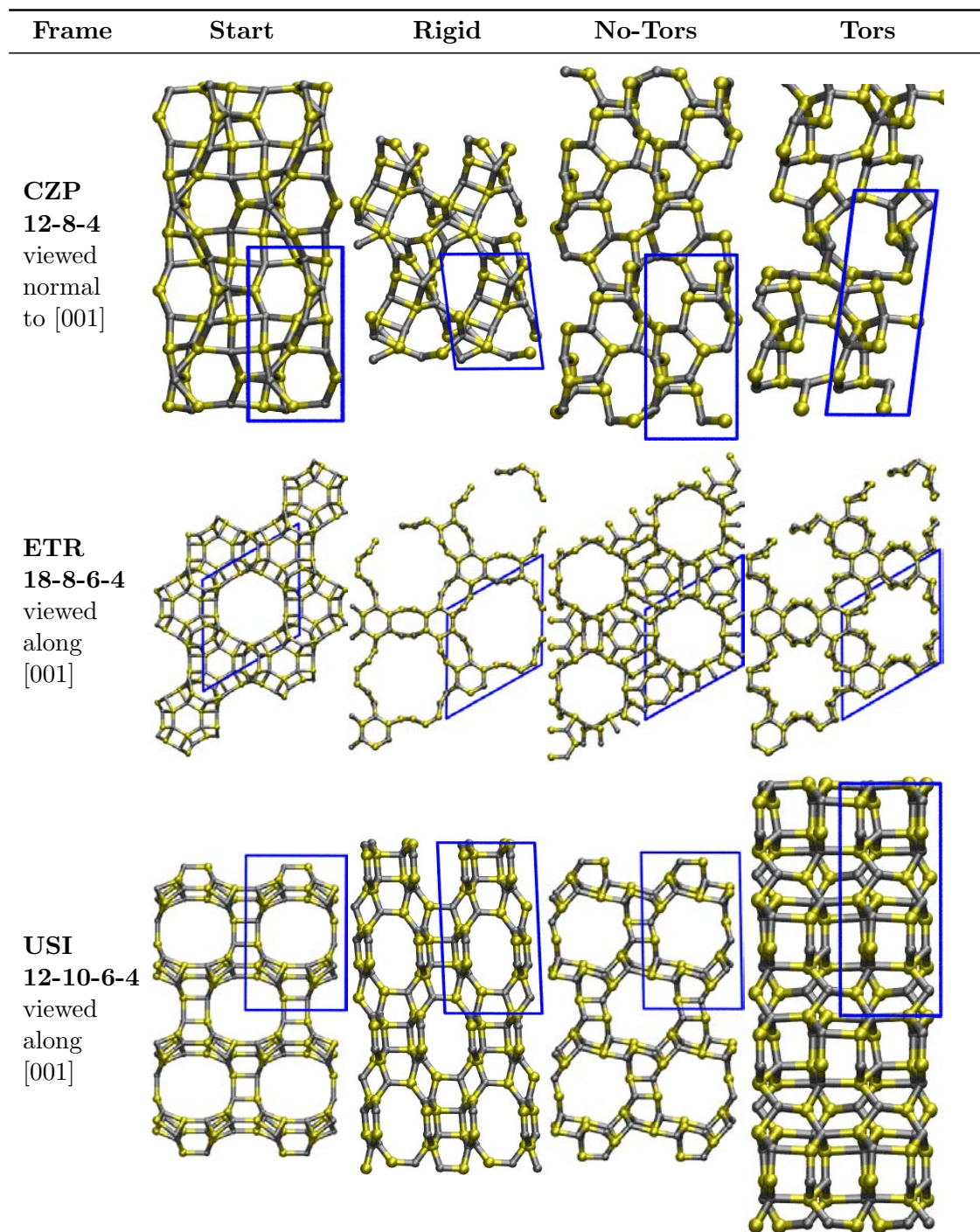
Continued on Next Page. . .

Table D.8: Frameworks with larger rings optimised with different forcefields – Cont.

Frame	Start	Rigid	No-Tors	Tors
AET 14-6-4 viewed along [001]				
VFI 18-6-4 viewed along [001]				
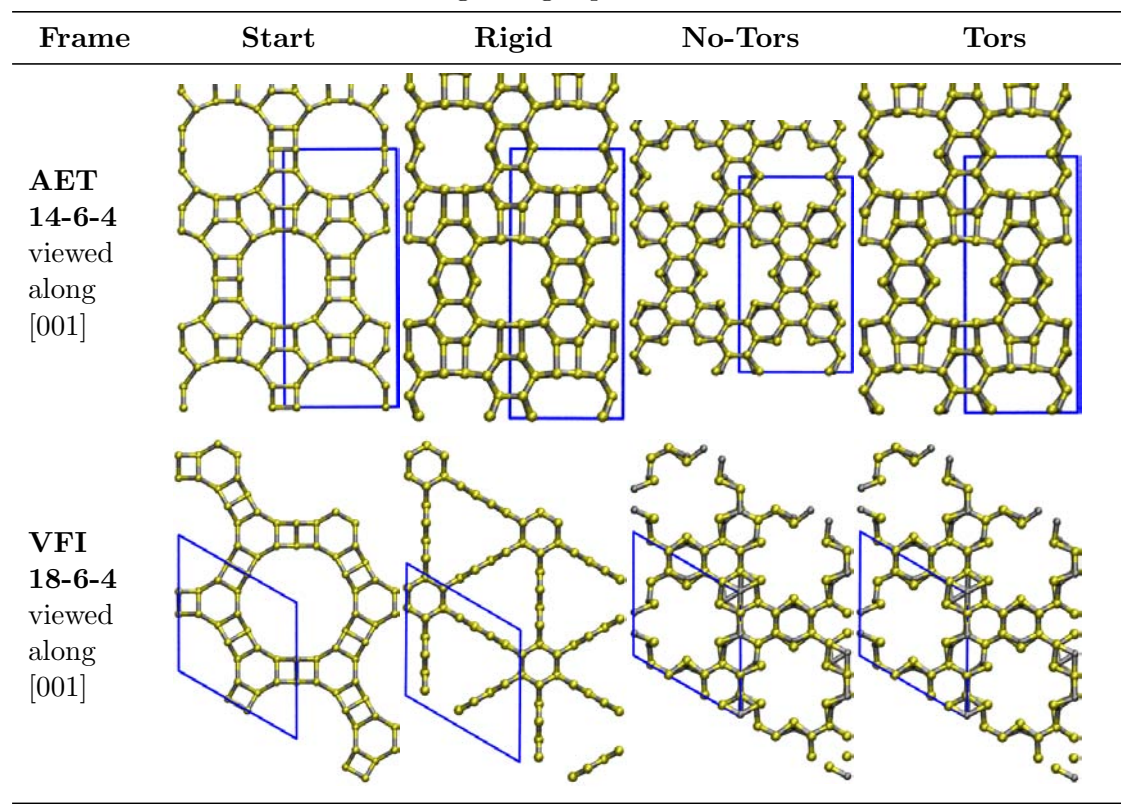
Bibliography

[1] R. M. Brydson and C. Hammond. Generic methodologies for nanotechnolgy: classification and fabrication. In R. W. Kelsall, I. W. Hamley, and M. Geoghegan, editors, *Nanoscale Science and Technology*, Chapter 1, pages 1–55. John Wiley & Sons Limited, (2005).

[2] A. P. Alivisatos. Semiconductor clusters, nanocrystals, and quantum dots. *Science*, **271**:933–937, (1996).

[3] C. P. Poole Jr and F. J. Owens, editors. *Introduction to Nanotechnology*. John Wiley & Sons Limited, (2003).

[4] A. P. Alivisatos. Birth of a nanoscience building block. *ACS Nano*, **2**(8): 1514–1516, (2008).

[5] P. Peercy. The drive to miniaturization. *Nature*, **406**:1023–1026, (2000).

[6] G. E. Moore. Cramming more components onto integrated circuits. *Electronics Magazine*, **38**(8), (1965).

[7] G. E. Moore. Progress in digital integrated electronics. *Technical Digest - Inernational Electron Devices Meeting*, **21**:11–13, (1975).

[8] S. E. Thompson and S. Parthasarathy. Moore's law: the future of Si microelectronics. *Mater. Today*, **9**(6):20–25, (2006).

[9] M. L. Green, E. P. Gusev, R. Degraeve, and E. L. Garfunkel. Ultrathin (<4 nm) SiO and Si-O-N gate dielectric layers for silicon microelectronics: Understanding the processing, structure, and physical limits. *J. Appl. Phys.*, **90**(5):2058–2121, (2001).

[10] V. L. Colvin. The potential environmental impact of engineered nanomaterials. *Nat. Biotech.*, **21**(10):1166–1170, (2003).

[11] J. F. Banfield and H. Zhang. Nanoparticles and the environment. In J. F. Banfield and A. Navrotsky, editors, *Nanoparticles and the environment*, Volume 44 of *Reviews in Mineralogy & Geochemistry*, Chapter 1. Mineralogical Society of America, (2001).

[12] A. S. Barnard. Nanohazards: Knowledge is our first defence. *Nat. Mater.*, **5**:245–248, (2006).

[13] P. W. Atkins. *Physical Chemistry.* Oxford University Press, 4th edition, (1990).

[14] R. W. Kelsall, I. W. Hamley, and M. Geoghegan, editors. *Nanoscale Science and Technology.* John Wiley & Sons Limited, (2005).

[15] C. Kittel. *Introduction to Solid State Physics.* John Wiley & Sons Limited, 7th edition, (1996).

[16] G. Ganteför. Photoelectron spectroscopy. In S. N. Khanna and A. W. Castleman, editors, *Quantum Phenomena in Clusters and Nanoclusters*, Cluster Physics, Chapter 3. Springer, (2003).

[17] F. Baletto and R. Ferrando. Structural properties of nanoclusters: Energetic, thermodynamic, and kinetic effects. *Rev. Mod. Phys.*, **77**:371–423, (2005).

[18] H. Jones. *The theory of Brillouin zones and electronic states in crystals.* North-Holland Publishing Company, 2nd edition, (1975).

[19] D. J. Vaughan and J. R. Craig. *Mineral chemistry of metal sulfides.* Cambridge earth science series. Cambridge university press, (1978).

[20] A. F. Golovin. The centennial of DK Chernov's discovery of polymorphous transformations in steel (1868–1968). *Met. Sci. Heat Treat.*, **10**(5):335–340, (1968).

[21] G. Grimvall and I. Ebbsjö. Polymorphism in metals I. Vibrational free energy. *Phys. Scr.*, **12**:168–172, (1975).

[22] G. Grimvall. Polymorphism in metals II. Electronic and magnetic free energy. *Phys. Scr.*, **12**:173–176, (1975).

[23] G. Grimvall. Polymorphism of metals III. Theory of the temperature-pressure phase diagram of iron. *Phys. Scr.*, **13**:59–64, (1976).

[24] K. Y. Shakhnazarov. Chernov's iron–carbon diagram, the structure and properties of steel. *Met. Sci. Heat Treat.*, **51**(1-2):3–6, (2009).

[25] T. Takahashi, H. K. Mao, and W. A. Bassett. Lead: X-ray diffraction study of a high-pressure polymorph. *Science*, **165**:1352–1353, (1969).

[26] H. K. Mao, Y. Wu, J. F. Shu, J. Z. Hu, R. J. Hemley, and D. E. Cox. High-pressure phase transition and equation of state of lead to 238 GPa. *Solid State Commun.*, **74**(9):1027–1029, (1990).

[27] C. A. Vanderborgh, Y. K. Vohra, H. Xia, and A. L. Ruoff. bcc lead at 109 GPa: Diffraction studies to 208 GPa. *Phys. Rev. B*, **41**(10):7338–7340, (1990).

[28] A. Kuznetsov, V. Dmitriev, L. Dubrovinsky, V. Prakapenka, and H.-P. Weber. Fcc–hcp phase boundary in lead. *Solid State Commun.*, **122**: 125–127, (2002).

[29] A. L. Mackay. A dense non-crystallographic packing of equal spheres. *Acta Crystallogr.*, **15**:916–918, (1962).

[30] L. S. Bartell, Y. G. Chushak, and J. Huang. Structure and transformation in clusters: Computational experiments. *Struct. Chem.*, **11**(2/3):105–110, (2000).

[31] Y. G. Chushak and L. S. Bartell. Melting and freezing of gold nanoclusters. *J. Phys. Chem. B*, **105**:11605–11614, (2001).

[32] B. D. Savage and J. S. Mathis. Observed properties of interstellar dust. *Annu. Rev. Astro. Astrophys.*, **17**:73–111, (1979).

[33] R. C. Bless and B. D. Savage. Ultraviolet photometry from the orbiting astronomical observatory. II. Interstellar extinction. *The Astrophysical Journal*, **171**:293–308, (1972).

[34] A. D. Code and B. D. Savage. Orbiting astronomical observatory: Review of scientific results. *Science*, **177**(4045):213–221, (1972).

[35] P. A. Aannestad and E. M. Purcell. Interstellar grains. *Annu. Rev. Astro. Astrophys.*, **11**:309–362, (1973).

[36] D. Massa, B. D. Savage, and E. L. Fitzpatrick. Peculiar ultraviolet interstellar extinction. *Astrophys. J.*, **266**:662–683, (1983).

[37] B. D. Savage. Ultraviolet photometry from the orbiting astronomical observatory XX. The ultraviolet extinction bump. *Astrophys. J.*, **199**: 92–109, (1975).

[38] E. A. Rohlfing, D. M. Cox, and A. Kaldor. Production and characterization of supersonic carbon cluster beams. *J. Chem. Phys.*, **81**(7):3322–3330, (1984).

[39] H. W. Kroto, J. R. Heath, S. C. O'Brien, R. F. Curl, and R. E. Smalley. C_{60}: buckminsterfullerene. *Nature*, **318**(14):162–163, (1985).

[40] R. C. Haddon, L. E. Brus, and K. Raghavachari. Electronic structure and bonding in icosahedral C_{60}. *Chem. Phys. Lett.*, **125**(5,6):459–464, (1986).

[41] W. Krätschmer, K. Fostiropoulos, and D. R. Huffman. The infrared and ultraviolet absorption spectra of laboratory-produced carbon dust: evidence for the presence of the C_{60} molecule. *Chem. Phys. Lett.*, **170**(2,3):167–170, (1990).

[42] W. Krätschmer, D. L. Lamb, K. Kostiropoulos, and D. R. Huffman. Solid C_{60}: a new form of carbon. *Nature*, **347**:354–358, (1990).

[43] E. Osawa. Superaromaticity. *Kagaku (Chemistry) Japan*, **25**:854–863, (1970).

[44] E. Osawa. The evolution of the football structure for the C_{60} molecule: a retrospective. *Phil. Trans. R. Soc. Lond. A*, **343**(1667):1–8, (1993).

[45] S. Iijima. Helical microtubules of graphitic carbon. *Nature*, **354**:56–58, (1991).

[46] E. T. Thostenson, Z. Ren, and T.-W. Chou. Advances in the science and technology of carbon nanotubes and their composites: a review. *Compos. Sci. Technol.*, **61**:1899–1912, (2001).

[47] J. W. G. Wildöer, L. C. Venema, A. G. Rinzler, R. E. Smalley, and C. Dekker. Electronic structure of atomically resolved carbon nanotubes. *Nature*, **391**:59–62, (1998).

[48] T. W. Odom, J.-L. Huang, P. Kim, and C. M. Lieber. Atomic structure and electronic properties of single-walled carbon nanotubes. *Nature*, **391**:62–64, (1998).

[49] S. Iijima, C. Brabec, A. Maiti, and J. Bernholc. Structural flexibility of carbon nanotubes. *J. Chem. Phys.*, **104**(5):2089–2092, (1996).

[50] L. E. Brus. Electron–electron and electronhole interactions in small semiconductor crystallites: The size dependence of the lowest excited electronic state. *J. Chem. Phys.*, **80**(9):4403–1109, (1984).

[51] L. E. Brus. Electronic wave functions in semiconductor clusters: experiment and theory. *J. Phys. Chem.*, **90**:2555–2560, (1986).

[52] L. E. Brus. A simple model for the ionization potential, electron affinity, and aqueous redox potentials of small semiconductor crystallites. *J. Chem. Phys.*, **79**(11):5566–5571, (1983).

[53] L. E. Brus. Zero-dimensional "excitons" in semiconductor clusters. *IEEE J. Quantum Electron.*, **QE-22**(9):1909–1914, (1986).

[54] A. P. Alivisatos. Perspectives on the physical chemistry of semiconductor nanocrystals. *J. Phys. Chem.*, **100**(31):13226–13239, (1996).

[55] C. B. Murray, D. J. Norris, and M. G. Bawendi. Synthesis and characterization of nearly monodisperse CdE (E= S, Se, Te) semiconductor nanocrystallites. *J. Am. Chem. Soc*, **115**:8706–8715, (1993).

[56] G. Baldinozzi, D. Simeone, D. Gosset, and M. Dutheil. Neutron diffraction study of the size-induced tetragonal to monoclinic phase transition in zirconia nanocrystals. *Phys. Rev. Lett.*, **90**(21):216103, (2003).

[57] M. W. Pitcher, S. Ushakov, A. Navrotsky, and B. Woodfield. Energy crossovers in nanocrystalline zirconia. *J. Am. Ceram. Soc.*, **88**(1):160–167, (2005).

[58] S. Xie, E. Iglesia, and A. T. Bell. Water-assisted tetragonal-to-monoclinic phase transformation of ZrO_2 at low temperatures. *Chem. Mater*, **12**(8): 2442–2447, (2000).

[59] A. S. Barnard and L. A. Curtiss. Prediction of TiO_2 nanoparticle phase and shape transitions controlled by surface chemistry. *Nano Lett.*, **5**(7): 1261–1266, (2005).

[60] H. Zhang and J. F. Banfield. Thermodynamic analysis of phase stability of nanocrystalline titania. *J. Mater. Chem.*, **8**(9):2073–2076, (1998).

[61] J. M. McHale, A. Auroux, A. J. Perrotta, and A. Navrotsky. Surface energies and thermodynamic phase stability in nanocrystalline aluminas. *Science*, **277**:788–791, (1997).

[62] M. Y. Gamarnik. Size-related stabilization of diamond nanoparticles. *Nanostruct. Mater.*, **7**(6):651–658, (1996).

[63] H. Zhang and J. F. Banfield. Understanding polymorphic phase transformation behavior during growth of nanocrystalline aggregates: Insights from TiO_2. *J. Phys. Chem. B*, **104**(15):3481–3487, (2000).

[64] X. Ye, J. Sha, Z. Jiao, and L. Zhang. Thermoanalytical characteristic of nanocrystalline brookite-based titanium dioxide. *Nanostruct. Mater.*, **8**(7): 919–927, (1997).

[65] T. Mitsuhashi and O. J. Kleppa. Transformation enthalpies of the TiO_2 polymorphs. *J. Am. Ceram. Soc.*, **62**:7–8, (1979).

[66] S. H. Tolbert and A. P. Alivisatos. Size dependence of a first order solid-solid phase transition: The wurtzite to rock salt transformation in CdSe nanocrystals. *Science*, **265**:373–376, (1994).

[67] A. Kasuya, R. Sivamohan, Y. A. Barnakov, I. M. Dmitruk, T. Nirasawa, V. R. Romanyuk, V. Kumar, S. V. Mamykin, K. Tohji, B. Jeyadevan, K. Shinoda, T. Kudo, O. Terasaki, Z. Liu, R. V. Belosludov, V. Sundararajan, and Y. Kawazoe. Ultra-stable nanoparticles of CdSe revealed from mass spectrometry. *Nat. Mater.*, **3**:99–102, (2004).

[68] D. Zaziski, S. Prilliman, E. C. Scher, M. Casula, J. Wickham, S. M. Clark, and A. P. Alivisatos. Critical size for fracture during solid-solid phase transformations. *Nano Lett.*, **4**(5):943–946, (2004).

[69] E. Makovicky. Crystal structures of sulfides and other chalcogenides. In D. J. Vaughan, editor, *Sulfide Mineralogy and Geochemistry*, Volume 61 of *Reviews in Mineralogy & Geochemistry*, Chapter 2, pages 7–125. Mineralogical Society of America, (2006).

[70] K. M. Rosso and D. J. Vaughan. Sulfide mineral surfaces. *Rev. Mineral. Geochem.*, **61**:505–556, (2006).

[71] D. J. Vaughan. Sulfide mineralogy and geochemistry: Introduction and overview. In D. J. Vaughan, editor, *Sulfide Mineralogy and Geochemistry*, Volume 61 of *Reviews in Mineralogy & Geochemistry*, Chapter 1. Mineralogical Society of America, (2006).

[72] R. M. Hazen. Genesis: rocks, minerals, and the geochemical origin of life. *Elements*, **1**:135–137, (2005).

[73] M. J. Russell and A. J. Hall. The emergence of life from iron monosulphide bubbles at a submarine hydrothermal redox and pH front. *J. Geol. Soc. London*, **154**:377–402, (1997).

[74] D. W. Blowes, C. J. Ptacek, J. L. Jambor, and C. G. Weisener. The geochemistry of acid mine drainage. In B. S. Lollar, editor, *Environmental Geochemistry*, Volume 9 of *Treatise on Geochemistry*, Chapter 9.05. Elsevier, (2005).

[75] B. Gilbert, F. Huang, Z. Lin, C. Goodell, H. Zhang, and J. F. Banfield. Surface chemistry controls crystallinity of ZnS nanoparticles. *Nano Lett.*, **6**(4):605–610, (2006).

[76] C. I. Pearce, A. D. Pattrick, and D. J. Vaughan. Electrical and magnetic properties of sulfides. In D. J. Vaughan, editor, *Sulfide Mineralogy and Geochemistry*, Volume 61 of *Reviews in Mineralogy & Geochemistry*, Chapter 3, pages 127–180. Mineralogical Society of America, (2006).

[77] G. E. Engel and R. J. Needs. Total energy calculations on zinc sulphide polytypes. *J. Phys.: Condens. Matter*, **2**:367–376, (1990).

[78] S. Mardix. Polytypism: A controlled thermodynamic phenomenon. *Phys. Rev. B*, **33**(12):8677–8684, (1986).

[79] I. Barin, O. Knacke, and O. Kubaschewski. *Thermochemical properties of inorganic substances - Supplement*, pages 827–829. Springer, (1977).

[80] P. J. Gardner and P. Pang. Thermodynamics of the zinc sulphide transformation, sphalerite wurtzite, by modified entrainment. *J. Chem. Soc., Faraday Trans. 1*, **84**(6):1879–1887, (1988).

[81] B. J. Skinner and P. B. Barton. The substitution of oxygen for sulfur in wurtzite and sphalerite. *Am. Mineral.*, **45**(5-6):612–625, (1960).

[82] S. D. Scott and H. L. Barnes. Sphalerite-wurtzite equilibria and stoichiometry. *Geochim. Cosmochim. Acta*, **36**(11):1275–1295, (1972).

[83] G. E. Engel and R. J. Needs. Calculations of the structural properties of cubic zinc sulfide. *Phys. Rev. B*, **41**(11):7876–7878, (1990).

[84] S. G. Louie, S. Froyen, and M. L. Cohen. Nonlinear ionic pseudopotentials in spin-density-functional calculations. *Phys. Rev. B*, **26**(4):1738–1742, (1982).

[85] J. L. Martins, N. Troullier, and S.-H. Wei. Pseudopotential plane-wave calculations for ZnS. *Phys. Rev. B*, **43**(3):2213–2217, (1991).

[86] B. K. Agrawal, P. S. Yadav, and S. Agrawal. *Ab initio* calculation of the electronic, structural, and dynamical properties of Zn-based semiconductors. *Phys. Rev. B*, **50**(20):14881–14887, (1994).

[87] R. A. Casali and N. E. Christensen. Elastic constants and deformation potentials of ZnS and ZnSe under pressure. *Solid State Communications*, **108**(10):793–798, (1998).

[88] K. Wright and R. A. Jackson. Computer simulation of the structure and defect properties of zinc sulfide. *J. Mater. Chem.*, **5**(11):2037–2040, (1995).

[89] K. Wright, G. W. Watson, S. C. Parker, and D. J. Vaughan. Simulation of the structure and stability of sphalerite (ZnS) surfaces. *Am. Mineral.*, **83**: 141–146, (1998).

[90] F. Benkabou, H. Aourag, and M. Certier. Atomistic study of zinc-blende CdS, CdSe, ZnS, and ZnSe from molecular dynamics. *Mater. Chem. Phys.*, **66**:10–16, (2000).

[91] Y. R. Wang and C. B. Duke. Atomic and electronic structure of ZnS cleavage surfaces. *Phys. Rev. B*, **36**(5):2763–2769, (1987).

[92] C. B. Duke and Y. R. Wang. Mechanism and consequences of surface reconstruction on the cleavage faces of wurtzite-structure compound semiconductors. *J. Vac. Sci. Technol. A*, **6**(4):693–695, (1988).

[93] C. B. Duke. Atomic and electronic structure of tetrahedrally coordinated compound semiconductor interfaces. *J. Vac. Sci. Technol. A*, **6**(3): 1957–1962, (1988).

[94] S. Hamad, S. Cristol, and C. R. A. Catlow. Surface structures and crystal morphology of ZnS: Computational study. *J. Phys. Chem. B*, **106**(42): 11002–11008, (2002).

[95] K. Wright and J. D. Gale. Interatomic potentials for the simulation of the zinc-blende and wurtzite forms of ZnS and CdS: Bulk structure, properties, and phase stability. *Phys. Rev. B*, **70**(3):035211, (2004).

[96] H. Zhang, B. Chen, B. Gilbert, and J. F. Banfield. Kinetically controlled formation of a novel nanoparticulate ZnS with mixed cubic and hexagonal stacking. *J. Mater. Chem.*, **16**(3):249–254, (2006).

[97] G. Ren, Z. Lin, B. Gilbert, J. Zhang, F. Huang, and J. Liang. Evolution of ZnS nanostructure morphology under interfacial free-energy control. *Chem. Mater.*, **20**(7):2438–2443, (2008).

[98] H. Zhang, F. Huang, B. Gilbert, and J. F. Banfield. Molecular dynamics simulations, thermodynamic analysis and experimental study of phase stability of zinc sulfide nanoparticles. *J. Phys. Chem. B*, **107**:13051–13060, (2003).

[99] H. Yoshiyama, S. Tanaka, I. Mikami, and S. Oshio. Role of surface energy in the thin-film growth of electroluminescent ZnS, CaS, and SrS. *J. Cryst. Growth*, **86**:56–60, (1988).

[100] V. L. Tauson, M. G. Abaramovich, V. V. Akimov, and V. A. Scherbakov. Thermodynamics of real mineral crystals: Equilibrium crystal shape and phase size effect. *Geochim. Cosmochim. Acta*, **57**:815–821, (1993).

[101] B. Gilbert, H. Zhang, F. Huang, M. P. Finnegan, G. A. Waychunas, and J. F. Banfield. Special phase transformation and crystal growth pathways observed in nanoparticles. *Geochem. Trans.*, **4**(4):20–27, (2003).

[102] S. B. Qadri, E. F. Skelton, A. D. Dinsmore, J. Z. Hu, W. J. Kim, C. Nelson, and B. R. Ratna. The effect of particle size on the structural transitions in zinc sulfide. *J. Appl. Phys.*, **39**(1):115–119, (2001).

[103] B. Gilbert, F. Huang, H. Zhang, G. A. Waychunas, and J. F. Banfield. Nanoparticles: Strained and stiff. *Science*, **305**(5684):651–654, (2004).

[104] B. Gilbert, H. Zhang, B. Chen, M. Kunz, F. Huang, and J. F. Banfield. Compressibility of zinc sulfide nanoparticles. *Phys. Rev. B*, **74**(11):115405, (2006).

[105] S. B. Qadri, E. F. Skelton, D. Hsu, A. D. Dinsmore, J. Yang, H. F. Gray, and B. R. Ratna. Size-induced transition-temperature reduction in nanoparticles of ZnS. *Phys. Rev. B*, **60**(13):9191–9193, (1999).

[106] H. Zhang, B. Gilbert, F. Huang, and J. F. Banfield. Water-driven structure transformation in nanoparticles at room temperature. *Nature*, **424**(6952): 1025–1029, (2003).

[107] H. Zhang, J. Rustad, and J. F. Banfield. Interaction between water molecules and zinc sulfide nanoparticles studied by temperature-programmed desorption and molecular dynamics simulations. *J. Phys. Chem. A*, **111**: 5008–5014, (2007).

[108] H. Zhang and J. F. Banfield. Aggregation, coarsening, and phase transformation in ZnS nanoparticles studied by molecular dynamics simulations. *Nano Lett.*, **4**(4):7130718, (2004).

[109] F. Huang, B. Gilbert, H. Zhang, and J. F. Banfield. Reversible, surface-controlled structure transformation in nanoparticles induced by an aggregation state. *Phys. Rev. Lett.*, **92**(15), (2004).

[110] S. Hamad, S. Cristol, and C. R. A. Catlow. Simulation of the embryonic stage of ZnS formation from aqueous solution. *J. Am. Chem. Soc.*, **127**: 2580–2590, (2005).

[111] E. Spanó, S. Hamad, and C. R. A. Catlow. Computational evidence of bubble ZnS clusters. *J. Phys. Chem. B*, **107**:10337–10340, (2003).

[112] E. Spanó, S. Hamad, and C. R. A. Catlow. ZnS bubble clusters with onion-like structures. *Chem. Commun.*, **7**:864–865, (2004).

[113] S. Hamad, C. R. A. Catlow, E. Spanó, J. M. Matxain, and J. M. Ugalde. Structure and properties of ZnS nanoclusters. *J. Phys. Chem. B*, **109**(7): 2703–2708, (2005).

[114] C. Roberts and R. L. Johnston. Investigation of the structures of MgO clusters using a genetic algorithm. *Phys. Chem. Chem. Phys.*, **3**:5024–5034, (2001).

[115] A. Burnin and J. J. BelBruno. $Zn_nS_m^+$ cluster production by laser ablation. *Chem. Phys. Lett.*, **362**:341–348, (2002).

[116] A. Burnin, E. Sanville, and J. J. BelBruno. Experimental and computational study of the Zn_nS_n and $Zn_nS_n^+$ clusters. *J. Phys. Chem. A*, **109**(23): 5026–5034, (2005).

[117] F. Jensen. *Introduction to Computational Chemistry.* John Wiley & Sons Limited, (1999).

[118] A. R. Leach. *Molecular Modelling: Principles and Applications.* Pearson Education Limited, 2nd edition, (2001).

[119] W. Koch and M. C. Holthausen. *A Chemist's Guide to Density Functional Theory.* Wiley-VCH, 2nd edition, (2001).

[120] A. Szabo and N. S. Ostlund. *Modern Quantum Chemistry.* McGraw-Hill, 1st edition, (1982).

[121] M. Born and J. R. Oppenheimer. Zur quantentheorie der molekeln (on the quantum theory of molecules). *Ann. Phys. (Leipzig)*, **84**:457–484, (1927).

[122] J. C. Slater. The theory of complex spectra. *Phys. Rev.*, **34**(10):1293–1322, (1929).

[123] P. Hohenberg and W. Kohn. Inhomogeneous electron gas. *Phys. Rev,* **136** (3B):B864–B871, (1964).

[124] W. Kohn and L. J. Sham. Self-consistent equations including exchange and correlation effects. *Phys. Rev,* **140**(4A):A1133–A1138, (1965).

[125] D. M. Ceperley and B. J. Alder. Ground state of the electron gas by a stochastic method. *Phys. Rev. Lett.*, **45**(7):566–569, (1980).

[126] S. H. Vosko, L. Wilk, and M. Nusair. Accurate spin-dependent electron liquid correlation energies for local spin density calculations: a critical analysis. *Can. J. Phys.*, **58**(8):1200–1211, (1980).

[127] J. P. Perdew and Y. Wang. Accurate and simple analytic representation of the electron-gas correlation energy. *Phys. Rev. B*, **45**(23):13244–13249, (1992).

[128] A. D. Becke. Density-functional exchange-energy approximation with correct asymptotic behavior. *Phys. Rev. A*, **38**(6):3098–3100, (1988).

[129] A. D. Becke. Density-functional thermochemistry. IV. A new dynamical correlation functional and implications for exact-exchange mixing. *J. Chem. Phys.*, **104**(3):1040–1046, (1996).

[130] C. Lee, W. Yang, and R. G. Parr. Development of the colle-salvetti correlation-energy formula into a functional of the electron density. *Phys. Rev. B*, **37**(2):785–789, (1988).

[131] J. P. Perdew, K. Burke, and M. Ernzerhof. Generalized gradient approximation made simple. *Phys. Rev. Lett.*, **77**(18):3865–3868, (1996).

[132] A. D. Becke. A new mixing of Hartree–Fock and local densityfunctional theories. *J. Chem. Phys.*, **98**(2):1372–1377, (1993). alytical.

[133] A. D. Becke. Density-functional thermochemistry. III. The role of exact exchange. *Chem. Phys*, **98**(1):5648–5652, (1993).

[134] P. J. Stephens, F. J. Devlin, C. F. Chabalowski, and M. J. Frisch. Ab initio calculation of vibrational absorption and circular dichroism spectra using density functional force fields. *J. Phys. Chem.*, **98**(45):11623–11627, (1994).

[135] C. C. J. Roothaan. New developments in molecular orbital theory. *Rev. Mod. Phys.*, **32**(2):69–89, (1951).

[136] J. S. Binkley, J. A. Pople, and W. J. Hehre. Self-consistent molecular orbital methods. 21. Small split-valence basis sets for first-row elements. *J. Am. Chem. Soc.*, **103**(3):939–947, (1980).

[137] R. Krishnan, J. S. Binkley, R. Seeger, and J. A. Pople. Selfconsistent molecular orbital methods. XX. A basis set for correlated wave functions. *J. Chem. Phys.*, **71**(1):650–654, (1980).

[138] J. M. Soler, E. Artacho, J. D. Gale, A. García, J. Junquera, P. Ordejón, and D. Sánchez-Portal. The SIESTA method for *ab initio* order-N materials simulation. *J. Phys. Condens. Matter*, **14**:2745–2779, (2002).

[139] N. Troullier and J. L. Martins. Efficient pseudopotentials for plane-wave calculations. *Phys. Rev. B*, **43**(3):1993–2006, (1991).

[140] J. D. Gale. SIESTA: A linear-scaling method for density functional calculations. In J. R. Reimers, editor, *Computational methods for large systems: Electronic structure approaches for biotechnology and nanotechnology*, Chapter 2, pages 45–75. John Wiley & Sons Limited, (2011).

[141] H. J. Monkhorst and J. D. Pack. Special points for brillouin-zone integrations. *Phys. Rev. B*, **13**(12):5188–5192, (1976).

[142] J. Moreno and J. M. Soler. Optimal meshes for integrals in real-and reciprocal-space unit cells. *Phys. Rev. B*, **45**(24):13891–13898, (1992).

[143] M. P. Allen and D. J. Tildesley. *Computer Simulation of Liquids.* Clarendon Press, (1987).

[144] A. K. Rappé and C. J. Casewit. *Molecular Mechanics across Chemistry.* University Science Books, (1997).

[145] T. L. Hill. On steric effects. *J. Chem. Phys.*, **14**:465, (1946).

[146] F. H. Westheimer and J. E. Mayer. The theory of the racemization of optically active derivatives of diphenyl. *J. Chem. Phys.*, **14**(12):733–738, (1946).

[147] P. M. Morse. Diatomic molecules according to the wave mechanics I: Electronic levels of the hydrogen molecular ion. *Phys. Rev.*, **34**:57–64, (1929).

[148] R. T. Morrison and R. N. Boyd. *Organic Chemistry.* Allyn and Bacon, 5th edition, (1987).

[149] H.-Q. Ding, N. Karasawa, and W. A. Goddard. Atomic level simulations on a million particles: The cell multipole method for Coulomb and London nonbond interactions. *J. Chem. Phys.*, **97**(6):4309–4315, (1992).

[150] D. Wolf, P. Keblinski, S. R. Phillpot, and J. Eggebrecht. Exact method for the simulation of Coulombic systems by spherically truncated, pairwise r^{-1} summation. *J. Chem. Phys.*, **110**(17):8254–8282, (1999).

[151] P. P. Ewald. Die berechnung optischer und elektrostatischer gitterpotentiale (The computation of optical and electrostatic lattice potentials). *Ann. Phys. (Berlin)*, **369**(3):253–287, (1921).

[152] L. Silberstein. VII. Molecular refractivity and atomic interaction. *Philos. Mag.*, **33**(193):92–128, (1917).

[153] L. Silberstein. XIX. Dispersion and the size of molecules of hydrogen, oxygen, and nitrogen. *Philos. Mag.*, **33**(194):215–222, (1917).

[154] L. Silberstein. L. Molecular refractivity and atomic interaction. II. *Philos. Mag.*, **33**(198):521–533, (1917).

[155] J. Applequist, J. R. Carl, and K.-K. Fung. Atom dipole interaction model for molecular polarizability. Application to polyatomic molecules and determination of atom polarizabilities. *J. Am. Chem. Soc.*, **94**(9):2952–2960, (1972).

[156] J. Applequist. A multipole interaction theory of electric polarization of atomic and molecular assemblies. *J. Chem. Phys.*, **83**:809–826, (1985).

[157] M. L. Olson and K. R. Sundberg. An atom monopole-dipole interaction model with charge transfer for the treatment of polarizabilities of π-bonded molecules. *J. Chem. Phys.*, **69**(12):5400–5404, (1978).

[158] P. A. Madden and M. Wilson. 'Covalent' effects in 'ionic' systems. *Chem. Soc. Rev.*, **25**(5):339–350, (1996).

[159] B. G. Dick and A. W. Overhauser. Theory of the dielectric constants of alkali halide crystals. *Phys. Rev.*, **112**(1):90–103, (1958).

[160] J. D. Gale and A. L. Rohl. The General Utility Lattice Program (GULP). *Mol. Simul.*, **29**(5):291–341, (2003).

[161] P. J. D. Lindan and M. J. Gillan. Shell-model molecular dynamics simulation of superionic conduction in CaF_2. *J. Phys. Condens. Matter*, **5**:1019–1030, (1993).

[162] P. J. Mitchell and D. Fincham. Shell model simulations by adiabatic dynamics. *J. Phys. Condens. Matter*, **5**:1031–1038, (1993).

[163] J. E. Jones. On the determination of molecular fields. I. From the variation of the viscosity of a gas with temperature. *Proc. R. Soc. London, Ser. A*, **106**(738):441–462, (1924).

[164] J. E. Jones. On the determination of molecular fields. II. From the equation of state of a gas. *Proc. R. Soc. London, Ser. A*, **106**(738):463–477, (1924).

[165] R. A. Buckingham. The classical equation of state of gaseous helium, neon and argon. *Proc. R. Soc. London, Ser. A*, **168**(933):264–283, (1938).

[166] D. C. Rapaport. *The art of molecular dynamics simulation.* Cambridge University Press, (1995).

[167] G. Henkelman, G. Jóhannesson, and H. Jónsson. Methods for finding saddle points and minimum energy paths. In S. D. Schwartz, editor, *Progress on Theoretical Chemistry and Physics*, Chapter 10, pages 269–300. Kluwer Academic Publishers, (2000).

[168] H. Eyring. The activated complex in chemical reactions. *J. Chem. Phys.*, **3** (2):107–115, (1935).

[169] E. Pollak and P. Talkner. Reaction rate theory: What it was, where is it today, and where is it going? *CHAOS*, **15**(2):026116, (2005).

[170] R. A. Marcus. On the analytical mechanics of chemical reactions. quantum mechanics of linear collisions. *J. Chem. Phys.*, **45**(12):4493–4499, (1966).

[171] R. A. Olsen, G. J. Kroes, G. Henkelman, A. Arnaldsson, and H. Jonsson. Comparison of methods for finding saddle points without knowledge of the final states. *J. Chem. Phys.*, **121**(20):9776–9792, (2004).

[172] J. Nocedal and S. J. Wright. Springer series in operations research. In P. Glynn and S. M. Robinson, editors, *Numerical Optimization.* Springer, (1999).

[173] P. J. W. Debye. Näherungsformeln für die zylinderfunktionen für grosse werte des arguments und unbeschränkt veränderliche werte des index. *Math. Ann.*, **67**(4):535–558, (1909).

[174] P. J. W. Debye. *The collected papers of Peter J. W. Debye.* Interscience, New York-London, English edition, (1954).

[175] M. R. Hestenes and E. Stiefel. Methods of conjugate gradients for solving linear systems. *J. Res. Natl. Bur. Stand.*, **49**(6):409–436, (1952).

[176] W. H. Press, B. P. Flannery, S. A. Teukolsky, and W. T. Vetterling. *Numerical Recipes in Fortran: The Art of Scientific Computing.* Cambridge University Press, (1992).

[177] T. J. Ypma. Historical development of the Newton-Raphson method. *SIAM Rev.*, **37**(4):531–551, (1995).

[178] R. Fletcher and M. J. D. Powell. A rapidly convergent descent method for minimization. *Comput. J.*, **6**:163–168, (1963).

[179] W. C. Davidon. Variable metric method for minimization. *SIAM J. Optimiz.*, **1**(1):1–17, (1991).

[180] M. J. D. Powell. An iterative method for finding stationary values of a function of several variables. *Comput. J.*, **5**(2):147–151, (1962).

[181] M. J. D. Powell. An efficient method for finding the minimum of a function of several variables without calculating derivatives. *Comput. J.*, **7**(2):155–162, (1964).

[182] C. G. Broyden. A class of methods for solving nonlinear simultaneous equations. *Math. Comput.*, **19**:577–593, (1965).

[183] R. Fletcher. A new approach to variable metric algorithms. *Comput. J.*, **13**(3):317–322, (1970).

[184] D. Goldfarb. A family of variable metric methods derived by variational means. *Math. Comput.*, **24**:23–26, (1970).

[185] D. F. Shanno. Conditioning of quasi-Newton methods for function minimization. *Math. Comput.*, **24**(111):647–656, (1970).

[186] D. F. Shanno and P. C. Kettler. Optimal conditioning of quasi-Newton methods. *Math. Comput.*, **24**(111):657–664, (1970).

[187] T. A. Halgren and W. N. Lipscomb. The synchronous-transit method for determining reaction pathways and locating molecular transition states. *Chem. Phys. Lett.*, **49**(2):225–232, (1977).

[188] M. J. S. Dewar, E. F. Healy, and J. J. P. Stewart. Location of transition states in reaction mechanisms. *J. Chem. Soc., Faraday Trans. 2*, **80**:227–233, (1984).

[189] I. V. Ionova and E. A. Carter. Ridge method for finding saddle points on potential energy surfaces. *J. Chem. Phys.*, **98**(8):6377–6386, (1993).

[190] A. Banerjee, N. Adams, J. Simons, and R. Shepard. Search for stationary points on surfaces. *J. Phys. Chem.*, **89**(1):52–57, (1985).

[191] H. Jónsson, G. Mills, and J. K. W. Nudged elastic band method for finding minimum energy paths of transitions. In B. J. Berne, G. Ciccotti, and D. F. Coker, editors, *Classical and Quantum Dynamics in Condensed Phase Simulations*, Chapter 16, pages 385–404. World Scientific, (1998).

[192] G. Henkelman, B. P. Uberuaga, and H. Jónsson. A climbing image nudged elastic band method for finding saddle points and minimum energy paths. *J. Chem. Phys.*, **113**(22):9901–9904, (2000).

[193] G. Henkelman and H. Jónsson. Improved tangent estimate in the nudged elastic band method for finding minimum energy paths and saddle points. *J. Chem. Phys.*, **113**(22):9978–9985, (2000).

[194] J. D. Gale. Simulating the crystal structures and properties of ionic materials from interatomic potentials. *Reviews in Mineralogy and Geochemistry*, **42**: 37–62, (2001).

[195] S. C. Parker, N. H. de Leeuw, E. Bourova, and D. J. Cooke. Application of lattice dynamics and molecular dynamics techniques to minerals and their surfaces. *Reviews in Mineralogy and Geochemistry*, **42**:63–82, (2001).

[196] K. Huang. *Statistical Mechanics*. John Wiley & Sons Limited, (1963).

[197] M. E. Tuckerman. *Statistical Mechanics: Theory and Molecular Simulation*. Oxford University Press, (2010).

[198] D. Frenkel and B. Smit. *Understanding Molecular Simulation: From Algorithms to Applications*. Academic Press, 2nd edition, (2002).

[199] N. Metropolis, A. W. Rosenbluth, M. N. Rosenbluth, and A. H. Teller. Equation of state calculations by fast computing machines. *J. Chem. Phys.*, **21**(6):1087–1092, (1953).

[200] B. J. Alder and T. E. Wainwright. Phase transition for a hard sphere system. *J. Chem. Phys.*, **27**:1208–1209, (1957).

[201] L. Verlet. Computer experiments on classical fluids. i. thermodynamical properties of Lennard-Jones molecules. *Phys. Rev*, **159**(1):98–103, (1967).

[202] W. C. Swope, H. C. Andersen, P. H. Berens, and K. R. Wilson. A computer-simulation method for the calculation of equilibrium-constants for

the formation of physical clusters of molecules – application to small water clusters. *J. Chem. Phys.*, **76**(1):637–649, (1982).

[203] R. W. Hockney. Potential calculation and some applications. *Methods Comput. Phys.*, **9**:135–211, (1970).

[204] C. W. Gear. *Numerical initial value problems in ordinary differential equations.* Prentice-Hall, (1971).

[205] L. V. Woodcock. Isothermal molecular dynamics calculations for liquid salts. *Chem. Phys. Lett.*, **10**(3):257–261, (1971).

[206] H. Berendsen, J. Postma, and W. van Gunsteren. Molecular dynamics with coupling to an external bath. *J. Chem. Phys.*, **81**(8):3684–3690, (1984).

[207] H. C. Andersen. Molecular dynamics simulations at constant pressure and/or temperature. *J. Chem. Phys.*, **72**(4):2384–2393, (1980).

[208] W. Hoover. Canonical dynamics: Equilibrium phase-space distributions. *Phys. Rev. A*, **31**(3):1695–1697, (1985).

[209] R. J. Allen, D. Frenkel, and P. R. ten Wolde. Simulating rare events in equilibrium or nonequilibrium stochastic systems. *J. Chem. Phys.*, **124**(2): 024102, (2006).

[210] C. Dellago. Transition path sampling and the calculation of free energies. In C. Chipot and A. Pohorille, editors, *Free Energy Calculations*, Volume 86 of *Springer series in chemical physics*, Chapter 7. Springer, (2007).

[211] G. M. Torrie and J. P. Valleau. Monte Carlo free energy estimates using non-boltzmann sampling: Application to the sub-critical Lennard-Jones fluid. *Chem. Phys. Lett.*, **28**(4):578–581, (1974).

[212] G. M. Torrie and J. P. Valleau. Nonphysical sampling distributions in Monte Carlo free-energy estimation: Umbrella sampling. *J. Comput. Phys.*, **23**: 187–199, (1977).

[213] U. H. E. Hansmann. Parallel tempering algorithm for conformational studies of biological molecules. *Chem. Phys. Lett.*, **281**:140–150, (1997).

[214] C. Jarzynski. Nonequilibrium equality for free energy differences. *Phys. Rev. Lett.*, **78**(14):2690–2693, (1997).

[215] E. A. Carter, G. Ciccotti, J. T. Hynes, and R. Kapral. Constrained reaction coordinate dynamics for the simulation of rare events. *Chem. Phys. Lett.*, **156**(5):472–477, (1989).

[216] P. G. Bolhuis, C. Dellago, P. L. Geissler, and D. Chandler. Transition path sampling: Throwing ropes over mountain passes. *J. Phys.: Condens. Matter*, **12**(8A):A147–A152, (2001).

[217] R. J. Allen, P. B. Warren, and P. R. ten Wolde. Sampling rare switching events in biochemical networks. *Phys. Rev. Lett.*, **94**(1):018104, (2005).

[218] A. Laio and M. Parrinello. Escaping free-energy minima. *PNAS*, **99**(20): 12562–12566, (2002).

[219] D. Donadio, P. Raiteri, and M. Parrinello. Topological defects and bulk melting of hexagonal ice. *J. Phys. Chem. B*, **109**(12):5421–5424, (2005).

[220] A. Stirling, M. Iannuzzi, A. Laio, and M. Parrinello. Azulene-to-naphthalene rearrangement: The Car-Parrinello metadynamics method explores various reaction mechanisms. *ChemPhysChem*, **5**:1558–1568, (2004).

[221] G. Bussi, F. L. Gervasio, A. Laio, and M. Parrinello. Free-energy landscape for β hairpin folding from combined parallel tempering and metadynamics. *J. Am. Chem. Soc.*, **128**(41):13435–13441, (2006).

[222] J.-G. Lee, E. Asciutto, V. Babin, C. Sagui, T. Darden, and C. Roland. Deprotonation of solvated formic acid: Car-Parrinello and metadynamics simulations. *J. Phys. Chem. B*, **110**:2325–2331, (2006).

[223] V. Babin, C. Roland, T. Darden, and C. Sagui. The free energy landscape of small peptides as obtained from metadynamics with umbrella sampling corrections. *J. Chem. Phys.*, **125**(20):204909, (2006).

[224] J. Blumberger, B. Ensing, and M. L. Klein. Formamide hydrolysis in alkaline aqueous solution: Insight from ab initio metadynamics calculations. *Angew. Chem. Int. Ed. (English)*, **45**(18):2893–2897, (2006).

[225] R. Martoňák, A. Laio, and M. Parrinello. Predicting crystal structures: The Parrinello-Rahman method revisited. *Phys. Rev. Lett.*, **90**(7):075503, (2003).

[226] W. van Gunsteren, X. Daura, and A. Mark. Computation of free energy. *Helv. Chim. Acta*, **85**:3113–3129, (2002).

[227] R. W. Zwanzig. High-temperature equation of state by a perturbation method. I. Nonpolar gases. *J. Chem. Phys.*, **22**(8):1420–1426, (1954).

[228] C. Chipot and A. Pohorille. Calculating free energy differences using perturbation theory. In C. Chipot and A. Pohorille, editors, *Free Energy Calculations*, Volume 86 of *Springer series in chemical physics*, Chapter 2. Springer, (2007).

[229] E. Darve. Thermodynamic integration using constrained and unconstrained dynamics. In C. Chipot and A. Pohorille, editors, *Free Energy Calculations*, Volume 86 of *Springer series in chemical physics*, Chapter 4. Springer, (2007).

[230] G. Hummer. Nonequilibrium methods for eequilibrium free energy calculations. In C. Chipot and A. Pohorille, editors, *Free Energy Calculations*, Volume 86 of *Springer series in chemical physics*, Chapter 5. Springer, (2007).

[231] A. F. Voter. A method for accelerating the molecular dynamics simulation of infrequent events. *J. Chem. Phys.*, **108**(11):4666–4677, (1997).

[232] A. F. Voter. Hyperdynamics: Accelerated molecular dynamics of infrequent events. *Phys. Rev. Lett.*, **78**(20):3908–3911, (1997).

[233] A. F. Voter, F. Montalenti, and T. C. Germann. Extending the time scale in atomistic simulation of materials. *Annu. Rev. Mater. Res.*, **32**(1):321–346, (2002).

[234] S. Kumar, D. Boudiza, R. H. Swendsen, P. A. Kollman, and J. M. Rosenberg. The weighted histogram analysis method for free-energy calculations on biomolecules. I. The method. *J. Comput. Chem.*, **13**(8):1011–1021, (1992).

[235] M. Sprik and G. Ciccotti. Free energy from constrained molecular dynamics. *J. Chem. Phys.*, **109**(18):7737–7744, (1998).

[236] Y. Komeiji. Implementation of the blue moon ensemble method. *Chem-Bio Inf. J.*, **7**(1):12–23, (2007).

[237] C. Dellago, P. G. Bolhuis, F. S. Csajka, and D. Chandler. Transition path sampling and the calculation of rate constants. *J. Chem. Phys.*, **108**(5): 1964–1977, (1998).

[238] C. Dellago, P. G. Bolhuis, and D. Chandler. Efficient transition path sampling: Application to Lennard-Jones cluster rearrangements. *J. Chem. Phys.*, **108**(22):9236–9245, (1998).

[239] C. Dellago, P. G. Bolhuis, and D. Chandler. On the calculation of reaction rate constants in the transition path ensemble. *J. Chem. Phys.*, **110**(14): 6617–6624, (1999).

[240] C. W. Gear, I. G. Kevrekidis, and C. Theodoropoulos. 'Coarse' integration/bifurcation analysis via microscopic simulators: micro-Galerkin methods. *Comput. Chem. Eng.*, **26**:941–963, (2002).

[241] T. Huber, A. Torda, and W. Gunsteren. Local elevation: a method for improving the searching properties of molecular dynamics simulation. *J. Comput.-Aided Mol. Des.*, **8**:695–708, (1994).

[242] A. Laio, A. Rodriguez-Fortea, F. L. Gervasio, M. Ceccarelli, and M. Parrinello. Assessing the accuracy of metadynamics. *J. Phys. Chem. B*, **109**:6714–6721, (2005).

[243] A. Barducci, G. Bussi, and M. Parrinello. Well-tempered metadynamics: A smoothly converging and tunable free-energy method. *Phys. Rev. Lett.*, **100** (2):020603, (2008).

[244] A. Laio and F. L. Gervasio. Metadynamics: a method to simulate rare events and reconstruct the free energy in biophysics, chemistry and material science. *Rep. Prog. Phys.*, **71**(12):126601, (2008).

[245] S. Piana and A. Laio. A bias-exchange approach to protein folding. *J. Phys. Chem. B*, **111**(17):4553–4559, (2007).

[246] G. A. Tribello, M. Ceriotti, and M. Parrinello. A self-learning algorithm for biased molecular dynamics. *PNAS*, **107**(41):17509–17514, (2010).

[247] M. E. Tipping and C. M. Bishop. Probabilistic principal component analysis. *J. R. Statist. Soc. B*, **61**(3):611–622, (1999).

[248] M. E. Tipping and C. M. Bishop. Mixtures of probabilistic principal component analyzers. *Neural computation*, **11**(2):443–482, (1999).

[249] S. M. Woodley and C. R. A. Catlow. Crystal structure prediction from first principles. *Nat. Mater.*, **7**:937–946, (2008).

[250] M. Parrinello and A. Rahman. Crystal structure and pair potentials: A molecular-dynamics study. *Phys. Rev. Lett.*, **45**(14):1196–1199, (1980).

[251] P. Raiteri, R. Martoňák, and M. Parrinello. Exploring polymorphism: the case of benzene. *Angew. Chem. Int. Ed. (English)*, **44**:3769–3773, (2005).

[252] T. Zykova-Timan, P. Raiteri, and M. Parrinello. Investigating the polymorphism in pr179: a combined crystal structure prediction and metadynamics study. *J. Phys. Chem. B*, **112**:13231–13237, (2008).

[253] R. Martoňák, D. Donadio, A. R. Oganov, and M. Parrinello. Crystal structure transformations in SiO_2 from classical and ab initio metadynamics. *Nat. Mater.*, **5**:623–626, (2006).

[254] B. Beest, G. Kramer, and R. Santen. Force fields for silicas and aluminophosphates based on *ab initio* calculations. *Phys. Rev. Lett.*, **64**(16):1955–1958, (1990).

[255] I. Saika-Voivod, F. Sciortino, T. Grande, and P. Poole. Phase diagram of silica from computer simulation. *Phys. Rev. E*, **70**(6):061507, (2004).

[256] R. Martoňák, D. Donadio, A. R. Oganov, and M. Parrinello. From four- to six-coordinated silica: Transformation pathways from metadynamics. *Phys. Rev. B*, **76**(1), (2007).

[257] A. Oganov, R. Martoňák, A. Laio, and P. Raiteri. Anisotropy of earth's D00 layer and stacking faults in the $MgSi_3$ post-perovskite phase. *Nature*, **438**: 1142–1144, (2005).

[258] R. Car and M. Parrinello. Unified approach for molecular dynamics and density-functional theory. *Phys. Rev. Lett.*, **55**(22):2471–2474, (1985).

[259] Y. Duan and P. A. Kollman. Pathways to a protein folding intermediate observed in a 1-microsecond simulation in aqueous solution. *Science*, **282**: 740–744, (1998).

[260] V. Pande and D. Rokhsar. Molecular dynamics simulations of unfolding and refolding of a β-hairpin fragment of protein G. *PNAS*, **96**:9062–9067, (1999).

[261] S. Piana. Atomistic simulation of the DNA helix coil transition. *J. Phys. Chem. A*, **111**:12349–12354, (2007).

[262] N. Basu, S. Nanda, and P. C. Nayak. *An Introduction to Mechanics*, Chapter 14 - Moment of Inertia. Narosa Publishing House, (1999).

[263] F. Pfeiffer. *Mechanical System Dynamics*, Volume 40 of *Lecture notes in applied and computational mechanics*, Chapter 2. Springer, (2008).

[264] P. Steinhardt, D. Nelson, and M. Ronchetti. Icosahedral bond orientational order in supercooled liquids. *Phys. Rev. Lett.*, **47**(18):1297–1300, (1981).

[265] P. Steinhardt, D. Nelson, and M. Ronchetti. Bond-orientational order in liquids and glasses. *Phys. Rev. B*, **28**(2):784–805, (1983).

[266] F. C. Frank. Supercooling of liquids. *PNAS*, **215**(1120):43–46, (1952).

[267] W. Baur. A three dimensionally periodic, eleven coordinated, dense packing of symmetry equivalent spheres. *Mater. Res. Bull.*, **16**(3):339–345, (1981).

[268] T. C. Hales. A proof of the Kepler conjecture. *Ann. Math.*, **162**(3): 1065–1185, (2005).

[269] T. C. Hales. The sphere packing problem. *J. Comput. Appl. Math.*, **44**: 41–76, (1992).

[270] T. Hales. Flyspeck project, (2010). URL `http://code.google.com/p/flyspeck/`.

[271] D. Nelson and J. Toner. Bond-orientational order, dislocation loops, and melting of solids and smectic-a liquid crystals. *Phys. Rev. B*, **24**(1):363–387, (1981).

[272] J. S. van Duijneveldt and D. Frenkel. Computer simulation study of free energy barriers in crystal nucleation. *J. Chem. Phys.*, **96**(6):4655–4668, (1992).

[273] D. A. Varshalovich, A. N. Moskalev, and V. K. Khersonskii. *Quantum Theory of Angular Momentum*. World Scientific, (1988).

[274] T. M. MacRobert. *Spherical Harmonics*. Pergamon Press, Third edition, (1967).

[275] R. D. Mountain and A. C. Brown. Molecular dynamics investigation of homogeneous nucleation for inverse power potential liquids and for a modified Lennard-Jones liquid. *J. Chem. Phys.*, **80**(6):2730–2734, (1984).

[276] S. Nosé and F. Yonezawa. Isothermal–isobaric computer simulations of melting and crystallization of a Lennard-Jones system. *J. Chem. Phys.*, **84**(3):1803–1814, (1986).

[277] R. M. Lynden-Bell, J. S. van Duijneveldt, and D. Frenkel. Free energy changes on freezing and melting ductile metals. *Mol. Phys.*, **80**(4):801–814, (1993).

[278] P. R. ten Wolde, M. J. Ruiz-Montero, and D. Frenkel. Numerical calculation of the rate of crystal nucleation in a Lennard-Jones system at moderate undercooling. *J. Chem. Phys.*, **104**(24):9932–9947, (1996).

[279] R. Radhakrishnan and B. L. Trout. Nucleation of hexagonal ice (I_h) in liquid water. *J. Am. Chem. Soc.*, **125**:7743–7747, (2003).

[280] D. Quigley and P. M. Rodger. Metadynamics simulations of ice nucleation and growth. *J. Chem. Phys.*, **128**:154518, (2008).

[281] D. Quigley and P. M. Rodger. Free energy and structure of calcium carbonate nanoparticles during early stages of crystallization. *J. Chem. Phys.*, **128**(22): 221101, (2008).

[282] D. Quigley and P. M. Rodger. A metadynamics-based approach to sampling crystallisation events. *Mol. Simul.*, **35**(7):613–623, (2009).

[283] J. M. Matxain, J. E. Fowler, and J. M. Ugalde. Small clusters of II-VI materials: Zn_iS_i, i= 1–9. *Phys. Rev. A*, **61**(5):053201, (2000).

[284] D. C. Sayle and R. L. Johnston. Evolutionary techniques in atomistic simulation: thin films and nanoparticles. *Curr. Opin. Solid State Mater. Sci.*, **7**:3–12, (2003).

[285] D. Wales and H. Scheraga. Global optimization of clusters, crystals, and biomolecules. *Science*, **285**:1368–1372, (1999).

[286] J. Johansson, K. A. Dick, P. Caroff, M. E. Messing, J. Bolinsson, K. Deppert, and L. Samuelson. Diameter dependence of the wurtzite-zinc blende transition in InAs nanowires. *J. Phys. Chem. C*, **114**(9):3837–3842, (2010).

[287] K. F. Lau, H. E. Alper, T. S. Thacher, and T. R. Stouch. Effects of switching functions on the behavior of liquid water in molecular dynamics simulations. *J. Phys. Chem.*, **98**(35):8785–8792, (1994).

[288] S. Fleming and A. L. Rohl. GDIS: A visualization program for molecular and periodic systems. *Zeitschrift für Kristallographie*, **220**(5-6):580–584, (2005).

[289] J. P. Perdew, A. Ruzsinsky, G. I. Csonka, O. A. Vydrov, G. E. Scuseria, L. A. Constantin, X. Zhou, and K. Burke. Restoring the density-gradient expansion for exchange in solids and surfaces. *Phys. Rev. Lett.*, **100**:136406, (2008).

[290] D. Spagnoli, K. Refson, K. Wright, and J. D. Gale. Density functional theory study of the relative stability of the iron disulfide polymorphs pyrite and marcasite. *Phys. Rev. B*, **81**(9):094106, (2010).

[291] J. Junquera, Ó. Paz, D. Sánchez-Portal, and E. Artacho. Numerical atomic orbitals for linear-scaling calculations. *Phys. Rev. B*, **64**(23):235111, (2001).

[292] D. Branduardi, F. L. Gervasio, and M. Parrinello. From A to B in free energy space. *J. Chem. Phys.*, **126**(5):054103, (2007).

[293] E. Catmull and R. Rom. A class of local interpolating splines. In R. E. Barnhill and R. F. Reisenfeld, editors, *Computer-Aided Geometric Design*, pages 317–326. New York Press, (1974).

[294] L. N. Kantorovich. Thermoelastic properties of perfect crystals with nonprimitive lattices. I. General theory. *Phys. Rev. B*, **51**(6):3520–3534, (1995).

[295] N. L. Allan, T. H. K. Barron, and J. A. O. Bruno. The zero static internal stress approximation in lattice dynamics, and the calculation of isotope effects on molar volumes. *J. Chem. Phys.*, **105**(18):8300–8303, (1996).

[296] P. A. Firby and C. F. Gardiner. *Surface Topology.* Mathematics and its applications. Ellis Horwood, 2nd edition, (1991).

[297] Zeolite structure database, (2009). URL `http://www.iza-structure.org/databases`.

[298] P. Raiteri, A. Laio, F. Gervasio, C. Micheletti, and M. Parrinello. Efficient reconstruction of complex free energy landscapes by multiple walkers metadynamics. *J. Phys. Chem. B*, , (2006).

[299] R. Radhakrishnan and B. L. Trout. A new approach for studying nucleation phenomena using molecular simulations: Application to CO_2 hydrate clathrates. *J. Chem. Phys.*, **117**(4):1786–1796, (2002).

[300] D. Quigley, P. M. Rodger, C. L. Freeman, J. H. Harding, and D. M. Duffy. Metadynamics simulations of calcite crystallization on self-assembled monolayers. *J. Chem. Phys.*, **131**:094703, (2009).

[301] S. Angioletti-Uberti, M. Ceriotti, P. Lee, and M. Finnis. Solid-liquid interface free energy through metadynamics simulations. *Phys. Rev. B*, **81** (12):125416, (2010).

[302] M. Bonomi, D. Branduardi, G. Bussi, C. Camilloni, D. Provasi, P. Raiteri, D. Donadio, F. Marinelli, F. Pietrucci, R. A. Broglia, and M. Parrinello. PLUMED: A portable plugin for free-energy calculations with molecular dynamics. *Comput. Phys. Commun.*, **180**:1961–1972, (2009).

[303] W. Smith and T. R. Forester. DL_POLY_2.0: A general-purpose parallel molecular dynamics simulation package. *J. Mol. Graphics*, **14**:136–141, (1996).

[304] S. Hamad and C. R. A. Catlow. Computational study of the relative stabilities of ZnS clusters, for sizes between 1 and 4 nm. *J. Cryst. Growth*, **294**:2–8, (2006).

[305] J. Wang, A. J. Kulkarni, K. Sarasamak, S. Limpijumnong, F. J. Ke, and M. Zhou. Molecular dynamics and density functional studies of a body-centered-tetragonal polymorph of ZnO. *Phys. Rev. B*, **76**(17):172103, (2007).

[306] J. Wang, A. J. Kulkarni, F. J. Ke, Y. L. Bai, and M. Zhou. Novel mechanical behavior of ZnO nanorods. *Comput. Meth. Appl. Mech. Eng.*, **197**:3182–3189, (2008).

[307] B. Wang, X. Wang, and J. Zhao. Atomic structure of the magic $(ZnO)_{60}$ cluster: First-principles prediction of a sodalite motif for ZnO nanoclusters. *J. Phys. Chem. C*, **114**(13):5741–5744, (2010).

[308] A. J. Kulkarni, K. Sarasamak, J. Wang, F. J. Ke, S. Limpijumnong, and M. Zhou. Effect of load triaxiality on polymorphic transitions in zinc oxide. *Mech. Res. Commun.*, **35**:73–80, (2008).

[309] K. Umemoto, R. M. Wentzcovitch, S. Saito, and T. Miyake. Body-Centered Tetragonal C$_4$: A Viable sp^3 Carbon Allotrope. *Phys. Rev. Lett.*, **104**(12): 125504, (2010).

[310] Y. Fujimoto, T. Koretsune, S. Saito, T. Miyake, and A. Oshiyama. A new crystalline phase of four-fold coordinated silicon and germanium. *New J. Phys.*, **10**(8):083001, (2008).

[311] W. A. Dollase and C. R. Ross. Crystal structures of the body-centered tetragonal tectosilicates: K$_{1.14}$Mg$_{0.57}$Si$_{1.43}$O$_4$, K$_{1.10}$Zn$_{0.55}$Si$_{1.45}$O$_4$, and K$_{1.11}$Fe$^3_{1.11}$Si$_{0.89}$O$_4$. *Am. Mineral.*, **78**(5-6):627–632, (1993).

[312] V. Kumar and V. Kumaran. Bond-orientational analysis of hard-disk and hard-sphere structures. *J. Chem. Phys.*, **124**(20):204508, (2006).

[313] B. J. Morgan and P. A. Madden. A molecular dynamics study of structural relaxation in tetrahedrally coordinated nanocrystals. *Phys. Chem. Chem. Phys.*, **9**:2355–2361, (2007).

[314] R. Agrawal, B. Peng, and H. D. Espinosa. Experimental-computational investigation of ZnO nanowires strength and fracture. *Nano Lett.*, **9**(12): 4177–4183, (2009).

[315] C. L. Freeman, F. Claeyssens, and N. L. Allan. Graphitic nanofilms as precursors to wurtzite films: Theory. *Phys. Rev. Lett.*, **96**(6):066102, (2006).

[316] A. Dyer. *An Introduction to Zeolite Molecular Sieves.* John Wiley & Sons Limited, (1988).

[317] IZA Structure Comission, (2009). URL `http://www.iza-structure.org`.

[318] H. van Koningsveld. Structural subunits in silicate and phosphate structures. In H. van Bekkum, E. M. Flanigen, and J. C. Jansen, editors, *Introduction to Zeolite Science and Practice*, Volume 58 of *Studies in surface science and catalysis*, Chapter 3, pages 35–76. Elsevier, (1991).

[319] C. Baerlocher, W. M. Meier, and D. H. Olson. *Atlas of Zeolite Framework Types.* Elsevier, 5th edition, (2001).

[320] L. Moscou. The zeolite scene. In H. van Bekkum, E. M. Flanigen, and J. C. Jansen, editors, *Introduction to Zeolite Science and Practice*, Volume 58 of

Studies in surface science and catalysis, Chapter 1, pages 1–12. Elsevier, (1991).

[321] D. W. Breck. *Zeolite Molecular Sieves: Structure, chemistry and use.* John Wiley & Sons Limited, (1974).

[322] S. M. Csicsery. Shape-selective catalysis in zeolites. *Zeolites*, **4**:202–213, (1984).

[323] C. Catlow. Zeolites: Structure, synthesis and properties - an introduction. In C. Catlow, editor, *Modelling of Structure and Reactivity in Zeolites*, Chapter Zeolites: Structure, Synthesis and Proerties - An Introduction, pages 1–17. Academic Press, (1992).

[324] C. R. A. Catlow, S. A. French, A. A. Sokol, A. A. Al-Sunaidi, and S. M. Woodley. Zinc oxide: A case study in contemporary computational solid state chemistry. *J. Comput. Chem.*, **29**(13):2234–2249, (2008).

[325] J. Carrasco, F. Illas, and S. T. Bromley. Ultralow-density nanocage-based metal-oxide polymorphs. *Phys. Rev. Lett.*, **99**:235502, (2007).

[326] S. T. Bromley and E. Flikkema. New materials from fully coordinated SiO_2 nanoclusters. *Comput. Mater. Sci.*, **35**:382–386, (2006).

[327] E. Flikkema and S. T. Bromley. Dedicated global optimization search for ground state silica nanoclusters: $(SiO_2)_N$ (N=6-12). *J. Phys. Chem. B*, **108**(28):9638–9645, (2004).

[328] J. C. Wojdel, M. A. Zwijenburg, and S. T. Bromley. Magic silica clusters as nanoscale building units for super-(tris)tetrahedral materials. *Chem. Mater.*, **18**(6):1464–1469, (2006).

[329] P. J. Ziemann and A. W. Castleman. Stabilities and structures of gas phase MgO clusters. *J. Chem. Phys.*, **94**(1):718–728, (1991).

[330] S. M. Woodley, M. B. Watkins, A. A. Sokol, S. A. Shevlin, and C. R. A. Catlow. Construction of nano-and microporous frameworks from octahedral bubble clusters. *Phys. Chem. Chem. Phys.*, **11**:3176–3185, (2009).

[331] M. B. Watkins, S. A. Shevlin, A. A. Sokol, B. Slater, C. R. A. Catlow, and S. M. Woodley. Bubbles and microporous frameworks of silicon carbide. *Phys. Chem. Chem. Phys.*, **11**:3186–3200, (2009).

[332] M. A. Zwijnenburg, F. Illas, and S. T. Bromley. Apparent scarcity of low-density polymorphs of inorganic solids. *Phys. Rev. Let.*, **104**:175503, (2010).

[333] D. Wagman, W. Evans, V. Parker, and R. Schumm. The NBS tables of chemical thermodynamic properties: selected values for inorganic and C1 and C2 organic substances in SI units. *J. Phys. Chem. Ref. Data*, **11**(Supp. 2):1, (1982).

[334] D. R. Lide, editor. *CRC Handbook of Chemistry and Physics*. CRC Press, 90th edition, (2010).

[335] G. A. Samara. Temperature and pressure dependences of the dielectric constants of semiconductors. *Phys. Rev. B*, **27**(6):3494–3505, (1983).

[336] N. J. Henson, A. K. Cheetham, and J. D. Gale. Theoretical calculations on silica frameworks and their correlation with experiment. *Chem. Mater.*, **6**: 1647–1650, (1994).

[337] B. J. Morgan. Preferential stability of the d-BCT phase in ZnO thin films. *Phys. Rev. B*, **80**(17):174105, (2009).

[338] A. Navrotsky, O. Trofymluk, and A. A. Levchenko. Thermochemistry of microporous and mesoporous materials. *Chem. Rev.*, **109**(9):3885–3902, (2009).

[339] A. Navrotsky. Energetics of nanoparticle oxides: interplay between surface energy and polymorphism. *Geochem. Trans.*, **4**(6):34–37, (2003).

[340] A. Navrotsky. Energetic clues to pathways to biomineralization: Precursors, clusters, and nanoparticles. *PNAS*, **101**(33):12096–12101, (2004).

[341] K. J. Edwards, P. L. Bond, G. K. Druschel, M. M. McGuire, R. J. Hamers, and J. F. Banfield. Geochemical and biological aspects of sulfide mineral dissolution: lessons from iron mountain, california. *Chem. Geol.*, **169**(3-4): 383–397, (2000).

[342] D. B. Johnson and K. B. Hallberg. Acid mine drainage remediation options: a review. *Sci. Total Environ.*, **338**:3–14, (2005).

[343] B. J. Baker and J. F. Banfield. Microbial communities in acid mine drainage. *FEMS Microbiol. Ecol.*, **44**:139–152, (2003).

[344] C. Blodau. A review of acidity generation and consumption in acidic coal mine lakes and their watersheds. *Sci. Total Environ.*, **369**:307–332, (2006).

[345] M. Labrenz, G. K. Druschel, T. Thomsen-Ebert, B. Gilbert, S. A. Welch, K. M. Kemner, G. A. Logan, R. E. Summons, G. D. Stasio, P. L. Bond, B. Lai, S. D. Kelly, and J. F. Banfield. Formation of sphalerite (ZnS) deposits in natural biofilms of sulfate-reducing bacteria. *Science*, **290**:1744–1747, (2000).

[346] S. F. Boys and F. Bernardi. The calculation of small molecular interactions by the differences of separate total energies. Some procedures with reduced errors. *Mol. Phys.*, **19**:533–566, (1970).

[347] B. Paizs and S. Suhai. Comparative study of BSSE correction methods at DFT and MP2 levels of theory. *J. Comput. Chem.*, **19**(6):576–584, (1998).

[348] F. B. van Duijneveldt, J. G. C. M. van Duijneveldt-van de Rijdt, and J. H. van Lenthe. State of the art in counterpoise theory. *Chem. Rev.*, **94**: 1873–1885, (1994).

[349] P. Raiteri, J. D. Gale, D. Quigley, and P. M. Rodger. Derivation of an accurate force-field for simulating the growth of calcium carbonate from aqueous solution: A new model for the calcite water interface. *J. Phys. Chem. C*, **114**(13):5997–6010, (2010).

[350] J. Aqvist. Ion-water interaction potentials derived from free energy perturbation simulations. *J. Phys. Chem.*, **94**(21):8021–8024, (1990).

[351] M. R. Shirts, J. W. Pitera, W. C. Swope, and V. S. Pande. Extremely precise free energy calculations of amino acid side chain analogs: Comparison of common molecular mechanics force fields for proteins. *J. Chem. Phys.*, **119** (11):5740–5761, (2003).

[352] T. C. Beutler, A. E. Mark, R. C. van Schaik, P. R. Gerber, and W. F. van Gunsteren. Avoiding singularities and numerical instabilities in free energy calculations based on molecular simulations. *Chem. Phys. Lett.*, **222**: 529–539, (1994).

[353] E. Lindahl, B. Hess, and D. van der Spoel. GROMACS 3.0: a package for molecular simulation and trajectory analysis. *J. Mol. Model.*, **7**:306–317, (2001).

[354] J. W. Pitera and W. F. van Gunsteren. A comparison of non-bonded scaling approaches for free energy calculations. *Mol. Simul.*, **28**(1-2):45–65, (2002).

[355] B. Hess and N. F. A. van der Vegt. Hydration thermodynamic properties of amino acid analogues: A systematic comparison of biomolecular force fields and water models. *J. Phys. Chem. B*, **110**(35):17616–17626, (2006).

[356] Y. Marcus. Thermodynamics of solvation of ions. part 5.—gibbs free energy of hydration at 298.15 k. *J. Chem. Soc., Faraday Trans.*, **87**(18):2995–2999, (1991).

[357] P. Raiteri. Personal communication, (2011).

[358] W. Bol, G. J. A. Gerrits, and C. L. van Panthaleon van Eck. The hydration of divalent cations in aqueous solution. An X-ray investigation with isomorphous replacement. *J. Appl. Cryst.*, **3**:486–492, (1970).

[359] Y. Marcus. Ionic radii in aqueous solutions. *Chem. Rev.*, **88**:1475–1498, (1988).

[360] G. Laurenczy, Y. Ducommun, and A. E. Merbach. Variable-pressure kinetic and equilibrium study of monocomplex formation of copper (ii) and zinc (ii) with 2-chloro-1, 10-phenanthroline in aqueous solution. *Inorg. Chem.*, **28** (15):3024–3028, (1989).

[361] H. Ohtaki and T. Radnai. Structure and dynamics of hydrated ions. *Chem. Rev.*, **93**(3):1157–1204, (1993).

[362] D. H. Gay and A. L. Rohl. MARVIN: A new computer code for studying surfaces and interfaces and its application to calculating the crystal morphologies of corundum and zircon. *J. Chem. Soc. Faraday Trans.*, **91** (5):925–936, (1995).

[363] C. B. Duke. Structure and bonding of tetrahedrally coordinated compound semiconductor cleavage faces. *J. Vac. Sci. Technol. A*, **10**(4):2032–2040, (1992).

[364] H. M. Steele, K. Wright, and I. H. Hillier. A quantum-mechanical study of the (110) surface of sphalerite (ZnS) and its interaction with Pb^{2+} species. *Phys. Chem. Minerals*, **30**:69–75, (2003).

[365] C. B. Duke, A. Paton, and A. Kahn. The atomic geometries of gap (110) and ZnS (110) revisited: A structural ambiguity and its resolution. *J. Vac. Sci. Technol. A*, **2**(2):515–518, (1984). ergy.

[366] M. J. Elrod and R. J. Saykally. Many-body effects in intermolecular forces. *Chem. Rev.*, **94**:1975–1997, (1994).

[367] L. Perera and M. L. Berkowitz. Many-body effects in molecular dynamics simulations of $Na^+(H_2O)_n$ and $Cl^-(H_2O)_n$ clusters. *J. Chem. Phys.*, **95**(3): 1954–1963, (1991).

[368] S. Iuchi, S. Izvekov, and G. A. Voth. Are many-body electronic polarization effects important in liquid water? *J. Chem. Phys.*, **126**:124505, (2007).

[369] C. C. Yang and S. Li. Size-dependent temperature-pressure phase diagram of carbon. *J. Phys. Chem. C*, **112**:1423–1426, (2008).

[370] J. D. Gale, P. Raiteri, and A. C. T. van Duin. A reactive force field for aqueous-calcium carbonate systems. *Phys. Chem. Chem. Phys.*, **13**: 16666–16679, (2011).

[371] M. F. Russo, R. Li, M. Mench, and A. C. T. van Duin. Molecular dynamic simulation of aluminum-water reactions using the ReaxFF reactive force field. *Int. J. Hydrogen Energy*, **36**:5828–5835, (2011).

[372] G. W. Luther and D. T. Rickard. Metal sulfide cluster complexes and their biogeochemical importance in the environment. *J. Nanopart. Res.*, **7**:389–407, (2005).